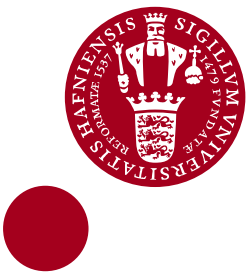

UNIVERSITY OF COPENHAGEN

Optical Frequency References

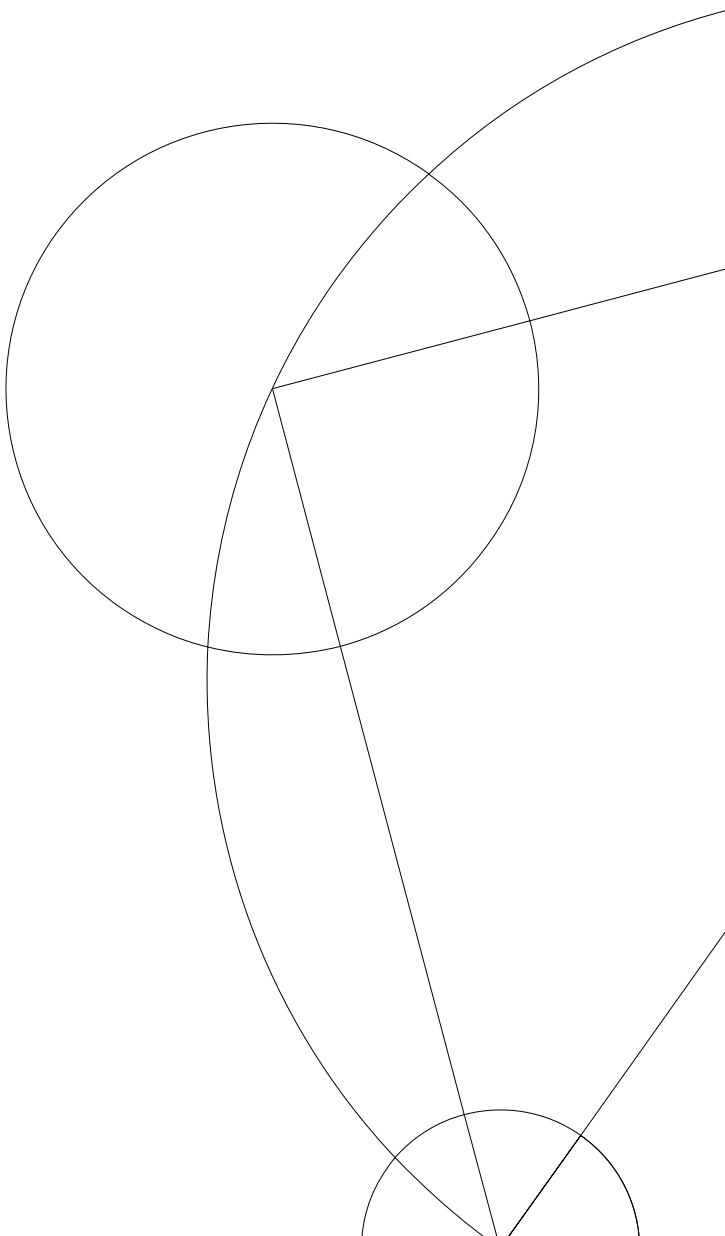

Ph.D. thesis

By

Martin Romme Henriksen

Niels Bohr Institutet

August 2019

Optical Frequency References

Author
Martin Romme Henriksen
romme@nbi.ku.dk

Academic advisor
Jan W. Thomsen

As partial fulfillment of the requirements for the degree of
Doctor of Philosophy

Submitted to the University of Copenhagen on August 22, 2019.

Quantum Metrology
Niels Bohr Institute
University of Copenhagen
Blegdamsvej 17
DK-2100 København Ø
Denmark

Abstract

Ultra-stable and accurate frequency references have a large number of applications within the fields of metrology, communication, and spectroscopy. This work presents three projects with focus on compactness and cost: An acetylene frequency reference, micro-resonator Kerr frequency combs, and a strontium atomic clock.

The acetylene frequency reference is a compact, frequency stabilized laser system with a frequency noise at the Hz-level. Here, a fiber laser is stabilized to the P(16)$\nu_1 + \nu_3$ ro-vibrational line in carbon-13 ethyne (acetylene) at 1542 nm. The setup is based on the Noise-Immune Cavity-Enhanced Optical Heterodyne Molecular Spectroscopy (NICE-OHMS) technique. This technique generates a spectroscopy signal of the acetylene line with a signal-to-noise ratio of 10^4 and a signal bandwidth of 2 MHz, allowing for stabilization using the molecular line alone. A frequency stability of 25 Hz at 0.2 s is achieved.

The combination of the acetylene frequency reference with a compact frequency comb will provide not only a broad bandwidth reference at optical frequencies but also at microwave frequencies. In this work chip-based micro-resonator Kerr frequency combs are investigated. A waveguide resonator design in aluminium gallium arsenide (AlGaAs) with tapered regions is presented. This design shows high flexibility of dispersion engineering while maintaining single-mode operation. The fabricated micro-resonators' dispersion profiles are measured on a system using a low-FSR Fabry-Pérot reference cavity. With this simple and low-cost system, low-noise measurements of the micro-resonators' dispersion are obtained. Alternative material platforms are also discussed as well as different stabilization techniques suitable for optical Kerr frequency combs.

The NICE-OHMS technique is also applied to a cold ensemble of strontium atoms. In this proof-of-principle experiment the $^1S_0 \leftrightarrow {}^3P_1$ transition in ^{88}Sr is used as a reference. Interrogation of a cold ensemble of strontium atoms, with a cycle time as low as 10 ms, is achieved producing a spectroscopic signal with a signal-to-noise ratio of 115.

Sammenfatning

Ultra-stabile og nøjagtige frekvensreferencer har mange anvendelser indenfor både metrologi, kommunikation og spektroskopi. Denne afhandling præsenterer tre projekter med fokus på kompakthed og omkostning: en acetylen-frekvensreference, mikro-resonator Kerr frekvenskamme og et strontium-atomur.

Acetylen-frekvensreferencen er et kompakt frekvensstabiliseret lasersystem med en frekvensstøj på Hz-niveau. Dette system er baseret på en fiberlaser, som er stabiliseret til den ro-vibrationelle linje P(16) ($\nu_1 + \nu_3$) i carbon-13 ethyn (acetylen). Dette giver en stabiliseret laser med en bølgelængde på 1542 nm. Denne laser anvender en spektroskopi teknik kaldet NICE-OHMS (Noise-Immune Cavity-Enhanced Optical Heterodyne Molecular Spectroscopy). Med denne teknik opnås et spektroskopisignal med et signal-til-støj-forhold på 10^4 og en båndbredde på 2 MHz. Dette spektroskopisignal giver en frekvensstabilitet på 25 Hz ved 0.2 s alene ved stabilisering til den molekylære linje.

Ved at kombinere denne acetylen frekvensreference med en optisk frekvenskam, kan man opnå frekvensreference der dækker et meget stort spektrum, både ved optiske frekvenser og mikrobølgefrekvenser. I denne afhandling præsenteres en række undersøgelser af chip-baseret mikroresonator-frekvenskamme der genereres ved hjælp af den optiske Kerr effekt. Mikroresonatorer lavet af bølgeledere i materialet aluminiumgalliumarsenid (AlGaAs) er blevet designet med specifikke indsnævringer. Denne resonatortype viser en høj grad af fleksibilitet i designet af resonator- dispersion. Dispersionsprofilerne for disse resonatorer måles i en opstilling hvor en optisk Fabry-Pérot kavitet bruges som reference. Derved opnås meget præcise målinger af resonatordispersionen med en simple metode der ikke kræver dyrt udstyr. Alternative materiale til generering af frekvenskamme i mikroresonatorer og stabilisering af frekvenskamme bliver også gennemgået.

NICE-OHMS-teknikken bliver også anvendt til spektroskopi på ultra kolde strontiumatomer. I dette eksperiment bliver den smalle $^1S_0 \leftrightarrow {}^3P_1$ overgang i ^{88}Sr brugt som en reference til frekvensstabilisering. Med denne metode er det muligt at måle på atomerne med meget høj rate og derved opnås en cyklustid ned til 10 ms. Et spektroskopisignal med et signal-til-støj-forhold på 115 bliver vist.

It has been a pleasure working in the quantum metrology group where I have enjoyed the company of Bjarke T. R. Christensen, Stefan A. Schäffer, Asbjørn A. Jørgensen, and Jan W. Thomsen. Thank you for the help, the late nights in the laboratory, and all the fun.

I am grateful to my parents for all the support they have given me. Additionally, my eternal gratitude goes to Tina, Laurits, Julie, Christoffer, Ellen and Magne. Through the last 4 years they have been the pillars of my everyday life. Thank you for all the meals and for your patience.

Contents

List of Figures

List of Abbreviations

AOM	Acousto-Optic Modulator. 35, 36, 43, 53, 54, 57, 58, 102, 104, 107, 114
CIPM	Comité International des Poids et Mesures. 1
DACs	Digital to Analogue Converters. 9
DDS	Direct Digital Synthesizer. 37
ECDL	External Cavity Diode Laser. 31, 101, 102, 111
EOM	Electro-Optic Modulator. 12, 13, 15, 16, 18, 19, 34, 35, 43, 52, 53, 56, 57, 61, 81, 94, 102, 105
FSR	Free Spectral Range. 7, 8, 15, 16, 20, 35, 36, 38, 58, 67, 68, 71, 74, 80, 81, 87, 97, 106
FWHM	Full Width Half Maximum. 82, 95
FWM	Four-Wave Mixing. 67, 69–73, 92
ITU	International Telecommunication Union. 4
LIDAR	Laser-based light detection and ranging. 8
MOT	Magneto-Optical Trap. 99, 100, 104, 105, 107, 108
MRR	Micro Ring Resonator. 68–70, 79–81, 83, 84, 93–97
NICE-OHMS	Noise-Immune Cavity-Enhanced Optical Heterodyne Molecular Spectroscopy. 9, 13, 15, 17–19, 27, 34, 35, 37, 38, 56, 57, 60, 99, 104–109, 111, 113, 115
OFC	Optical Frequency Comb. 5–9, 65
PBS	Polarizing Beam Splitter. 102
PDH	Pound-Drever-Hall. 11–14, 16, 17, 34–36, 39, 43, 57, 58, 93, 94, 102, 103, 105, 111
PSD	Power Spectral Density. 46, 48, 49
RAM	Residual Amplitude Modulation. 17, 18, 34, 35, 48, 50, 52, 53, 56, 57

RF	Radio Frequency. 6, 7
SPM	Self-phase Modulation. 70
TOD	Third Order Dispersion. 75
TPA	Two Photon Absorption. 68, 87
VCO	Voltage Controlled Oscillator. 35, 36, 102

Preface

In this thesis I will present some of the work done during my time as a Ph.D. fellow at the Niels Bohr Institute in Copenhagen. Here I have had the joy of being part of the Quantum Metrology group under supervision of Jan W. Thomsen. This thesis presents the 3 major projects that I have been working on, an acetylene frequency reference, micro-resonator Kerr frequency combs and a strontium frequency reference. The Ph.D. project has been a part of the SPOC center of excellence. The SPOC center's goals include fundamental research on optical silicon chips with the focus of telecommunication capacity and energy efficiency. As such, I have had a lot of collaboration with DTU Photonics across various research groups.

Additional founding for acetylene frequency reference has been given by the Danish innovation foundation under the quantum technology grants known as QuBiz. Though this QuBiz project I have had the pleasure of working with the Danish National Metrology Institute (DFM) where Jan Hald has been very helpful with both loan of equipment and the supply of isotope pure acetylene.

During my time as a Ph.D. fellow I spend 5 months at the University of California, Los Angeles (UCLA) in the Mesoscopic Optics and Quantum Electronics Laboratory under Professor Chee Wei Wong. There I worked on stabilizing a Si_3N_4 micro-resonator Kerr frequency comb to an acetylene referenced laser. My stay at UCLA gave me a lot experience in working with micro-resonator Kerr combs and some good friends along the way.

Publications

- B. T. R. Christensen, **M. R. Henriksen**, S. A. Schäffer, P. G. Westergaard, D. Tieri, J. Ye, M. J. Holland, and J. W. Thomsen, *Nonlinear Spectroscopy of Sr Atoms in an Optical Cavity for Laser Stabilization*, Physical Review A, 2015, Vol. 92(5), pp. 053820. American Physical Society.

- P. G. Westergaard, J. W. Thomsen, **M. R. Henriksen**, M. Michieletto, M. Triches, J. K. Lyngsø, and J. Hald, *Compact, CO_2-stabilized tuneable laser at 2.05 microns*, Optics Express, 2016, Vol. 24(5), pp. 4872. Optical Society of America.

- S. A. Schäffer, B. T. R. Christensen, S. M. Rathmann, M. H. Appel, **M. R. Henriksen**, and J. W. Thomsen, *Towards passive and active laser stabilization using cavity-enhanced atomic interaction*, Journal of Physics: Conference Series, 2017, Vol. 810(1), pp. 012002.

- S. A. Schäffer, B. T. R. Christensen, **M. R. Henriksen**, and J. W. Thomsen, *Dynamics of bad-cavity-enhanced interaction with cold Sr atoms for laser stabilization*, Physical Review A, 2017, Vol. 96(1), pp. 1-10.

- Y. Zheng, M. Pu, A. Yi, B. Chang, T. You, K. Huang, A. N. Kamel, **M. R. Henriksen**, A. A. Jørgensen, X. Ou, and H. Ou, *High quality factor, high confinement microring resonators in 4H-silicon carbide-on-insulator*, Optics Express, 2019, Vol. 27(9), pp. 13053-13060, Optical Society of America.

Under Review

- S. A. Schäffer, M. Tang, **M. R. Henriksen**, A. A. Jørgensen, B. T. R. Christensen, and J. W. Thomsen, *Lasing on a narrow transition in a cold thermal strontium ensemble*, Physical Review A, 2019.

Conference Contributions

IFCS-EFTF (Denver, CO, U.S.A.), 2015
B. T. R. Christensen, S. A. Schäffer, **M. R. Henriksen**, P. G. Westergaard, J. Ye and J. W. Thomsen, *Laser Stabilization on Velocity Dependent Nonlinear Dispersion of Sr Atoms in an Optical Cavity*, Talk, Poster prize, Proceeding paper.

ECAMP (Frankfurt, Germany), 2016
S. A. Schäffer, B. T. R. Christensen, S. M. Rathmann, M. H. Appel, **M. R. Henriksen**, J. Ye, and J. W. Thomsen, *Superflourescent-like Behaviour of an Ensemble of Thermal Stronitum Atoms with Cavity-Enhanced Interaction*, Poster.

ICSLS (Torún, Poland), 2016
S. A. Schäffer, B. T. R. Christensen, S. M. Rathmann, M. H. Appel, **M. R. Henriksen**, J. Ye, and J. W. Thomsen, *Towards passive and active laser stabilization using an ensemble of thermal strontium atoms with cavity-enhanced interaction*, Invited talk.

CLEO (Santa Jose, CA, USA), 2017
M. R. Henriksen, A. N. Kamel, M. Pu, K. Yvind and J. W. Thomsen, *Towards Actively Stabilized Micro Ring Resonator Based Frequency Combs*, Poster.

7th International Workshop on Ultra-cold Group II Atoms, (Beijing, China), 2018
B. T. R. Christensen, S. A. Schäffer, **M. R. Henriksen**, M. Tang, A. A. Jørgensen, and J. W. Thomsen, *Laser Stabilization with Thermal Atom-cavity Systems*, Talk.

ICAP (Barcelona, Spain), 2018
M. Tang, S. A. Schäffer, **M. R. Henriksen**, A. A. Jørgensen, J. W.

Thomsen, *Modelling Lasing on a Forbidden Transition in a Thermal Cloud of Sr Atoms*, Poster.

676 W.E. Haereus Seminar (Bonn, Germany), 2018

- **M. R. Henriksen**, C. Raahauge, S. A. Schäffer, A. A. Jørgensen and J. W. Thomsen, *Acetylene Frequency Reference*, Talk.
- S. A. Schäffer, M. Tang, **M. R. Henriksen**, and J. W. Thomsen, *Lasing on a forbidden transition in a thermal cloud of Strontium atoms*, Talk.
- A. A. Jørgensen, **M. R. Henriksen**, S. A. Schäffer, and J. W. Thomsen, *Folded-beam waist-expanding cavity for Iodine based frequency reference*, Poster.

DFS (Fyn, Denmark) 2018

- S. A. Schäffer, M. Tang, **M. R. Henriksen**, and J. W. Thomsen, *Lasing on a forbidden transition in cold ^{88}Sr — frequency references*, Talk.
- M. Tang, S. A. Schäffer, **M. R. Henriksen**, A. A. Jørgensen, and J. W. Thomsen, *Dynamics of a laser using cold Sr atoms*, Poster.

CLEO (Santa Jose, CA, USA), 2019

Y. Zheng, M. Pu, A. Yi, A. N. Kamel, **M. R. Henriksen**, A. A. Jørgensen, X. Ou and H. Ou, *Fabrication of high-Q, high-honfinement 4H-SiC microring resonators by surface roughness reduction*, Talk.

In Writing

- **M. R. Henriksen**, A. A. Jørgensen, S. A. Schäffer, and J. W. Thomsen, *Acetylene frequency reference*, 2019.
- A. A. Jørgensen, **M. R. Henriksen** and D. Zibar, *Laser frequency noise estimation using machine learning*, 2019.

1

An Introduction to Optical Metrology

In this chapter I give a brief introduction into the field of optical frequency metrology. The relationship between the speed of light, the SI base units, and the definition of the second is presented. This is followed by an introduction to the concept of atomic clocks and optical molecular frequency references. Concluding this chapter is an overview of the applications of optical frequency combs within metrology and other areas of research and technology.

In the start of the 20th century, Planck, Einstein [1], and Bohr [2] first described the idea that light and atoms have discrete quanta of energy. This was the foundation of one of the hottest fields within physics today: Quantum mechanics. Since the very beginning, precise spectroscopy of atoms and molecules has been an important tool within quantum mechanics. The need for high-precision spectroscopy generated a lot of research resulting in an impressive development within the field of optical frequency metrology. The evolution within this field has led to the most precise measurements across all fields of science and technology. Optical atomic clocks and optical ion clocks are the most precise and accurate absolute references known. Today, the best atomic clocks allow for measurement of the 18th digit [3, 4, 5, 6, 7, 8, 9, 10, 11, 12].

Mise en Pratique

In 1955 the first caesium atomic clock was build by L. Essen and J. Parry [13]. Only 12 years later in 1967 the Comité International des Poids et Mesures (CIPM) redefined the second from being based on the earth's motion to being based on the transition frequency of the caesium clock transition. As time measurements have become more stable and precise, other units of measure have been redefined and are now based on the second. In 1983 the definition of the meter was changed to:

> "The metre is the length of the path travelled by light in vacuum during a time interval of 1/299 792 458 of a second." [14]

Here the speed of light in vacuum is a fundamental constant taking the value $c_0 = 299792458$ m/s.

Today, length is thought of as the path a plane electromagnetic wave travels in a time t. Length measurements are thereby done by measuring time:

$$l = c_0 t.$$

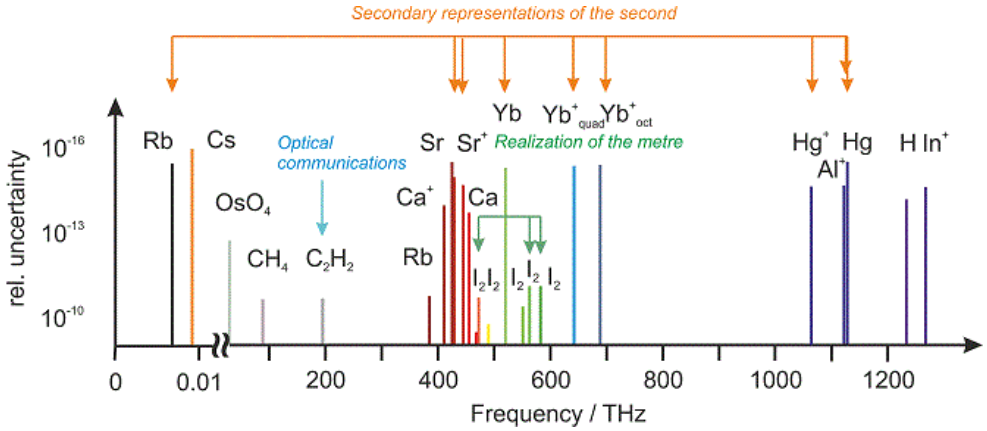

Figure 1.1: The atomic, ionic, and molecular references for the practical realization of the meter. The illustration show the reference frequency of the different reference species and their achieved relative uncertainty as of November 2018. Figure taken from [16].

Equivalently, length can be measured based on the wavelength, λ, of a plane electromagnetic wave in vacuum, based on the relation: $\lambda = c/f$. Thus, an electromagnetic wave with a low frequency uncertainty will allow for length measurements of low uncertainty.

A number of atomic, ionic, and molecular references have been chosen as practical realizations of the meter, known as *Mise en Pratique for the definition of the metre* [15, 16]. A subset of these can also be used as secondary representations of the second. Figure 1.1 shows the different species currently defined as references for the meter, arranged according to their transition frequency.

In November 2018, the 26th General Conference on Weights and Measures voted unanimously to redefine the kilogram, Kelvin, Ampere, and mole to be based on fixed fundamental constants. This meant that all SI base units now are tied to the definition of the second[1] and thereby referenced to the caesium clock transition. Optical frequency references have, thereby, become an important tool for precision measurements of any physical quantity.

1.1 Optical Frequency References

Optical clocks have undergone a tremendous development and continue to improve. Today's state-of-the-art clocks all use the same basic principle where the clock's stability is based on an optical reference cavity and the clock's accuracy on an atomic or ionic reference (see figure 1.2). The advantage of the optical clock is the access to references with ultra-high Q resonances: transitions in atoms, ions, and molecules. The achievable instability is inversely

[1]With the exception of the mole which is based on the Avogadro constant.

proportional to the Q-value of the reference used to stabilize an oscillator [17]:

$$\sigma(\tau) = \frac{1}{K}\frac{1}{Q}\frac{1}{SNR}\sqrt{\frac{T_C}{\tau}}. \tag{1.1}$$

Here, $\sigma(\tau)$ is the uncertainty of the mean frequency for a measurement time τ. K is a constant that depends on the line shape and is of the order unity. The SNR is the signal-to-noise ratio of the interrogation signal from the reference, and T_C is the clock cycle time.

The strontium atom has a strongly forbidden optical transition with a narrow linewidth, $\delta\nu$, compared to its optical resonance frequency, ν. For the commonly used clock transition in Sr-atoms, $^1\mathrm{S}_0 \leftrightarrow {}^1\mathrm{P}_1$, a $Q = \frac{\nu}{\delta\nu}$ of the order of 10^{14} has been realized. The upper level of the clock transition used in Sr lattice clocks has been measured to have a lifetime of 140 s [18]. This corresponds to a radiative linewidth of 1.1 mHz. This would in theory give a Q of 4×10^{17}. The difference between the theoretical and realized Q is due to limitations on the spectroscopic resolution. The limitations include the linewidth of the interrogation laser and the achievable interrogation time of the atomic sample. Because of this, a lot of effort has gone into improving the stability of the interrogation laser, also called the clock laser.

Current state-of-the-art, ultra-narrow linewidth lasers utilize Fabry-Pérot optical resonators, also known as optical cavities. These cavities typically consist of two high-reflecting mirrors facing each other, fixed to a mechanically stable spacer. The relative frequency stability of a resonant mode, $\delta\nu/\nu$, is proportional to the cavity's length stability, $\delta L/L$. To increase the stability, there are two options: increase the length of the cavity or reduce the length fluctuations. The length of the cavity spacer is quickly limited by the high requirement for mechanical stability. By careful consideration of the material and the geometric design of the cavity spacer holding the mirrors, the length fluctuation have been reduced to a level of $\delta L/L \approx 10^{-16}$ at 1 s [19, 20, 21]. At this level the Brownian motion of the atoms, forming the reflective coating on the mirrors, will be a limitation to the stability of a resonant mode. One technique to reduce this effect is crystalline, multi-layer mirror coatings [22]. This has shown a tenfold improvement of the thermal noise level in optical reference cavities compared to conventional, dielectric mirror coatings. Further improvement of optical reference cavities requires cryogenic cooling and thorough mitigation of vibrations.

One of the efforts in the metrology community is to develop a highly stable and ultra-narrow resonance to be used as a reference for an optical local oscillator. The work presented in this thesis is based on the idea of using a narrow optical transition in atoms or molecules as a primary reference for stabilization. It has been shown that the narrow intercombination line at 689 nm in ^{88}Sr can be used as a substitute for a high-finesse optical reference cavity [23, 24, 25, 26]. A theoretical shot-noise limited linewidth of an oscillator

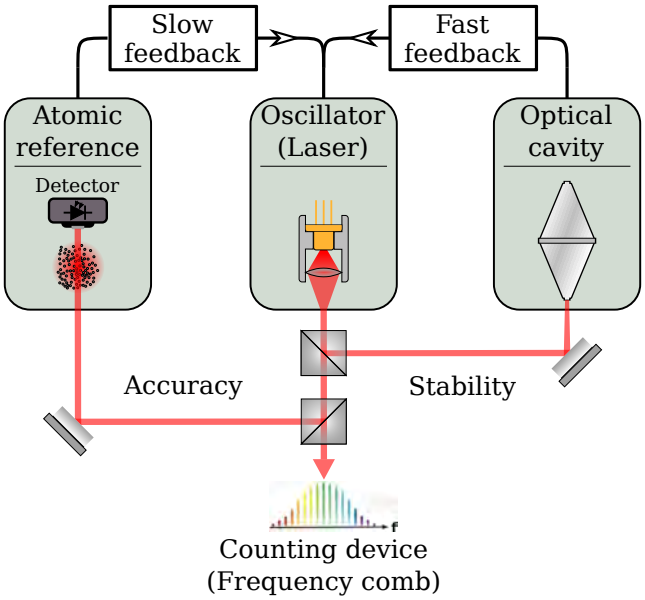

Figure 1.2: The principle of an atomic clock. The combination of the high Q-value and high bandwidth response of an optical Fabry-Pérot resonator (cavity) provides a high degree of stability to the oscillator. The fundamental nature of an atomic transition's resonance frequency allows for an absolute reference. This reference provides a very high degree of accuracy for the oscillator.

stabilized in this way will be approximately 40 mHz. In chapter 5, the first realization of active feedback on a local oscillator using the error-signal from cavity enhanced spectroscopy of ^{88}Sr-atoms is presented.

Molecular References

As laser technology has improved, more and more systems rely on lasers. Telecommunication is a good example. Today all the major data transmission networks use optical signals in fibers. A lot of research is currently being conducted across industry and academia focused on doing the signal processing in the optical regime. As more and more aspects of telecommunication move to the optical regime, the need for high-performance lasers increases, and ultra-low phase-noise lasers could prove to be a necessity.

The exponential increase in traffic on the Internet requires a persistent expansion of the capacity of optical communication. Employing highly stable lasers for optical communication will allow for a significant reduction of guard-bands in the ITU-grid[2], facilitating much more data within a given bandwidth.

[2]The International Telecommunication Union (ITU) grid is a frequency grid that governs which frequency are allowed for use in fiber-optic communication.

Requirements on phase-tracking will also be greatly reduced, possibly removing the need for computational phase correction in the optical-to-electronic signal conversion. For this to be possible, the lasers will need a stability far greater than low-cost commercial lasers offer today. At the same time, the size, the price, and the system complexity have to be compatible with use in optical communication hubs around the world.

Interrogation of narrow atomic transitions requires complex systems including ultra-high vacuum, several stages of laser cooling, and expert personnel for maintenance and operation. This makes current atomic clocks unsuitable for integration into today's communication network. Cavity enhanced molecular spectroscopy is possible with a substantially simpler system. Molecular based frequency references are typically based on spectroscopy of room temperature molecules, removing the need for laser cooling and vacuum system. The coupling between rotational, vibrational, and electron-dipole modes of molecules results in Q-values of more than 10^{10} limited by line broadening effects of the spectroscopy of a gas. As shown in this work, the implementation of cavity enhanced spectroscopy can help mitigate these broadening effects and keep the spatial footprint of the required optics to a minimum. Molecular references can thereby offer a low-cost, low maintenance, and compact alternative to state-of-the-art atomic references.

The market for optical references is currently limited to state-of-the-art frequency stability ($<$ 1 Hz @ 1 s) at a very high cost or low-cost systems with inferior stability performance ($>$ 1 kHz @ 1 s). In this work we aim to achieve a highly stable, low-cost, and compact system.

The Clock

> "The three essentials of clocks are as follows: a source of regular events, a counter/integrator to totalize the events, and a suitable readout mechanism to present the current result to an interested human or machine."
>
> - *John L. Hall*, [27]

Optical frequency references are often referred to as optical clocks, when in fact they only constitute a part of a clock, namely a stabilized oscillator. In the quote above from John L. Hall's Nobel lecture, the three essential elements of a clock is given: the oscillator, the counter and the readout mechanism. Here, the strength of the optical frequency reference - the high oscillation frequency, becomes a challenge. How do you count 400 000 000 000 000 events in one second? The next section in this chapter gives an introduction to the extremely powerful tool that is the Optical Frequency Comb (OFC).

1.2 Optical Frequency Combs

One of the major breakthroughs within optical metrology was the development of the OFC. In 2005 John L. Hall received a Nobel prize (shared with Theodor W. Hänsch and Roy J. Glauber) for his work with mode-locked lasers and precision spectroscopy. Since then the OFC has proven an important tool, not only in optical clocks but, within a wide array of optics. The properties of an OFC allow for a direct link between the optical frequency and Radio Frequency (RF). It is, in a way, a tool that has allowed us to explore technology and science in the optical spectrum.

Here follows a brief overview of some of the fields where the OFC have had, or will have, a major impact.

Spectroscopy

Applying the OFC to the field of optical spectroscopy permits both a broad bandwidth and a high spectral resolution. A broad bandwidth of spectroscopy enables a direct and fast mapping of atomic and molecular spectra. As all molecules have a unique spectrum, comb spectroscopy is able to rapidly identify molecular species. The high spectral resolution possible with a low phase-noise comb also enables precise measurements of the individual line shapes, spectral position, distribution, and relation of lines in a molecular spectrum. From this, a number of properties can be extracted: gas temperature, gas pressure, molecular rotational and vibrational energy, and external electromagnetic perturbations.

Commonly used techniques for frequency comb spectroscopy include:

VIPA Virtually Imaged Phased Array spectroscopy is a technique that uses a dispersive device such as a prism or diffraction grating together with a detector array such as a CCD camera. The OFC is first passed through the molecular or atomic sample after which the dispersive device spatially separates the comb lines. From the resulting pattern on a CCD camera the absorption spectra of the sample can be obtained. As all frequency components are detected in parallel, the detection enables a very high data acquisition speed. [28, 29].

DCS Dual Comb Spectroscopy utilizes the beat between two frequency combs with a small offset between their comb line spacing [30]. Beating two combs, either before or after interaction with the sample, converts the optical absorption spectrum and allows data acquisition in the RF-domain. DCS is a robust, compact, and simple technique especially if based on micro-resonator Kerr combs [31]. However, it does require two mutually referenced and stable frequency combs.

FC-FTS Frequency Comb Fourier Transform Spectroscopy employs an interferometer with a variable optical path difference. The frequency comb

is passed to the interferometer after interaction with the sample and by taking the Fourier transform of the interferometer signal both the absorption and the dispersion spectrum can be obtained [32, 33].

Vernier Spectroscopy This technique is based on cavity-enhanced frequency comb spectroscopy. The sample is placed inside an optical cavity and the frequency comb is coupled into the cavity modes. By scanning the length of the cavity, and thereby the Free Spectral Range (FSR), followed by detection using a dispersive device and a CCD camera, it is possible to extract the spectrum. The enhancement of the interaction length, due to the optical cavity, results in a very high sensitivity. Furthermore, the mode filtering of the frequency comb by the cavity greatly reduces the requirements of the dispersion device and CCD camera. [34, 35]

A number of practical realizations of OFC spectroscopy have been presented. In [36, 37] the OFC is used in long distance spectroscopy for real time environmental surveillance of green house gases and methane leak detection. In [38] an OFC is used in cavity-enhanced spectroscopy for human breath analysis with the purpose of medical diagnosis.

Telecommunication

Today, each channel in optical communication is based on individual non-referenced single frequency lasers. As low-cost tunable lasers are subject to long-term frequency drift, significant guardbands are required to avoid channel-to-channel interference. By encoding data onto an OFC using each line as a channel for data transmission, great amounts of energy can be saved. Instead of having one laser per channel, the entire spectrum can be obtained from a single source greatly reducing the power consumption. Furthermore, the lines in a frequency comb have a fixed relationship between them, thereby ensuring that two channels will never drift too close to each other. This means that the guardbands can be significantly reduced allowing a far greater number of channels within the same spectral bandwidth.

In [39] data is successfully encoded onto a frequency comb and transmitted through a multi-core fiber. The encoded comb spectrum covers almost 35 nm with a comb line spacing (i.e. channel spacing) of 10 GHz resulting in 2400 parallel channels. The achieved data transmission rate is an impressive 661 Tbit per second using a single laser source.

Optical Clocks

The OFC is an integral part of an optical clock. The OFC makes it possible to count optical frequencies in the RF domain [40]. It can be used to transfer and compare stability between different references over a wide spectrum and functions as a direct link between optical and microwave frequencies. [41, 42]

Astronomical Observations

Astronomical spectrographs require both high stability and accurate frequency calibration in order to measure the extremely small Doppler shifts from distant orbiting planets or cosmological and gravitational red-shifts. These spectrographs cover a wide spectral bandwidth where calibration using atomic references have proven insufficient. Here, the OFC is ideal as a broad bandwidth reference that supply equidistant markers over the required spectrum. The challenge here is the mismatch between the line spacing of the comb teeth and the resolution of the spectrographs. Currently, there are no commercially available frequency combs with a line spacing large enough to be resolved by astronomical spectrographs. One solution is the application of filter cavities to increase the comb line spacing as shown in [43, 44].

The current development of micro-resonator combs is followed with great interest within the astronomical field. The high FSR of these micro-resonators provide frequency combs with an intrinsically large line spacing making them suitable for integration with astronomical spectrographs.

Remote Sensing

Laser-based light detection and ranging (LIDAR) has become an important tool in many areas of industry and metrology. One example is the great interest in autonomous navigation of, among others, cars and aerial drones. The OFC has, also in this field, shown a record breaking performance. Here, an OFC can be used in calibration of continuous-wave interferometers allowing for highly accurate measurements. Another approach is to utilize the pulse train that is the frequency comb in the temporal domain. A pulsed laser can be used to make very precise time-of-flight measurements, e.g. with a dual comb scheme as in [45].

Again the development of micro-resonator combs is of interest. The high repetition rate of the pulse train, associated with a large line spacing comb, enables high-speed distance measurements with acquisition times as low as 500 ns [46]. This, together with the possible compactness and robustness of micro-resonator combs, makes them extremely suitable for LIDAR technology.

Microwave References and Arbitrary Optical Waveforms

One of the earliest demonstrations of an OFC as a direct link between the microwave and optical domains was in a clock system for comparison between optical frequency standards and the 9.19 GHz cesium frequency standard [47, 40]. Now, the OFC has become a common tool in optical clock laboratories. With the prospect of chip-scale frequency combs the focus of combs and microwaves have moved towards the generation of ultra-low-noise microwave sources. Utilizing the high Q-values available in the optical regime for OFC stabilization makes generation of microwaves with extreme spectral purity possible. This

is due to the fact that the comb provides a coupling of optical and microwave frequencies while retaining the fractional stability [48]. These ultra low-noise microwave references will allow for a significant improvement of the accuracy of e.g. radar systems.

Through modulation of the individual lines of an OFC it is possible to produce arbitrary waveforms both in the microwave and the optical domains. This will help to circumvent the limitation of arbitrary RF waveforms imposed by Digital to Analogue Converters (DACs). In the optical domain arbitrary waveform generation will be of use within all the fields mentioned in this section. A realization of a chip-based optical frequency synthesizer was presented in [49].

1.3 Overview

Chapter 2 - Experimental Techniques

Three different experimental systems are covered in this work: molecular frequency references, micro-resonator Kerr combs, and a strontium frequency reference. This chapter gives a brief description of four techniques common in all three systems: the Pound-Drever-Hall technique, the NICE-OHMS technique, large waist optical cavities, and the Allan deviation for frequency noise analysis.

Chapter 3 - Acetylene Frequency Reference

The work on an acetylene frequency reference based on the cavity enhanced spectroscopy technique called NICE-OHMS is presented in this chapter. The first section provides a description of the ro-vibrational lines of acetylene and discusses some considerations of spectroscopy for frequency stabilization. The next section describes the configuration of the acetylene spectroscopy setup followed by two sections where the achieved spectroscopy signals are analyzed. The focus of these analyzes is on optimization for laser frequency stabilization.

In the following section the frequency stability of the acetylene stabilized laser is presented and discussed. The different noise components and noise sources are evaluated. This section is followed by a brief discussion on the use of FM-spectroscopy as an alternative to NICE-OHMS. The chapter concludes with an overview of future investigations of interest.

Chapter 4 - Micro-Resonator Kerr Frequency Combs

In this chapter the work done on frequency comb generation through the Kerr effect in micro-ring resonators is presented. The primary focus is on planar AlGaAs-on-insulator micro-ring resonators developed at the SPOC center. We start with a short review of what a frequency comb is, and which parameters are used to describe it. Different methods of frequency comb generation are examined, and the strength and weaknesses

are discussed. Following this, a review of the requirements for efficient comb generation in micro-resonators is given.

In section 4.2 the work on dispersion engineering of AlGaAs micro-ring resonators through tapered waveguides is presented. This is followed by a discussion of the achieved frequency comb generation in AlGaAs resonators and Silicon Nitride resonators.

Section 4.4 provides a brief review of different techniques for stabilization of micro-resonator frequency combs. This section is followed by an outlook where future investigations of the AlGaAs material are discussed together with some prospect of other material platforms.

Chapter 5 - Strontium Atomic Clock

The work on a strontium frequency reference based on a thermal ensemble of atoms is presented in this chapter. The idea behind this experiment is to utilize the narrow clock transition in strontium for both stability and accuracy and in that way circumvent the limitations of optical reference cavities. This chapter only gives a small insight into the experimental system.

A description of the key elements of the setup is given, followed by preliminary results.

Chapter 6 - Summary of Conclusions

This chapter contains a summary of the conclusions of the work with the acetylene frequency reference, the micro-resonator Kerr frequency combs and the strontium optical clock.

2 Experimental Techniques

Three different experimental systems are covered in this work: molecular frequency references, micro-resonator Kerr combs, and a strontium frequency reference. This chapter gives a brief description of four techniques common in all three systems: the Pound-Drever-Hall technique, the NICE-OHMS technique, large waist optical cavities, and the Allan deviation for frequency noise analysis.

2.1 Pound-Drever-Hall Stabilization

When an oscillating electric field, like a mono-chromatic laser beam, interacts with a resonant system, the resonance will impose a phase shift on the field. This phase response is anti-symmetric with respect to frequency. The Pound-Drever-Hall (PDH) technique uses this fundamental feature to generate an error-signal for stabilization to the peak center of a resonance profile.

The PDH technique for frequency stabilization was developed by R. W. P. Drever, J. L. Hall, and others [50] based on R. V. Pounds previous work [51]. The technique utilizes optical heterodyne detection of the phase shift imposed on a laser beam by an optical resonator. Figure 2.1 shows the configuration of a system where a laser is stabilized to the resonant mode of a Fabry-Perot optical cavity. Here, a set of sidebands are applied to the laser light by phase modulation at a frequency ω_m, preferably much greater than the resonance linewidth. The sidebands act as a reference for measuring the phase imposed on the carrier by the cavity. This is done by detecting the beat-note of the carrier and sidebands in the light reflected from the cavity. The beat-note's amplitude is proportional to the cavity-induced phase shift of the carrier. By demodulating the detected signal at a frequency equal to the modulation frequency, ω_m, a DC-signal showing the cavity-induced phase is achieved.

The electric field of the laser reflected from the cavity can be written as

$$E(t) = \frac{E_0}{2}\left[J_0(\beta)e^{i\omega t+\theta} + J_1(\beta)e^{i(\omega+\omega_m)t} - J_1(\beta)e^{i(\omega-\omega_m)t}\right] + \text{c.c.} \qquad (2.1)$$

where $J_n(\beta)$ is the Bessel functions of the first kind, β is the modulation index of the phase modulation, and θ is the carrier phase. Following the derivation in section 9.2.2 of [17] we find the photo-current on the detector diode to be

$$I_{PD} \propto J_0(\beta)J_1(\beta)\left[A(\Delta\omega)\cos(\omega_m t) + D(\Delta\omega)\sin(\omega_m t)\right]. \qquad (2.2)$$

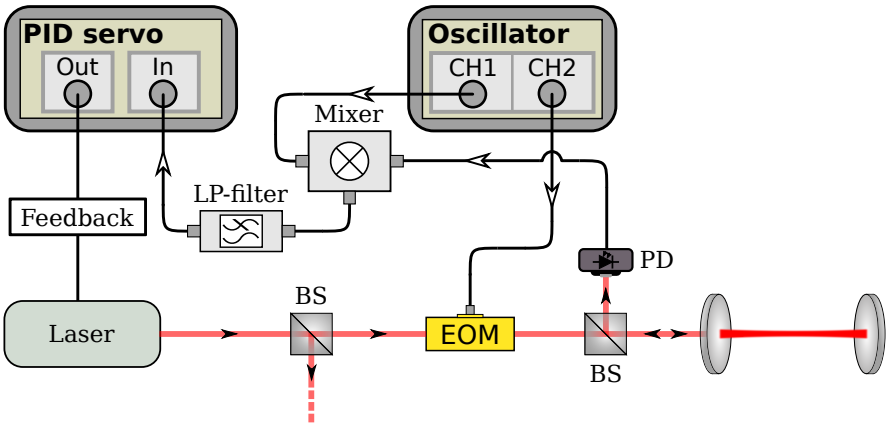

Figure 2.1: The Pound-Drever-Hall stabilization scheme. A laser beam is phase modulated using an EOM and coupled into an optical cavity. The reflection from the cavity is extracted using a beam splitter (BS) and detected at the modulation frequency. The photo detector (PD) signal is demodulated using an RF-mixer and then low-pass filtered (LP-filter). This results in an anti-symmetric DC-signal proportional to the cavity-induced phase shift of the laser. A servo-system uses this signal to apply feedback on the laser frequency.

This signal contains two terms: a cosine term with an absorption component $A(\Delta\omega)$ and a sine term with a dispersion component $D(\Delta\omega)$. These two components take the form

$$D(\Delta\omega) = -4\frac{\omega_m^2\Delta\omega\left[(\Gamma/2)^2 - \Delta\omega^2 + \omega_m^2\right]\Gamma/2}{\left[\Delta\omega^2 + (\Gamma/2)^2\right]\left[(\Delta\omega+\omega_m)^2 + (\Gamma/2)^2\right]\left[(\Delta\omega-\omega_m)^2 + (\Gamma/2)^2\right]} \tag{2.3}$$

and

$$A(\Delta\omega) = 4\frac{\omega_m\Delta\omega\left[(\Gamma/2)^2 + \Delta\omega^2 + \omega_m^2\right](\Gamma/2)^2}{\left[\Delta\omega^2 + (\Gamma/2)^2\right]\left[(\Delta\omega+\omega_m)^2 + (\Gamma/2)^2\right]\left[(\Delta\omega-\omega_m)^2 + (\Gamma/2)^2\right]}. \tag{2.4}$$

Here $\Delta\omega$ is the carrier-cavity detuning and Γ is the linewidth of the cavity resonance.

The photo-current is the sum of these two terms oscillating at a frequency ω_m with a phase difference of $\pi/2$. When demodulating the signal from the photodetector, the phase can be chosen so that either the dispersive or absorptive part is obtained. In figure 2.2(a) and 2.2(b) the two signals are shown. These data are from the Acetylene setup presented in chapter 3 where $\omega_m = 10$ MHz and $\Gamma \approx 1.6$ MHz.

The signal amplitude is proportional to the product of $J_0(\beta)$ and $J_1(\beta)$ as seen in equation 2.2. Optimizing the PDH error-signal slope with respect to the modulation index is a question of maximizing $J_0(\beta)J_1(\beta)$. This optimum

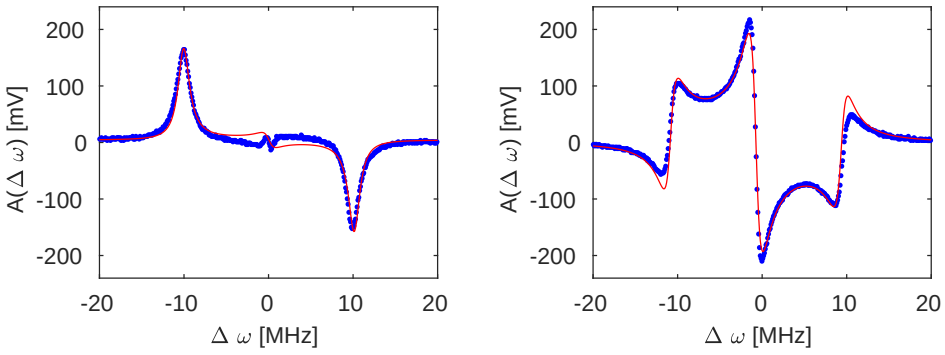

(a) The absorption component of the PDH-signal.

(b) The dispersion component of the PDH-signal.

Figure 2.2: A measurement of the PDH-signals corresponding to equations (2.3) and (2.4). The blue curves show signals recorded on the Acetylene setup described in chapter 3. The red curves is a fit of equations (2.3) and (2.4) to the data yielding $\omega_m = 10$ MHz and $\Gamma \approx 1.6$ MHz.

is found to be at $\beta = 1.08$, corresponding to a power in the sideband relative to the power in the carrier of $\frac{P_{sideband}}{P_{carrier}} = 0.4$. The power in higher order sidebands are assumed to be zero so that $P_{carrier} + 2P_{sideband} = P_{total}$. This estimate is supported by the analysis in [52] where the same result is obtained through a different approach. The modulation index can be experimentally controlled through the RF power applied to the EOM.

The method of heterodyne phase detection has a number of inherent advantages. The detection itself is not bandwidth limited, meaning that it is not limited by the characteristic time of the cavity. Furthermore, by doing the detection at RF, common $1/f$ noise is circumvented in the detection. As a result the PDH technique provides high bandwidth signal with a high signal-to-noise ratio.

2.2 NICE-OHMS

The Noise-Immune Cavity-Enhanced Optical Heterodyne Molecular Spectroscopy (NICE-OHMS) technique was first presented in 1998 by Jun Ye, Long-Sheng Ma, and John L. Hall [53]. In the following year these authors also showed its usefulness for laser frequency stabilization [54].

The technique utilizes optical heterodyne detection of the phase shift imposed on a laser beam by a molecular or atomic resonance. This is the same principle as the PDH technique. As described above, the PDH technique is heterodyne spectroscopy of an optical resonator, typically a Fabry-Pérot cav-

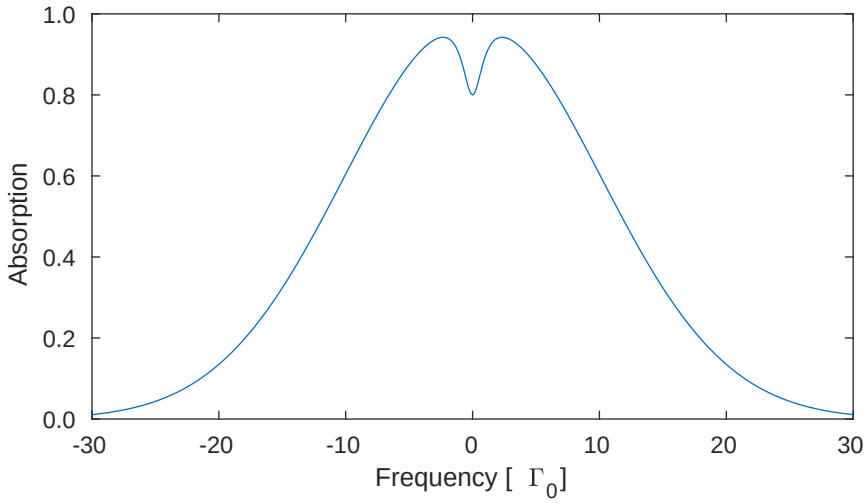

Figure 2.3: An illustration of a saturated spectroscopy absorption profile. As the laser frequency is scanned across the resonance of the atomic or molecular sample, the absorption will mainly follow a Gaussian distribution with a width, Γ_D, determined by the sample's temperature-induced Doppler-shifts. In the center of the Gaussian Doppler-profile is a saturation dip, the so-called Lamb-dip. The Lamb-dip mainly has a Lorentzian line shape with a width Γ_0. On this graph $\Gamma_D/\Gamma_0 = 10$, where Γ_0 is the Doppler-free Lorentzian width.

ity. In NICE-OHMS the Fabry-Pérot cavity is switched with a molecular or atomic sample, and the basic concept of the PDH technique is combined with cavity-enhanced saturated spectroscopy.

Saturated Spectroscopy

In saturated spectroscopy a set of counter-propagating laser beams saturate a transition of atoms or molecules, but only if their velocities are perpendicular to the k-vectors of the laser beams. Therefore, only atoms or molecules with zero Doppler-shift will saturate. The absorption within the Doppler-free linewidth will be lower, and a so-called Lamp-dip will appear in the center of the absorption profile as illustrated in figure 2.3.

The broad absorption profile is typically referred to as the Doppler-profile since the main contribution to its shape comes from the Doppler-broadening of the sample's natural linewidth. This is an inhomogeneous broadening since the Doppler-shifts of the individual atoms or molecules are determined by the thermal distribution. This results in a Gaussian line shape. In the case of laser-cooled atoms with a very low Doppler-broadening, other contributions to the line shape cannot be neglected. The transition linewidth and homoge-

neous broadening effects will have a Lorentzian line shapes. This results in the convolution of the Gaussian and the Lorentzian line shapes known as a Voigt-profile.

The line shape of the Lamb-dip is determined by the Lorentzian natural linewidth, homogeneously broadened by pressure-broadening and power broadening. The main, inhomogeneous broadening effect is the transit-time-broadening where the spectroscopic resolution of a transition is limited by the interaction time. This is a consequence of the thermal velocities of the atom or molecules and the width of the interrogation laser beam. In the systems presented in this work inhomogeneous broadening effects of the Lamb-dip are small and can thereby be neglected. Thus, the Lamb-dips will be modeled as Lorentzian lines.

A detailed review of saturated spectroscopy can be found in [55].

The NICE-OHMS Setup

Figure 2.4 shows an example of a NICE-OHMS setup. The laser light is phase modulated by an EOM. This generates sidebands at a frequency equal to one cavity FSR[1]. The laser light now consists of three separate frequency components which are coupled into neighboring cavity modes (see fig. 2.5). The length of the cavity is locked so that one mode is always resonant with the laser carrier frequency. Only the carrier is on resonance with the sample line, and it is therefore only the carrier component that saturates the sample and is affected by the sample's dispersion. The dispersion will affect the phase relation between the carrier and sidebands causing a non-zero beat-note of the three frequency components in the cavity field. This beat-note is detected in the cavity transmission and will have an amplitude proportional to the sample's dispersion. Demodulation using an RF-mixer produces a DC signal proportional to the optical phase shift imposed on the light by the sample. This is a simplified description where the influence of the cavity's phase contribution is assumed to be zero. This only holds for an infinitely fast cavity lock. A detailed analysis of the combined transfer function of the cavity and the sample, and its influence on NICE-OHMS, is given in [25].

As this technique is based on saturated spectroscopy, the signal will consist of the sum of both the Doppler-free line profile and the broad Doppler profile. The Doppler-free part, i.e. the dispersion signal of the Lamp-dip, will be skewed by the Doppler-broadened signal in the background. However, as the Doppler profile often is orders of magnitude wider than the Lamp-dip, this background can be approximated to a straight line and is easily accounted for in data analysis.

[1] FSR of an optical cavity is the spectral distance between two neighboring modes of the same kind.

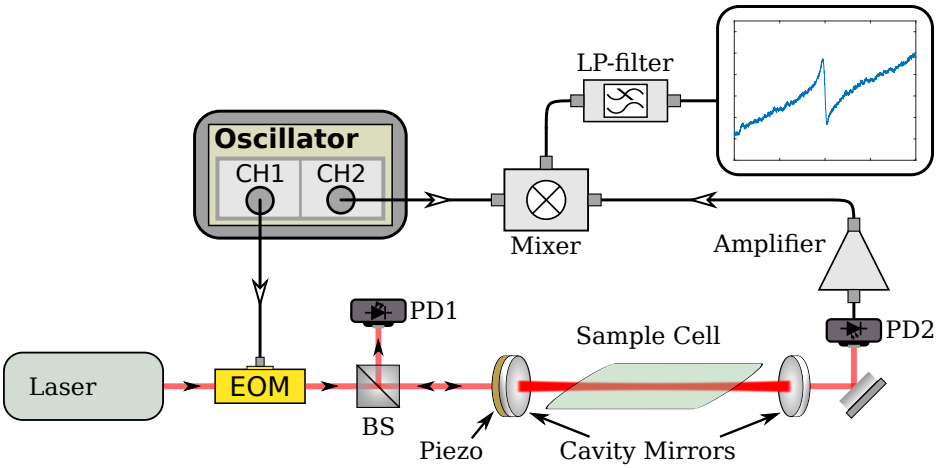

Figure 2.4: A simplified schematic of a NICE-OHMS setup. An EOM is used to generate sidebands at a frequency equal to the cavity FSR. The photo detector, PD1, is used for locking the cavity length to resonance with the laser's carrier frequency (e.g. using the PDH technique). The cavity transmission is detected on a fast photo detector with a bandwidth capable of measuring optical beat-note between the laser carrier and sidebands. An RF-mixer is used to down-convert the detected signal to DC which shows the phase response of the sample cell. Black lines are electrical connections, and red lines are optical paths.

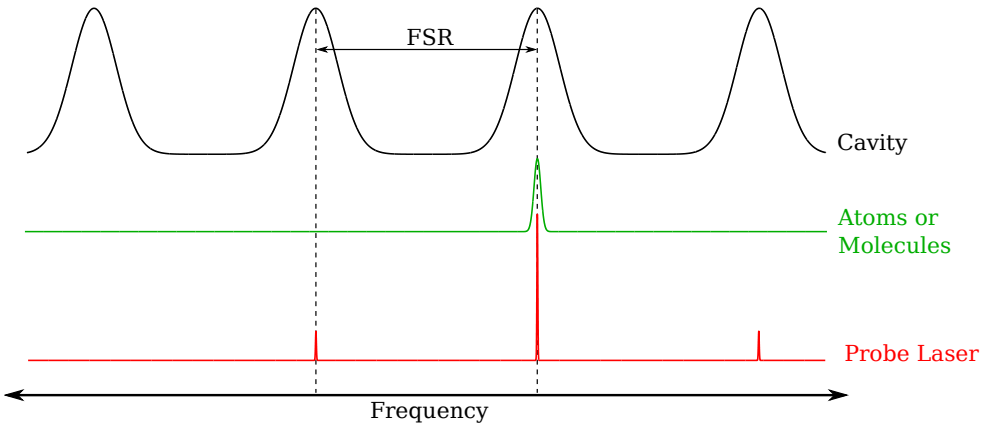

Figure 2.5: The spectra of the NICE-OHMS technique. The cavity modes of a single mode family separated by one FSR are shown in black. The atomic or molecular sample line is shown in green, and the interrogation laser's spectrum is shown in red. The cavity modes' frequencies are locked to the laser so that the cavity and laser modes always overlap. The figure is adapted form [56].

Signal Optimization

The mathematics describing the PDH technique can be applied to NICE-OHMS as well. Doing the analysis as in section 2.1 will yield a similar result where the optimum modulation index is concerned. As in equation (2.2), the amplitude of the NICE-OHMS signal will be proportional to $J_0(\beta)J_1(\beta)$, and we find the optimum to be $\beta = 1.08$. However, in this system the optical power in the carrier will cause power broadening of the sample line. In systems like the ones described in this work, where the goal is to use NICE-OHMS as an error-signal for stabilization purposes, the center-slope of the signal is the figure of merit. More power in the carrier will thus make the line wider and thereby the slope smaller. Optimizing the NICE-OHMS signal for laser stabilization depends on both the modulation index and the broadening effects of the interrogated line.

The optimal power when doing saturated spectroscopy depends on the power broadening coefficient and the saturation intensity of the sample. If the system in question is limited by optical power, and the optimal degree of saturation versus power broadening can not be achieved, the modulation index that results in the steepest slope is not necessarily $\beta = 1.08$.

Residual Amplitude Modulation

A good signal-slope is not the only requirement of a good error-signal. Fluctuations of the signal's off-set voltage will have a direct impact on the achievable stability. A major source of such fluctuations in modulation spectroscopy is Residual Amplitude Modulation (RAM). RAM has been a challenge in modulation based laser stabilization schemes for many years, and a lot of effort has been put into counteracting it [57, 58, 59, 60].

The effect of RAM can be described as an imperfect modulation which causes the phase relation of the carrier and sidebands to fluctuate. In the case of perfect phase modulation, the carrier and lower sideband will have a fixed phase difference of π while the carrier and the upper sideband will have a fixed phase difference of 0. The unperturbed phase modulated beam should therefore not carry any beat-note, as the contribution from each sideband cancel each other out.

If RAM is present in a NICE-OHMS setup, the laser beam will carry a beat-note prior to the interrogation of the sample. This will appear in the dispersion signal as a non-zero voltage off-set. The main problem in systems for frequency stabilization arises as RAM fluctuates in time thereby causing a varying voltage off-set to the error-signal, limiting the achievable stability.

RAM is typically counteracted by detecting the beat-note after the modulator but prior to the cavity. The amount of RAM can be measured by demodulating this signal, and feedback can be applied in the form of a bias voltage

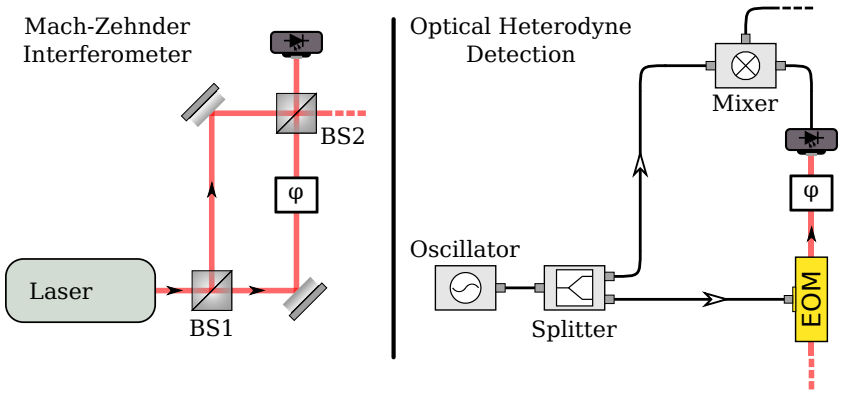

Figure 2.6: A comparison of a Mach-Zehnder interferometer and optical heterodyne detection. The oscillator in the heterodyne detection is the counterpart to the laser in the interferometer. Likewise, the beam splitters ,BS1 and BS2, and the RF splitter and the RF-mixer, respectively, can be though of as counterparts. The black lines are electrical connections and the red lines are optical paths.

on the modulator's electrodes. In this way a fixed phase relation between the carrier and the sidebands can be ensured.

Modulation Instability

Other effects than RAM in the EOM can lead to a fluctuating signal off-set. In heterodyne detection schemes such as NICE-OHMS, where the interrogation laser is modulated, modulation instability can occur. This can to some extent be described by comparing the NICE-OHMS scheme to a Mach-Zehnder interferometer. In NICE-OHMS the RF modulation is split into two arms. In one arm the RF wave is written onto the laser light and travels through some optics before it is detected and sent to an RF-mixer. The second arm is a coaxial cable going from the RF source to the mixer. This is equivalent to the Mach-Zehnder interferometer where a wave is split into two and travels different paths before they are recombined. An illustration showing the similarities can be seen on figure 2.6.

In the same way as with an interferometer, unwanted changes in the path-length leads to signal fluctuations. This can be described by an example of a NICE-OHMS setup and the effect of changes in optical path-length, δL.

We have a modulation frequency of $\Omega_m = 650$ MHz and are assuming that the variation in the effective path-length of the RF cables and RF components is negligible. The wavelength of 650 MHz is $\lambda_m = \frac{c}{\Omega_m} = 0.461$ m. A change in the optical path-length of 0.461 m will thus correspond to a phase change

of 360 degrees, giving

$$\frac{\delta\phi}{\delta L} = \frac{360\ ^\circ}{\lambda_m} = 0.781 \text{ deg/mm}.$$

The dispersion signal made with NICE-OHMS is sensitive to the phase relation between the detected RF signal and the RF demodulation signal. And, as the optical path-length between the EOM and the detector can be several meters, even small δL can pose a problem.

Proper grounding of RF components can be difficult when operating with frequencies of hundreds of MHz. If proper grounding is not achieved, small fluctuations in the environment can cause changes in the effective capacitance of the cables and other components. This leads to significant changes in the effective RF path-length through amplifiers, cables, and the mixer.

2.3 Large Waist Cavity

Saturated spectroscopy is a powerful technique for narrow molecular or atomic lines as it allows for Doppler-free detection of room temperature samples. Doppler-broadening is typically the most significant line broadening so circumventing this is a big step for narrow linewidth detection. There are, however, other considerations to be taken when the goal is to achieve the best possible signal with a minimum of line broadening.

A high degree of saturation requires a high optical intensity. This means either a small beam size or a lot of optical power. Optical cavities are a great way to achieve power enhancement. However, they impose strict boundaries on the beam size. A small beam size of a cavity mode can lead to transit-time-broadening being the limitation on the achievable spectroscopic linewidth. Transit time broadening is a Fourier limitation on the spectral resolution of a molecule or atom moving through a laser beam. The broadening effect is imposed since the atom or molecule only interacts with the laser beam for the time $t = \frac{2w}{v_\perp}$ where w is the laser beam radius, and $v_\perp$ is the velocity of the atom or molecule perpendicular to the laser beam's k-vector.

In this work a novel optical cavity configuration was developed: the large waist cavity. In this configuration an intra-cavity telescope is implemented allowing for up to 6 mm waist radius in an optical cavity with standard 1 inch optics. This provides the possibility of spectroscopy with incredibly low transit-time-broadening. This cavity design was first presented in [61].

A schematic of the large waist cavity is shown in figure 2.7. The cavity is configured in a folded geometry where the intra-cavity telescope consists of a mirror and a lens. This reduces the number of surfaces inside the cavity by one compared to a telescope with two lenses. It also introduces an angle θ. Four optical elements make up the cavity. M1 and M4 are the cavity end-mirrors which are concave with a radius of curvature (ROC) of -9 m. M1 is used for

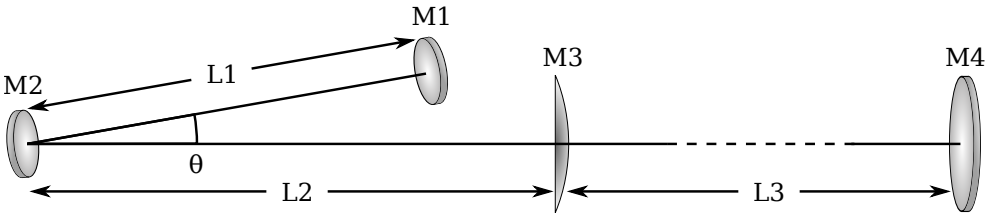

Figure 2.7: A schematic of the large waist cavity. M1 and M4 are the cavity end-mirrors with $ROC = -9$ m. The M2 mirror has a $ROC = -24$ mm and makes up the intra-cavity telescope together with the lens, M3.

	θ [deg]	L1 [mm]	L2 [mm]	f_{M3} [mm]	w [mm]
Configuration 1	10	110	62.4	50	1.31
Configuration 2	10	67	163.45	150	2.95

Table 2.1: The parameters, as shown on figure 2.7, of the two configurations used and their corresponding cavity waist radii.

in-coupling and has a power reflectance of $r^2 = 98.6$ %, chosen based on cavity impedance matching. M2 is the 'corner-mirror' with a $ROC = -24$ mm which forms the telescope together with the lens, M3. Both M2 and M4 have a power reflection of $r^2 > 99.95$ %. The large waist region of the cavity is the space between the lens, M3, and the end mirror, M4, marked as L3. The mode is well collimated in that region, and it is here the spectroscopy sample is placed. The stability of the fundamental cavity mode is not sensitive to changes to the length L3. L3 can therefore be adjusted for the requirements imposed by the sample's geometry. L3 can also be used for adjustment of the cavity FSR.

Two different large waist cavities are used in the work presented here. The first has a waist radius of 1.3 mm at L3, and the second has a waist radius of 3.0 mm at L3. Here, the waist radius, w, is defined as the Gaussian width of the radial intensity variation described by

$$I(r) = I_0 \exp\left(-2\frac{r^2}{w^2}\right).$$

The parameters for the two configurations are shown in table 2.1.

The waist radius along the cavity axis is shown in figure 2.8 for configuration 1 and in figure 2.9 for configuration 2. The graphs show the radii of the cavity mode of both the plane of the folding angle θ and the orthogonal plane. As the cavity is folded, the cavity mode will have a degree of astigmatism which is evident by the difference in the waist of the two planes.

A small misalignment of the lens position results in significant astigmatism as shown in figure 2.10. Here the length, L2, was changed by 1 mm to

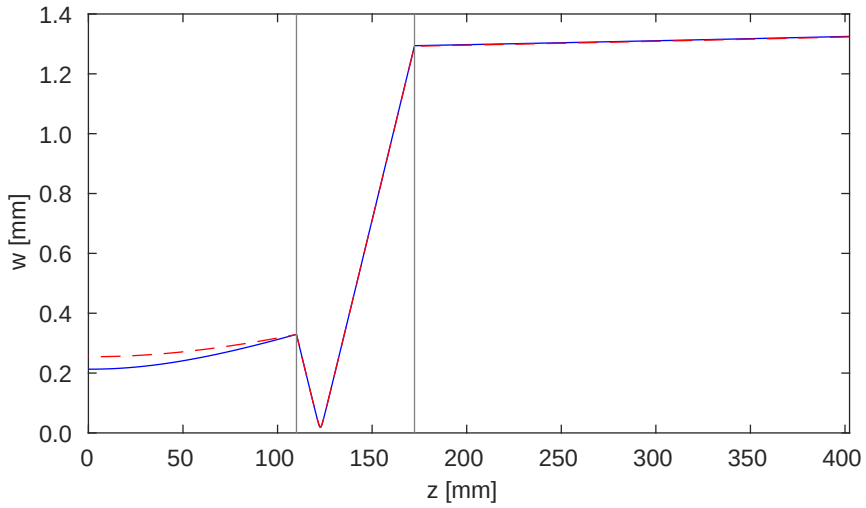

Figure 2.8: The width, w, of the cavity mode in configuration 1 of the large waist cavity along the cavity axis z. The blue (solid) curve is the waist width in the plane of the folding angle, and the red (dashed) curve is the width in the orthogonal plane.

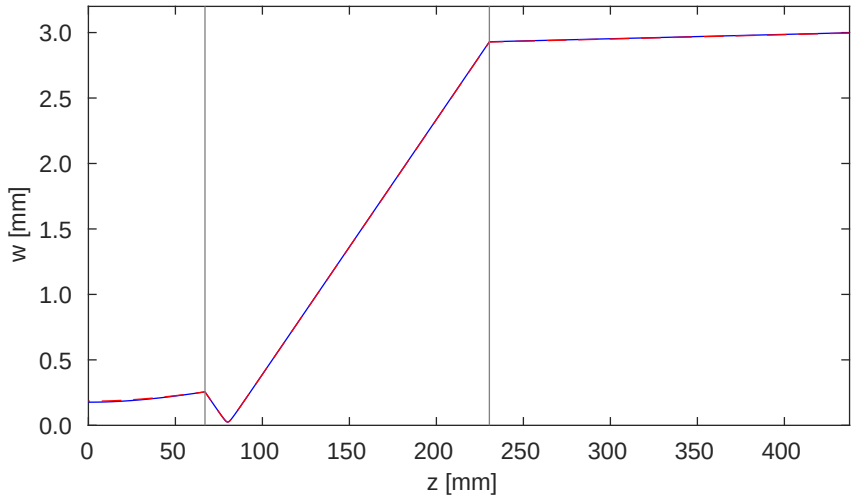

Figure 2.9: The width, w, of the cavity mode in configuration 2 of the large waist cavity along the cavity axis z. The blue (solid) curve is the waist width in the plane of the folding angle, and the red (dashed) curve is the width in the orthogonal plane.

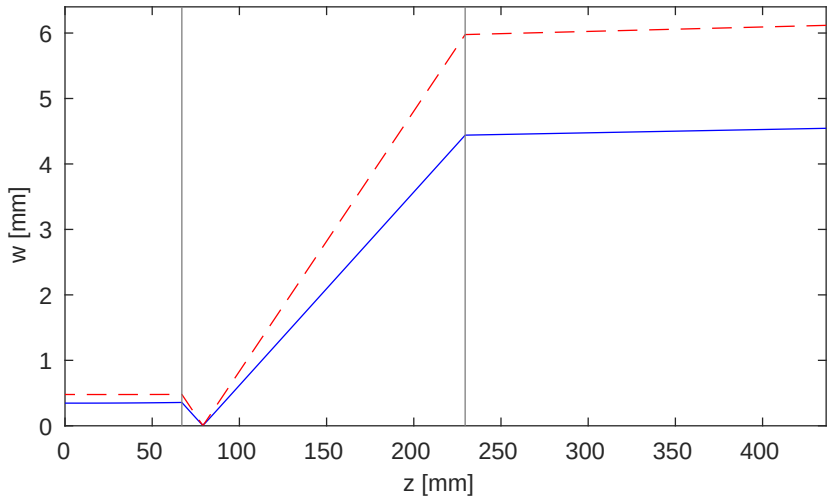

Figure 2.10: The width, w, of the cavity mode in configuration 1 of the large waist cavity where L2 is slightly misaligned. The blue (solid) curve is the waist width in the plane of the folding angle, and the red (dashed) curve is the width in the orthogonal plane. Lens position is off by 1 mm resulting in significant astigmatism of the cavity mode.

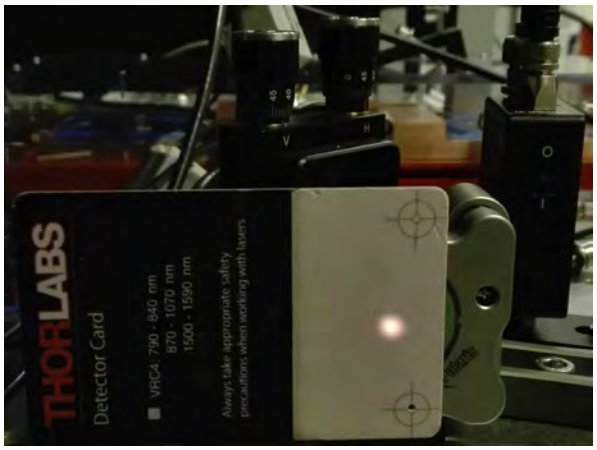

Figure 2.11: A picture of the large waist cavity mode seen on a Thorlabs IR detector card. The radius of the beam seen here is roughly 3 mm.

162.45 mm. Furthermore, a small misalignment of the lens angle will greatly increase the lens error causing loss to the cavity mode. Careful alignment is therefore necessary to achieve a high finesse and a stable cavity mode.

A picture of the cavity mode is shown in figure 2.11. The picture was taken by removing the in-coupling mirror and placing an IR detector card in front of the end-mirror.

2.4 Allan Deviation

The Allan variance or Allan deviation is a powerful tool for analyzing the phase or frequency noise of an oscillator. The most commonly used methods are the plain Allan deviation, the overlapping Allan deviation, and the modified Allan deviation. These are methods used in this work, and a brief description based on [62] is given in this section.

Frequency Noise and the Allan Variance

The output from a laser or any other frequency source can be described as a sine wave:

$$U(t) = U_0 \sin(2\pi\nu_0 t + \phi(t)).$$

Here U_0 is the peak output voltage, ν_0 is the carrier frequency, and $\phi(t)$ is the phase fluctuation. The phase fluctuation is the parameter of interest when analyzing the noise of a frequency reference. We commonly measure the frequency as a function of time, and the data we wish to analyze is therefore in the form:

$$\nu(t) = \nu_0 + \frac{1}{2\pi}\frac{\mathrm{d}\phi}{\mathrm{d}t}.$$

A simple and good description of the noise in a signal like this is the standard deviation $s(\nu(t))$. The standard variance, s^2, is defined as

$$s^2 = \frac{1}{N-1}\sum_{i=1}^{N}(y_i - \bar{y})^2$$

where $\bar{y}$ is the average of all the data points y. It is simply the average distance to the mean of N data points.

Allan variance calculates the average distance to the mean over different averaging time intervals τ, making it possible to distinguish noise contributions with different frequencies:

$$\sigma_y^2(\tau) = \frac{1}{2(M-1)}\sum_{i=1}^{M-1}(y_{i+1} - y_i)^2.$$

Here y is the averaged over the time τ. Let us look at an example of a frequency measurement with a total measurement time of $T = 10$ s and a gate time[2] of 0.1 s. We have a total of 100 frequency measurement points. For a τ of 1 s we have $M = \frac{T}{\tau} = 10$, and each y will be the average of $m = 10$ points. In this case $\sigma(\tau = 1\text{ s})$ is the average distance of the 10 y's to the overall mean where

[2]The gate time is the time over which a frequency counter counts zero-crossing for one measurement. The gate time of a measurement series thereby sets the minimum averaging time possible for the Allan variance.

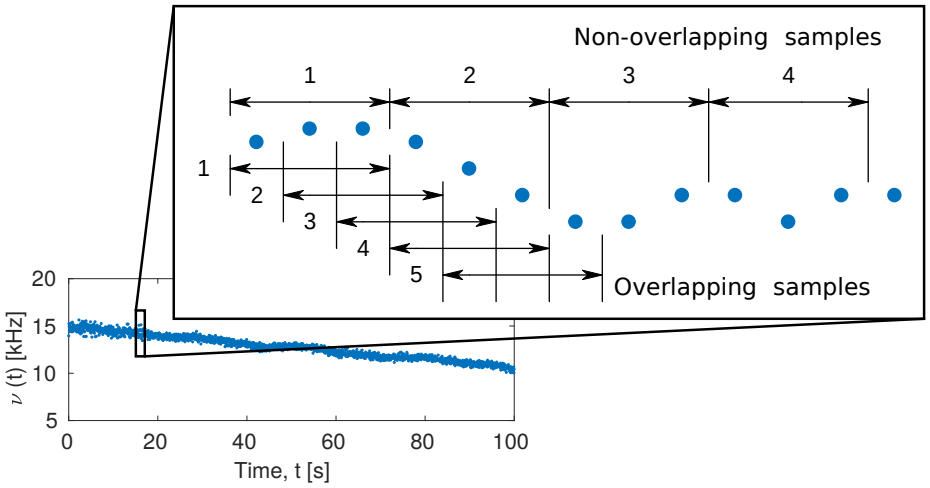

Figure 2.12: An illustration of the averaging in Allan variance and overlapping Allan variance. In this example $m = 3$. In the case of the plain Allan variance (non-overlapping) a total of 4 y's are indicated. In the case of overlapping Allan variance 5 y's are indicated, but a total of 12 y's are possible as this section of the data set consists of $N = 13$ points.

each y is the mean of 10 data points. All noise with a frequency above 1 Hz will not contribute to σ as the noise will be averaged out.

In overlapping Allan variance the averaging y's are overlapping similar to a moving average:

$$\sigma_y^2(\tau) = \frac{1}{2m^2(M-2m+1)} \sum_{j=1}^{M-2m+1} \left[\sum_{i=j}^{j+m-1} (y_{i+m} - y_i) \right]^2 .$$

Taking the example from earlier with a total of $N = 100$ points. With overlapping averages, each σ for a given averaging time τ will be over $N - 1$ number of y's instead of only M number of y's. The illustration in figure 2.12 shows the averaging of both Allan variance and overlapping Allan variance.

Modified Allan variance is defined as

$$\sigma_y^2(\tau) = \frac{1}{2m^4(M-3m+2)} \sum_{j=1}^{M-3m+2} \left\{ \sum_{i=j}^{j+m-1} \left[\sum_{k=i}^{i+m-1} (y_{k+m} - y_k) \right] \right\}^2 .$$

Here, an additional phase averaging is added. The advantage of the modified Allan variance is the ability to distinguish between white and flicker phase-noise, which will be described in the following sub-section.

All three variants are commonly expressed as the Allan deviation, i.e. the square root of the Allan variance.

Noise	α	μ
White phase	2	-2
Flicker phase	1	$\approx$ -2
White frequency	0	-1
Flicker frequency	-1	0
Random walk frequency	-2	1
Frequency drift	-3	2

Table 2.2: The noise types, the noise spectrum power dependency, α, and their corresponding sigma-tau slopes, μ. These noise types are shown on sigma-tau plots on figure 2.13.

Sigma-Tau Plots and Power Law

Plotting the Allan deviation, σ, as a function of the averaging time τ provides a lot of information about the noise in a dataset.

In a system with only white noise, the uncertainty of the mean value will always decrease for longer averaging times.

$$\sigma_{mean} = \frac{s}{\sqrt{N}}$$

That means if the measurement time goes to infinity, the uncertainty of the mean will go to zero. There are, however, not many systems where this is true. The Allan deviation can reveal at which averaging time the uncertainty of the mean is at a minimum. The plot in figure 2.13 shows an example of an Allan deviation of a dataset containing different types of noise modulations. Here, σ reaches a minimum at $\tau = 10^{-1}$ s. If this was frequency data from a laser source, and the goal was to achieve the highest possible coherence in some sort of interaction, the optimum interaction time would be 0.1 s.

The slope of the sigma-tau plot provides information about the frequency dependence of the noise modulation. The noise in a frequency source can be described as a power law of the spectral density of the frequency fluctuations $S_y(f) \propto f^\alpha$ where f is the frequency of the noise. If the noise spectrum is flat, i.e. $\alpha = 0$, the noise is called white frequency modulation. This will correspond to a slope on the sigma-tau plot of $\sigma(\tau) \propto \tau^{-1/2}$. Other α-values have similar names and follow the relation $\mu = -\alpha - 1$, where the sigma-tau slope is $\approx \tau^{\mu/2}$. Table 2.2, figure 2.13, and figure 2.14 show the relation between noise spectra and the sigma-tau slope.

Based on the Allan deviation and a sigma-tau plot one can get a lot of information about a system's noise. Through these analyzes, one can determine the prominent noise types at different time scales and thereby identify noise sources. That is why the Allan deviation is the tool of choice within metrology when it comes to noise and stability characterization.

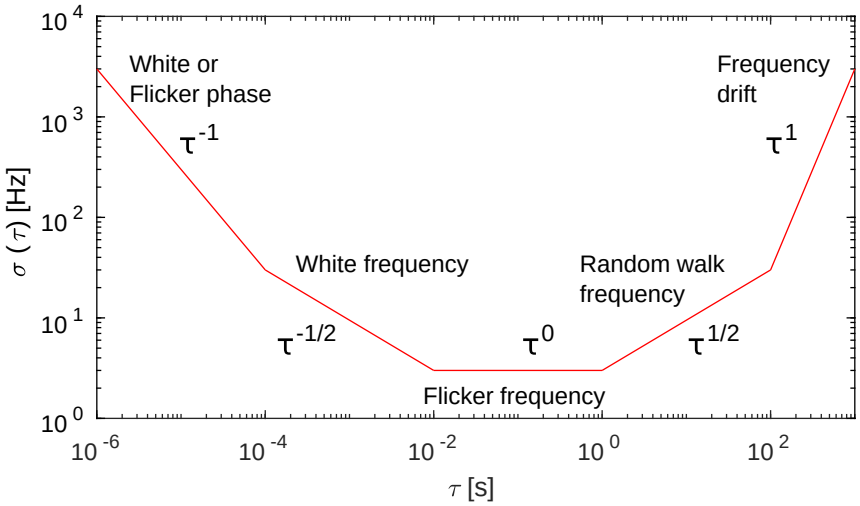

Figure 2.13: The sigma-tau plot of a plain Allan deviation annotated with the noise types associated with the τ-dependency. Notice that both white phase noise and flicker phase noise have the same τ-dependency.

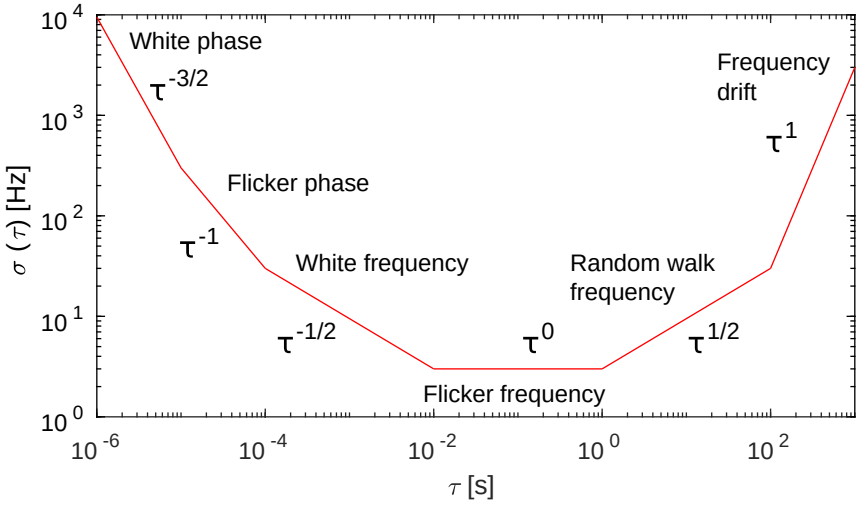

Figure 2.14: The sigma-tau plot of a modified Allan deviation annotated with the noise types associated with the τ-dependency. In contrast to the plain Allan deviation, white phase noise and flicker phase noise can now be distinguished.

3 Acetylene Frequency References

The work on an acetylene frequency reference based on the cavity enhanced spectroscopy technique called NICE-OHMS is presented in this chapter. The first section provides a description of the ro-vibrational lines of acetylene and discusses some considerations of spectroscopy for frequency stabilization. The next section describes the configuration of the acetylene spectroscopy setup followed by two sections where the achieved spectroscopy signals are analyzed. The focus of these analyzes is on optimization for laser frequency stabilization.

In the following section the frequency stability of the acetylene stabilized laser is presented and discussed. The different noise components and noise sources are evaluated. This section is followed by a brief discussion on the use of FM-spectroscopy as an alternative to NICE-OHMS. The chapter concludes with an overview of future investigations of interest.

The acetylene frequency reference is a spectroscopically referenced laser based on the NICE-OHMS technique (see section 2.2). A low pressure acetylene gas cell is place inside an optical interrogation cavity, and NICE-OHMS is used to measure the molecular induced phase shift of the cavity field.

Similar systems, where a laser is referenced to a narrow molecular line, have been presented by others. In [63, 64] simple saturated spectroscopy setups have shown impressive performance. In [65, 54] the NICE-OHMS technique is used in a similar way as presented here. These examples all use a Lock-In amplifier to achieve a high signal-to-noise ratio which inevitably lowers the signal bandwidth of the spectroscopic signal. Based on the spectroscopic signal-to-noise ratio and signal bandwidth presented here, it is expected that this work will out-perform these systems without additional system complexity.

3.1 The Acetylene Molecule

The spectral line of interest in this work is the P(16)$\nu_1 + \nu_3$ line in carbon-13 acetylene as this is the line adopted by BIPM as a practical realization of the meter [15]. However, since isotope-pure carbon-13 acetylene is no longer commercially available, possible lines in carbon-12 acetylene will also be considered. These considerations will be based solely on the aptitude of the line for laser frequency stabilization.

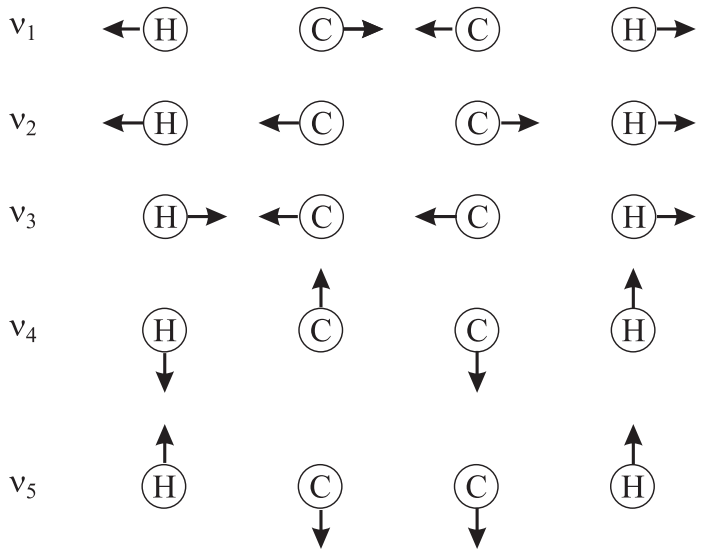

Figure 3.1: Vibration modes of the acetylene molecule. Figure taken from [17].

Ro-vibrational Structure

Ethyne (C_2H_2; H−C≡C−H), commonly known as acetylene, consists of two carbon atoms and two hydrogen atoms. The geometry of this molecule allows for 5 different vibrational modes, denoted as ν_1 to ν_5 (see figure 3.1). The resonant frequency of the ν_1 mode is 101.1 THz, and the resonant frequency of the ν_3 mode is 98.4 THz for the carbon-12 isotope [66]. These modes can couple through non-linear interactions and give rise to a combined resonance, $\nu_1 + \nu_3$, conveniently placed in the telecommunication C-band at 196.6 THz. The larger mass of the carbon-13 atoms relative to the carbon-12 atoms changes the frequency of the vibrational mode shifting the carbon-13 $\nu_1 + \nu_3$ combination to 195.5 THz. As illustrated on figure 3.1 both the ν_1 and the ν_3 modes vibrate along the molecule's axis. As the molecule is centrosymmetric, the dipole moment associated with these vibrational modes is zero, and it is not possible to optically excite the ν_1 or the ν_3 modes, or a combination of the two[1]. However, the vibrational modes can couple to the rotational modes J of the molecule. This coupling creates dipoles and as a result a large number of lines exist around the vibrational mode's resonance frequencies.

We can state a selection rule for the $\nu_1+\nu_3$ combination that is $\Delta J \neq 0$, i.e. if there is no rotational transition involved, no line exists. Furthermore, as the spin angular momentum of a photon is 1, the rotational state can only change by 1: $\Delta J = \pm 1$. An optical transition involving the $\nu_1 + \nu_3$ combination can only exist if the vibrational mode v couples to a change of the rotational mode

[1]This also include the ν_2 mode and any combination with the ν_2 mode

J. The energy of such a transition is

$$\Delta E = (v'' - v')hc\omega + (h^2/4\pi^2 I)(J'' - J') \tag{3.1}$$

where h is Planck's constant, I is the molecules moment of inertia, v' and v'' are respectively the vibrational ground and exited state quantum numbers ($v = 0, 1, 2, 3 ...$), and J' and J'' are respectively the rotational ground and exited state quantum numbers ($J = 0, 1, 2, 3 ...$). Here we neglect the effects of non-rigid, rotational motion and interactions between vibration and rotation. The J's can take any integer value only limited by the thermal distribution of the rotational ground states, as long as $\Delta J = J'' - J' = \pm 1$. The vibrational quantum numbers can take any integer value and can change by any integer value[2]. However, $v' = 0 \leftrightarrow v'' = 1$ is by far the strongest transition, and the only one we will consider.

As evident by equation (3.1) two bands of ro-vibronic lines exist. Transitions where $\Delta J = J'' - J' = -1$ have energies lower than the pure vibrational transition and constitute the P-branch. Transitions with $\Delta J = J'' - J' = 1$ have energies larger than the pure vibrational transition and constitute the R-branch. The ro-vibronic lines are identified by their rotational ground state. For example, the transition $v' = 0, J' = 3 \leftrightarrow v'' = 1, J'' = 2$ is called P(3), and the transition $v' = 0, J' = 4 \leftrightarrow v'' = 1, J'' = 5$ is called R(4).

The Linestrength Distribution

In an acetylene gas at room temperature it is highly unlikely that a molecule exists in a vibrationally excited state. The energy gap between $v = 0$ and $v = 1$ is simply to large for the molecule to be thermally excited. This is, however, not the case for the rotational states where the energy gaps are significantly lower. The energy of the rotational states are given by

$$E_J = \frac{h^2}{4\pi I} J$$

following the notation of equation (3.1). We then state that the number of molecules occupying a given rotational state in a gas at equilibrium will follow a Boltzmann distribution:

$$N_J \propto e^{\frac{-E_J}{k_B T}}.$$

The linestrengths of the lines will follow this distribution as the probability of an interaction with a line of a specific rotational state will be

$$P_{J'' \to J'} \propto g_{J''} N_{J''}. \tag{3.2}$$

Here g_J is the degeneracy of the J'th rotational state.

[2]Except $\Delta v = 0$, as this would not be a ro-vibronic line but a pure rotational transition.

The degeneracy of the rotational states in acetylene is caused by the nuclear spin statistics governed by the Pauli exclusion principle. The Pauli exclusion principle for a many-particle system requires the total wavefunction to be anti-symmetric with respect to the exchange of two indistinguishable particles. We can approximate the total wavefunction as a product of the electronic, vibrational, rotational, and nuclear spin wavefunctions:

$$\Psi_{tot} = \psi_{elec}\psi_{vib}\psi_{rot}\psi_{ns}.$$

Here, the electronic and vibrational wavefunctions are symmetric with respect to the exchange of nuclei. The rotational wavefunction alternates between symmetric and anti-symmetric for even and odd J's respectively[3]. In order to fulfill the requirement of the Pauli principle, the nuclear spin wavefunction must be anti-symmetric for even J states and symmetric for odd J states.

Let us start by looking at the simple case of $^{12}C_2H_2$ where the carbon atoms have zero spin and do not contribute to the combined spin wavefunction. The hydrogen are spin-$\frac{1}{2}$ atoms and can have either a spin of $-1/2$ or $+1/2$, denoted as $|\downarrow\rangle$ and $|\uparrow\rangle$ respectively. Four spin states can exist:

$$\begin{aligned}
|1,1\rangle &= |\uparrow\uparrow\rangle\,, \\
|1,0\rangle &= \frac{1}{\sqrt{2}}\left(|\uparrow\downarrow\rangle + |\downarrow\uparrow\rangle\right), \\
|1,-1\rangle &= |\downarrow\downarrow\rangle\,,
\end{aligned}$$

and

$$|0,0\rangle = \frac{1}{\sqrt{2}}\left(|\uparrow\downarrow\rangle - |\downarrow\uparrow\rangle\right).$$

Here we use the notation of $|I, m_I\rangle$ where I is the total nuclear spin of the molecule, and m_I is the associated spin projection sub-levels with values $[-I, -I+1, ..., I-1, I]$. The first states have symmetric wavefunctions ($I = 1$), and the last has an anti-symmetric wavefunction. This means that in a gas of $^{12}C_2H_2$ there will be three times as many molecules that can exist in odd J states as can exist in even J states. The degeneracy factor in equation 3.2 is

$$\begin{aligned}
g_{\text{odd}} &= 3, \\
g_{\text{even}} &= 1.
\end{aligned}$$

For the case of $^{13}C_2H_2$ the picture is more complicated as the carbon atoms contribute to the total nuclear spin wavefunction. The combination of 4 spin-$\frac{1}{2}$ particles results in 16 states. Of these 16 wavefunctions 10 are symmetric, and

[3]The symmetry analysis is beyond this work.

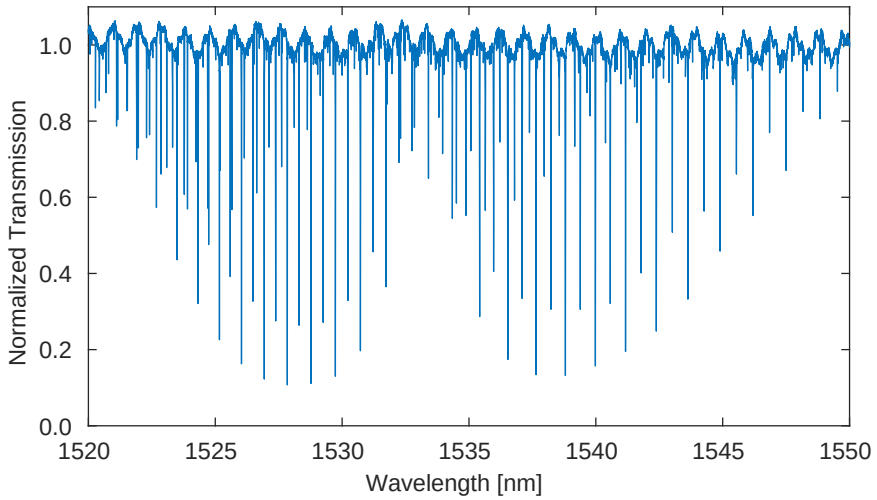

Figure 3.2: A transmission spectrum of the $\nu_1 + \nu_3$ ro-vibrational lines of $^{13}C_2H_2$. The spectrum was measured on a 10 cm long glass cell with 10 hPa of $^{13}C_2H_2$ using a widely tunable ECDL. The Boltzmann distribution of the linestrengths and the alternation of the strength between odd and even J ground states are clearly visible.

6 are anti-symmetric resulting in a linestrength ratio between the even and odd J'' lines of 5/3, this time in favor of the even J'' lines.

A spectrum of the $\nu_1 + \nu_3$ ro-vibrational lines of $^{13}C_2H_2$ is shown on figure 3.2. This is the spectrum of the optical transmission through a 10 cm long glass cell with a pressure of 10 hPa. The linestrengths follow the thermal Boltzmann distribution and the alternation between odd and even J lines as defined by the nuclear spin statistics.

Choosing a Line for a Frequency Reference

The P(16)$\nu_1 + \nu_3$ transition in $^{13}C_2H_2$ is, as mentioned, a practical realization of the meter as defined by BIPM. This transition was most likely chosen based on considerations of resonance wavelength and linestrength. Because of this, the P(16) transition has been the predominant focus for frequency references in the telecommunications C-band. Looking at the other transitions in the $\nu_1 + \nu_3$ bands of $^{13}C_2H_2$, the P(10) transition should be superior for stabilization purposes. This is based on the transition linestrength relative to self-pressure-broadening which is directly linked to the spectroscopic signal strength and achievable Q-value. However, the spectroscopic signal for stabilization will only improve by approximately 1.3 when going from P(16) to P(10).

Isotope-pure $^{13}C_2H_2$ is currently not commercially available, and it has proven very difficult to acquire. Alternative lines in $^{12}C_2H_2$ have been consid-

	$^{13}C_2H_2$ P(16)$\nu_1+\nu_3$	$^{12}C_2H_2$ P(11)$\nu_1+\nu_3$
Wavelength [nm]	1542.3837	1531.5878
Linestrength [10^{-21} cm/mol]	4.836	11.7
Self pres. broad. [kHz/Pa]	234	279

Table 3.1: The parameters for the P(16)$\nu_1+\nu_3$ line in $^{13}C_2H_2$ as measured in [63, 68] and for the P(11)$\nu_1+\nu_3$ line in $^{12}C_2H_2$ as reported in [67].

ered for future use. As mentioned above the only significant difference in ^{12}C and ^{13}C acetylene is the roughly 8 nm shift in spectrum of the $\nu_1+\nu_3$ band. The lines in $^{12}C_2H_2$ are thus centered around 1525 nm placing the lines in the R-branch outside the telecommunication C-band. The focus is therefore on the P-branch placed at the edge of the telecommunication C-band from 1525 nm to around 1540 nm.

When looking for the optimal line, we again consider linestrength and self-pressure-broadening. Even though the P(9) line is the strongest line, it has a high pressure-broadening coefficient. As the goal is to get the highest possible slope of the spectroscopy signal (signal strength vs. linewidth), the linestrengths are weighted by their pressure-broadening coefficients. Figure 3.3 shows the linestrength for the P-branch of the $\nu_1+\nu_3$ band of $^{12}C_2H_2$ with blue columns. The red columns show the linestrength divided by the normalized self-broadening coefficients

$$w_{pressure} = \frac{\Gamma_p^{P(J)}}{\left(\sum_{J=N}^{N} \Gamma_p^{P(J)}\right)/N} \tag{3.3}$$

where $N = 21$ is the number of lines included. This indicates the optimal relation between linestrength and pressure-broadening coefficients to be that of the P(11) line at 1531.59 nm. It is therefore the best candidate for frequency stabilization purposes. This weighting should be valid as pressure-broadening is the greatest contribution limiting the spectroscopically achievable linewidth.

Table 3.1 shows the line parameters for $^{13}C_2H_2$ P(16)$\nu_1+\nu_3$ and $^{12}C_2H_2$ P(11)$\nu_1+\nu_3$. The linestrength of the ^{12}C line is a factor of 2.4 stronger than that of the ^{13}C line and has a similar pressure-broadening coefficient. A significantly higher slope of the spectroscopic signal should be achievable using the P(11)$\nu_1+\nu_3$ line of ^{12}C-acetylene.

Thermal Distribution of Rotational States

As mentioned above, the fraction of molecules in a given rotational state J is given by the Boltzmann distribution. The fraction of molecules in the ground

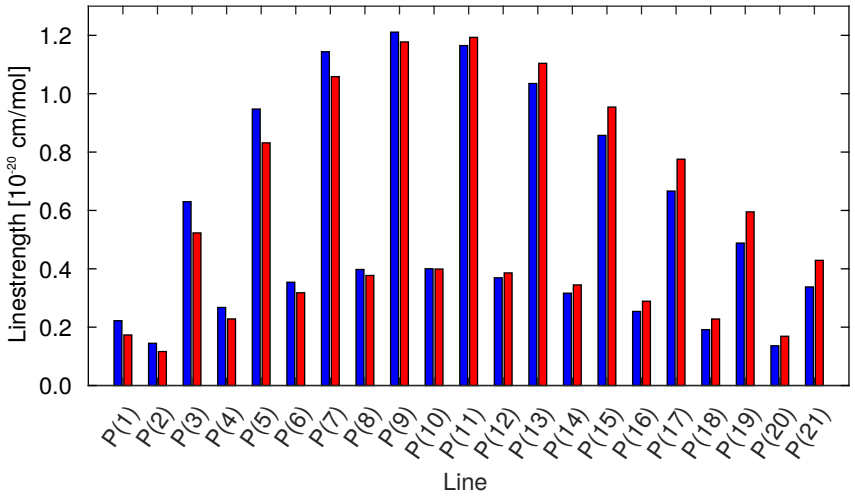

Figure 3.3: The linestrengths of the P-branch in the $^{12}C_2H_2$ $\nu_1 + \nu_3$ rovibrational band. The blue bars show the linestrength and the red bars show line strength weighted by their pressure-broadening coefficients as described by equation (3.3). The data used is from the HITRAN database [67].

state for the P(16) transition is given by

$$\frac{N_{J=16}}{N} = \frac{e^{\frac{-E_{J=16}}{k_B T}}}{\sum_{J=0}^{\infty} e^{\frac{-E_J}{k_B T}}}. \tag{3.4}$$

The energy of the rotational state is $E_J = hcBJ(J+1)$ where $B_{\text{C-13}} = 1.119574$ cm^{-1} and $B_{\text{C-12}} = 1.176646$ cm^{-1} [69]. For the ^{13}C isotope at $T = 295$ K about 4.1 % of the molecules will be in the P(16) rotational ground state. For the ^{12}C isotope at $T = 295$ K about 6.2 % of the molecules will be in the P(11) rotational ground state. The probability of having a molecule in a given ground state is dependent on the gas temperature so for a specific ground state there will be an optimum temperature where the highest possible number of molecules occupy that state. For the P(16) state of the ^{13}C isotope this optimum temperature is approximately 430 K (157 °C) where the fraction of P(16) molecules is 4.5 %. Raising the temperature 135 °C from room temperature will only increase the fraction of molecules contributing to the spectroscopic signal with 0.4 percentage points. For the P(11) state of the ^{12}C isotope the optimum temperature is approximately 220 K having 6.4 % of the molecules in the P(11) state. Operating the gas at a high temperature adds significantly to the complexity of the system and increases the pressure-broadening and the transit-time-broadening. We can therefore conclude that

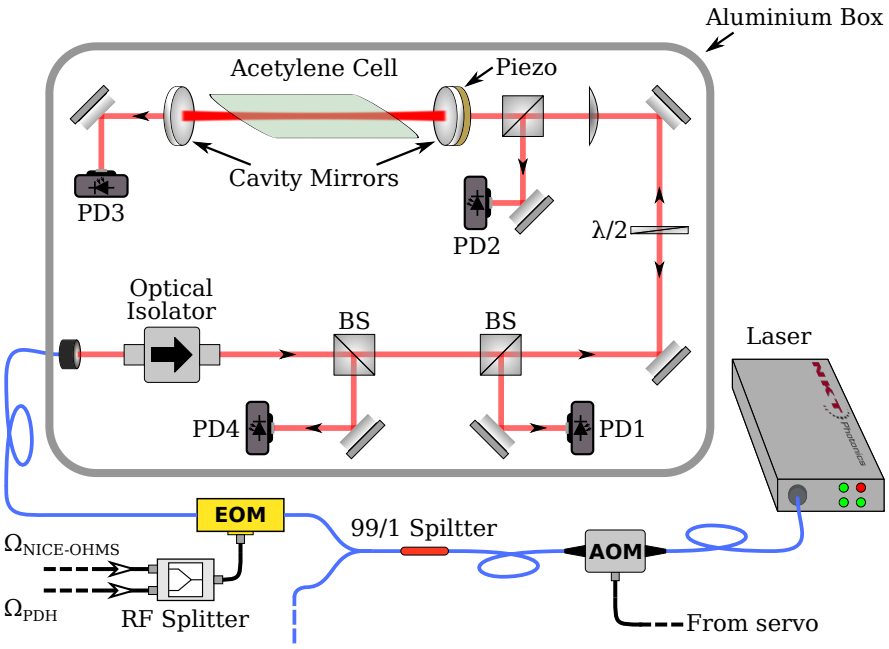

Figure 3.4: A schematic of optical components in the acetylene frequency reference. Blue lines are optical fibers, and red lines are free-space beams. AOM: Acousto-Optic modulator. EOM: Electro-Optic Modulator. BS: Beam Sampler. $\lambda/2$: half-wave plate. PD: photodetector. PD1 is used for PDH-stabilization locking the cavity length on resonance with the laser frequency. PD2 is used for RAM-stabilization. PD3 is used for the NICE-OHMS detection. PD4 is used for optical power stabilization. The mirror mounts holding the cavity mirrors are placed on a Zerodur plate, not included in the schematic.

rotational state manipulation through temperature with the goal of increasing the linestrength is not desirable.

3.2 Configuration of the Experimental Setup

A total of 3 nearly identical spectroscopy systems have been built and are referred to as acetylene 1, 2, and 3. With only two lasers, AOMs, and EOMs available, two setups can be run simultaneously. A schematic of the optical components that constitutes one experimental setup is shown in figure 3.4.

The two lasers that are used are both NKT Photonic Koheras BASIK E15 modules. One is an older module, and the other one is a newer module. These lasers are erbium-doped fiber lasers with thermal tuning and piezo tuning of the frequency. The piezo tuning has a range of 800 MHz with a bandwidth of 20 to 30 kHz, and the thermal tuning has a range of 1 nm. The older model

has a maximum output power of 48 mW and the newer model has a maximum output power of 40 mW.

The laser output is coupled into a fiber Acousto-Optic Modulator (AOM) allowing for fast frequency modulation with a bandwidth of up to a few MHz. The modulation carrier frequency is 80 MHz with a span of ±5 MHz giving a maximum modulation amplitude of 10 MHz peak-peak. The AOM is driven by a low-noise Voltage Controlled Oscillator (VCO) (Mini-Circuits ZX-78+) with additional RF power control through a voltage variable attenuator (Mini-Circuits ZX73-2500+). As the optical power through the AOM is dependent on the RF power driving the AOM, the RF power can be used to control the optical power and allow for high bandwidth feedback for power stabilization.

Following the AOM, 1 % of the laser power is split off using a 20 dB polarization-maintaining fiber splitter. This is the stabilized system's output and is used for characterization of the stabilized laser's frequency noise.

The laser light is then phase modulated with a fiber EOM at frequencies of both $\nu_{PDH} = 10$ MHz and ν_{NO} which is set to be equal to the cavity FSR. An RF splitter is used to combine the modulation frequencies thereby generating modulation for both the PDH locking of the cavity length and for the NICE-OHMS detection with a single EOM. On one of the EOMs an RF bias-tee is used to apply a DC-bias to counteract RAM. The other EOM has separate electrodes for DC-biasing. Both the EOMs are placed in a copper mounting to ensure a stable temperature and effective RF shielding.

After the EOM the fiber enters an air-tight aluminium box where the laser light is coupled to free-space propagation. The aluminium box contains all the free-space optics in the setup and takes up a volume of $144 \times 388 \times 528$ mm (see appendix A.1). The optical components are mounted on a half-inch thick aluminium breadboard which is placed on vibration-isolating rubber on the floor of the aluminium box. The box is also placed on vibration-isolating rubber thereby giving two coupled vibration-damping coefficients ensuring a high degree of vibration isolation.

The first component of the free-space optics is an optical Faraday isolator. The optical isolator ensures both that the back-reflection into the fiber is suppressed by 40 dB, and that the polarization of the light is constant and linear. Right after the isolator, a beam-sampler extracts a fraction of the beam onto a photo detector, PD4, monitoring optical power fluctuations. This beam-sampler is followed by another beam-sampler extracting a part of the back reflection from the cavity onto the detector PD1. PD1 is used for PDH-locking of the cavity length keeping the cavity on resonance with the laser at all times (see section 2.1).

Just before the cavity in-coupling mirror, a third beam-sampler provides light for detector PD2 that is measuring the modulation phase off-set, i.e. RAM. The RAM signal is demodulated as described in section 2.2. This signal is inputted to a Red Pitaya microcomputer functioning as a P-I servo that applies feedback to the EOM bias voltage. The Red Pitaya is a FPGA-

chip controlled by a small ARM-processor allowing for easily programmable signal-processing, like a P-I loop, up to a bandwidth of 50 MHz.

Three different cavity configurations have been investigated for this system. Two of the configurations are the versions of the large waist cavity described in section 2.3 and the third is a standard two-mirror linear cavity as depicted in figure 3.4. In all three cavity configurations the in-coupling mirror is a half-inch mirror with radius of curvature of 9 m. The mirror is glued onto a piezo-electric element which is again glued to a copper hemisphere with center hole for optical access and an off-center tin filling. The use of the copper hemisphere helps to minimize mechanical resonances of the mirror mounting and thereby enables a better cavity stability. The out-coupling mirror of the cavity is a 1 inch mirror also with a radius of curvature of 9 m. In the case of the linear cavity the distance between the mirrors is 23 cm resulting in an FSR of 650 MHz and a waist radius of 0.7 mm. In the large waist cavity configurations the total length of the cavity is 44 cm resulting in an FSR of 340 MHz and a waist radius of either 1.3 mm or 3 mm, depending on the configuration.

Using the PDH technique (see section 2.1), the cavity length is resonantly locked to the frequency of the laser. This ensures that light is coupled into the cavity at all times even when the laser frequency is scanned. The cavity lock acts on the piezo moving the in-coupling mirror. This keeps the cavity length on resonance with the laser's frequency. Slow temperature variations of the aluminium breadboard leads to expansion or compression of the cavity. As the piezo does not move the mirror perfectly along the cavity axis, small changes in cavity finesse and in-coupling efficiency can occur. To minimize this effect the mirror mounts of the linear cavity is glued onto a Zerodur glass plate that is thermally isolated from the aluminium breadboard. Due to the low thermal expansion coefficient of Zerodur, the cavity resonance can be maintained within a piezo voltage range of a few volts.

A glass cell with acetylene is placed inside the cavity. In order to have as low an intra-cavity optical loss as possible, the glass cell has Brewster angled, fused-silica windows. The Brewster windows are parallel to avoid different optical path-length across the cavity mode wavefront as this could cause further astigmatism in the large waist cavity. The cell has an effective length of 15 cm. A technical drawing of the glass cell is shown in appendix A.2.

The cavity transmission, carrying information about the molecular dispersion, is detected by a photodetector (PD3). The dispersion signal is recovered as described in section 2.2 and used as an input on a Vescent D2-125 laser servo. The servo has configurable gain and corner-frequencies allowing for various combinations of proportional gain, two integration corner-frequencies, and a derivative gain and corner-frequency. The servo can be set up to act only on the internal laser's piezo or to act on the AOM-VCO with a fast feedback simultaneously with a slow feedback on the laser's piezo.

An example of the acetylene Lamb-dip, measured in the cavity transmis-

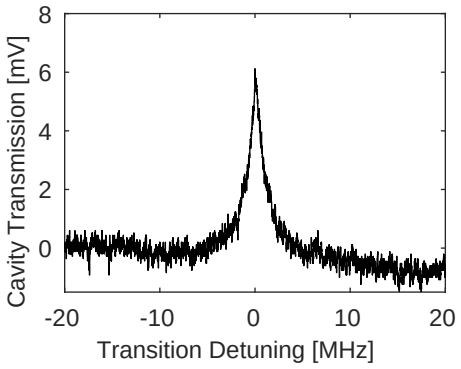

Figure 3.5: The Lamb-dip as detected in the pure cavity transmission signal on the Acetylene 2 setup. The intra-cavity power is 2.35 W, and the cavity finesse is approximately 300. The signal-to-noise is 50.

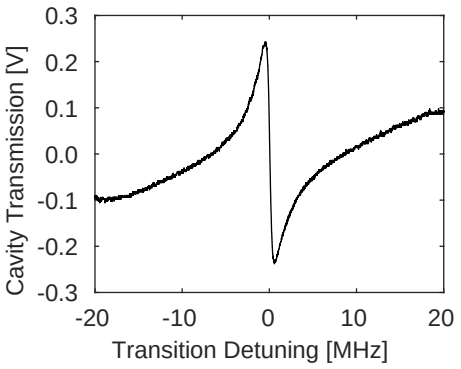

Figure 3.6: The dispersion signal from the Acetylene 2 setup with an intra-cavity power of 2.0 W and a cavity finesse of approximately 300. The signal-to-noise is 10000.

sion without any modulation, is shown in figure 3.5. An example of the acetylene dispersion signal, measured with the NICE-OHMS technique, is shown in figure 3.6. Here we clearly see the impressive signal-to-noise of the NICE-OHMS compared to the pure cavity transmission signal. The signal-to-noise, defined here as the RMS signal amplitude over the RMS amplitude of the noise squared, is $(U_{signal,rms}/U_{noise,rms})^2 \approx 10^4$ for the NICE-OHMS signal and $(U_{signal,rms}/U_{noise,rms})^2 \approx 50$ for the pure cavity transmission signal.

High Frequency DDS

In order to achieve low-noise and easy control of the modulation and demodulation RF signals for the NICE-OHMS detection, two high frequency Direct Digital Synthesizer (DDS) systems were built. The DDS is based on the Analog Devices AD9959 chip. This is designed for a frequency output of up to 200 MHz on 4 individual channels with a 500 MHz clock input. The required modulation frequency for the acetylene systems is, as mentioned above, approximately 650 MHz in the case of the linear cavity. This is well above the maximum output frequency of the chip. As a consequence of the inner workings of a DDS, the generated frequency ν_0 will be reflected in the clock frequency thereby generating frequencies at $\nu_{clk} - \nu_0$, $\nu_{clk} + \nu_0$, and the harmonics thereof. The frequency at $\nu_{clk} - \nu_0$ is isolated by a 330 MHz to 375 MHz bandpass filter (Mini-Circuits SXBP-350), amplified by a low-noise amplifier (ZX60-P103LN+), and frequency doubled. The resulting output has a frequency of

$$\nu = 2(\nu_{clk} - \nu_0)$$

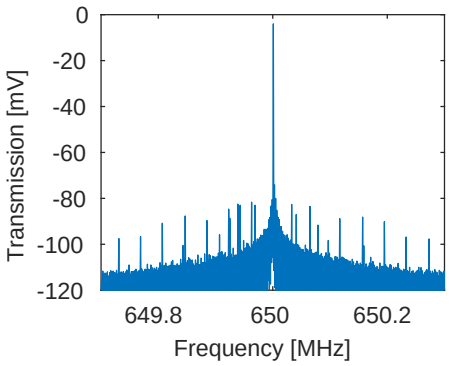

Figure 3.7: The RF spectrum of the DDS clock with a resolution bandwidth of 10 Hz.

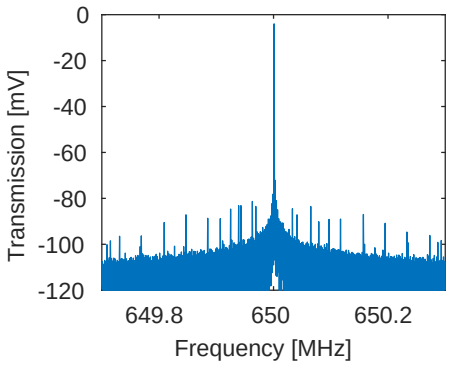

Figure 3.8: The RF spectrum of the DDS output with a resolution bandwidth of 10 Hz.

with a maximum amplitude of -4 dBm. When the large waist cavity is used, the cavity FSR is 340 MHz. This frequency is easily achieved by bypassing the frequency doubler.

A HP8648A frequency synthesizer is used to generate the clock frequency for two DDS-chips simultaneously using an RF splitter to divide the signal to the DDS-chips. To compare the DDS system's noise and the HP8648A's noise, the HP was set to output 650 MHz at 1 dBm of power and coupled through an RF splitter before the spectrum was recorded with a spectrum analyzer. The RF spectrum of the clock input and DDS output is shown in figure 3.7 and 3.8, respectively. Here a small increase in phase-noise of the DDS of approximately 4 dB is visible at 300 kHz off-set. This is most likely due to the amplifier and frequency doubling of the DDS-chip output.

Despite the slightly increased phase-noise compared to the HP frequency synthesizer, this DDS system has proven a great tool in the NICE-OHMS setup. The DDS system provides up to 8 high frequency signal outputs which are all phase locked and with individual frequency, amplitude, and phase-offset adjustments. If compared to the alternative of a system with RF splitters, combiners, and analog phase-shifters, the DDS system allows for far easier optimization of the RF parameters.

3.3 Spectroscopic Linewidth Analysis

We will now take a look at the spectroscopic signals of the P(16)$\nu_1 + \nu_3$ line in $^{13}C_2H_2$ as measured in the setup described above. The following analysis focuses only on the linewidth of the Doppler-free Lamb-dip. The system specific saturation power, using the linear cavity, is found, and the gas pressure is estimated based on the measured linewidths.

Three glass cells were filled with carbon-13 acetylene at the Danish National Metrology Institute (DFM). The acetylene gas has a specified isotopic purity of 99 %. The target pressure was 1 Pa, and the background pressure in the gas filling vacuum setup was approximately 1×10^{-3} Pa. The achieved cell pressure in cell number 2 and 3 was significantly better than in Cell number 1. As a consequence only cell number 2 and 3 were used.

In the linewidth analysis of the P(16)$\nu_1 + \nu_3$ line, it is assumed that the natural linewidth is negligible compared to the different broadening mechanisms in play. This assumption is based on natural linewidth estimations of similar ro-vibrational lines [53].

The cavity mode waist in the linear cavity is $w_0 = 0.7$ mm, and thus the transit-time-broadening can be found to be

$$\Gamma_{tt} = \frac{1}{2\pi}\sqrt{2\ln(2)}\sqrt{\frac{\pi k_B T}{2M}}\frac{1}{2w_0} = 99 \text{ kHz} \tag{3.5}$$

where k_B is the Boltzmann constant, $T = 295$ K is the gas temperature, and M is the mass of the molecule. The contributions from power- and pressure-broadening are significantly larger, and the line shape will mainly be based on homogeneous broadening effects. The parameter of interest is the width of the spectroscopy signal, and here the difference between a Lorentzian model and a Voigt model is negligible. The line shape is therefore modeled as purely Lorentzian.

The linewidth measurements are done using the dispersion signal where the frequency-axis is calibrated using the 10 MHz sidebands from the PDH phase modulation. As the dispersion signal of the Lamb-dip is superimposed on the dispersion signal from the broad Doppler profile, the model of the Lorentzian dispersion profile includes a linear slope:

$$D(\Delta) = A\frac{\Delta}{\Delta^2 + \gamma^2} + B\Delta + C. \tag{3.6}$$

Here A is a scaling factor, B is the background slope attributed to the dispersion of the Doppler profile, and γ is the HWHM of the Lorentzian line of the Lamb-dip. The linewidth is found by fitting this expression to the recorded data.

A series of the dispersion signals was recorded at 14 different intra-cavity powers for cell 2 and 17 different intra-cavity powers for cell 3. In all, 9 signals at each optical power was recorded and fitted with the purpose of estimating the measurement uncertainty. The intra-cavity power was estimated by measuring the cavity output power and dividing by 1.8 to account for the optical power in the sidebands (see section 2.2). A representative sample of fits to the dispersion signals is shown in figure 3.9 and 3.11. The resulting Γ versus P_{cav}

	Acetylene 2	Acetylene 3
Γ_0	567 ±19 kHz	476 ±21 kHz
P_{sat}	194 ±17 mW	396 ±48 mW
Γ_{tt}	99 kHz	99 kHz
p	2.0 Pa	1.6 Pa

Table 3.2: Gas cell parameters as measured in the setup with the linear cavity configuration. The pressure p, is estimated based on the pressure-broadening coefficient measured in [63].

is plotted and fitted to the power broadening expression

$$\Gamma(P) = \Gamma_0 \sqrt{1 + \frac{P}{P_{sat}}}. \tag{3.7}$$

Here $\Gamma_0 = \Gamma_N + p\Gamma_p + \Gamma_{tt}$ is a combination of the natural linewidth, the pressure-broadening, and transit-time-broadening. The fits are shown in figure 3.10 and 3.12. The error bars on the data points represent the standard deviations of the 9 Γ-values from the dispersion fits. From the fits in figure 3.10 and 3.12 we learn the system-specific parameters, Γ_0 and P_{sat}, of acetylene 2 and acetylene 3 with a linear cavity configuration. The acetylene pressure in the cells can now be estimated as the natural linewidth of the transition, Γ_N, is assumed to be negligible. Using the pressure-broadening coefficient $\Gamma_p = 234$ kHz/Pa as reported in [63], the acetylene pressure in the cells are calculated. The parameters are presented in table 3.2.

3.4 The Dispersion Signal

As evident from the previous section, two parameters determine the width of the dispersion signal: the optical power and the size of the interrogation beam. In this section we investigate the optima of these parameters for laser stabilization purposes. Here, not only the signal width but also the signal amplitude and noise characteristics are important as it is the signal slope and signal noise that determine the achievable frequency stability. This means that there exists a combination of power and beam size that will result in the best possible signal for a given gas pressure.

Beam Waist Dependency

The three different optical cavity configuration described in section 2.3 were used on acetylene cell number 2. The relation between power-broadening, transit-time-broadening, and the molecular transition saturation intensity determines the optimal relation between the beam radius and the optical power.

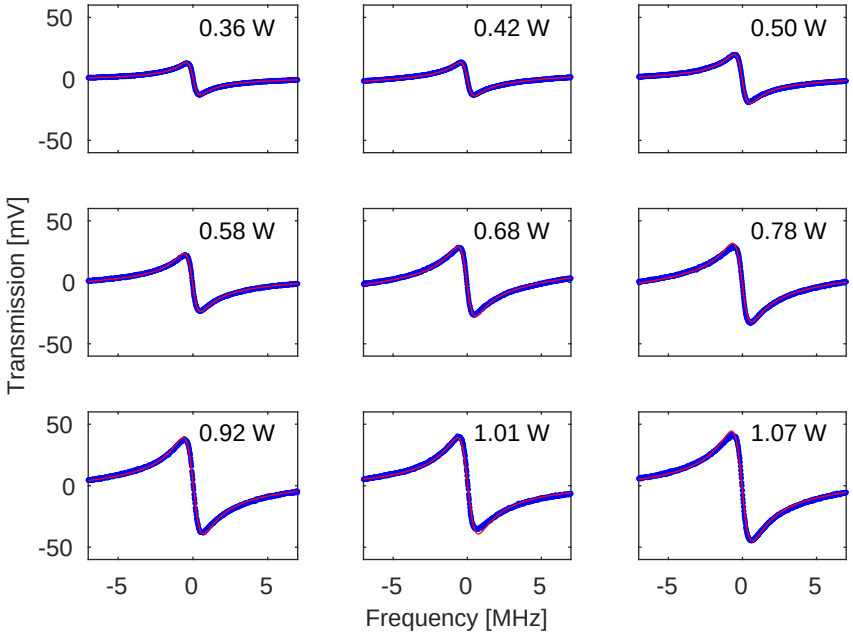

Figure 3.9: The measured dispersion signals at different intra-cavity powers of acetylene cell 2. The powers noted on the plots are the measured intra-cavity optical powers at the line resonance. The red lines are fits of equation (3.6) to the measured data shown in blue.

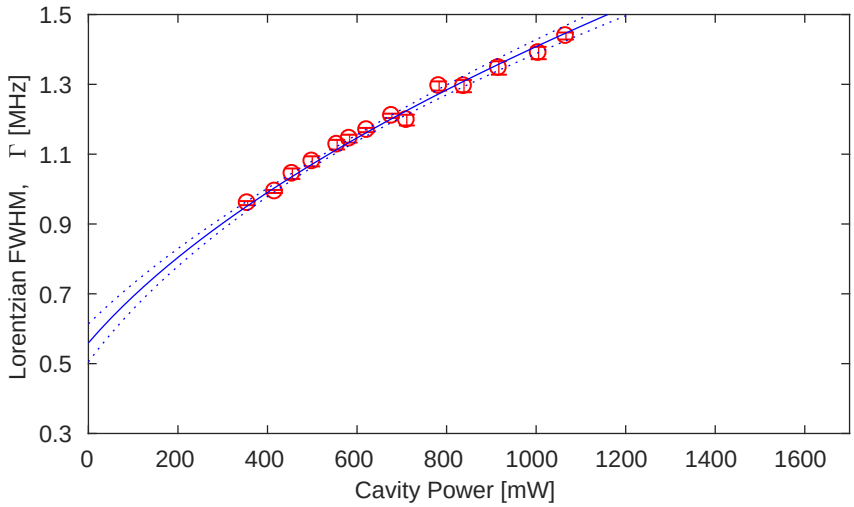

Figure 3.10: The power-broadening profile of acetylene cell 2. The red circles show the linewidth as found by the fits shown in figure 3.9. The blue curve is a fit of equation 3.7 to the red circles. The dotted blue lines indicate the 95 % confidence bounds of the fit.

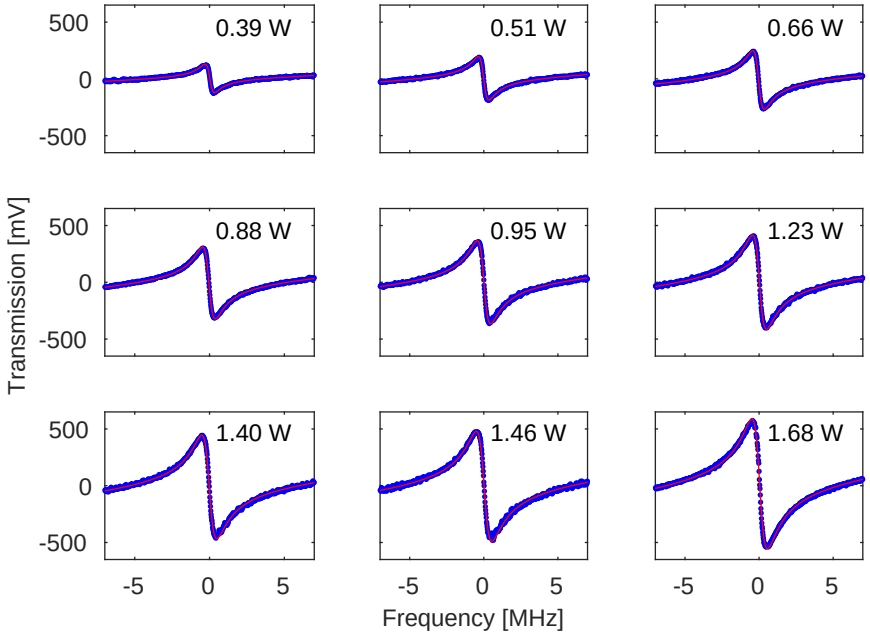

Figure 3.11: The measured dispersion signals at different intra-cavity powers of acetylene cell 3. The powers noted on the plots are the measured intra-cavity optical powers at the line resonance. The red lines are fits of equation (3.6) to the measure data shown in blue.

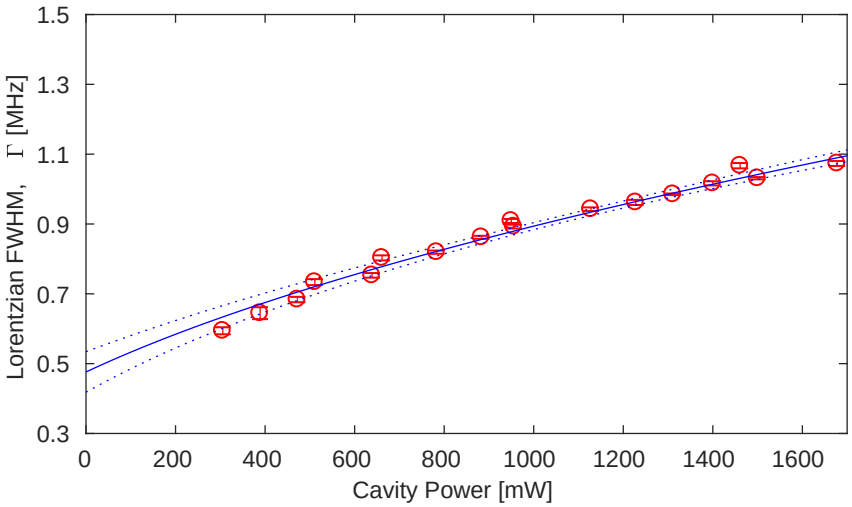

Figure 3.12: The power broadening profile of acetylene cell 3. The red circles show the linewidth as found by the fits shown in figure 3.11. The blue curve is a fit of equation 3.7 to the red circles. The dotted blue lines indicate the 95 % confidence bounds of the fit.

The intensity needs to be high enough to adequately saturate the transition, and the beam radius needs to be large enough that transit-time-broadening is not dominant. In the case of ro-vibrational lines in acetylene the pressure-broadening is the main factor influencing the saturation intensity as the natural linewidth is negligible. This means that if the gas pressure is lowered, the saturation intensity is lowered, and transit-time-broadening becomes more dominant leading to a large beam radius as the optimum.

As described in section 3.2 the NKT laser can deliver a maximum of 40 mW of optical power. The EOM and AOM each have an insertion loss of roughly 2.5 dB resulting in an available power of just above 10 mW at the cavity input. The measurements of the beam size dependency was done without the AOM allowing for measurements with a power of up to 20 mW.

The decrease in intensity is two-fold when the cavity beam radius is expanded as the cavity finesse is significantly lower in the large waist cavity. To determine the optimal cavity configuration for stabilization purposes, the highest achievable signal slope for each cavity is investigated. As in the linewidth analysis a series of signals is recorded for each optical power so that each point is the mean of now 23 signal slopes. Again, the errorbars are representing the standard deviation of the 23 slopes. The slopes were found by linear fitting of the center part of the dispersion signal. The x-axis was again calibrated by the 10 MHz PDH sidebands. Figure 3.13 shows the signal slope power dependency for the three cavities.

The data presented on figure 3.13 indicate that the optimum beam radius lies between 0.7 mm and 1.3 mm. It has not been possible to achieve a stable cavity mode in the large waist cavity with a waist radius below 1.3 mm. Taking into account the far superior mechanical stability and simplicity of the linear cavity, this configuration is the best choice for the laser stabilization setup. In the case where the acetylene cell has a lower gas pressure, the large waist cavity configuration will allow for a larger slope and will be the better choice.

Optical Power Dependency

Having chosen the linear cavity with a mode radius of 0.7 mm, the optimal intra-cavity power is now investigated. A higher optical power will give a higher saturation and a bigger signal, but it will also broaden the line (equation (3.7)). The parameters found in section 3.3 can be used to estimate the specific system's optimal intra-cavity power in relation to the dispersion signal slope.

The size of the molecular phase shift that is measured is proportional to the saturation induced Lamp-dip. The size of the Lamp-dip can be described by the absorption at the center of the Gaussian Doppler profile

$$\alpha(P,\Delta) = \alpha_0 e^{-\frac{\Delta^2}{2\sigma^2}} \frac{1}{1+\frac{P}{P_{sat}}} \tag{3.8}$$

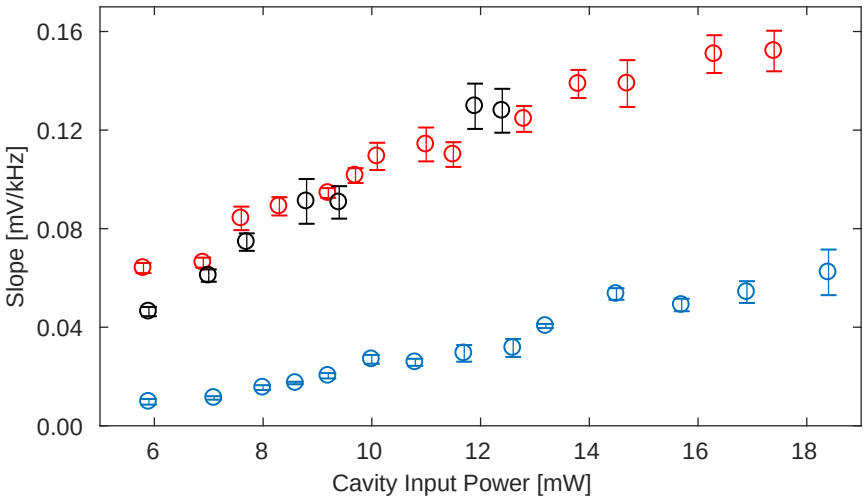

Figure 3.13: The dispersion signal slope versus cavity input power. The blue points show signal slopes obtained with a cavity waist radius of 3.0 mm, the black points are for a waist radius of 1.3 mm, and the red are for a waist radius of 0.7 mm.

and the absorption at zero detuning of the saturated line

$$\alpha(P, \Delta = 0) = \alpha_0 \frac{1}{1 + 2\frac{P}{P_{sat}}} \tag{3.9}$$

where $\alpha_0 = 6.93\ \mathrm{m}^{-1}\ \mathrm{Pa}^{-1}$ [68]. By subtracting equation (3.8) and (3.9) the size of the Lamp-dip is obtained. Furthermore, the signal amplitude is proportional to the power incident on the photo detector (PD3 on figure 3.4). The signal slope is given by the signal amplitude divided by the power-broadened width of the line $\Gamma(P)$ shown in figure 3.10 and 3.12. We can now write an expression for the signal slope:

$$s(P) = A\left(\frac{1}{1 + \frac{P}{P_{sat}}} - \frac{1}{1 + 2\frac{P}{P_{sat}}}\right)\frac{P}{\Gamma(P)}. \tag{3.10}$$

Here the constant A includes the absorption in the cell $\alpha_{cell} = \alpha_0 p L_{cell}\frac{F}{\pi}$ where $L_{cell} = 0.15$ m is the length of the acetylene cell, and $F = 380$ is the cavity finesse. A also includes constants related to the detector: $U_{det} = t^2\eta_{det}R_{det}$ with unit V/W where $t^2 = 0.001$ is the power transmission of the cavity output mirror, $\eta_{det} = 1.1$ A/W is the detector efficiency, and $R_{det} = 50\ \Omega$ is the resistance over which the diode current is measured. Figure 3.14 and 3.15 show the slope dependency on the intra-cavity power for acetylene cell 2 and 3 in the linear cavity configuration. These graphs show the optimal

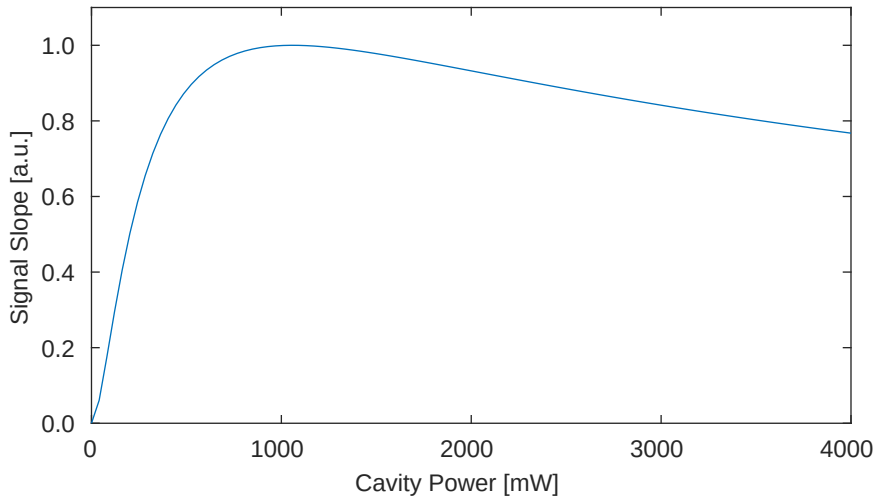

Figure 3.14: The optical power dependency of the dispersion signal slope $s(P)$ (equation (3.10)) for the acetylene 2 cell in the linear cavity configuration. The plot shows a normalized curve and does not include the contributions from the constant A. The curve is based on the system specific saturation power and power broadening as presented in table 3.2 and figure 3.10.

total intra-cavity power to be 1 W for acetylene 2 and 2.6 W for acetylene 3. The graph for acetylene show a fairly flat dependency between 2 W and 3 W. Running the setup at maximum laser output power corresponds to an intra-cavity power just above 2 W. This corresponds to a saturation power of approximately 1.1 W, as the sidebands do not contribute to the saturation of the line (see section 2.2). This is the optimum saturation power in the case of the acetylene 2 cell and somewhat below the optimum of the 2.6 W of the acetylene 3 cell.

Signal-to-Noise

The optimized signal from the acetylene 3 cell is shown in figure 3.16. This signal is achieved with two RF-amplifiers with a gain of 18 dB on the photo detector output (PD3 on figure 3.4) and an operational amplifier with a gain of 10 on the RF-mixer output (Mixer on figure 2.4). The slope at zero detuning is 1.47 V/MHz. The signal noise is estimated by disabling the laser's frequency scan and tuning the laser frequency to be on the 'shoulder' of the dispersion signal, i.e. where the signal slope is zero. The noise of the dispersion signal, as recorded on an oscilloscope, is shown in figure 3.17. The oscilloscope was configured with a sampling rate of $f_s = 2.5$ MHz ensuring a spectral resolution within the expected servo-loop bandwidth. The standard deviation of the noise

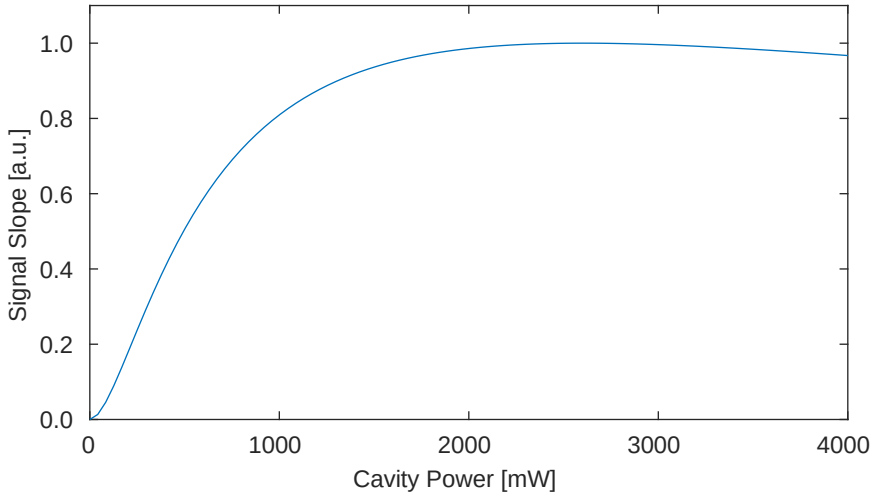

Figure 3.15: The optical power dependency of the dispersion signal slope $s(P)$ (equation (3.10)) for the acetylene 3 cell in the linear cavity configuration. The plot shows a normalized curve and does not include the contributions from the constant A. The curve is based on the system specific saturation power and power broadening as presented in table 3.2 and figure 3.12.

is 3.6 mV.

In order to investigate the frequency components of the noise, an estimation of the Power Spectral Density (PSD) is calculated. The PSD is based on the Fast Fourier transform of the noise data and calculated as a one-sided spectrum in the unit of dBm/Hz. The estimated, one-sided PSD is shown in figure 3.18.

Even though the laser is tuned to a frequency where the signal slope is zero the noise is believed to be primarily caused by the laser frequency noise of the free-running laser. This recording is therefore not a good representation of the intrinsic signal noise. This is substantiated by the clear identification of a 33 kHz peak in the PSD, perfectly matching the laser's piezo resonance as specified by the manufacturer. Subsequent analysis of the dispersion error-signal noise under lock will further substantiate this (see figure 3.19). The integrated noise power over the 600 kHz bandwidth of the PSD is $P_{noise} = -36.5$ dBm yielding a signal-to-noise of $P_{signal} - P_{noise} = 40.6$ dB where

$$P_{signal} = 10\log_{10}\left(\frac{{U_{rms}}^2/R}{1\text{ mW}}\right) = 10\log_{10}\left(\frac{0.36^2/50\Omega}{1\text{ mW}}\right) = 4.1\text{ dBm}.$$

This is in good agreement with the signal-to-noise value calculated simply as

$$SNR = \left(\frac{U_{signal,rms}}{U_{noise,rms}}\right)^2 = \left(\frac{359\text{ mV}}{3.6\text{ mV}}\right)^2 \approx 10^4 = 40\text{ dB}.$$

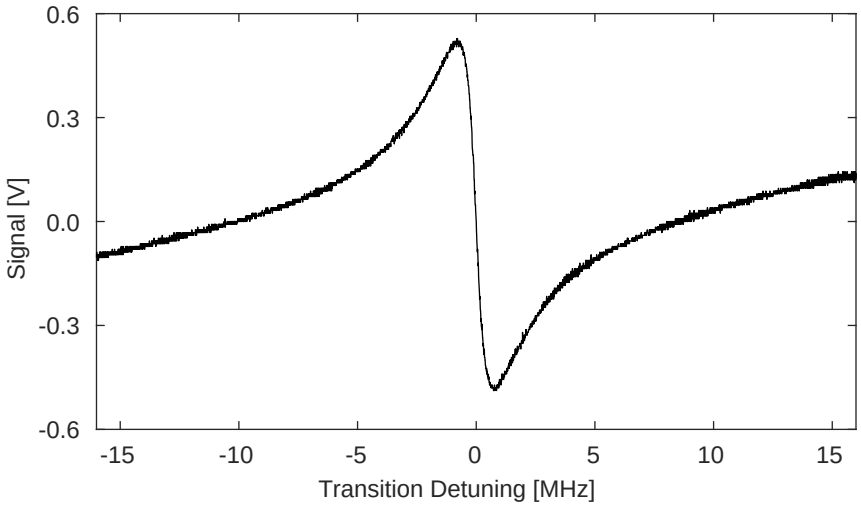

Figure 3.16: The optimized dispersion signal of the Acetylene 3 cell. This signal was bandwidth-limited with a 2 MHz low-pass filter as shown on figure 2.4. The signal amplitude is $U_{PP} = 1$ V with a noise amplitude of $N_{rms} = 3.6$ mV.

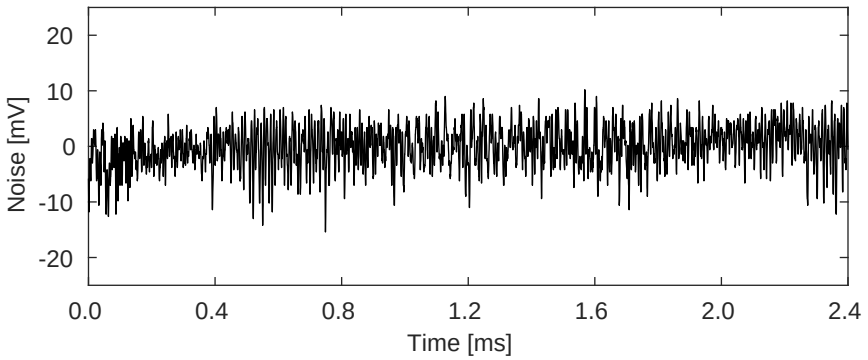

Figure 3.17: The dispersion signal noise measured with a free-running laser. The noise recording is of the dispersion signal shown in figure 3.16 where the laser's frequency was tuned to the 'shoulder' (zero-slope) of the dispersion signal. The sampling time was $\tau_0 = 0.2$ µs with a total of 6000 points.

The PSD shows a noise floor of white noise at approximately -95 dBm between 400 kHz and 600 kHz. If we assume that this white noise is the only noise component intrinsic to the signal, and thereby that the 33 kHz harmonics and the $1/f$-noise is attributed to laser frequency noise, we get the integrated noise to be

$$P_{noise} = 10^{\frac{-95\ \mathrm{dBm}}{10}} \cdot 600\ \mathrm{kHz} = 0.15\ \mu\mathrm{W} = -38.2\ \mathrm{dBm}$$

This would result in an $SNR = 42.3$ dB.

Using these parameters of the dispersion signal (figure 3.16) in equation (1.1) we can now estimate the theoretically achievable frequency stability for this setup for a given feedback bandwidth BW:

$$\sigma(\tau) \approx \frac{1}{Q}\frac{1}{SNR}\sqrt{\frac{1}{BW\tau}}.$$

Based on this noise analysis, the acetylene reference setup should allow for frequency stabilization of a fractional instability of $1 \times 10^{-15}/\sqrt{\tau}$ when the $SNR = 10^4$ and with a feedback bandwidth of $BW = 600$ kHz. If an $SNR = 1.7 \times 10^4$ is achieved, an instability of $6 \times 10^{-16}/\sqrt{\tau}$ should be possible. The $6 \times 10^{-16}/\sqrt{\tau}$ is just above the level of some of the best performing cavity-reference lasers [20, 19, 21, 5]. This estimation is only valid if the noise of the error-signal can be limited to the white noise described above. In the following section we will take a look at the achieved stability of the acetylene reference setup.

3.5 Stability Analysis

Evaluation of the lasers' frequency stability is done by measuring the beat frequency of the two setups (acetylene 2 and 3) when locked. The locking set-points on the dispersion signal of the two setups were chosen to be slightly off-center in opposite directions, thereby generating a beat-note frequency of 30 kHz to 70 kHz. The beat-note frequency is measured with a Pendulum CNT-90 frequency counter. Two Rohde & Schwarz HMC8012 digital multimeters and a National Instruments data acquisition board is used to monitor the optical power, RAM, and temperature synchronously with the beat frequency.

The servo-loop bandwidth is estimated by the RF spectrum of the 650 MHz signal from the cavity transmission photodetector (PD3 in figure 3.4). An RF-coupler is used to monitor the signal just before demodulation with the RF-mixer (see figure 2.4). This RF spectrum shows the in-loop noise of the error-signal of the stabilized laser with a resolution bandwidth of 100 Hz and is shown in figure 3.19. The so-called servo-bump is seen on the spectra and

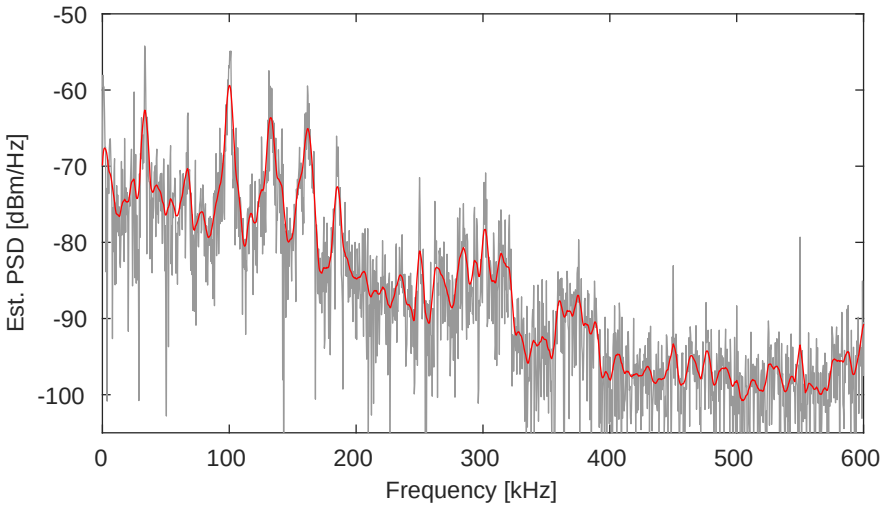

Figure 3.18: The estimation of the one-sided power spectral density of the dispersion signal noise shown in figure 3.17. The resolution bandwidth of the PSD is $RBW = 417$ Hz, where the red curve is the PSD of a time-averaged spectrum over 10 points. Harmonics of a 33 kHz component is prominent. This frequency component coincides with a laser piezo resonance. The integrated noise power from 0 kHz to 600 kHz is -36.5 dBm.

peaks at 360 kHz for acetylene 2 and 370 kHz for acetylene 3. The noise floor seen on the RF spectrum is in good agreement with the PSD of the noise on the DC error-signal shown in figure 3.18[4]. Furthermore, the noise on the PSD in figure 3.18, believed to originate with the laser's frequency noise, is not visible in the measured spectra for the lasers when locked (figure 3.19). This substantiates the assumption that the intrinsic noise of the error-signal is significantly lower than shown in figure 3.17 and 3.18. The spurious frequency components stem from the DDS-clock. The difference of the spurious component between acetylene 2 and acetylene 3 is because of a small difference in the FSR of the two setups' cavities leading to a small difference in the modulation frequency of the two setups.

Frequency Noise Analysis

The following analysis is made based on the data showing the best achieved frequency stability of the setups. In this measurement, active feedback was applied to stabilize RAM fluctuations, but no feedback was applied to stabilize the optical power.

[4]We most keep in mind that there is a small difference in the resolution bandwidth when comparing the spectra.

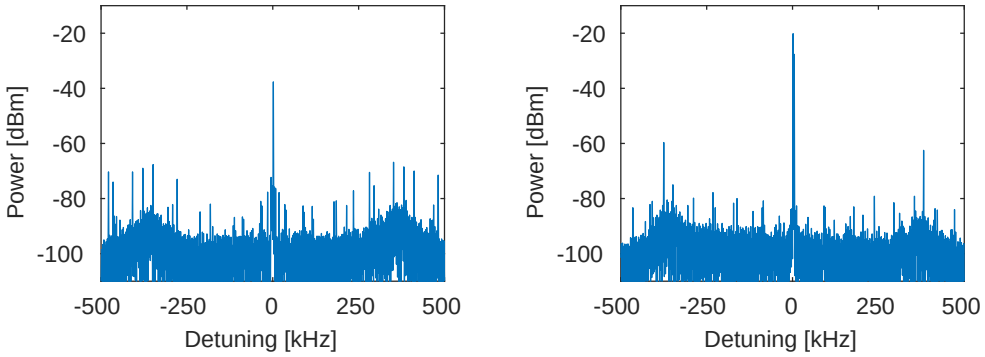

Figure 3.19: The RF power spectrum of the error-signal under lock recorded with a resolution bandwidth of 100 Hz. Left: acetylene 2. Right: acetylene 3.

An overlapping Allan deviation is calculated as described in section 2.4, and the corresponding sigma-tau plot is shown in figure 3.20. As the two setups are believed to be identical with similar noise characteristics, the calculated Allan deviation is multiplied by $\frac{1}{\sqrt{2}}$. The slope of the sigma-tau plot show that white frequency noise is dominant up to $\tau = 0.2$ s with a slope of 12 Hz $\tau^{-1/2}$ corresponding to a fractional frequency instability of 6.2×10^{-14} $\tau^{-1/2}$. At $\tau = 0.2$ s the flicker noise floor is reached as the slope flattens out at 25 Hz τ^0. Frequency drift becomes present at $\tau \approx 1$ s and ends up dominating with a slope of ≈ 20 Hz τ^1.

The rising slope from for $\tau > 1$ s is slightly off the τ^1 slope, indicating the presence of random walk frequency noise. In order to characterize the noise contribution from random walk frequency noise, a linear frequency drift of 43 Hz/s is removed from the data, and a new overlapping Allan deviation is calculated. The black points in figure 3.20 show the Allan deviation with the linear drift removed. Here, the presence of random walk noise is clearly visible from $\tau = 1$ s to $\tau = 10$ s with a slope of 24 Hz $\tau^{1/2}$. The measurement of the beat-note frequency versus time is shown in figure 3.21.

In order to determine the origin of the different noise types visible in the Allan deviation, we will now look into the possible noise sources in the setups. To this effect a number of measurements were taken focusing on different parts of the setups believed to contribute to the instability of the setup.

Effects of Residual Amplitude Modulation

Fluctuating RAM has a direct effect on the dispersion error-signal off-set voltage. A fluctuating voltage off-set of the error-signal will give a proportional fluctuation in the frequency of the stabilized laser. An example of this is shown in figure 3.22. Here the stabilized RAM of acetylene 2 and 3 is shown together

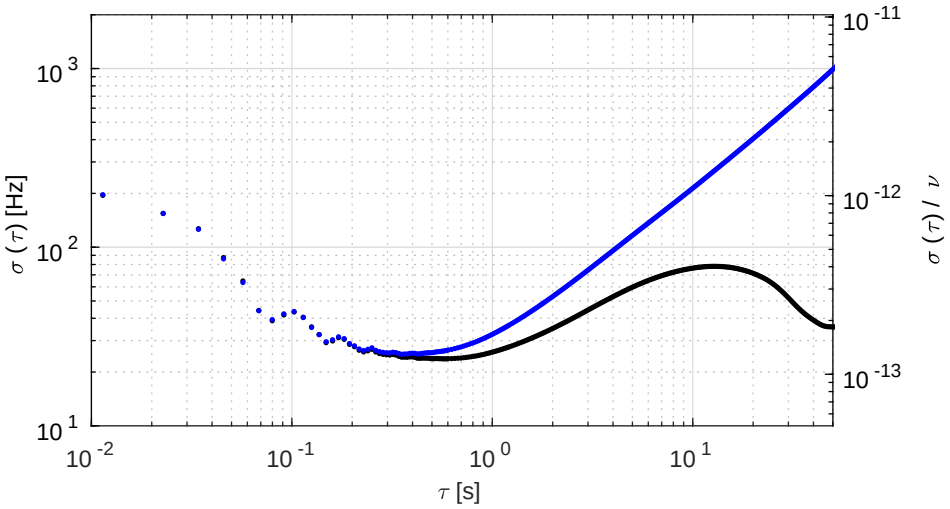

Figure 3.20: An overlapping Allan deviation of the beat-note between acetylene 2 and 3. A linear frequency drift of 43 Hz/s is removed from the data of the black point indicating the presence of random walk noise. The beat-note data used for this Allan deviation is shown in figure 3.21.

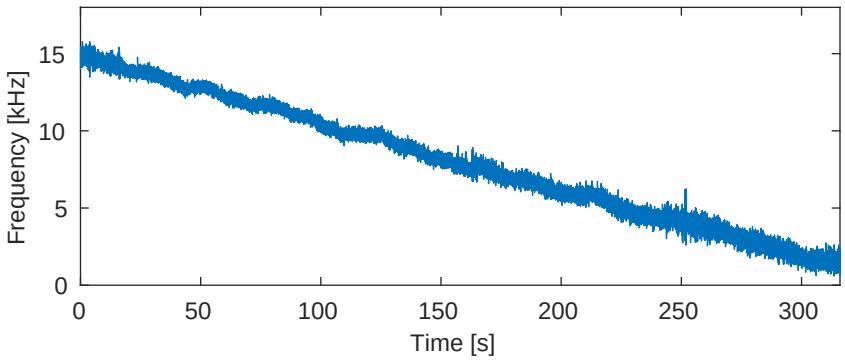

Figure 3.21: The recorded beat-note of acetylene 2 and 3 as used for the Allan deviation calculation shown in figure 3.20.

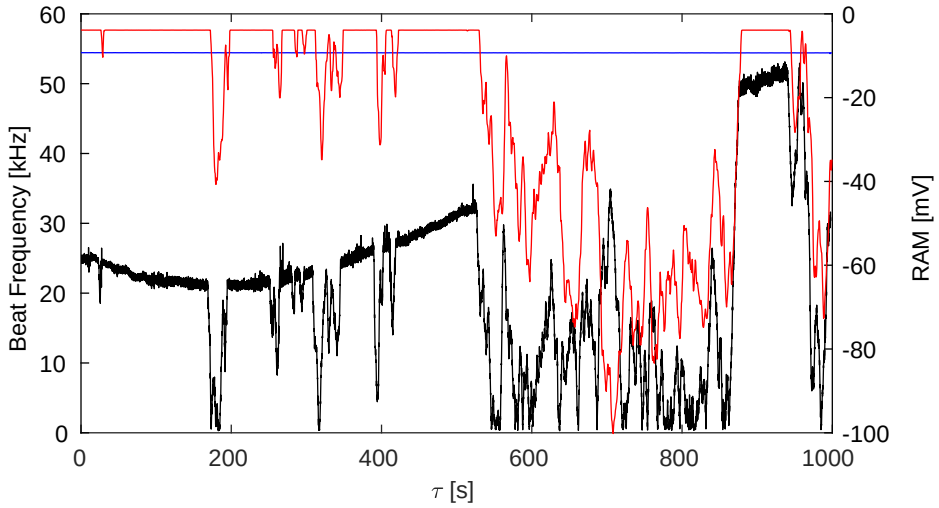

Figure 3.22: An In-loop measurement of the RAM fluctuations of acetylene 2 (blue line) and acetylene 3 (red line), both plotted against the right axis. The black line shows the beat-note frequency between the acetylene 2 and 3 setups. A clear correlation between RAM instability and laser frequency fluctuation is visible.

with the beat-note frequency. The RAM-signal from acetylene 2 is nicely stabilized, and no noise is detected in this in-loop measurement. The RAM-signal from the acetylene 3 setup is seen moving in and out of the dynamic range of the RAM-error-signal. This shows clearly the significant impact of fluctuating RAM on the frequency of the stabilized laser. The power spectral density of the un-stabilized RAM fluctuations follow an f^{-3} dependency characterizing it as flicker walk frequency noise or frequency drift. When the RAM stabilization is active, the fluctuations of the RAM-error-signal is below 10 μV over a period of 1000 s and follow a f^0 dependency, i.e white noise. This rules out RAM as a dominant noise source at $\tau > 0.2$ s.

The RF spectrum of the in-loop RAM-error-signal on detector PD2 in figure 3.4 is shown in figure 3.23. The figure shows both the spectrum of the RAM-signal with an active servo and without a servo. The servo systems yields RAM suppression of 28 dB for acetylene 2 and 39 dB for acetylene 3. The difference between the two is most likely due to the fact that the servo-feedback is applied differently on the EOM's. For the EOM in the acetylene 2 setup the servo acts with a bias voltage on the RF-electrodes through an RF bias-tee. The EOM in the acetylene 3 setup has an extra set of bias electrodes where a voltage can be applied independent of the RF-electrodes. Furthermore, the setups use different high frequency photo detectors for RAM detection.

These results show a RAM suppression that is 17 dB lower than the results

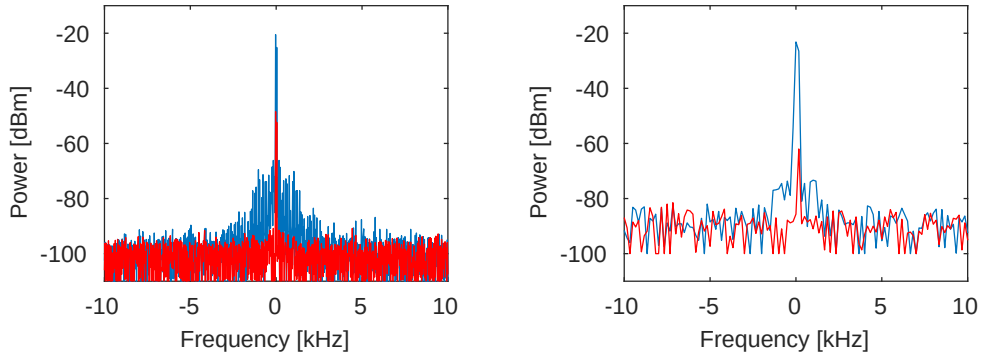

Figure 3.23: The RF spectrum of the RAM error-signal with an active servo (red line) and without a servo (blue line). Left: acetylene 2 (RBW: 10 Hz). Right: acetylene 3 (RBW: 100 Hz)

presented in [59]. However, the setups presented here only utilize a small fraction of the light, corresponding to about 200 µW, for RAM detection. A RAM suppression of 39 dB in this setup is believed to be sufficient to ensure that RAM is not currently limiting the achievable frequency stability.

Optical Power Fluctuation

The Relative Intensity Noise (RIN) of the NKT Photonics Basik E15 laser is specified by the manufacturer to be below -100 dBc/Hz throughout the noise spectrum. Thus, optical power fluctuations of the lasers' output is not a concern. However, the laser travels through an AOM, an EOM, and 5 to 6 m of polarization-maintaining fiber, all adding polarization noise. The Faraday isolator in the setups act as a polarization discriminator and any polarization noise will appear as optical power noise. Fluctuations in the RF power driving the AOM will also induce optical power noise. This effect has not been independently characterized.

The optical power fluctuation is measured by the photodetector PD4 shown on figure 3.4. A measurement of the power fluctuations in the acetylene 2 and 3 setups with a simultaneous beat-note measurement of the two stabilized laser frequencies is shown in figure 3.24. The correlation coefficients between the beat frequency and the power fluctuations in acetylene 2 and 3 are 0.56 and 0.69 respectively. A maximum correlation of 0.71 is calculated between the beat frequency and a combination of the power fluctuations of $0.5 \cdot \delta P_{ace2} - \delta P_{ace3}$.

As the dominating variation in the beat-note frequency is on a time scale of hundreds of seconds, and this analysis is based on 1000 s of data, there is a large degree of uncertainty of the correlation coefficients. With that in mind, a correlation of 0.71 is not so large as to prove a connection between the optical power fluctuations and the frequency stability on long time scales. The power

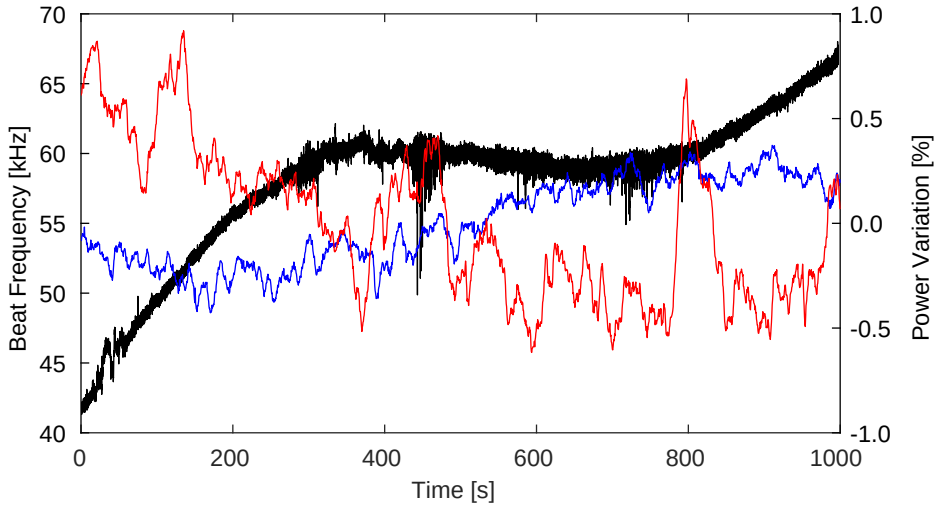

Figure 3.24: The optical power fluctuations recorded on PD4 (see figure 3.4) for acetylene 2 (blue line) and acetylene 3 (red line) with the beat-note frequency (black line).

spectrum of the power fluctuation shows a slope of f^{-2} thereby characterizing the noise as random walk. This indicates that the power fluctuations could be the source of the random walk noise found in the Allan deviation sigma-tau plot (figure 3.20).

The power fluctuation can be easily stabilized with a simple PI-servo acting on the RF power driving the AOM. Frequency drift (f^{-3}) is currently dominant, and implementation of the optical power stabilization has not shown any effect on the lasers' frequency stability. Reducing the frequency drift will most likely result in power fluctuations becoming the limitation on the achievable stability and will at that point warrant further investigation.

Temperature Fluctuation, Modulation Instability, and Etalon Effects

A measurement of the breadboard temperature of the two setups and the beat-note frequency is shown in figure 3.25. The linear nature of the temperature change of acetylene 2 shown by the blue line and the sinusoidal nature of the beat frequency agrees with what is expected based on the considerations in section 2.2. As the optical path-length changes due to temperature variations, the modulation phase will also change. This results in a variation of the dispersion signal off-set voltage, as shown on figure 3.26, directly influencing the stabilized frequency.

Close to the optimum demodulation phase the variation in off-set voltage was measured to be 4 mV/deg on a dispersion signal with a peak-peak am-

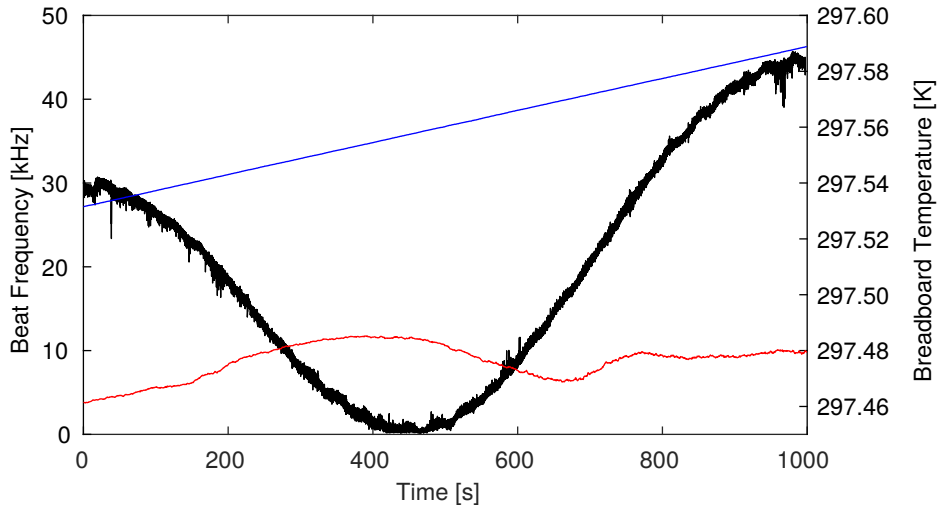

Figure 3.25: The temperature of the acetylene 2 (blue line) and acetylene 3 (red line) optics breadboard and the beat-note frequency (black line).

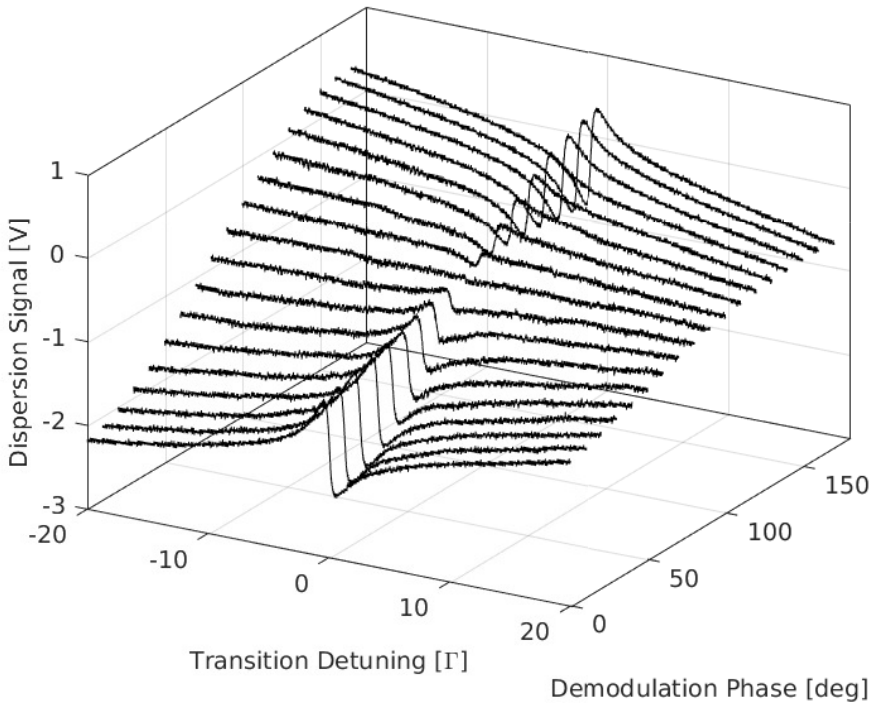

Figure 3.26: The dispersion signal at various demodulation phases in the acetylene 3 setup. In this measurement we see a voltage offset of 4 mV/deg.

plitude of 1 V. The modulation wavelength is $\frac{c}{\nu_{NO}} = \lambda_{NO} = 0.461$ m so the phase relation between modulation and demodulation changes by 1 ° if the optical path changes by $\lambda_{NO}/360 = 1.3$ mm. The off-set voltage relative to the signal path-length change is

$$U_{off} = \frac{4 \text{ mV/deg}}{\lambda_{NO}/(360 \text{ deg})} = 3.158 \frac{\text{V}}{\text{m}}.$$

The slope of the dispersion signal is $s = 1.47 \times 10^{-6}$ V/Hz resulting in a frequency change per optical path-length (OPL) change of

$$\frac{\delta\nu}{\delta OPL} = \frac{U_{off}[\text{V/m}]}{s[\text{V/Hz}]} = 2.148 \times 10^6 \text{ Hz/m} = 2.15 \text{ Hz/}\mu\text{m}.$$

The fluctuations in the dispersion signal off-set voltage, due to the change in optical path-length, will cause a frequency drift of ≈ 2 Hz/μm. The thermal expansion coefficient of aluminium is $\alpha_{alu} = 2.2 \times 10^{-5}$ m/(m K), and there is approximately 70 cm of free space beam path on an aluminium breadboard. This results in an optical path-length change of 15.4 μm/K. On figure 3.25 the temperature changes 60 mK over a period of 1000 s. This will lead to a frequency drift of approximately 2 Hz. The temperature fluctuation of the optical breadboard can not, in this way, account for the stabilized lasers' frequency drift.

The influence of the temperature fluctuation is typically not identical for the two setups to a degree that can not be explained through the method above where we only look at the change in optical path-length. If we, however, include etalon effects in the analysis as described in [70], the difference seen in the two setup can be explained by a tiny difference in alignment. As mentioned before, the NICE-OHMS technique is a measure of the combined cavity and molecular dispersion. Any etalon effects between the EOM and the photodetector, PD3, in the setup is equivalent to adding a cavity and thereby an extra dispersion profile to the measured dispersion. The magnitude of the dispersion from this etalon will be highly dependent on the finesse of the etalon and therefore highly dependent on alignment.

The RAM stabilization should counteract any contribution from an etalon that occurs prior the RAM detector PD2. The etalon is therefore most likely to be found after the cavity. A prime suspect for an etalon is between the cavity output mirror and the detector PD3. It is highly feasible that temperature fluctuation on the order of 100 mK would significantly change the finesse of the etalon. This would change the size of the dispersion of the etalon and thereby the off-set voltage of the dispersion signal from the cavity-molecule ensemble.

Another possible etalon is in the 1.3 meters of optical fiber after the EOM. Even though the fibers have angled connectors, there is a possibility of reflections creating an etalon. The finesse of such an etalon is expected to be

very low, and the effects from this etalon should be mitigated by the RAM stabilization.

3.6 An Alternative to NICE-OHMS

It has proven a major challenge to achieve long-term stability when using the NICE-OHMS technique. Possible solutions to this problem are discussed in the Outlook section of this chapter. As an alternative to NICE-OHMS, we will briefly consider a cavity enhanced FM-spectroscopy technique.

FM-spectroscopy

Cavity enhanced FM-spectroscopy using a lock-in amplifier is a possible alternative to NICE-OHMS-based stabilization. By using a lock-in amplifier, a very high signal-to-noise can be achieved. This is, however, often at the cost of signal bandwidth.

All optical components are similar to the NICE-OHMS setup shown in figure 3.4. The only difference to the setup is that the fiber splitter giving the stabilized laser's output is placed before the AOM. The lock-in amplifier generates a modulation signal at a frequency ν_{ref}. This modulation is applied to the AOM frequency giving a frequency modulation of the laser. The EOM is solely used for PDH stabilization of the cavity length to the laser frequency. The cavity transmission is detected and sent directly to the lock-in amplifier. The lock-in amplifier filters out the modulation signal at ν_{ref} and demodulates the signal producing a DC-signal equivalent to the derivative of the DC cavity transmission. Figure 3.27 shows the DC cavity transmission signal with the acetylene saturation peak. Figure 3.28 shows the derivative as generated by the lock-in amplifier. When using a lock-in amplifier, the signal-to-noise ratio can be greatly improved. These preliminary data do not show an improvement of the signal-to-noise, but further optimization of system parameters should lead to a better signal.

As the lock-in amplifier gives the derivatives of the detected signal, the lock-in signal is immune to fluctuation of the signal off-set voltage. This makes the lock-in amplifier a great tool for stabilization on long time scales. The signal in figure 3.28 is obtained with a modulation frequency of $\nu_{ref} = 100$ kHz. The signal bandwidth can thus never be higher than 100 kHz and is often significantly lowered by a low-pass filter. High frequency noise on the laser's frequency can therefore not be addressed using this technique alone. Another stabilization loop with a different reference, e.g. an optical cavity, can be implemented for high bandwidth feedback. The setup will then be divided into a fast feedback loop ensuring low phase-noise and a slow feedback loop ensuring long-term stability.

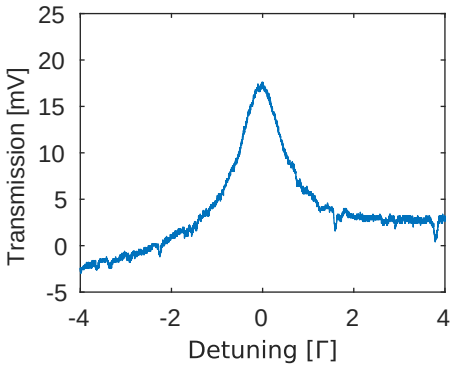

Figure 3.27: The acetylene saturation peak as seen in the cavity transmission DC-signal. The asymmetry of the signal is due to an imperfect cavity lock, causing a mis-alignment of the cavity mirror as the frequency is scanned. The x-axis is in units of the measured linewidth, Γ.

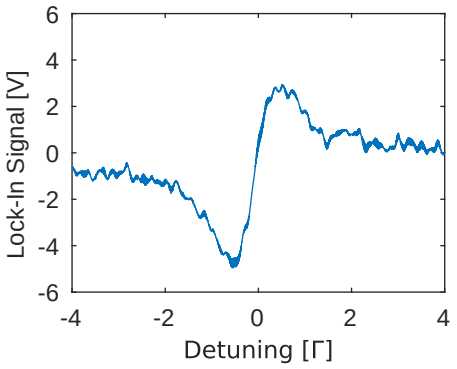

Figure 3.28: The derivative of the acetylene saturation peak as generated by the lock-in amplifier.The x-axis is in units of the measured linewidth, Γ.

Pre-stabilization

Pre-stabilization of the laser to a low linewidth reference like an optical cavity will provide low phase-noise within a large bandwidth. A small test setup was built where the two NKT Photonics lasers are locked to two high finesse cavities. The cavities have an FSR of 5.2 GHz and a resonance linewidth of approximately 8 kHz giving a finesse of $> 6 \times 10^5$. The laser's frequency was stabilized using the PDH-technique. Two configurations were tested where feedback was applied on either an AOM or the lasers' piezo. The achieved locking bandwidth was 640 kHz using the AOM and 20 kHz using the piezo.

Figure 3.29 shows the overlapping Allan deviation of the beat-note between the two stabilized lasers. The red curve shows the stability with the high bandwidth AOM feedback, and the blue curve shows the stability with the piezo feedback. The dashed line indicates the achieved stability of 2.2 Hz $\tau^{-1/2}$ where white frequency noise is dominant. Due to problems with the cavity temperature controllers the cavities temperatures were not stable. Because of this the Allan deviation is seen to increase already at $\tau = 0.03$ s. Furthermore, this test setup shows that the high feedback bandwidth is only important for addressing noise at high frequencies. The piezo feedback achieves at least the same level of stability for $\tau > 10^{-3}$. If the applications of the stabilized laser does not include measurements or interactions of timescales below 10^{-3} s, the AOM will be redundant.

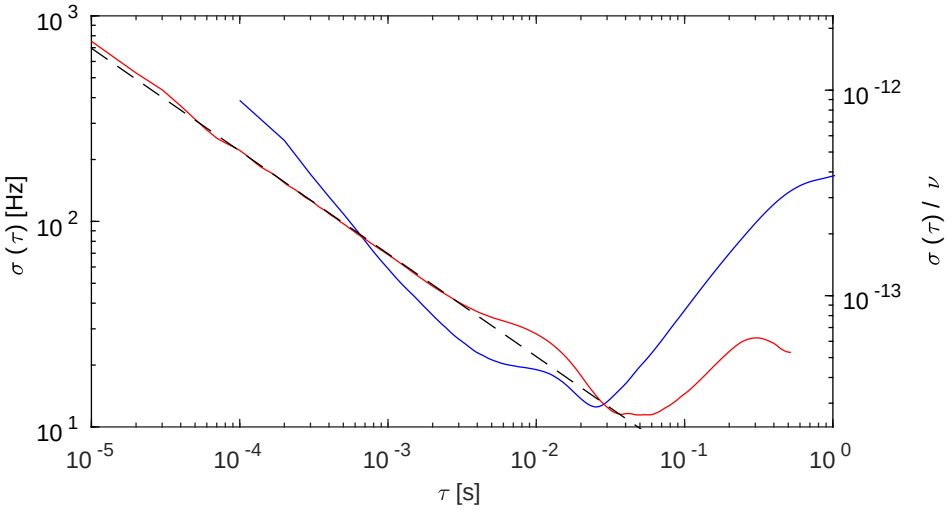

Figure 3.29: An overlapping Allan deviation of the high finesse cavity stabilized lasers. The red curve shows the Allan deviation of stabilization with AOM feedback, and the blue curve is of stabilization solely with piezo feedback. The black dashed line follows 2.2 Hz $\tau^{-1/2}$, indicating white frequency noise.

3.7 Outlook

Noise in NICE-OHMS

It is the current assessment that modulation instability combined with etalon effects is the cause of the dominant noise in the acetylene setups. To further investigate the contribution of modulation instability, an advanced RAM detection scheme is proposed. By demodulating both quadratures of the signal from the RAM detector, both RAM and other modulation instabilities can be detected. Inducing a varying RAM by ramping the bias voltage on the EOM allows for optimization of the demodulation phase, ϕ_{RAM}, for RAM detection. If modulation instability is present, the other quadrature will have a non-zero signal proportional to the phase drift caused by modulation instability. Any variations in the signal with the demodulation phase $\phi_{RAM} + 90°$ will indicate modulation instability. This signal should make stabilization of the modulation possible. A similar solution is presented in [71].

The detection of the orthogonal phase will not yield any information about an etalon contribution to the dispersion signal. This effect should, however, be heavily suppressed by introducing an optical isolator into the beam path constituting the etalon. The next step in improving the long-term stability of the acetylene setups should be to insert an optical isolator between the cavity output mirror and detector PD3.

Figure 3.20 shows a significant presence of random walk frequency noise. Further investigated into the origin of this noise is needed.

When the long-term stability of the setups is achieved, the accuracy needs to be measured. The influence of the environment will also be an important characterization. This includes the line shift of the acetylene transition due to temperature and magnetic fields.

Carbon-12 Acetylene

As carbon-13 acetylene might be increasingly difficult to procure, an investigation into carbon-12 acetylene was initiated. An analysis of possible lines for laser stabilization purposes is done in section 3.1. Here, the P(11)$\nu_1 + \nu_3$ line shows great potential with a linestrength more than a factor of 2 larger than the P(16) line in carbon-13 acetylene.

A high-vacuum system for filling gas cells with carbon-12 acetylene has been built. This system should allow for cells with background pressures at the 10^{-9} mBar level which is three to four orders of magnitude below the background pressure of the current carbon-13 acetylene cells. Furthermore, a lower acetylene pressure in the cells will be possible. By having carbon-12 acetylene cells at lower pressure, we expect to go to a regime where the large waist cavity will be advantageous. This will give a substantially lower pressure-broadening and transit-time-broadening resulting in a much lower linewidth. This in turn result in a higher Q leading to a better frequency stability.

Iodine Frequency Reference

The a_3 component in the P(13) 43-0 manifold of di-iodine ($^{127}I_2$) is also a practical realization of the meter [16]. The lines in iodine are, like the lines in acetylene, transition between vibrational states. The vibrational state that gives rise to the P(13) 43-0 manifold at 515 nm is close to the point where the vibrational energy breaks up the iodine molecule. This point is the dissociation limit and sets an upper bound on the possible vibrational energy and thereby frequency. As the transition frequencies approach the dissociation limit, the natural linewidth will decrease faster than the linestrength, making them interesting for frequency stabilization [72]. The coupling of the vibrational states to rotational and electron states leads to a complex hyperfine structure giving a large number of lines. The a_3 component in the P(13) 43-0 manifold is placed at 514.673 nm with a natural linewidth of approximately 240 kHz. Also of interest is the a_2 component at 514.67352 nm with a natural linewidth of ≈ 48 kHz [73].

The iodine setup will be similar to the acetylene setup and use NICE-OHMS to get a dispersion signal from cavity enhanced saturation spectroscopy. The iodine is enclosed in a glass cell with Brewster angled windows. A cold-finger allows for direct control of the iodine vapor pressure in the cell through

temperature. Currently, a setup for cavity enhanced saturated absorption spectroscopy has been built. The laser system is based on an NKT Photonics Adjustik Y10 fiber laser. The laser's wavelength is centered at 1030 nm, and an internal fiber amplifier gives the laser a maximum optical output power of 100 mW.

In the first experimental configuration, described in [74], the Y10 fiber laser was frequency doubled using a 1.5 mm long periodically poled potassium titanyl phosphate (PPKTP) crystal. The crystal's doubling efficiency was measured to be $\gamma = 2.3$ %/W at a pumping power of 80 mW, following the convention

$$P_{2\omega} = \gamma {P_\omega}^2 = 0.023 \text{ W}^{-1} \cdot (0.08 \text{ W})^2 = 1.472 \times 10^{-4} \text{ W}.$$

Due to optical loss through an optical isolator and beam shaping optics, a maximum of 80 mW of power was coupled into the PPKTP crystal generating approximately 150 µW of power at 515 nm. Further optical loss in the optics used for separating the 1030 nm light and the 515 nm light, and loss in an EOM resulted in an optical power of 60 µW at the cavity input. At this power level we were unable to saturate the iodine lines. To get a higher optical power of 515 nm light, a waveguide-based PPLN crystal for frequency doubling was bought from NTT Electronics. The high precision possible in optical waveguide manufacturing allows for a very high precision in the periodic poling of the crystal making a much better phase matching possible. The PPLN crystal has an efficiency of 270 %/W at 100 mW of 1030 nm input. A total of 27 mW of 515 nm light is now available.

A simple saturation spectroscopy setup was built and the saturated lines were immediately visible. Figure 3.30 shows the simple spectroscopy configuration where counter-propagating laser beams are aligned to spatially overlap in two passes through the cell. The PPLN waveguide generates the 515 nm light, and a prism is used to separate the 515 nm light and 1030 nm light from the PPLN output. A quarter-wave plate and a polarizing beam splitter is used to separate the reflected light, that has passed through the iodine, onto a photodetector. The recorded signal is shown in figure 3.31. The interrogation length through the iodine was 30 cm, and the cold-finger temperature was −10 °C corresponding to a vapor pressure of approximately 1.3 Pa, [74]. The optical power was 1.8 mW with a beam radius of approximately 1 mm.

Direct control of the iodine vapor pressure allows for an extra parameter for signal optimization compared to the acetylene reference. Obtaining an iodine pressure where the large waist cavity is advantageous is easily achievable. The large waist cavity was recently assembled, and some preliminary measurement were done. Figure 3.32 shows the iodine cell in the large waist cavity where the intra cavity beam is clearly visible. A preliminary spectrum of iodine in the large waist cavity is shown on figure 3.33. Here the laser's frequency scans a range of roughly 90 MHz, and the Lamb-dips are the a_5, a_4, and a_3 component

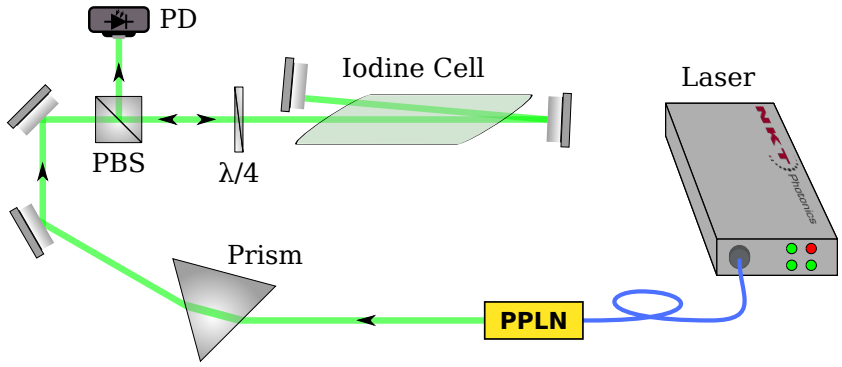

Figure 3.30: The saturated spectroscopy setup for Iodine cell test. PD is the photo detector, $\lambda/4$ is a quarter-wave plate, and the PBS is a polarizing beam splitter.

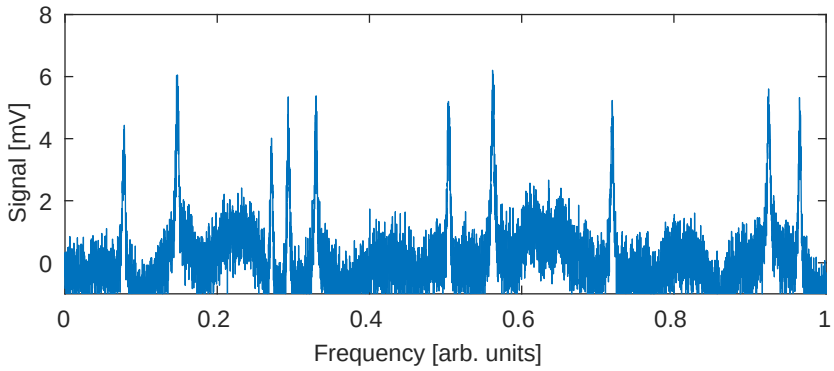

Figure 3.31: The saturation spectroscopy signal, from the setup shown in figure 3.30, showing the lines of iodine at 515 nm. The signal was recorded with an optical power of 1.8 mW and a cold-finger temperature of -10 °C corresponding to a vapor pressure of 1.3 Pa.

of P(13)43-0 manifold. These result were presented at the 676 W.E. Haereus Seminar in Bonn, Germany, [75].

An iodine frequency reference will have all the same benefits as the acetylene reference. With the advantage of the direct control of the iodine pressure, it will be possible to minimize pressure-broadening and transit-time-broadening. The dispersion signal of the a_2 component in P(13)43-0 should therefore have a very high slope for frequency stabilization. If the pressure-broadening and transit-time-broadening becomes negligible, the limiting factor will the natural linewidth of 48 kHz. A factor of 10 improvement in width of the dispersion signal compared to the acetylene setup is therefore not unrealistic. We expect to be able to achieve a fractional instability below 10^{-15} at 1 s.

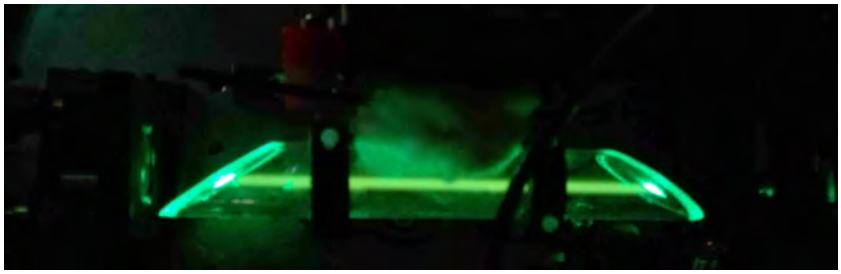

Figure 3.32: The iodine cell in a large waist cavity. The large TEM_{00} cavity mode is clearly visible as the iodine molecules fluoresce.

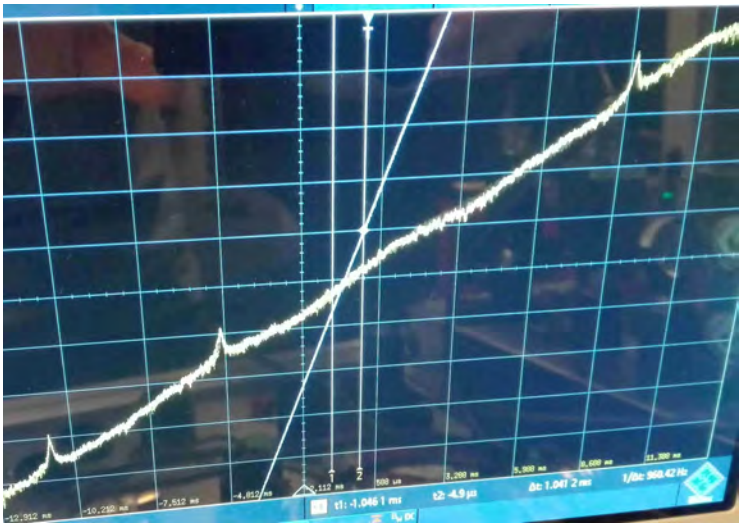

Figure 3.33: Cavity enhanced saturation spectroscopy of the a_5, a_4, and a_3 component of P(13)43-0 manifold in iodine using the large waist cavity (See section 2.3). The oscilloscope is set to 8.1 mV/div showing saturation peaks with a height of approximately 6 mV. The laser's frequency scan spans roughly 90 MHz.

4 Micro-Resonator Kerr Frequency Combs

In this chapter the work done on frequency comb generation through the Kerr effect in micro-ring resonators is presented. The primary focus is on planar AlGaAs-on-insulator micro-ring resonators developed at the SPOC center. We start with a short review of what a frequency comb is, and which parameters are used to describe it. Different methods of frequency comb generation are examined, and the strength and weaknesses are discussed. Following this, a review of the requirements for efficient comb generation in micro-resonators is given.

In section 4.2 the work on dispersion engineering of AlGaAs micro-ring resonators through tapered waveguides is presented. This is followed by a discussion of the achieved frequency comb generation in AlGaAs resonators and Silicon Nitride resonators.

Section 4.4 provides a brief review of different techniques for stabilization of micro-resonator frequency combs. This section is followed by an outlook where future investigations of the AlGaAs material are discussed together with some prospect of other material platforms.

The generation of an optical frequency comb can be achieved through many different techniques. The developments within micro- and nano-fabrication in non-linear optical materials have allowed for a new branch of OFC generation: chip-based Kerr frequency combs. This chip-based technology promises a highly compact and low-cost platform for optical frequency combs.

Although there has been tremendous progress within the field of chip-based Kerr combs over the last decade, on-chip comb generation still requires a significant amount of optical power. Chip-based comb generation is mainly interesting if the entire system can be compact. If a high-power laser or laser amplifier is required, it is of little use that the comb generation itself is chip-based. As of now, chip-based comb generation has not been presented at power levels compatible with chip-based laser sources.

My work in the SPOC center has focused on micro-resonators on the AlGaAs-on-insulator material platform with the purpose frequency comb generation.

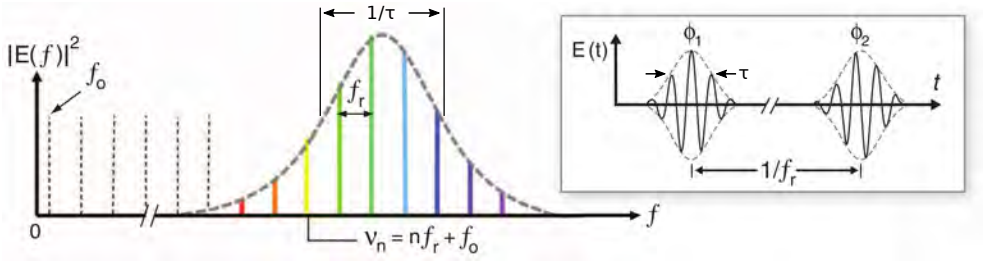

Figure 4.1: Frequency and time domain representation of a frequency comb. In the frequency domain the comb is a series of lines with equidistant frequency separation. In the time domain the comb is a pulsed electro-magnetic field where the time separation of the pulse is equal to the inverse of the line separation in the frequency domain. This figure is adapted from [76].

4.1 Theory of Comb Generation

The frequency comb can be described as a series of equidistant lines in the frequency domain or as a periodic train of pulses in the time domain. The repetition rate of the pulses, f_r, in the time domain corresponds to the spacing between the lines in the frequency domain. The frequency of each of these lines, or modes in the comb, is given by their mode number n, f_r, and f_{ceo}:

$$\nu_n = nf_r + f_{ceo}. \tag{4.1}$$

Here f_{ceo} is the comb offset frequency which in time domain describes the evolution of the carrier-envelope phase.

$$f_{ceo} = f_r \frac{\Delta\phi}{2\pi} \tag{4.2}$$

Here $\Delta\phi = \phi_2 - \phi_1$ is the carrier phase difference between two successive pulses, as shown in figure 4.1. The width of the pulses in the time domain, illustrated as τ on figure 4.1, is inversely proportional to the width of the comb spectrum in the frequency domain. This is also called the comb bandwidth and is thus given by $1/\tau$.

The ideal frequency comb has the property that all its comb lines have a fixed phase relation. This does not mean that each comb line can be described as a Dirac delta function, but rather that frequency and phase-noise of one line in the comb is correlated with the noise in the other lines. The spectral widths of the comb lines are in theory identical, and determines how well the distance between two lines, f_r, is known. In other words, it sets the limit on the measurement uncertainty of f_r.

A commonly used way of generating frequency combs is through mode-locking of a multi-mode laser [41, 77, 78, 79]. The technique is based on a laser

with a broad gain medium, like an Erbium-doped fiber with a gain bandwidth of several tens of nanometers. Another common gain medium is Ti:sapphire with hundreds of nanometers gain bandwidth. A laser cavity around such a gain medium will allow for lasing in several cavity modes. For this to become a frequency comb there has to be a fixed phase relation, such that the sum of lasing modes appears as a pulse circulating in the cavity. This can be achieved by adding an intensity dependent absorber or a saturatable absorber. Such an absorber will introduce high loss for low intensity fields and low loss for high intensity fields. Modes that at some point in the cavity have overlapping maxima and thus have a fixed phase, will saturate the absorber and experience low loss. Modes that do not contribute to a shared maximum, i.e. the pulse, will not saturate the absorber and will therefore experience a high loss. The comb bandwidth, $1/\tau$, will be limited by either the spectral width of the gain medium, dispersive effects, or non-linearities. The pulse repetition rate, f_r, will be given by the FSR of the laser cavity, e.i. the optical path-length of the cavity. The boundaries on f_r are thereby given by geometrical limitations on the cavity. The repetition rate of mode-locked lasers typically lies between 100 MHz and a few GHz.

A frequency comb can also be generated through electro-optic (EO) modulation [80]. The EO-comb is generated by modulation of a continuous-wave laser. The modulation creates sidebands on the laser by either phase or amplitude modulation. The comb repetition rate can be far greater than what is possible in a mode-locked laser. However, the number of lines achievable in an EO-comb are far fewer compared to a mode-locked laser. This is due to the technical limitation on the modulation depth of optical modulators. Low bandwidth combs, like EO-combs, can be amplified and broadened in a non-linear medium, e.g. highly non-linear fiber or waveguides made of a non-linear material. In [39] a 6.4 nm wide comb with 10 GHz comb spacing is broadened using an AlGaAs chip-based waveguide to cover 44 nm.

Finally, a frequency comb can be generated through the non-linear processes of Four-Wave Mixing (FWM). FWM originates from the Kerr effect and is a third-order, non-linear parametric process which for most materials requires very high intensity. One way of achieving high intensities is by utilizing the power build-up of optical resonators. Another way of getting high intensity is to compress the size the optical mode. This can be done by coupling an optical mode into a waveguide with high mode confinement. Combining these two into optical waveguide resonators has been shown to produce FWM in materials such as silica-glass, silicon nitride, CaF_2, and diamond [81, 82, 83, 84]. As these combs are generated solely by non-linear effects of the material, there are no requirement on gain mediums, and broadband combs can in principle be generated at any wavelength. Furthermore, by employing chip-based waveguide resonators, a high resonator mode spacing can be achieved, making comb repetition rates of THz-level possible.

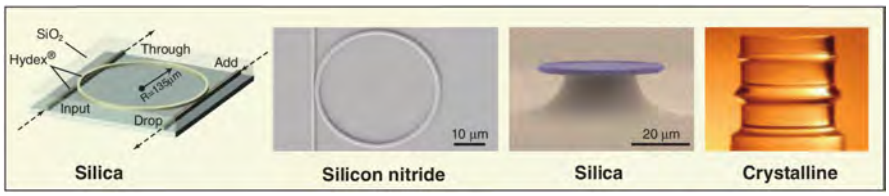

Figure 4.2: Examples of micro resonators used for frequency comb generation. From left to right: Silica waveguide ring resonator on chip [81], Silica nitride waveguide ring resonator on chip [82], Silica toroid whispering gallery mode resonator [85],h and a crystalline millimeter-scale whispering gallery mode resonator [83]. Figure taken from [76].

Micro-Resonator-Based Kerr Comb Generation

Micro-resonators have been investigated with great interest during the last decade. The majority of the work with micro-resonators has been done with either toriod whispering gallery mode resonators or planar waveguide ring resonators (Micro Ring Resonator (MRR)). Figure 4.2 shows examples of micro-resonators used for frequency comb generation. The parameter often used to describe these resonators is their quality factor or Q-factor. This is defined as the spectral width of a resonant mode in the resonator relative to the mode frequency. The Q-factor is complementary to the finesse of the resonator where finesse is defined as FSR divided by the spectral width of a mode. The finesse can also be expressed in terms of optical loss,

$$F \approx \frac{2\pi}{L_{tot}} \tag{4.3}$$

where L_{tot} is the total optical loss per round-trip of a resonant mode. In an MRR losses can be caused by scattering of photons in the waveguide or by optical effects related to the material properties of the waveguide, e.g. Two Photon Absorption (TPA). TPA can happen when two photons combined have an energy close to the material band-gap and are absorbed, creating an electron-hole pair. Scattering effects typically arise from impurities in the crystal structure and the roughness of the waveguide surfaces.

In optical resonators there will be a build-up of optical power when light is coupled into a resonant mode. This power build-up, like finesse, is dependent on the round-trip loss of a mode.

$$P_{res} \approx \Gamma \left(\frac{2}{L_{tot}}\right)^2 P_{in} = \Gamma \left(\frac{2}{\Gamma + L}\right)^2 P_{in} \tag{4.4}$$

Here P_{res} is the power in the resonator mode, P_{in} is the power in the input mode, and Γ is the coupling parameter describing the ratio of power coupled from the input mode to the resonator mode. As the coupling is symmetrical,

the total round-trip loss of the resonator is $L_{tot} = \Gamma + L$. L is the internal loss from the resonant mode, i.e. not including loss due to coupling to the outside mode.

Let us look at a planar ring resonator with a single waveguide for coupling, similar to the design of the silica-nitride ring resonator in fig. 4.2. With a realistic Q-value of 500000 the total round-trip loss is approximately 2.5 %. The maximum power build-up is achieved when the coupling is equal to the resonators internal loss, L. This is also referred to as perfect impedance matching. The power enhancement will then be

$$\Gamma \left(\frac{2}{\Gamma + L} \right)^2 = 0.0125 \cdot \left(\frac{2}{0.0125 + 0.0125} \right)^2 = 80.$$

With only 10 mW of power in the coupling waveguide, there will be 800 mW of power circulating in the resonator.

The cross section of a planar waveguide of an MRR typically has a width in the order of 1 µm and a height of several hundreds of nanometers. If the waveguide material has a significantly different refractive index compared to the cladding surrounding the waveguide, a high degree of mode confinement is possible. A large difference in the refractive index of the waveguide and cladding will not only allow for a geometrically small mode but also help to minimize the mode interaction with the waveguide sidewalls. Figure 4.3 shows a comparison of the fundamental TE-mode in a waveguide made of AlGaAs and a waveguide made of Si_3N_4, both with a SiO_2 cladding. The high refractive index of AlGaAs allows for much better mode confinement compared to Si_3N_4, thereby making a high intensity easier to achieve. There is an optimum waveguide dimension for the highest possible intra-cavity intensity, balancing the Q-factor and mode volume. For Si_3N_4-resonators waveguide dimensions are often far larger than AlGaAs waveguide and have waveguide widths of between 1 and 2 µm [86].

Four-Wave Mixing in Micro-Ring-Resonators

FWM arises from the optical Kerr effect where two pump photons are converted into two photons with new energies, a so-called signal-idler pair. This effect can be the foundation of frequency comb generation from a single frequency pump beam.

The Kerr effect describes a non-linear change in the refractive index of a material due to an applied electric field. The change in the refractive index is given by

$$\Delta n = \lambda K E^2 = n_2 I$$

where K is the Kerr constant of the material, E is the strength of the electric field, n_2 is the non-linear index, and I is the intensity of the electric field. The optical Kerr effect is the case where the changes in n is caused by the electric

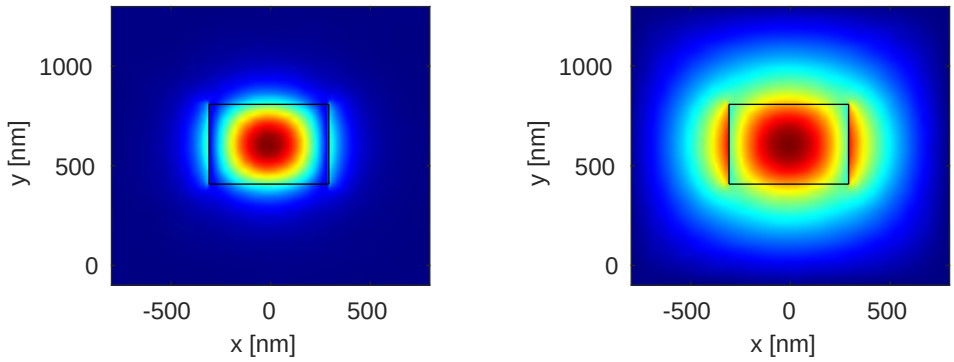

Figure 4.3: A TE-mode with a wavelength of 1500 nm in an AlGaAs waveguide (left) and a Si_3N_4 waveguide (right) with dimensions of 600 nm by 400 nm. The refractive index of AlGaAs is 3.29 at 1550 nm where Si_3N_4 has a refractive index of 2.00 at 1550 nm. The cladding surrounding the waveguides is SiO_2 with a refractive index of 1.44. The relatively low difference in the refractive index of the Si_3N_4 and the cladding, results in a much weaker mode confinement compared to the AlGaAs waveguide.

field of the light itself. This effect creates a modulation of the refractive index and thereby causes modulation instability where a continues wave is broken up into a train of pulses. This corresponds to sideband generation in the frequency domain, as described earlier. Modulation instability is a degenerate case of FWM where

$$2\omega_p = \omega_s + \omega_i.$$

Here ω_p is the frequency of the pump photons. ω_s and ω_i are the signal-idler frequencies, describing the generated sidebands. As MRR-based frequency combs are typically generated from a single frequency pump, the degenerate case of modulation instability is the initial process that creates the primary comb lines [87].

Once a pulse train has formed from modulation instability, Self-phase Modulation (SPM) begins to occur. In the time domain SPM is a time compression of a pulse of light. This is also a consequence of the optical Kerr effect as the intensity distribution across the pulse leads to a varying refractive index across the pulse. This results in a compression of the pulse width, τ. In the frequency domain a smaller pulse width corresponds to a wider comb spectrum. SPM is related to the non-degenerate form of FWM,

$$\omega_{p1} + \omega_{p2} = \omega_s + \omega_i$$

where $\omega_{p1} \neq \omega_{p2}$ are two pump photons generating two photons at new frequencies, ω_s and ω_i. Figure 4.4 shows an illustration of degenerate and non-degenerate four-wave mixing.

Figure 4.4: Illustration of degenerate and non-degenerate four-wave mixing. In the case of degenerate FWM, two identical photons combine, and two photons with different energies are created. In the case of non-degenerate FWM, two photons with different energies combine, and two photons of again different energies are created. The figure is taken from [88].

The generation of sidebands in a specific mode starts to occur when the parametric gain, g, is larger than the loss in the cavity mode. The parametric gain,

$$g = \sqrt{(\gamma P_p)^2 - (\Delta k_{NL}/2)^2} \tag{4.5}$$

is proportional to the pump power, P_p, and the non-linear coefficient, γ, but also to the non-linear wave-vector mismatch [89]:

$$\Delta k_{NL} = k_s + k_i - 2k_p + 2\gamma P_p. \tag{4.6}$$

The increase in parametric gain with increasing power can be greatly suppressed by the wave-vector mismatch. This is due to the fact that photons generated in the FWM-process cannot break energy conservation. Meaning, the sum of the pump photons' energy has to be equal to the sum of the signal and idler photons' energy. In vacuum that would lead to $k_s + k_i - 2k_p = 0$. There are, however, two effects responsible for a non-zero Δk in a non-linear material. First, we look at the term $2\gamma P_p$ where the non-linear coefficient is given as

$$\gamma = \frac{n_2 \omega_p}{c n A_{eff}}. \tag{4.7}$$

Here, n is the material's refractive index, and A_{eff} is the effective mode area. This non-linear phase contribution is due to self-phase modulation and cross-phase modulation. As we are currently discussing FWM in a ring-resonator, we also have to account for the boundaries imposed by the modes of the ring-resonator. The photons created by FWM have to match the resonators modes,

$$k_{res} = \frac{2\pi\mu}{L n_{eff}} \tag{4.8}$$

where μ is the resonator mode number, and Ln_{eff} is the resonator's effective round-trip length. Here, n_{eff} is dependent on the frequency and thereby mode number, μ, resulting in a change of mode spacing with respect to the frequency (e.i. non-constant resonator FSR with respect to the optical frequency). This

effect is called chromatic dispersion. In the case of normal dispersion the mode spacing will decrease as the mode frequency increases which results in $k_s + k_i - 2k_p > 0$. In the case of anomalous dispersion the mode spacing will increase with the mode frequency resulting in $k_s + k_i - 2k_p < 0$. As $2\gamma P_p$ will be positive, anomalous dispersion will balance the wave-vector mismatch, allowing for parametric gain at higher optical powers.

The resonator input threshold power, P_{th}, for parametric oscillation is again based on the relation between the resonator mode loss and the parametric gain. The threshold power is dependent on the non-linear refractive index, the mode volume, the Q-factor, and the coupling efficiency [90].

$$P_{th} \approx 1.54 \frac{\pi}{2} \frac{Q_c}{2Q_L} \frac{n^2 L A_{eff}}{n_2 \lambda_p} \frac{1}{Q_L^2} \tag{4.9}$$

Here, Q_c is the coupling Q-factor, Q_L is the loaded Q-factor[1]. n is the refractive index, n_2 is the non-linear refractive index, L is the resonator round-trip length, A_{eff} is the effective mode area, and λ_p is the pump wavelength.

Frequency Comb Formation Mechanism in Micro-Resonators

To achieve frequency comb generation in a micro-resonator, the pump laser's frequency can be slowly tuned into resonance with a resonator mode, thereby slowly increasing the optical power in the resonator. The first comb lines are generated as sidebands on the pump via modulation instability. The frequency separation between the pump and sideband are denoted as Δ and is normally significantly larger than the resonator mode spacing ($\Delta \gg FSR$). As the power in the resonator mode increases, higher-order sidebands are generated at Δ_n. The value of Δ_n is determined by the combination of power in the resonators mode, pump-resonator detuning, and the resonator dispersion. These lines are called the primary comb lines.

As the pump-resonator detuning is decreased, and thereby the power in the resonator increased, secondary lines are created around the primary lines. The secondary lines are generated by either degenerate or non-degenerate FWM and are spaced by the resonator FSR. The secondary lines constitute subcombs around the primary lines. As the power in the resonator is increased further, these subcombs grow and expand through non-degenerate FWM and eventually merge into the complete spectrum of a full comb.

Materials

Equations (4.5) to (4.9) show the parameters of interest for efficient comb generation in micro-resonators: a high non-linear refractive index, a high Q-

[1]The loaded Q includes all losses in the resonator in contrast to the intrinsic Q where the loss related to the coupling is not included.

Material	n	n_2 [m^2/W]	Refs.
Silica	1.4	2.2×10^{-20}	[91, 92]
Hydex	1.7	1.2×10^{-19}	[81, 93]
Si_3N_4	2.0	2.5×10^{-19}	[94]
AlN	2.1	2.1×10^{-19}	[95]
Diamond	2.4	8.2×10^{-20}	[84]
a-Si:H	3.5	3×10^{-17}	[96]
AlGaAs	3.3	2.6×10^{-17}	[88]
4H-SiC	2.6	$\approx 10^{-18}$	[97]

Table 4.1: Material parameters of interest for Kerr comb generation in micro-resonators. n is the material refractive, and n_2 is the material non-linear index. All values are given for a wavelength close to 1550 nm.

factor, and a small mode-volume. Table 4.1 shows the refractive index, n, and the non-linear refractive index, n_2, for a series of materials that have been suggested as planar ring resonators for FWM. Materials like AlGaAs and amorphous Silicon quickly draw attention with non-linear refractive index two orders of magnitude larger than the rest.

AlGaAs has a high refractive index which allows for high mode confinement and thereby a small mode area, A_{eff}. This together with the high, non-linear refractive index makes it a very promising candidate. The band-gap energy can be engineered by tuning the aluminium composition of the AlGaAs. By optimizing x, where $Al_xGa_{1-x}As$, two photon absorption can be heavily suppressed at telecom wavelengths. However, the complicated bounding process required for the fabrication of AlGaAs-on-insulator, combined with the need for high temperature annealing, could pose a challenge with CMOS-compatibility. Materials, where waveguide fabrication is easily compatible with the current CMOS industry, will have a great advantage in future large scale productions [98]. Furthermore, throughout the work presented here the achieved Q-factors have been quite low compared to resonators of the other materials. A Q-factor of 2×10^5 has been presented in a 98 GHz FSR resonator, showing a threshold power of 6 mW [88].

Resonators in hydrogenated amorphous silicon (a-Si:H) is still at an early stage. a-Si:H also has a tunable band-gap energy through the crystal growth conditions. A number of ring resonators in a-Si:H have been presented, and a-Si:H shows a lot of potential with a nonlinear refractive index slightly higher than of AlGaAs [99, 100, 101, 102]. The main challenge with amorphous silicon is that the crystal structure is unstable at high optical powers, leading to waveguide degradation and an irreversible increase in loss with increased optical power. Recently, a method using deuterium passivation has proven to greatly increase the power handling capability of amorphous silicon [96]. This a-Si:HD is a very interesting candidate for Kerr frequency comb generation.

SiC also has good material properties for Kerr comb generation, and SiC-wafers are currently commercially available. However, manufacturing high confinement waveguides have proven difficult since the etching process of SiC produces waveguides with high surface roughness leading to low Q resonators. Work in the SPOC center by Yi Zheng, using the 4H-SiC polytype, has shown record high Q-values in SiC planar waveguide resonators of up to 7.3×10^4. This is achieved by utilizing the Smart Cut process [103] and applying wet oxidation after etching. The work also shows good possibilities for dispersion engineering of the resonators, presenting dispersions ranging from -4.6×10^5 fs^2/mm (anomalous dispersion) to 2.6×10^6 fs^2/mm (normal dispersion) in waveguides with widths from 1065 nm (anomalous dispersion) to 350 nm (normal dispersion) [97].

The Hydex composition is also an interesting candidate as this does not require high temperature annealing making it easily adaptable with the CMOS industry. The material parameters are very similar to Si_3N_4. A Q-factor above 1 million has been presented in a 200 GHz FSR resonator, showing a threshold power of 54 mW [81].

As mentioned above, the chromatic dispersion of the resonator modes is of great importance to the frequency comb generation. In the following section, the definition of waveguide ring resonator dispersion is introduced, followed by a description of how we have engineered resonator dispersion through the waveguides' geometry.

4.2 Dispersion Engineering

Dispersion in a resonator is a change of mode spacing in frequency and can be described as a Taylor series:

$$\omega_\mu = \omega_0 + D_1\mu + \frac{1}{2}D_2\mu^2 + \frac{1}{6}D_3\mu^3 \dots \tag{4.10}$$

Here, ω_μ is the resonance frequency for mode number μ, D_1 is the first order dispersion (corresponding to the resonator FSR), and D_2 is the second order dispersion proportional to the group velocity dispersion. D_3 is the third order dispersion. D_2 and D_3 are given by

$$D_2 = -\frac{c}{n}\frac{\partial^2\beta}{\partial\omega^2}{D_1}^2 \tag{4.11}$$

$$D_3 = -\frac{c}{n}\frac{\partial^3\beta}{\partial\omega^3}{D_1}^3 + 3\left(\frac{c}{n}\frac{\partial^2\beta}{\partial\omega^2}\right)^2 {D_1}^3. \tag{4.12}$$

Here, β is the propagation constant of the electric field in the waveguide.

The waveguide geometry is described by an x-, y-, and z-axis. The x- and y-axis go along the width and height of the waveguide, respectively, and the

z-axis is in the direction of the guided mode propagation. The electric field in the waveguide can be expressed as

$$\mathbf{E}(\mathbf{r}) = \mathbf{E}(x, y)e^{-i\beta z}. \tag{4.13}$$

Based on the Maxwell equations, the following expression can be derived:

$$\frac{\partial^2 \mathbf{E}(x, y)}{\partial x^2} + \frac{\partial^2 \mathbf{E}(x, y)}{\partial y^2} = (\beta^2 - k_0^2 n^2)\mathbf{E}(x, y). \tag{4.14}$$

Here, $k_0 = \frac{2\pi}{\lambda}$ is the vacuum wave vector. Solving this equation provides information about both the mode profile in the waveguide and the effective refractive index $n_{eff} = \frac{\beta}{k_0}$.

The group velocity dispersion in a waveguide can now be calculated as

$$GVD = \frac{\partial^2 \beta}{\partial \omega^2}. \tag{4.15}$$

Figure 4.5 shows the dispersion profile of a 400 by 300 nm waveguide, a 600 by 300 nm waveguide, and 800 by 300 nm waveguide, all three in AlGaAs. As mentioned above, an increase in mode spacing with an increase in mode number corresponds to anomalous dispersion. For Kerr frequency comb generation it is necessary for the resonator to have a positive D_2-value, corresponding to a negative GVD-value.

The blue curve on figure 4.5, showing the 600 nm wide waveguide, shows a negative GVD for a large wavelength range between 1.45 µm and 2.0 µm. As the waveguide dimension becomes more narrow, the anomalous dispersion moves to the lower wavelengths, and the Third Order Dispersion (TOD) (the slope of the GVD-curve) gets considerably higher. This results in a smaller wavelength interval with anomalous dispersion. Going to a wider waveguide moves the anomalous dispersion to a higher wavelength and reduces the TOD, giving a much wider wavelength range with anomalous dispersion. Depending on the application of the comb, the center wavelength of the comb spectrum can be important. For telecommunication application it is often desirable to have the center wavelength close to 1550 nm with a flat and homogeneous spectrum across the c-band. This translates to a desired dispersion profile centered around 1550 nm with minimal TOD.

Design of the dispersion profile of a waveguide resonator can be done by introducing a varying waveguide width along the resonator's propagation axes. This allows for a combination of the wide dispersion profile of the wide waveguide with the low dispersion profile center wavelength of the narrow waveguide. By carefully choosing the widths, the ratios of different widths, and the design of the tapered regions, the average resonator dispersion can be finely tuned and optimized for the desired comb generation.

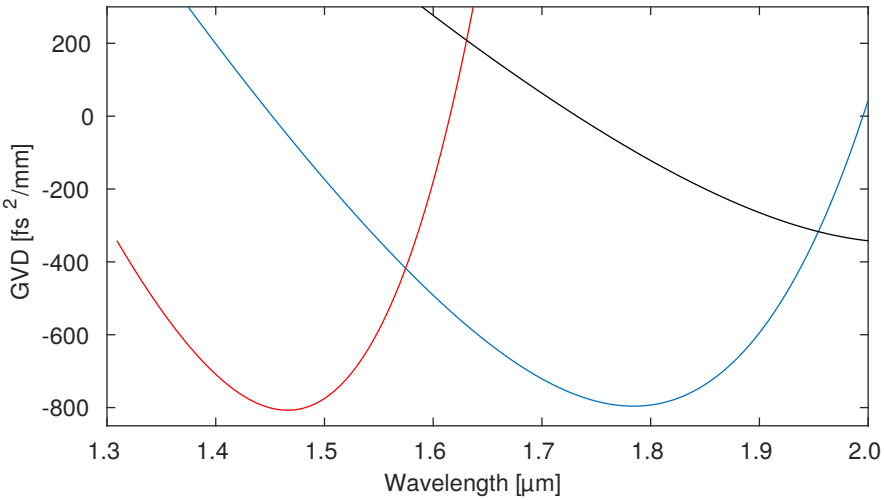

Figure 4.5: Simulated group velocity dispersion of AlGaAs waveguides with dimensions of 400 by 300 nm (red), 600 by 300 nm (blue), and 800 by 300 nm (black).

Tapered Waveguide Resonators

The waveguide geometry is an easily accessible parameter for manipulation of the resonator dispersion. However, other properties of the resonator are also influenced by the waveguide geometry. A narrow waveguide will increase the interaction between the waveguide sides and the optical mode, thereby increasing the optical loss. A wide waveguide will allow other optical modes than the fundamental TE and TM modes to exist. At certain wavelengths, where the TE_{10} mode and a possible higher order mode overlap, light can couple between modes. This results in a different amount of optical loss for the different resonances of the TE_{10} mode. Furthermore, it allows for comb lines to exist outside the nf_r set of values stated in equation (4.1). These two effects make the generation of a phase-coherent, uniform comb, also known as a soliton comb, impossible if higher order modes exist. The goal is to have a wide waveguide that only supports TE_{10} modes and has an anomalous dispersion over a wide wavelength range around 1550 nm.

The resonators designed in this work have a narrow part eliminating higher order modes and a wide part making the average round-trip dispersion optimal. Figure 4.6 shows a drawing of the tapered resonator design.

As described in [86], the path-average dispersion can be calculated as

$$\overline{GVD} = \frac{1}{L_c} \int GVD(L) \mathrm{d}L. \tag{4.16}$$

The numerical solver, COMSOL, was used to solve equation (4.14) for a wa-

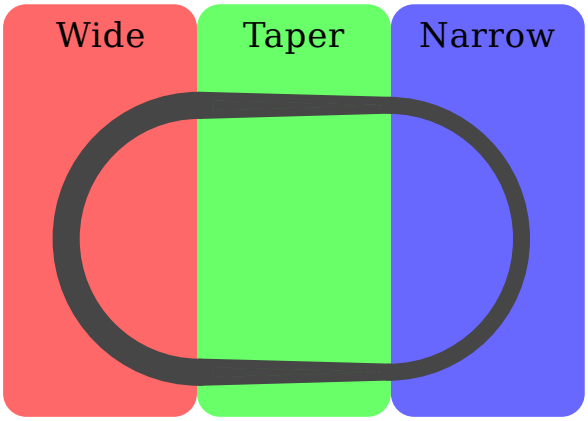

Figure 4.6: Tapered resonator schematic.

veguide height of 300 nm and waveguide widths ranging from 400 nm to 1 µm in 20 nm increments. The waveguide height was in this case specified by the available AlGaAs wafers. The $\overline{GVD}$ was subsequently calculated for a number of different combinations of waveguide widths and taper lengths.

Six different resonator designs were chosen for fabrication. Table 4.2 shows the parameters for the six designs. The parameters describing the resonators are:

W_w The width of the wide part

R_w The ratio of the wide part and the total resonator round-trip length

W_n The width of the narrow part

R_n The ratio of the narrow part and the total resonator round-trip length

L_t The length of one tapered region

FSR The free spectral range of the resonator at the mode-resonance of 1542 nm

L_c The total resonator round-trip length

When introducing a varying waveguide width in a resonator, effects that increase loss must be considered. One such effect is diffraction from the fundamental mode into higher order modes when going from a small to a larger width. In [104] a requirement for adiabatic tapering is given:

$$\theta < 1.4\frac{\lambda}{2Wn_{eff}}. \tag{4.17}$$

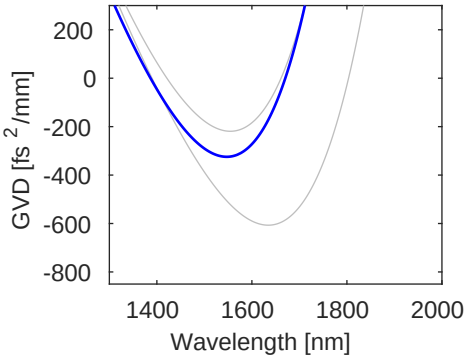

(a) $W_n = 420$ nm, $W_w = 740$ nm, $R_n = 30$ %, and $R_w = 20$ %.

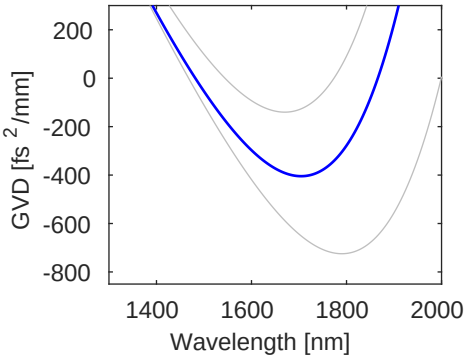

(b) $W_n = 480$ nm, $W_w = 800$ nm, $R_n = 15$ %, and $R_w = 15$ %.

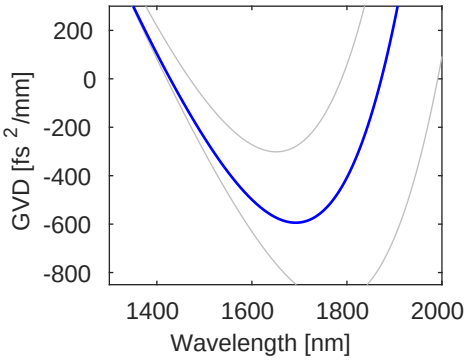

(c) $W_n = 480$ nm, $W_w = 680$ nm, $R_n = 15$ %, and $R_w = 20$ %.

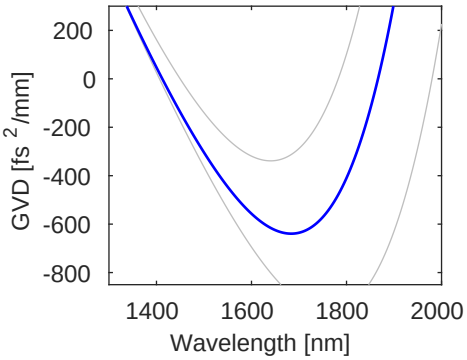

(d) $W_n = 480$ nm, $W_w = 680$ nm, $R_n = 15$ %, and $R_w = 5$ %.

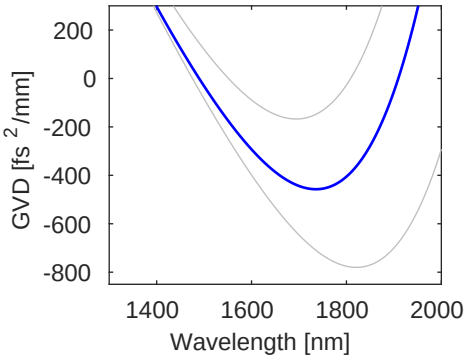

(e) $W_n = 500$ nm, $W_w = 820$ nm, $R_n = 15$ %, and $R_w = 5$ %.

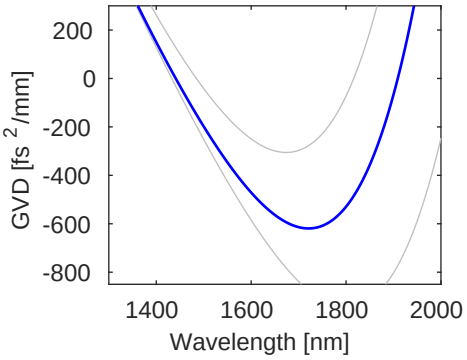

(f) $W_n = 500$ nm, $W_w = 740$ nm, $R_n = 15$ %, and $R_w = 10$ %.

Figure 4.7: The simulated dispersion profiles for different waveguide geometries of tapered waveguides. W_n and W_w are the widths of the narrow and wide parts respectively. R_n and R_w are the round-trip lengths ratio of the narrow and wide parts respectively.

W_n [nm]	R_n [%]	W_w [nm]	R_w [%]	L_t [µm]	FSR [GHz]	L_c [µm]
420	30	740	20	499.00	38.5	1996
480	15	800	15	720.30	38.5	2058
480	15	680	20	668.85	38.5	2058
480	15	680	5	324.00	96	810
500	15	820	5	324.00	96	810
500	15	740	10	303.75	96	810

Table 4.2: Design parameters for the resonators on the chip named CG49. The FSR is calculated based on the waveguides' effective refractive index as simulated in COMSOL. A description of the other parameters is given in the text.

Here, θ is the angle between the waveguide sidewall and the z-axis, and W is the width of the waveguide. The largest sidewall angle of the presented designs is in the design with a 500 nm to 820 nm taper and a taper length of 324 µm. Here the angle is below 0.05 ° while the limit imposed by equation (4.17) has a minimum of 27 °. These tapers are thereby all deep within the adiabatic regime as defined by [104], and diffraction into higher order modes in the taper should be negligible.

Backscattering of photon propagating in the waveguide is mainly caused by scattering on crystal defects and impurities. However, as evident from equation (4.14), the propagation constant, and thereby the effective refractive index, is dependent on the waveguide geometry. A changing refractive index along the propagation axis will lead to a reflection of light into the mode propagating in the opposite direction, i.e. backscattering. Backscattering in a ring resonator will cause mode splitting and thereby loss as described in [105].

The difference in this case is that the change in refractive index is not localized to a specific point in the waveguide. It is a continuous change over a length of at least two orders of magnitude larger than the wavelength of the light propagating in the waveguide. The light reflected due to the change in the refractive index will have a random phase, because the probability of a photon being reflected is constant throughout the taper. As a result the photons reflected by the taper will destructively interfere. We can thus assume that backscattering caused by the tapers will be negligible as long as the taper length is larger than the wavelength of the guided light.

Dispersion Measurements

Measuring the dispersion of an MRR can be done by measuring the spectral distance between consecutive modes. Fitting equation (4.10) to this measurement will allow for an estimation of the dispersion parameters D_1, D_2, and D_3. The challenge with the measurement is to have an accurate measurement

of frequency. When scanning across the resonators modes, it is important to have a constant scan speed or a well defined reference to linearize the scan during data analysis. Currently, no commercially available lasers are capable of frequency scanning over a wide area (≈ 100 nm) with the required linearity of the scan.

A commonly used method is to use a fiber interferometer as a frequency reference [106]. This allows for closely spaced reference markers as the length of the interferometer can be arbitrarily long. The width of the markers, corresponding to the width of the interferometer resonances, is typically on the order of MHz. This sets the limitation on the achievable precision. A disadvantage of using a fiber-based interferometer is that fiber dispersion will bias the measurements. The fiber dispersion can be measured and corrected for by including a molecular reference in the setup.

Another method is to use a stabilized frequency comb as a reference [107]. Here, the beat of the scanning laser and a frequency comb is recorded simultaneously with the MRR resonances. Commercially available, fiber-based frequency combs have a comb line spacing of hundreds of MHz. The beat-detection can be done with an RF bandpass filter on the detector, thereby generating two markers per comb line. The choice of the RF filter determines the measurement precision. The spectral width of the bandpass filter determines the width of the markers. The RF filter's center frequency typically sets a limitation on the possible scan speed. This is because the detection bandwidth must match the speed at which the scanning laser passes a through resonance with a comb line.

For dispersion measurements of the tapered AlGaAs resonators, a setup using a free space optical Fabry-Pérot cavity as a reference was built. Two high-reflectance mirrors are placed on an approximately 800 mm long aluminium profile, giving an FSR of 175.3 MHz. This provides a sufficiently high number of markers between two resonance modes of the MRR. The cavity mirrors are concave with a radius of curvature of 9 m and a power reflectance of 99.95 %. The high reflectance of the mirrors results in a resonance linewidth of approximately 28 kHz. In order to optimize the resonance linewidth relative to the scan speed, detector bandwidth, and signal recording sampling rate, an iris was inserted into the free space cavity. By adjusting the iris, the cavity loss can be increased, thereby also increasing the cavity linewidth. Due to the large radius of curvature of the mirrors, the cavity's TEM_{00} mode has a waist radius of 0.96 mm. This allows for fine adjustment of the cavity linewidth using the iris. Furthermore, the iris helps to eliminate higher order modes in the free space cavity, thereby simplifying subsequent data analysis as all cavity transmission peaks are equidistant markers of the TEM_{00} mode.

A great advantage of using a free space cavity as a reference is that the intrinsic dispersion of the reference cavity itself is negligible compared to the dispersion of the MRR. The change in the refractive index of air from 1530 nm to 1630 nm is $\Delta n = 8 \times 10^{-8}$. The equivalent change in effective refractive

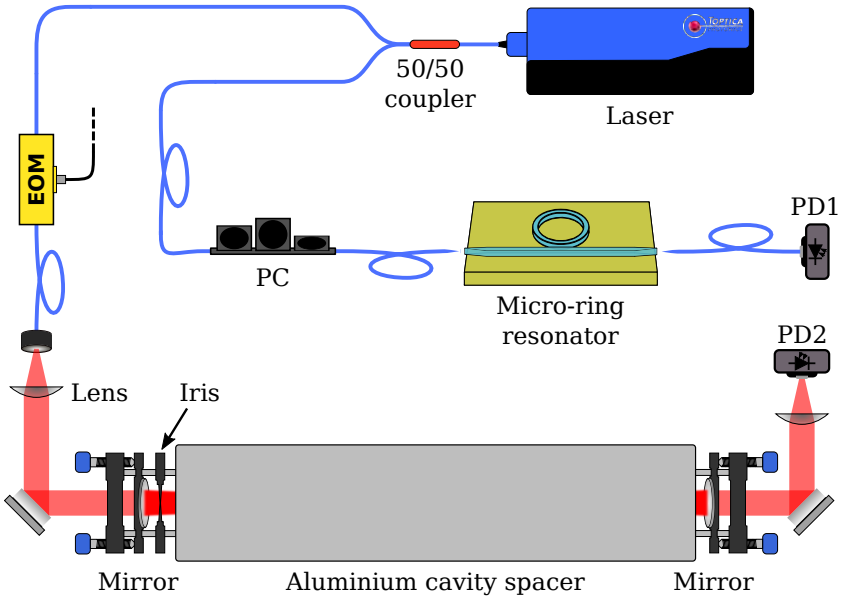

Figure 4.8: Schematic of the dispersion measurement setup. The free space mirror cavity is used as a frequency reference, giving narrow equidistant markers every 175 MHz on PD2. This allows for linearization of the frequency axis of the MRR transmission data from PD1. EOM: electro-optic modulator, PC: polarization controller, PD: photo detector

index for a waveguide of 500 nm by 300 nm is $\Delta n = 1 \times 10^{-1}$. The effect of the dispersion in air can safely be assumed to be negligible when measuring the dispersion of an MRR. In this setup, the dispersion from the cavity mirror coating has not been directly measured. However, using the free space cavity as a reference, the dispersion of a Thorlabs-bought fiber was measured. The measurement showed great agreement with the Thorlabs specifications. Based on this measurement, the total dispersion of the free space cavity, including contributions from the cavity mirrors, is assumed to be negligible.

Figure 4.8 shows a schematic of the setup. A continuously tunable laser from Toptica is used for scanning the wavelength from 1530 nm to 1630 nm. The laser output is split into two paths using a 3 dB fiber splitter. One of the fiber outputs is sent through a polarization controller and is coupled into the MRR bus waveguide using lensed fibers. The transmission signal from the MRR is detected on the photo detector, PD1, and recorded on an oscilloscope. The other fiber output from the splitter is coupled to an EOM before being coupled into the free space cavity. The EOM is used to accurately measure the FSR of the free space cavity. The cavity transmission signal from detector PD2 is also recorded on the oscilloscope.

Figures 4.9 to 4.11 show the recorded data from a measurement of resonator 177 on the CG49-chip. In figure 4.9 the MRR transmission is shown. The plot

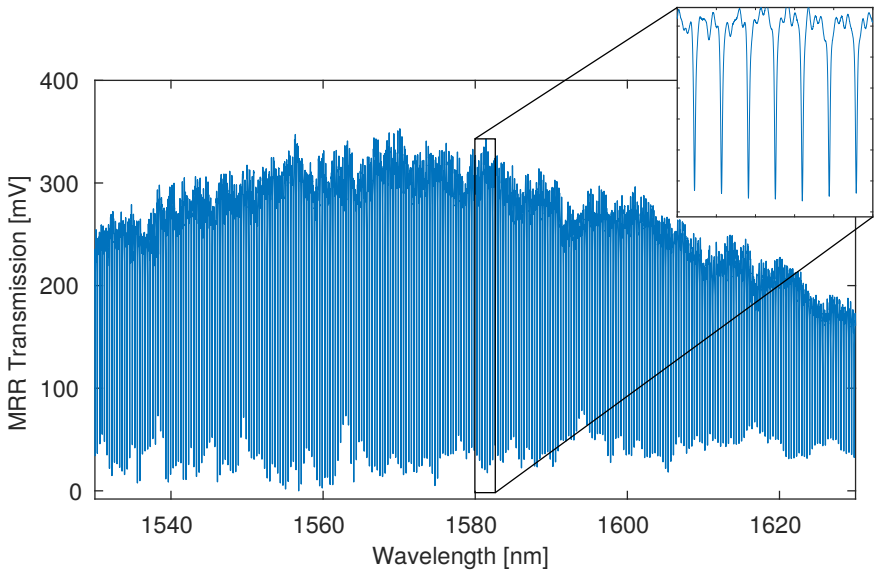

Figure 4.9: Transmission spectrum of MRR number 177 on chip CG49 as recorded on PD1 on figure 4.8.

shows the bus waveguide transmission as a function of wavelength as recorded on PD1 (figure 4.8). The overall parabolic nature of the transmission is due to the change in fiber-to-waveguide coupling as the focal length of the lensed fibers changes slightly over the span of 100 nm. The more random high-frequency noise is believed to be caused by impurities and scattering in the bus waveguide. The transmission is close to zero on resonance. This indicates a close to perfect coupling ratio between the bus waveguide and the resonator.

In figure 4.10 the measured Q-values versus mode number are shown. The Q-values are calculated based on individual Lorentzian fits to each mode. The Q-value at $\mu = 0$ ($\lambda_{\mu=0} \approx 1580$ nm) of this resonator is 5.6×10^4, corresponding to a Lorentzian Full Width Half Maximum (FWHM) of 3.5 GHz. With an FSR of 38 GHz, the resonator finesse is approximately 11. The Q-value increases with the mode number and thereby decreases with the resonance wavelength. This is mainly due to higher mode confinement as the refractive index of AlGaAs increases for lower wavelengths. The change in Q-value can also be caused by a variation in coupling efficiency between the bus waveguide and the resonator. There is, however, no correlation between the coupling efficiency, as visible on the transmission plot, and the variation in the Q-values.

In order to estimate the D_2 and D_3 parameters, the frequency variation to the FSR is plotted and fitted using equation (4.10) in the form

$$\omega_\mu - \omega_0 - D_1\mu = \frac{1}{2}D_2\mu^2 + \frac{1}{6}D_3\mu^3. \tag{4.18}$$

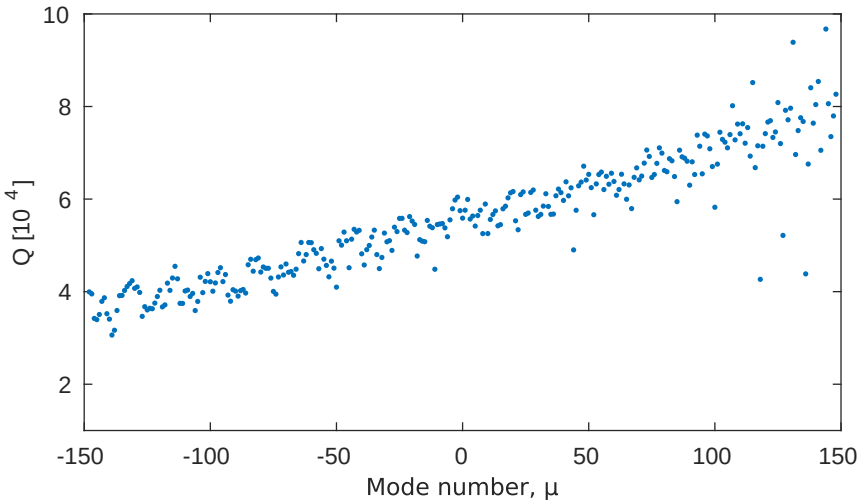

Figure 4.10: Q-values of the modes in MRR number 177 on chip CG49. The Q-values are found through fitting of a Lorentzian lineshape to each resonance shown on figure 4.9. $\mu = 0$ is the MRR mode closest to the laser scan's center wavelength of 1580 nm.

Figure 4.11 shows the resonator dispersion profile. The red curve shows the fit to the measured data, and the black curve shows the calculated dispersion profile using equations (4.14) to (4.16) and the resonator's design parameters from table 4.2. The fit to the measurement gives the values for the dispersion parameters $D_2 = 159$ kHz and $D_3 = -248$ Hz with ω_0 corresponding to the center of the scan at 1580 nm. These values are equivalent to a GVD of -1151 fs^2/mm. This is significantly lower (more anomalous) than the design GVD of -306 fs^2/mm as shown on figure 4.7(a).

All the points on figure 4.11 follow a continues curve. This is an indication that the resonator is single-mode. If higher order modes did exist, mode crossings would be visible in the dispersion profile. An example of a mode crossing can be seen in the dispersion profile of resonator number 79 at $\mu = 58$ in appendix B figure B.6.

In table 4.3 an overview the measurements of the CG49-chip is shown. Only a small subset of the 189 resonators on the chip has been characterized as resonators with damaged waveguides or bad coupling efficiency have been left out. The corresponding plots of the measured transmissions, Q-values, and dispersion profiles can be seen in appendix B.

The Q-values range from 4.4×10^4 to 1.1×10^5 without any apparent correlation with their taper designs. When comparing the Q-values to those of resonators without tapering on the same chip, there is no discernible difference. This is a strong indication, that the tapers do not affect the Q-value of the resonator at this level. Based on these measurement, with Q-values of this

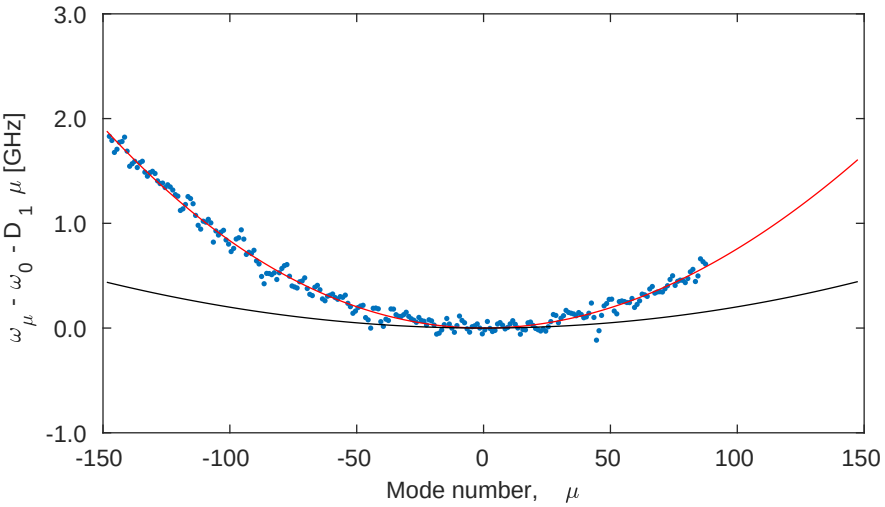

Figure 4.11: Dispersion profile of MRR number 177. The red curve is a fit of equation (4.18) to the measured data with $D_2 = 159$ kHz and $D_3 = -248$ Hz. The black curve is the simulated dispersion profile based on the resonator's design parameters where $D_2 = 44$ kHz and $D_3 = 0.5$ Hz.

magnitude and with the low number of taper designs, it is difficult draw a conclusion on the effect of the tapers on the Q-values. Further investigation into the loss introduced by the taper is required.

The measured GVD is consistently lower than the design GVD. The most probable explanation for this discrepancy is that the fabrication process did not produce the target geometry of the waveguides. The AlGaAs layer thickness was measured doing the etching process to 295.64 nm. This is only a deviation of 1.5 % and can not account for a lower GVD but should rather give a higher GVD. Only a small degree of over-etching[2] will, however, have a large impact on the GVD and would result in a lower GVD at $\lambda_{\mu=0} = 1580$ nm.

The GVD is negative, and the dispersion is thereby anomalous. This means that comb generation should be possible in these resonators. As described by equations (4.5) and (4.6), it is the non-linear phase shift that gives the requirement of anomalous dispersion. When the optical power in the resonator is above the threshold power (equation 4.9), the resonator dispersion has to match the non-linear phase shift. The optimum dispersion for a given set of resonator parameters can be found through simulations as described in [108]. Here, we will simply compare the dispersion to that of resonators where comb generation have been reported.

[2]In the fabrication process the waveguides are etched from a uniform wafer where the etching removes all the material not forming the waveguides. Over-etching will thereby result in a more narrow waveguide.

For comparison of dispersion profiles across material platforms, we have to account for the effect that the material properties have on the threshold power and the non-linear phase shift. The size of the non-linear phase shift at the threshold pump power is $\phi_{NL} = 2\gamma P_{threshold}$. If the phase shift at the threshold pump power is small, a low degree of anomalous dispersion is required. If the phase shift is large, a higher anomalous dispersion is necessary. From equations (4.7) and (4.9) we know that

$$\gamma \propto \frac{n_2}{nA_{eff}}$$

and

$$P_{threshold} \propto \frac{n^2 A_{eff}}{n_2}.$$

This gives the relation $\phi_{NL} \propto 2n$. Doing a comparison between AlGaAs and Si_3N_4, we get a non-linear phase shift at the threshold pump power of:

$$\begin{aligned} &\text{AlGaAs: } \phi_{NL} \propto 6.6 \\ &Si_3N_4: \quad \phi_{NL} \propto 4.0 \end{aligned}$$

The anomalous dispersion of an AlGaAs resonator should be roughly a factor of 1.7 larger than that of a Si_3N_4 resonator of similar Q and FSR. In [86] a frequency comb is generated in a Si_3N_4 planar ring resonator with a dispersion of -50 fs^2/mm which is significantly lower than the GVDs measured in the tapered AlGaAs resonators. Others have shown comb generation in Si_3N_4 resonator with a $GVD \approx -5000$ fs^2/mm, [82], which is a significantly larger anomalous dispersion than measured in the AlGaAs resonators. Based on this comparison the dispersion in the AlGaAs resonators should allow for comb generation.

Even though all resonators are designed to be single mode, higher order modes have been observed in some resonators. According to [86], coupling to higher order modes are more likely to happen in bends. An effort should be done to keep bends restricted to narrow parts of the resonator in future designs. This was not prioritized in the current design as the short resonator length made it impractical to limit bending to narrow regions.

MRR number	W_n [nm]	W_w [nm]	L_t [µm]	FSR [GHz]	$Q_{\mu=0}$ [10^4]	Design GVD [fs^2/mm]	Meas. GVD [fs^2/mm]
75	480	680	668.85	38.12	10.1	-456.6	-1182
79	480	680	668.85	38.12	5.5	-456.6	-747
80	480	680	668.85	38.15	6.8	-456.6	-982
85	480	800	720.30	38.36	6.8	-256.3	-350
90	480	800	720.30	38.36	5.6	-256.3	-196
95	420	740	499.00	38.87	6.3	-305.7	-1146
98	420	740	499.00	38.87	4.4	-305.7	-729
99	420	740	499.00	38.90	6.2	-305.7	-762
173	420	740	499.00	38.88	11.1	-305.7	-993
174	420	740	499.00	38.88	8.4	-305.7	-1150
176	420	740	499.00	38.88	7.0	-305.7	-970
177	420	740	499.00	38.88	5.6	-305.7	-1151
115	500	700	303.75	96.95	6.0	-423.3	-329
124	500	820	324.00	97.43	7.0	-246.5	-231
142	480	680	324.00	96.42	6.9	-516.2	-1408

Table 4.3: CG49-chip characterization results. FSR-, Q-, and GVD-values are calculated for $\mu = 0$ at 1580 nm. The design GVD is calculated as described above in subsection "Tapered Waveguide Resonators".

The dispersion measurement setup presented here shows a very high spectral accuracy. The setup is able to produce dispersion curves of high FSR resonators with a noise-level comparable to those made using commercial fiber-based frequency combs as a reference. This setup is a simple and low-cost setup only requiring a continuously tunable laser and an optical cavity with a low and well known FSR.

4.3 Comb Generation

Characterization of the micro-ring resonators is normally done at low optical power to prevent thermal effects of high intensity light in the waveguide. As a result the optical power is always significantly below the threshold power for parametric oscillation (equation (4.9)) when characterization is done. Once the sufficient information has been obtained in the characterization process, the resonators are pumped with an incremental increase of optical power until parametric oscillation and comb generation occur.

Pumping AlGaAs Resonators

Only a small subset of the fabricated AlGaAs resonators have shown parametric oscillation when pumped. In 2016 Minhao Pu published the first ever frequency comb generation in AlGaAs-on-insulator showing a record low threshold power, [88]. The challenge is to obtain high enough parametric gain without overstepping the waveguide's optical power damage threshold. In AlGaAs, typical damage is burning of the bus waveguide facets or burning of the resonator waveguide due to impurities in the AlGaAs. Irreversible damage typically occurs above 23 dBm of optical power at the bus waveguide input facet.

The tapered waveguide resonators described above have not shown any parametric oscillation when pumped at high powers. Non-linear loss is believed to be the problem. Even though TPA should be negligible, free surface states on the waveguide surface are believed to alter the band-gap, making TPA a significant loss at higher intensities. This prevents a sufficient parametric gain at optical powers below the waveguide damage threshold.

Some of the early resonator chips, namely CG13 and CG15 (used in [88]), have generated full comb spectra. In an effort to analyze the AlGaAs-based frequency comb's noise characteristics, the same resonators were pumped again approximately two years after fabrication. The resonators on the CG13-chip experienced irreversible, intensity induced waveguide degradation. When pumped just above threshold, parametric oscillation occurred, and primary comb lines appeared forming a spectrum similar to the one shown in figure 4.12 a). The pumping power was then slightly increased with the expectation of more comb lines appearing in the spectrum. This, however, resulted in an increase in the threshold power. Regardless of pumping power only primary

comb lines appeared, and after pumping the Q-value of the resonator was significantly reduced.

The resonators on CG15 showed comb generation, and a variety of different comb states were observed (figure 4.12). The evolution of the comb as the pumping power is increased above the threshold is clearly visible. As the optical power is increased, the parametric gain also increases resulting in more and more comb lines. Abrupt changes in the comb states are observed as sub-combs start to form around the primary comb lines. The sub-combs change between states with different line spacings, and new sub-combs are generated. These different states are highly dependent on both the pumping power and the frequency detuning between the pump laser and the resonator mode. The spectra on figure 4.12 d) and e) show two different comb states with the same pumping power but with different frequency detuning. A full comb spectrum was not achieved in these measurements.

Comb Generation in Silicon Nitride

An 18-GHz-FSR, Si_3N_4 micro-resonator designed at the Electrical Engineering Department at UCLA was also pumped. The resonator is identical to the one presented in [109]. A full comb was realized spanning more than 200 nm. In these investigations the comb was pumped so that a series of sub-combs covered a full comb spectrum. The pumping was done in a way so that the sub-combs overlapped but did not merge into a single coherent comb.

Figure 4.13 shows the spectrum of the resonator output after a optical wavelength low-pass filter. The optical low-pass filter had a cut-off wavelength at 1585 nm and was used to filter out the high power pump at 1596 nm. The RF-spectrum of the comb was recorded simultaneously with the optical spectrum and is shown in figure 4.14. The $1/f$ noise in the RF-spectrum indicates that the sub-combs have a random phase relation. By slightly changing the pumping parameters, the comb state changed into a low-noise state with a fixed phase relation between the sub-combs. Figure 4.15 shows the optical spectrum, and figure 4.16 shows the RF-spectrum. In this comb state, the sub-combs have a highly correlated phase, and the RF-spectrum now shows a single narrow beat-note. As shown in [109] the frequency of this beat-note is correlated to the repetition rate of the comb and can be locked to a low-frequency stable oscillator, thereby locking the repetition rate of the comb.

4.4 Stabilizing the Optical Frequency Comb

The main attraction of optical frequency combs, within a wide array of applications, is their ability to act as a ruler in the optical spectrum. It is a tool that allows for easy comparison and down sampling of frequency measurements across a broad spectrum. These measurement applications rely on

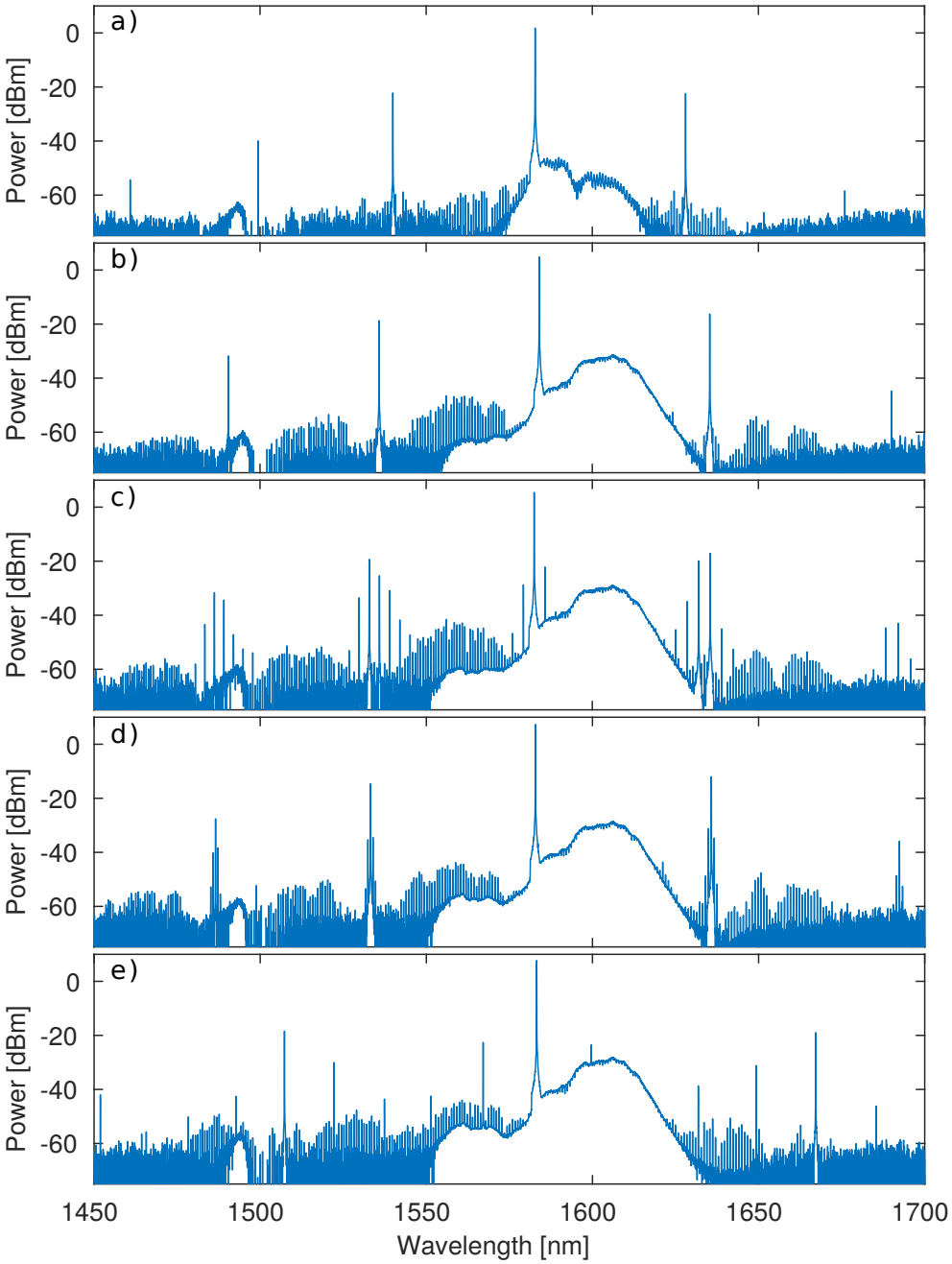

Figure 4.12: The evolution of comb states in an AlGaAs resonator with increasing pump power. a) pumped just above the threshold power at 11 dBm in the bus waveguide. b) pumped at 15 dBm, c) 16 dBm, d) 17 dBm, e) 17 dBm with a slightly different detuning between pump laser and resonator compared to d).

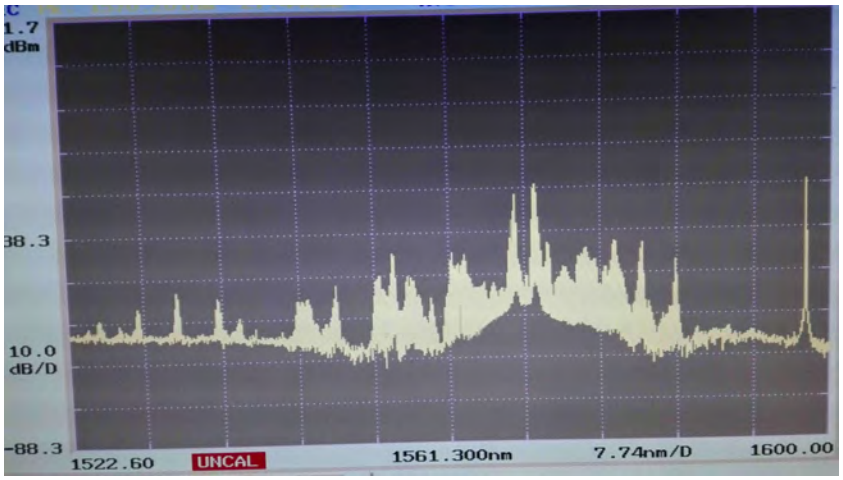

Figure 4.13: The optical comb spectrum of the Si_3N_4 comb after an optical low-pass with a cut-off wavelength at 1585 nm.

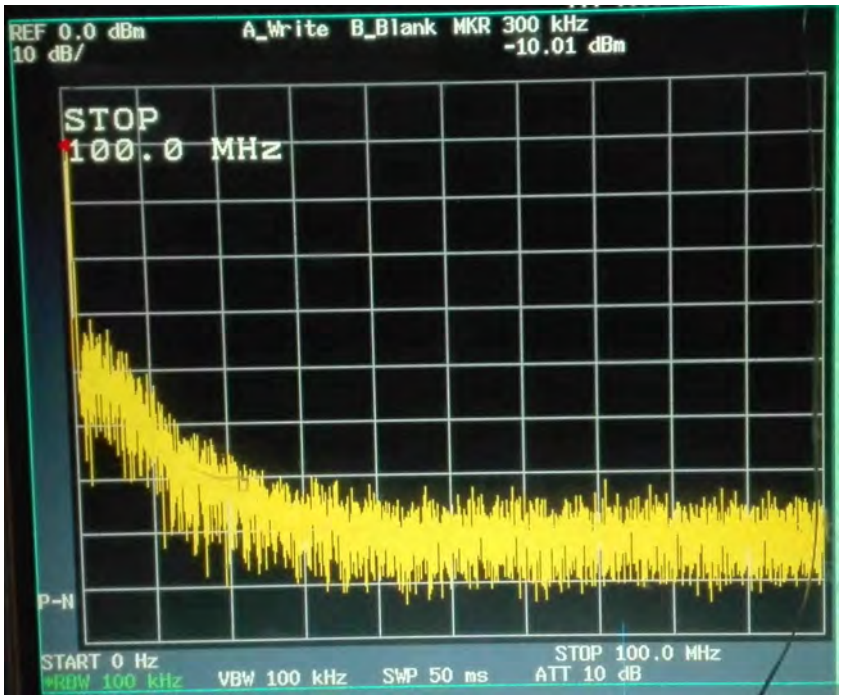

Figure 4.14: The RF spectrum of the Si_3N_4 comb shown in figure 4.13. The $1/f$ noise indicates a noisy and incoherent comb state.

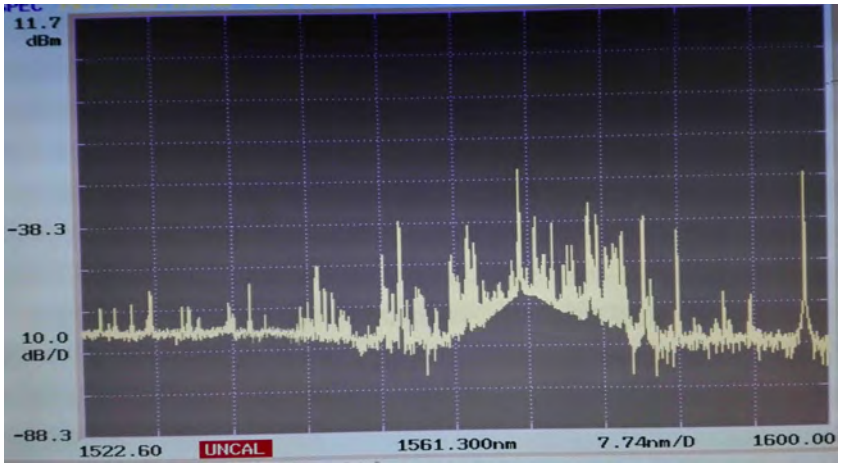

Figure 4.15: The optical comb spectrum of a low-noise state of the Si_3N_4 comb after an optical low-pass with a cut-off wavelength at 1585 nm.

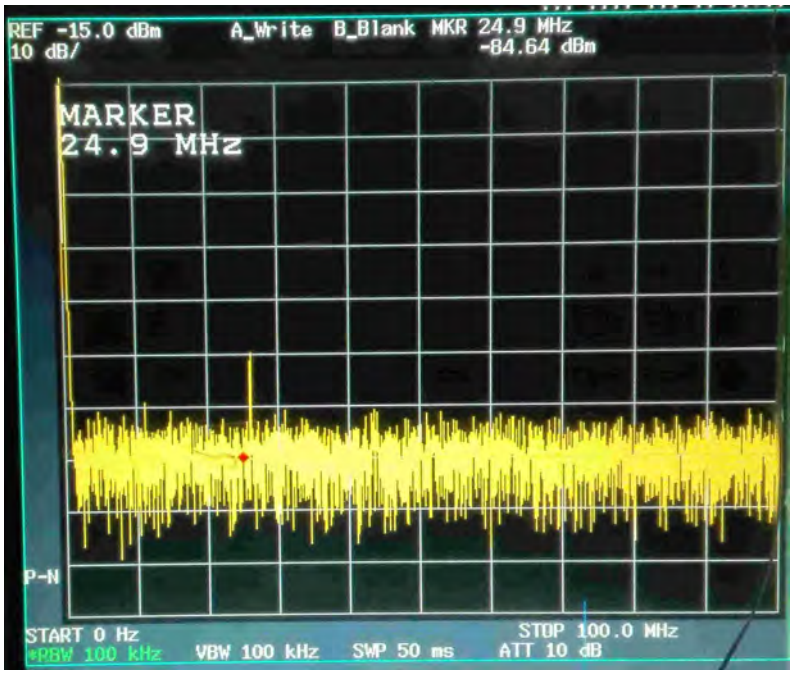

Figure 4.16: The RF spectrum of the Si_3N_4 comb shown in figure 4.15. The single narrow beat-note indicates a low-noise and coherent comb state.

a high degree of accuracy and are based on two specific properties of the frequency comb: a precise and accurate f_{rep} and f_{ceo}. In other words, an optical frequency comb is only useful to a certain level determined by the frequency stability of the repetition rate and the individual comb lines. Stabilization of these parameters is therefore of great importance.

A number of different parameters of the comb generation are responsible for the different noise types in a micro-resonator Kerr comb. The repetition rate, f_{rep}, and thereby its instability, is determined by the FSR of the micro-resonator together with the non-linear wave-vector mismatch (eq. (4.6)). The wave-vector mismatch is again dependent on optical power and frequency detuning between the pump laser and resonator mode. Stabilization of the repetition rate should therefore be possible through feedback on:

1. the micro-resonator's temperature affecting the FSR and mode frequency,
2. the optical pump power affecting the micro-resonator's temperature and cross phase modulation, and
3. the pump laser frequency.

The frequency noise, or linewidth, of the pump laser is inherited by the photons generated by FWM. Stabilizing the pump laser will result in low frequency noise of the individual comb lines. By locking the f_{rep} and one of comb lines (e.g. the pump laser frequency), the f_{ceo} will, as a consequence, also be locked.

A commonly used technique for micro-resonator Kerr combs is to stabilized the repetition rate through feedback on the pump power and use the pump laser frequency to achieve line-narrowing of the individual comb lines. This have been shown by [110, 111, 112, 113], among others.

Techniques for Comb Stabilization

An optical reference, such as a narrow-linewidth optical resonator or an absolute reference (e.g. molecularly or atomically referenced), can be used for optical frequency comb stabilization. One option is to lock a comb line to an optical reference, thereby fixing one point of the comb. Simultaneously, the repetition rate can be stabilized by direct detection of the comb pulse train and locked to an RF-reference. For commercially available combs like fiber-based frequency combs or mode-locked lasers, this is usually a good option. The repetition rate of such combs are typically below the GHz-level where affordable and highly stable RF-references are available. When stabilizing micro-resonator combs with repetition rates of several GHz, the RF-references available today are inadequate.

An alternative to using an RF-reference is to use a second optical reference. By locking two different lines in the comb, both the repetition rate and carrier

offset frequency will be locked. In this case, the noise on the repetition rate will be given by the sum in quadrature of the noise of the two references divided by the number of comb lines between the two references[3].

$$\delta f_{rep} = \frac{\sqrt{\delta f_A{}^2 + \delta f_B{}^2}}{\mu_A - \mu_B}$$

where δf_A and δf_B are the noise of the two references, and μ_A and μ_B are the mode-numbers of the two stabilized lines of the comb. The disadvantage of this option is the requirement of two optical references, preferably with an operating wavelength hundreds of nanometers apart.

The so-called self-referenced comb utilizes a technique called $f-2f$ locking. Here, f_{ceo} is measured by self-referencing. This is done by choosing a comb line with a frequency ν_n where a comb line with frequency $2\nu_n$ also exists. This means that the technique can only be used on an octave spanning comb. The frequency of this comb line is given by $\nu_n = f_{ceo} + nf_{rep}$, and the comb line at double the frequency is given by $2\nu_n = f_{ceo} + 2nf_{rep}$. By using second harmonic generation to double the frequency of the comb line at ν_n and beating it with the comb line at $2\nu_n$, the f_{ceo} can be directly measured. Locking the beat-note of these two comb lines ensures a fixed relation between f_{rep} and f_{ceo}. For a fully stabilized comb one of these parameters still needs an additional lock. This can either be done by locking the f_{rep} directly to an RF-reference as described above or by locking a comb line tao an optical reference. When the f_{ceo} is stabilized in this way, the frequency division factor between the optical reference and the repetition rate is equal to n. Remember that n is the mode number of the comb line locked to the optical reference, counting from ν_0. In [48] a 12 GHz microwave signal is generated from the repetition rate of an $f-2f$ stabilized comb reference to a high-finesse optical cavity operating at a wavelength of 1542 nm ($\nu \approx 194$ THz). This gives a frequency devision factor of $\frac{194 \text{ THz}}{12 \text{ GHz}} \approx 1.6 \times 10^4$, resulting in a phase-noise below -172 dBc/Hz at 1 kHz for a 12 GHz carrier.

Thermal Feedback on AlGaAs Resonators

A proposal for combining the stability and spectral properties of an acetylene molecular referenced laser with an MRR Kerr comb was investigated. An AlGaAs micro-resonator was fitted with a titanium heater on top of the SiO cladding enclosing the waveguide. Using an absolute stabilized laser as the pump laser for comb generation excludes the use of pump laser frequency tuning as feedback for comb stabilization. Changing the temperature of the AlGaAs resonator will cause a change in the resonance frequency, thereby changing the laser-MRR detuning. Employing the PDH technique (see section 2.1) will allow for a high degree of control of the detuning. Figure 4.17

[3]Assuming that the noise of the two references are uncorrelated.

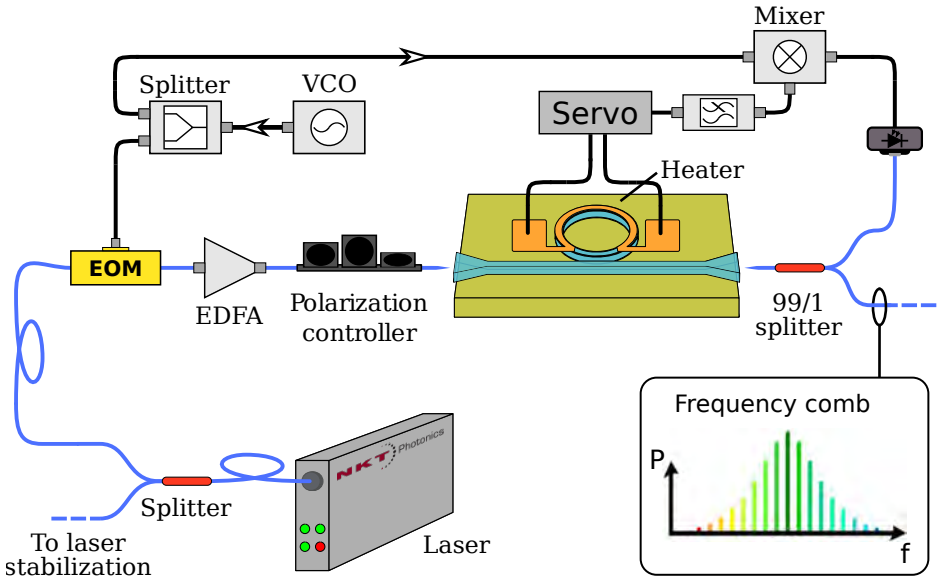

Figure 4.17: The stabilization scheme for locking an MRR to a referenced pump laser. This setup is based on the PDH technique which is described in section 2.1. EOM: electro-optic modulator, EDFA: erbium-doped fiber amplifier, VCO: voltage-controlled oscillator. This figure is adapted from [114].

shows the proposed setup for a PDH stabilization of an MRR to a pump laser. Here, an EOM is used to phase modulate the pump laser before amplification in a fiber amplifier (EDFA). 1 % of the bus waveguide transmission is split off, detected, and demodulated, generating the PDH signal.

The bandwidth of the heater tuning is assumed to be limited by the heat dissipation and thereby by the thermal conductance of the SiO cladding. The bandwidth of the heater tuning is measured by coupling a probe laser through the bus waveguide, tuned to a frequency that places the laser on the red side of an MRR mode. The electrical power in the heater is then changed rapidly by applying a step-function to the heater voltage. The power in the heater changes from 2.76 mW to 2.38 mW, causing the MRR mode to move slightly out of resonance with the probe laser. When scanning the MRR mode, the total height of the resonance, as measured by a photo detector, is approximately 110 mV. The measured transmission signal changes 50 mV when applying the step-function, making any contribution from the Lorentzian shape of the MRR resonance negligible. An exponential function is fitted which gives a characteristic time of the heater response of $\tau = 15.1$ µs, corresponding to a bandwidth of 10.5 kHz.

The FWHM of the MRR mode was measured to be 3.8 GHz. A frequency of 5.26 GHz was used for the PDH modulation, generating the signal shown in figure 4.19. This signal was made using a probe laser with 0.5 mW of optical

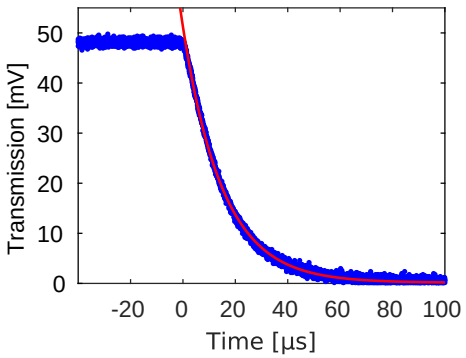

Figure 4.18: The step response of a heater controlled MRR resonance. The heater power changes from 2.76 mW to 2.38 mW at $t = 0$ s, changing the frequency relation between the laser and MRR from on-resonance to off-resonance. The characteristic time of the fitted exponential is $\tau = 15.1$ µs.

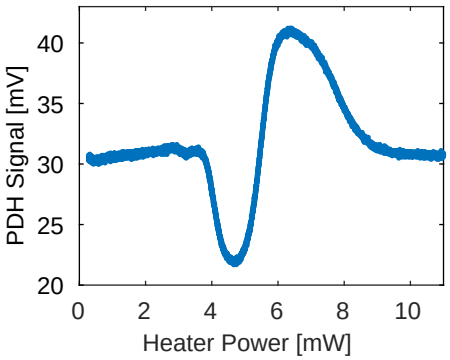

Figure 4.19: The PDH-signal of an MRR mode, when scanning the heater power. The FWHM of the Lorentzian MRR mode is 3.8 GHz, and the PDH modulation frequency is 5.259 GHz. The signal is low-pass filtered at 7.3 kHz. This figure is also presented in [114].

power in the bus waveguide. The signal was low-pass filtered at 7.3 kHz, thereby limiting the bandwidth slightly.

The MRR mode was locked to the probe laser using a PI^2 servo. Figure 4.20 shows an overlapping Allan deviation of an in-loop stability measurement of the laser-MRR detuning. The blue curve shows the stability with active feedback, and the black curve shows the stability without feedback. In both cases the MRR-chip holder was temperature stabilized. The probe laser used was an NKT Photonics Koheras BASIK X15 module. According to the manufacturer's specifications, long-term frequency drift is approximately $\sigma(\tau) = 1$ MHz at $\tau = 100$ s. The limitation to the free running stability measurement is most likely due to frequency drift of the probe laser, and not the MRR. The overlapping Allan deviation shows a minimum of 220 kHz corresponding to a line-splitting of 17000.

For comb generation to occur in the MRR, a significantly higher optical power is required. Pumping the MRR at high power will greatly deform the Lorentzian line shape of the MRR mode due to thermal effects. Even at high pump powers, locking using the heater was possible on the blue side of the MRR mode but was unstable on the red side. This could be problematic for soliton generation as they are formed with an effectively red detuned MRR mode [115].

The AlGaAs resonators fabricated with heaters did not show any parametric oscillation, and comb generation was not achieved. Comb stabilization using this technique was therefore not investigated further. Any of the above-

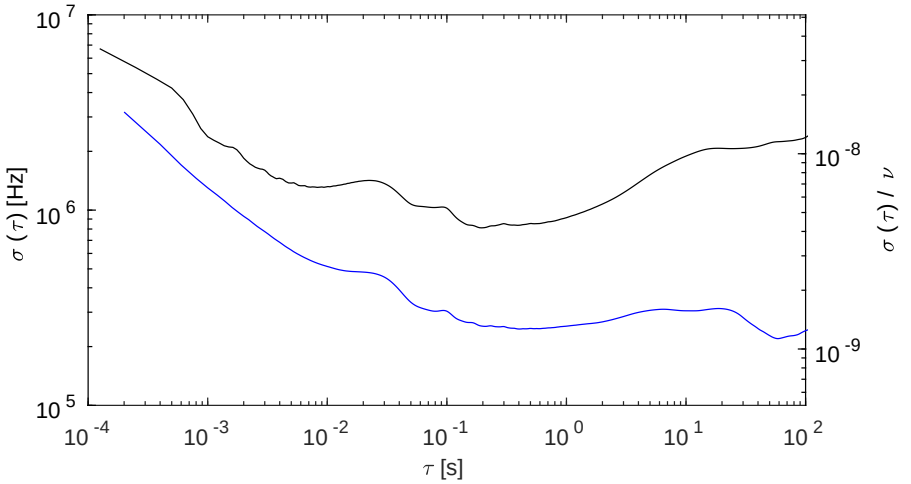

Figure 4.20: The overlapping Allan deviation of the frequency detuning between an MRR mode and the pump laser. Black: free running. Blue: locked.

mentioned stabilization schemes (e.i. $f - 2f$, optical reference) could be used in connection with this setup to achieve a fully stabilized comb. Even though this technique is a good tool for controlling the MRR-laser detuning, it will not be the best solution for stabilization purposes. The MRR's temperature can be modulated at far greater bandwidth through the optical power of the pump laser.

4.5 Outlook

Thorough investigations into the AlGaAs material are being done at the SPOC center. This should lead to a better understanding of why comb generation in AlGaAs has been difficult to obtain. The resonators presented here have high anomalous dispersion and did not show any parametric oscillation. Other AlGaAs resonators with significantly lower anomalous dispersion have also failed to produce parametric oscillation, and it is thus unlikely that dispersion engineering alone will solve the issue. If stable and reliable comb generation is not achieved in AlGaAs, other material platforms can benefit from the investigations presented here.

Tapered Waveguides

Further investigation of the Q-dependency on the waveguide widths and tapers is required. Improvement of the AlGaAs resonator fabrication will hopefully lead to resonators with higher Q-values, leading to higher requirement on the

tapers. In this work only a single chip with tapered resonators is presented. Far more data is needed to get good statistical certainty on the different characteristics like loss in the taper, deviation between dispersion calculation and measurements, and requirements on purely single-mode resonators.

New designs, where bending only occurs in the narrow parts of the resonator, should be considered. This should help to further reduce the possibility of higher order modes in the resonator.

Dispersion Measurement

A new reference cavity for dispersion measurement has been designed and is currently being assembled. The new reference cavity will have a total length of 1.5 m, giving an FSR of 100 MHz. The mirrors have a radius of curvature of 2 m, giving a slightly more stable cavity mode and easier alignment.

This new reference cavity will be used in a project. The dispersion of AlGaAs, Hydex, Si_3N_4, and a-Si resonators will be measured and compared. The connection between the dispersion profile and the comb spectrum produced will be analyzed, and new tapered resonator designs will be based on these findings.

Other Material Platforms

Fabrication of deuterium-passivated a-Si resonators [96] and SiC resonators [97] are being developed. Dispersion engineering of these resonators is the next step before comb generation and characterization. a-Si is especially interesting with both high refractive index and high non-linear index which should allow for record low comb generation threshold power.

Si_3N_4 and Silica MRRs are achieving extremely high Q-values of tens and hundreds of millions [94, 91]. This allows for comb generation threshold powers below what has been demonstrated in AlGaAs. Furthermore, it has shown to be very durable materials capable of high power handling. The low thermal perturbation of the resonances compared to AlGaAs also suggest, that stable soliton generation is much easier. Through collaboration with our partners we plan to investigate these platforms further.

Data Transmission with a Kerr Comb

Following the work in [39], we plan on using a Kerr frequency comb for data transmission. This is expected to show a record high energy efficiency for optical data transmission. For this experiment a full, coherent, and stable comb is preferred. Furthermore, a comb line spacing matching the ITU-grid will be desirable. In this experiment we plan to investigate the correlation between the frequency noise of the comb and the achievable bit-error rate. Does a highly coherent comb with ultra low phase-noise of the individual lines allow

for more efficient data transmission? The research within integrated photonics will undoubtedly have a great impact on society in the coming decades.

5

Strontium Atomic Clock

The work on a strontium frequency reference based on a thermal ensemble of atoms is presented in this chapter. The idea behind this experiment is to utilize the narrow clock transition in strontium for both stability and accuracy and in that way circumvent the limitations of optical reference cavities. This chapter only gives a small insight into the experimental system. Further in-depth analysis can be found in [23, 24, 25, 26].

A description of the key elements of the setup is given, followed by preliminary results.

Strontium-based, optical atomic clocks are the leading contender as a replacement for the caesium reference used for the definition of the second [4]. The strontium atom has been chosen in many clock laboratories due to its level structure which allows for efficient cooling and trapping at commercially available wavelengths.

Current state-of-the-art, strontium-based atomic clocks use a conventional clock scheme. Here, the stability is mainly achieved with a high finesse optical cavity, and the accuracy is based on atomic spectroscopy as illustrated in figure 1.2. Such systems use the doubly-forbidden $^1S_0 \leftrightarrow {}^3P_0$ line as the clock transition [3, 8, 7, 116]. This line has a width of ≈ 1 mHz [18]. Utilizing the extremely high Q-value of this transition requires high-resolution spectroscopy and, among other things, high suppression of thermal-broadening effects. Atoms are therefore cooled and trapped in an optical lattice. The loading of a lattice is usually done by first trapping the atoms in a Magneto-Optical Trap (MOT) using the wide $^1S_0 \leftrightarrow {}^1P_1$ line, thereby cooling the atoms to mK temperatures. The atoms are then loaded into a second-stage MOT using the narrow $^1S_0 \leftrightarrow {}^3P_1$ line reducing the temperature to tens of μK. Only then can the atoms be loaded into the lattice, resulting in a temperature of a few μK. A Sr-lattice typically holds $10^3 - 10^5$ atoms.

Our work is mainly focused on using the NICE-OHMS technique as a tool for frequency stabilization. We present a scheme where a laser is stabilized to a thermal ensemble of ^{88}Sr-atoms, utilizing a narrow atomic transition as both a stability and accuracy reference. This greatly reduces the requirements of the optical cavity used for pre-stabilization of the clock laser. We employ cavity-enhanced saturated spectroscopy of the 7.5-kHz-wide $^1S_0 \leftrightarrow {}^1P_1$ line. This is done with a single-stage MOT, greatly reducing the system complexity compared to conventional lattice clocks. Furthermore, we achieve a high cycling rate, doing hundreds of measurements on the atoms per second. This greatly minimizes the Dick effect compared to optical lattice clocks.

Recently our efforts have also been put into the generation of superradiant pulses. A cloud of atoms is placed in an optical cavity with a sufficiently high coupling between the atoms and the cavity mode. The atoms will, through the cavity field, have a high coupling causing a synchronization of the atomic dipoles. When at least half the atoms in the cavity mode are excited, a coherent decay can occur generating a flash of light into the cavity mode. Recent theoretical work suggest that superradiant light from the 7.5-kHz-wide $^1S_0 \leftrightarrow {}^1P_1$ line can achieve a linewidth of down to 1 Hz [117]. This estimation is based on a non-thermal ensemble of atoms with otherwise experimentally realistic parameters similar to those presented here.

Publications on this work include [26, 23, 24, 25]. These publications give a detailed analysis of the system dynamics as the setup has evolved. In [118] a next-generation setup is presented. This is based on a continuous beam of cold atoms allowing for continuous atom interrogation and possibly continuous superradiance. In [119] a theoretical model of the superradiant pulses from a thermal atom ensemble is presented.

5.1 The Strontium Setup

This section describes the configuration of the Strontium experiment. The setup's main laser system is the clock laser. The key components of the clock laser and its performance are presented. Following this is a brief description of the system configuration of the cavity-enhanced spectroscopy.

The Strontium Atoms

The core of the setup is a single-stage MOT of ^{88}Sr-atoms. The level-scheme of the ^{88}Sr is shown in figure 5.1. Only levels and transitions relevant for this work have been included in the figure. Transition wavelengths and linewidths are shown in table 5.1. The broad line at 461 nm $^1S_0 \leftrightarrow {}^1P_1$, is used for cooling and trapping. Here, the decay channel from $^1P_1$ into the long-lived state of $^3P_2$ limits the number of atoms in the ground state. Two repumper lasers drive the $^3P_2 \leftrightarrow {}^3S_1$ and the $^3P_0 \leftrightarrow {}^3S_1$ transitions, filling the $^3P_1$ state from where the atoms can decay into the $^1S_0$ ground state, allowing them to interact with the cooling laser. This increases the number of atoms in the MOT by a factor of 13 [56]. The maximum number of atoms in the MOT is approximately 2×10^8. The temperature of the MOT has been estimated through numerical simulations to be approximately 5 mK [119].

The narrow intercombination line $^1S_0 \leftrightarrow {}^3P_1$ is used as the clock transition. This dipole-forbidden transition has a linewidth of 7.5 kHz with a resonance wavelength of 689 nm.

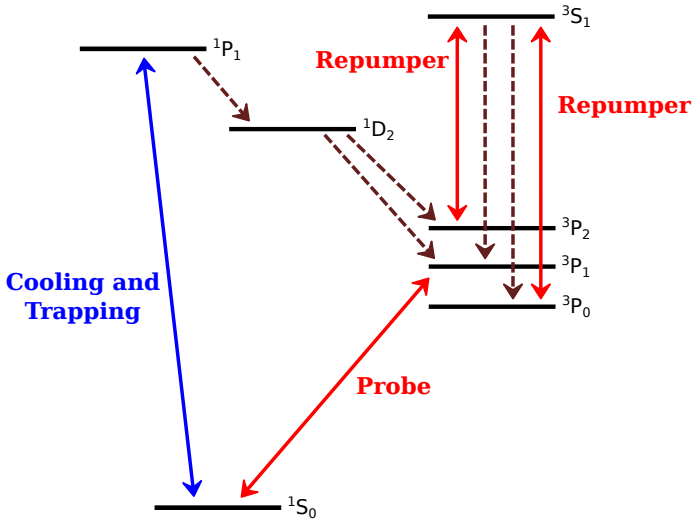

Figure 5.1: The electronic level structure of ^{88}Sr. Full lines indicate transitions that are used for preparation and interrogation of the atoms. Dashed lines indicate decay channels. The resonance wavelengths and transition widths are shown in table 5.1.

Transition	Wavelength [nm]	Linewidth [Hz]
$5s^2\ ^1\mathrm{S}_0 \leftrightarrow 5s5p\ ^1\mathrm{P}_1$	460.73	3.2×10^7
$5s5p\ ^3\mathrm{P}_2 \leftrightarrow 5s6s\ ^3\mathrm{S}_1$	707.01	6.7×10^6
$5s5p\ ^3\mathrm{P}_1 \leftrightarrow 5s6s\ ^1\mathrm{P}_1$	687.83	4.3×10^6
$5s5p\ ^3\mathrm{P}_0 \leftrightarrow 5s6s\ ^3\mathrm{S}_1$	679.10	1.4×10^6
$5s^2\ ^1\mathrm{S}_0 \leftrightarrow 5s5p\ ^3\mathrm{P}_1$	689.26	7.5×10^3

Table 5.1: The transitions of ^{88}Sr that are of interest in this experiment. The data is taken from the NIST Atomic Spectra Database [120].

The Clock Laser

The clock laser used to interrogate the Sr-atoms is a pre-stabilized ECDL. This ECDL is based on the Littrow configuration (fig. 5.2) where an optical grating is used to create the lasing cavity. Due to the angular dependency on the wavelength reflected from the grating, the lasing cavity has a restraint beyond a mirror-cavity. By tuning the grating angle, it is possible to tune the frequency of the laser tens of GHz without mode-jumps. A piezo-electric element allows for electronic control of the grating angle and thereby tuning of the laser frequency.

Lasing of the diode occurs when the optical gain from the diode-gain-medium is greater than the total optical loss in the ECDL. The gain is achieved as an electrical current through the diode excites electrons from the valence

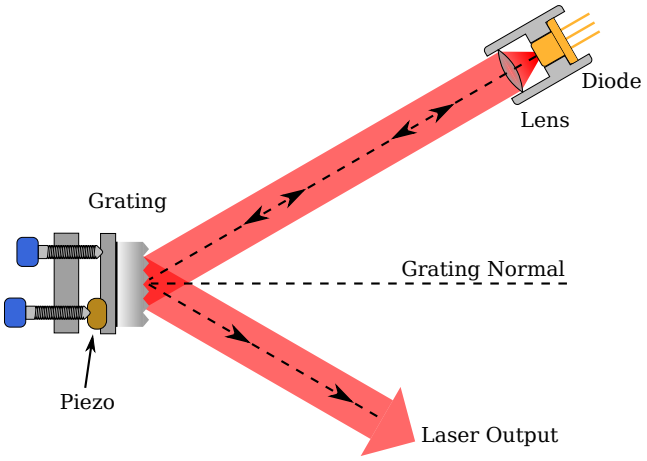

Figure 5.2: The Littrow ECDL configuration. The angle of incident of the diode light is the same as the -1'st order diffracted light. A lasing cavity is thereby formed between the grating and the diode. The grating position can be used to change the lasing frequency.

band to the conductance band. The voltage applied across the gain-medium, that causes the current, changes the band-gap and thereby changes the frequency of the photons generated. As diodes are small, they typically have a low electronic capacitance. This allows for high frequency modulation of the applied voltage, i.e. diode current, and thereby high modulation bandwidth of the laser's frequency. Because of this access to high bandwidth feedback, it is possible to build a stabilized ECDL-system with a very low phase-noise.

The ECDL is stabilized to a Fabry-Pérot cavity with a finesse of approximately 7500. As the clock laser needs to be on resonance with the atomic transition, an AOM is implemented between the laser and the cavity. This allows for the frequency of the laser to be shifted into resonance with the reference cavity while the laser is on resonance with the Sr-clock transition.

The PDH technique (see sec. 2.1) is used to generate an error-signal of the laser's frequency relative to the cavity resonance. The clock laser setup is shown in figure 5.3. Light from the ECDL is split into two paths using a half-wave plate and a Polarizing Beam Splitter (PBS). The first path is coupled into a PM-fiber going to the Sr spectroscopy setup. The second path is used for stabilization. The above-mentioned AOM is set up in a double-pass configuration in order to achieve the required frequency shift. The AOM is driven by a high-end VCO to ensure a minimum of added frequency and phase-noise. After the AOM the light is phase-modulated at 10 MHz using an EOM. The EOM is equipped with a 10 MHz resonance circuit, making a high modulation index possible. The light is then coupled into the reference cavity through a PBS and quarter-wave plate. The cavity reflection is split off by the PBS and is detected with a high bandwidth photo-detector.

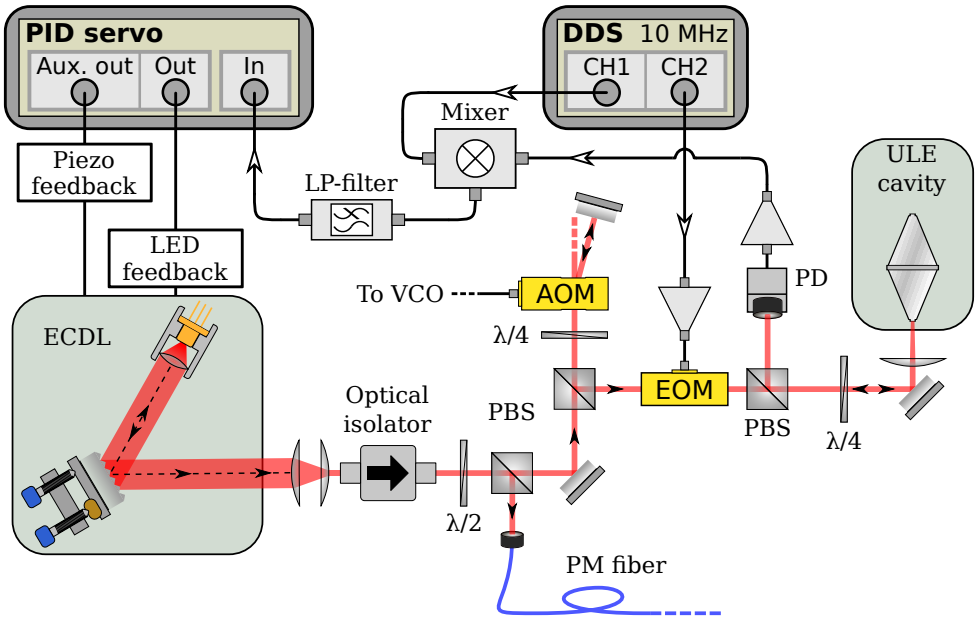

Figure 5.3: The schematic of the Sr clock laser.

Demodulating the cavity reflection signal gives an antisymmetric error-signal. This error-signal is inputted to a Vescent Photonics laser servo (D2-125). The servo generates a fast feedback signal acting on the diode current and a slow feedback signal acting on the ECDL-piezo.

The frequency stability of the laser system was evaluated with an in-loop measurement of the PDH error-signal. Figure 5.4 shows the error-signal as the frequency of the laser is scanned. The signal consists of a superposition of the three dispersion profiles for the carrier and sideband resonances. Figure 5.5 shows the corresponding signal of the cavity transmission. Calibration of the x-axis is done using the sidebands which are known to have a 2×10 MHz spacing. The frequency scan is assumed to be linear which gives rise to a small error. The slope of the PDH-signal on fig. 5.4, at zero detuning from the cavity resonance, gives a conversion factor from volt to frequency detuning. It should be noted that there is a significant uncertainty of this conversion factor due to the noise in the signal. The PDH-signal is recorded when the laser is locked on resonance with the cavity. By applying the conversion factor, the laser-cavity detuning as a function of time can be plotted (figure 5.6). It is safe to assume that the cavity resonance is much more stable than the laser frequency on the relevant timescales, and the data in figure 5.6 is therefore a good representation of the frequency noise of the laser.

The frequency noise is analyzed by calculating and plotting the overlapping Allan deviation (see figure 5.7). The data was recorded with a sampling time of 2 μs. In calculating the overlapping Allan deviation, zero dead time is

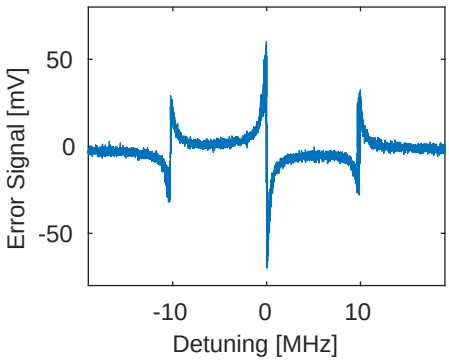

Figure 5.4: The PDH-signal from the Sr clock laser.

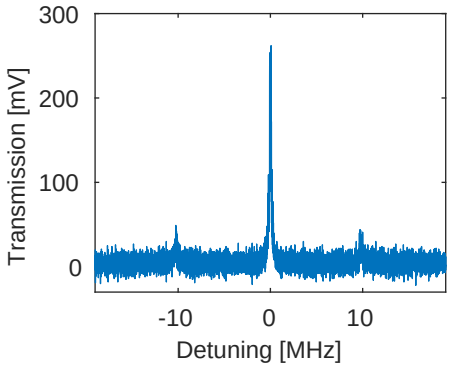

Figure 5.5: The transmission signal from the reference cavity in the Sr clock laser.

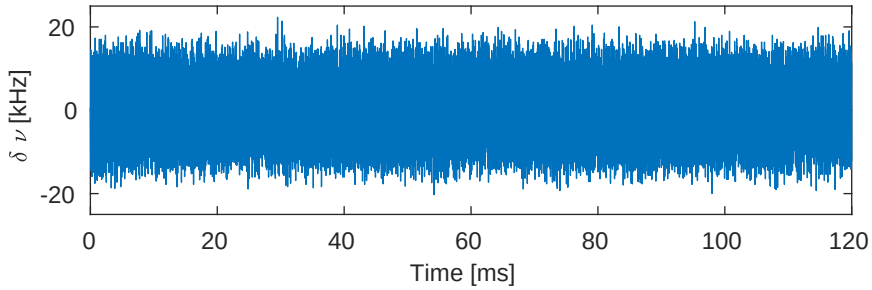

Figure 5.6: In-loop frequency-noise measurement of the Sr clock laser. $\delta\nu$ is the laser-cavity detuning. The sampling time is 2×10^{-6} s.

assumed. This is known not to be true for the oscilloscope used in these measurements. However, the error is believed to be negligible. It is evident that the calculated $\sigma(\tau)$ values follows a $\tau^{-\frac{1}{2}}$ dependency. This indicates that the noise is dominated by white frequency noise.

Cavity-Enhanced Atom Spectroscopy

A schematic of the spectroscopy setup, including components relevant for the NICE-OHMS measurements, is shown in figure 5.8. A more detailed description of the setup, including cooling and trapping lasers, the Sr-oven, and the Zeeman-slower can be found in [26, 118].

The setup is controlled by a computer with a National Instruments PCI-6259 data acquisition board (DAQ-board). This allows the computer to turn on and off the MOT laser beams with a TTL signal controlling an RF switch connected to an AOM. The DAQ-board also records the NICE-OHMS-signal on an analog input port. The analog input records voltage with a sampling rate of 1.25 MS/s.

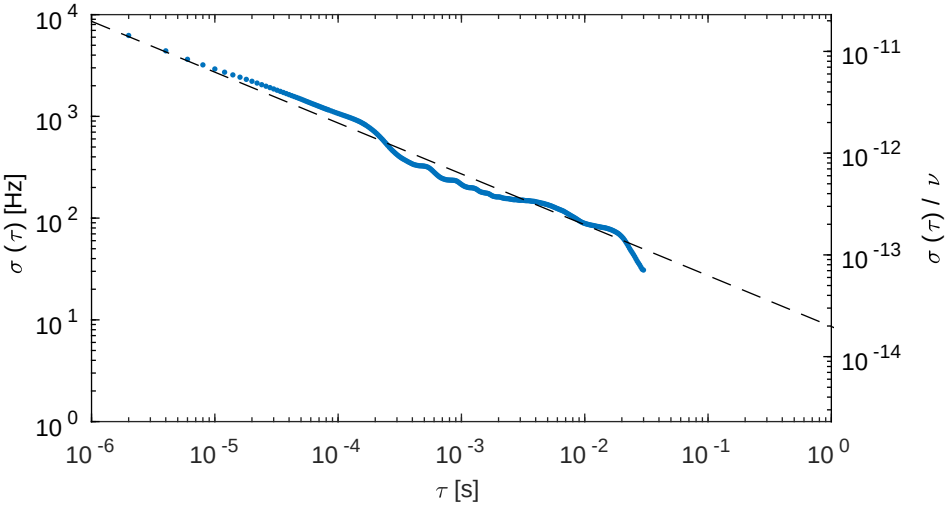

Figure 5.7: An overlapping Allan deviation of an in-loop frequency measurement of the Sr clock laser. The black dashed line indicates 8.6 Hz $/\sqrt{\tau}$. Zero dead time is assumed.

Light from the clock laser is used to injection-lock a so-called slave diode. This is done with the purpose of optical power amplification. AOM1 applies a fixed frequency shift of -345 MHz. AOM2 is used in a double-pass configuration for frequency tuning. The AOM is driven by an HP8648 frequency generator connected to the computer through GPIB. This allows the computer to control the frequency tuning of the clock laser.

A fiber-coupled EOM applies phase modulation for both PDH-locking at 10 MHz and for NICE-OHMS at 781 MHz. After the EOM a fraction of the light is split off to photo detector 2 (PD2) for power stabilization. A simple PI-circuit that feedback on the RF-power for AOM1 locks the optical power to a fixed level on the photo detector PD2. Photo detector 1 (PD1) detects the 10 MHz beat-note in the reflection from the optical cavity. This is used for the PDH-lock, keeping the cavity length on resonance with the clock laser at all times.

The light is coupled into an optical cavity placed inside the vacuum chamber. The cavity consists of two concave mirrors with a radius of curvature of 9 m, resulting in a waist of 450 µm of the TEM_{00} mode. The cavity has a finesse of 1240 and a resonance linewidth of 630 kHz. The cavity mirrors are placed on a Zerodur spacer, milled to allow MOT-beams to trap the atoms in the center of the cavity. A piezo-electric crystal on one of the mirrors makes it possible to tune the resonance frequency of the cavity and allow for locking of the cavity length.

The phase modulation generating sidebands at 781 MHz, which corre-

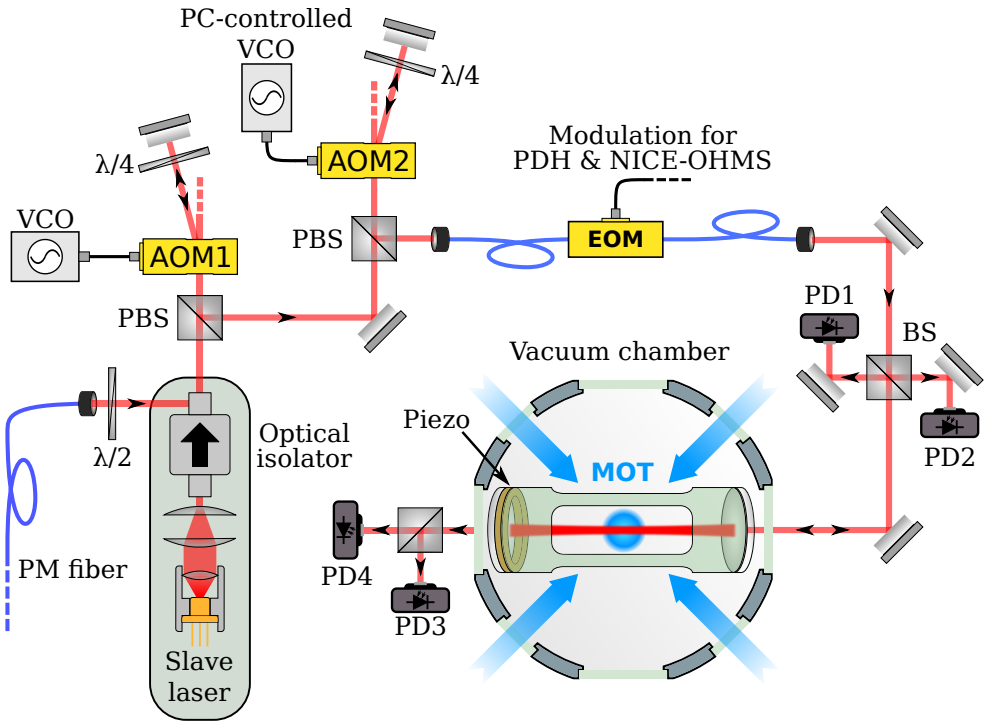

Figure 5.8: A simplified schematic of the Sr cavity spectroscopy setup. AOM: acusto-optic modulator. EOM: electro-optic modulator. MOT: Magneto-optical trap. PBS: Polarizing beam splitter. PD1 is used for PDH-locking of the optical cavity inside the vacuum chamber. PD2 is used for power stabilization of the probe laser. PD3 is an amplified detector recording the intensity of the cavity transmission. PD4 is a high-speed avalanche detector recording the 781 MHz beat-note.

sponds to the FSR of the cavity, allows for both the carrier and the sidebands to couple into the cavity. The cavity output field contains the 781 MHz beat-note from which the atom-cavity dispersion can be extracted. The cavity output is detected by both a Menlo APD210 high-speed avalanche photo detector with 1 GHz bandwidth and a Thorlabs amplified photo detector.

5.2 Locking with NICE-OHMS

The dispersion signal of the saturated transition is detected with the NICE-OHMS technique (see section 2.2). An example of the NICE-OHMS signal is shown in figure 5.9. The quality of the laser stabilization is, as described in section 1.1, dependent on the signal-to-noise ratio and the spectral width of the line.

A number of dynamics come into play here. A higher optical power will increase the number of photons on the detector, giving a bigger signal. At the

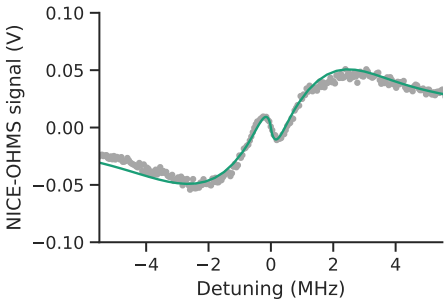

Figure 5.9: The NICE-OHMS signal of ^{88}Sr. The grey dots are measured data, and the green line is a simulation based on experiment parameters. The figure is taken from [25].

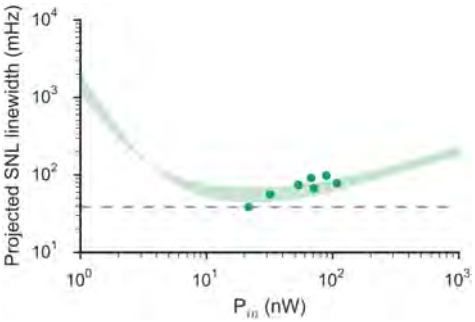

Figure 5.10: The projected shut-noise-limited linewidth of the Sr-stabilized laser. The dots are calculated values based on measured NICE-OHMS-slopes. The shaded area indicates uncertainties based on fluctuation in atom temperature and atom number as measured in the experiment. The figure is taken from [25].

same time, a higher power will increase the power-broadening thus increasing the spectral width of the atomic line. Because of this, there is an optimal power giving the optimal stabilization. Figure 5.10 shows the projected shut-noise-limited cavity input power as described in [25].

Furthermore, the signal is dependent on the number of atoms, the temperature of the atoms, and the finesse of the interrogation cavity. A detailed investigation of the signal dynamics is presented in [25]. Here, it is concluded that, assuming shut-noise-limited detection, the achievable noise floor of the stabilized frequency will result in a minimum laser linewidth of $\Delta\nu \approx 40$ mHz, also indicated on figure 5.10.

Experiment Cycle

The locking sequence operates in a cyclic manner as illustrated in figure 5.11. First, the atoms are trapped and cooled in an MOT. The MOT-beams are then turned off before the NICE-OHMS signal is recorded. This is done to avoid AC-Stark shift of the clock transition due to the high intensity MOT-beams. After the MOT-beams are turned off, a short delay of 50 µs ensures that the afterglow from the AOM is insignificant. The NICE-OHMS signal is then recorded over a period of 1 ms. The correction to the laser frequency is calculated and the frequency of the frequency generator, driving AOM1, is changed accordingly. The MOT-beams are turned on again, and the atoms are cooled and recaptured for a period of 200 ms. The total cycle time is 201.05 ms.

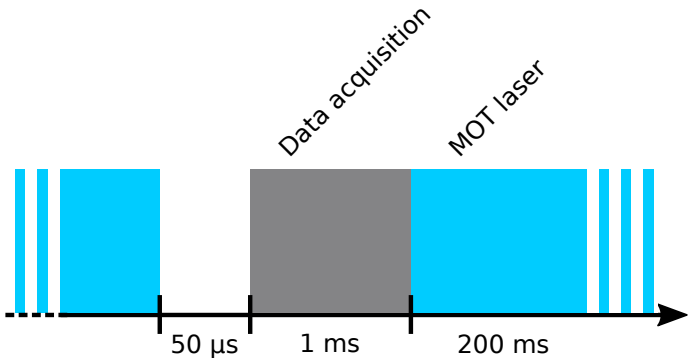

Figure 5.11: The locking cycle for the Strontium-referenced laser. The blue area shows when the MOT-laser-beams are turned on. The gray area shows the timing of the NICE-OHMS measurement.

This cycle time was chosen based on optimization of the feedback-loop. A cycle time as low as 10 ms is possible and may be preferable if the noise of the error-signal can be reduced.

Stability analysis

The center part of the NICE-OHMS signal was recorded prior to locking. The frequency of the clock laser was scanned with a stepsize of ≈ 6.5 kHz for each cycle. The resulting signal is shown in figure 5.12. The slope of the center region is 1 mV/kHz. Fitting a straight line to the center region gives residuals between the points and the fit with a standard deviation of 2.0 mV, giving an SNR of approximately 115. The primary noise source is believed to be intensity fluctuations of the MOT-beams causing a shot-to-shot variation in the atom number and the temperature of the atoms.

During locking, the error-signal is recorded and used as an in-loop evaluation of the frequency stability. Figure 5.13 shows the evolution of the laser frequency detuning $\delta\nu = \nu - \nu_0$ where ν is the laser frequency and ν_0 is the atomic resonance frequency. The standard deviation of this data is 1.19 kHz.

An overlapping Allan deviation of the data is shown in figure 5.14. The achieved stability is 880 Hz τ^{-1} averaging down until $\tau = 100$ s with a minimum linewidth of 3.2 Hz at 2000 s. The overlapping Allan deviation follows a τ^{-1}-slope up to a τ of 100 s. This indicates that the laser frequency is dominated by either white phase-noise or flicker phase-noise. To determine whether it is white or flicker phase-noise, a modified Allan deviation is also calculated (figure 5.15). This shows a stability of 495 Hz τ^{-1} averaging down until $\tau = 100$ s with a minimum of 2.9 Hz at 1000 s. As the slope of the modified Alan deviation also follows a τ^{-1}-slope, the dominating noise is flicker phase-noise.

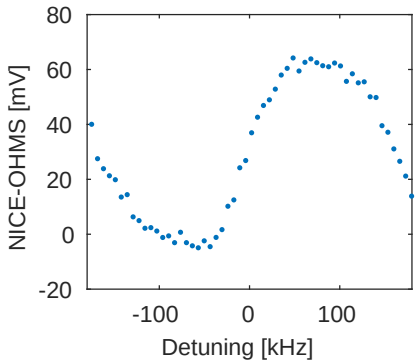

Figure 5.12: The NICE-OHMS-signal used for laser stabilization on Sr. The standard deviation of the signal noise in the center region is 2.0 mV, and the signal-slope is 1.0 mV/kHz.

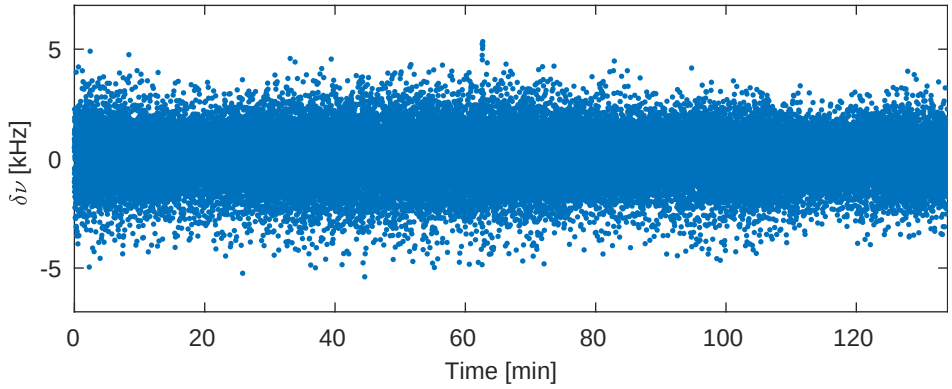

Figure 5.13: In-loop frequency measurement of the Strontium referenced laser using NICE-OHMS.

The dominating noise source in this measurement is believed to be electronic noise in the NICE-OHMS signal. From the Allan deviation of the pre-stabilized clock laser (figure 5.7), we know that the stability at $\tau = 1$ s is 9 Hz. The achieved signal-to-noise on the NICE-OHMS-signal does not allow for improvement of the laser's frequency at short time scales. It is not possible to accurately determine the long-term stability of a system using an in-loop measurements, and effect causing frequency drift, similar to what is seen in the acetylene reference (section 3.5), can not be detected. In order to get a full characterization of the stabilized laser's frequency noise, a stable and independent reference laser is needed.

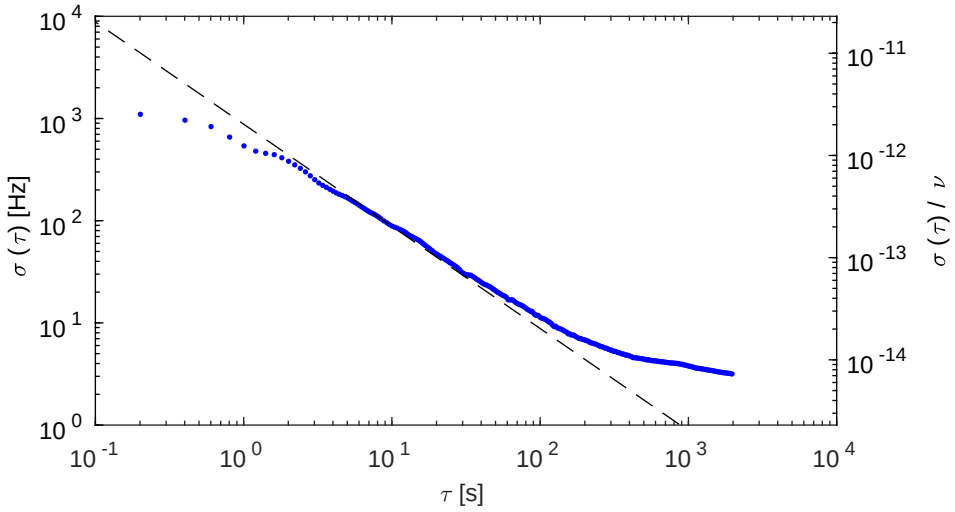

Figure 5.14: An overlapping Allan deviation of the Strontium referenced laser using NICE-OHMS. Them dashed lines indicate 880 Hz/τ. It reaches a minimum of 3.2 Hz at 2000 s.

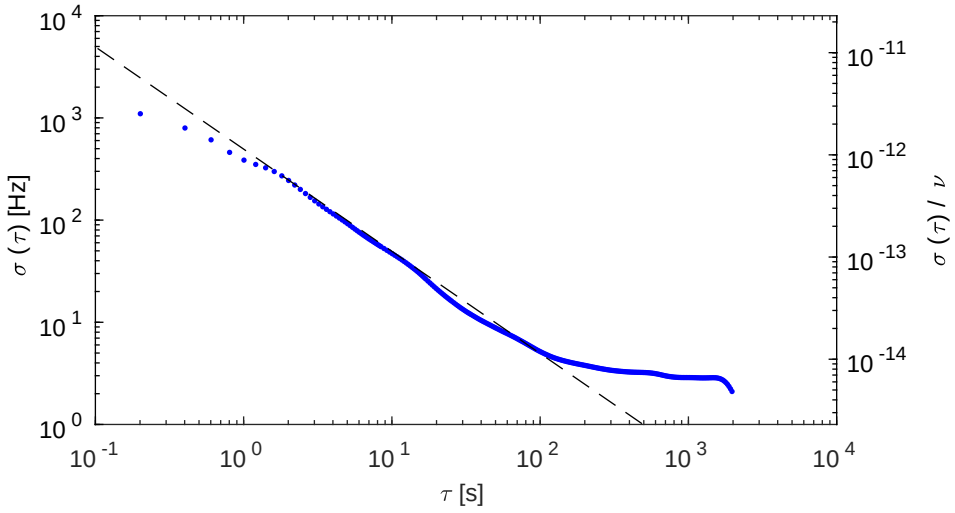

Figure 5.15: A modified Allan deviation of Strontium referenced laser using NICE-OHMS. The dashed lines indicate 495 Hz/τ. It reaches a minimum of 2.9 Hz at 1000 s.

5.3 Outlook

Clock Laser

After the data presented here was recorded, the clock laser was optimized. A new low-noise DDS frequency generator for the PDH-modulator was implemented. The diode in the ECDL was replaced, and the diode current controller was swapped out with a new low-noise diode current controller. This resulted in an improvement of the PDH signal-to-noise ratio, and the feedback bandwidth was increased by almost a factor of 2.

New Reference Laser

Recently, equipment for a stable reference laser system has been acquired. This includes a highly stable, ULE based, high finesse cavity from Stable Laser Systems together with an ECDL from MOGLabs. We hope to achieve a sub-Hz linewidth at 1 s with this new system.

This laser will act as a reference in future measurement in the Sr experiments. Primarily, the spectral properties of the Sr superradiance will be characterized.

NICE-OHMS

The instability extrapolated from the in-loop measurement of the Sr NICE-OHMS stabilization is much higher than the instability of the clock laser. This indicates that the noise of the NICE-OHMS signal dominates, and that we only improve stability at long timescales.

The signal-to-noise of the NICE-OHMS-signal is expected to be improved with the implementation of a DDS-system for the phase modulation. The fluctuations of the atom number in the cavity mode also contribute to noise in the NICE-OHMS-signal. These fluctuations are a result of unstable optical power in the blue MOT-light. A new laser system for 461 nm MOT-light has already been acquired and will be implemented.

6 Conclusions and Summary

Here follows a short summary of the conclusions of the work with the acetylene frequency reference, the micro-resonator Kerr frequency combs, and the strontium optical clock.

The NICE-OHMS technique does indeed combine the advantages of cavity-enhanced spectroscopy with those of heterodyne frequency modulation spectroscopy. In both the acetylene setup and the strontium setup impressive spectroscopy signals were obtained in regard to both the signal-to-noise ratio and the signal bandwidth. These two parameters are *the* figure-of-merit for spectroscopy in absolute frequency references. There are, however, challenges as well. Significant problems with a varying off-set voltage of these spectroscopy signals have shown to be the limitation of the frequency stability at time scales larger than half a second.

The combination of optical frequency references and optical frequency combs in an affordable and compact package will be revolutionary for a broad area of industry and research. Micro-resonator Kerr frequency combs will most likely play an important roll here. The research area of Kerr frequency combs has seen a lot progress with impressive results over the last few years. The AlGaAs material have, however, not yet been able to prove its worth, and a lot of work still needs to done. If the fabrication process can be improved to produce resonators with higher Q-values, and non-linear losses can be mitigated, AlGaAs might still prove worthy of attention.

6.1 Acetylene Frequency References

Three optical frequency references, stabilized purely to the ro-vibrational P(16) $\nu_1 + \nu_3$ line in acetylene have been built. The references are based on cavity-enhanced saturated spectroscopy where the NICE-OHMS technique is used as the spectroscopic tool for generating an error-signal for laser frequency stabilization. The error-signal's signal-to-noise ratio is estimated to be ≥ 40.6 dB with a signal bandwidth of 2 MHz.

Of the three acetylene gas cell, the two with the lowest amount of pressure-broadening are chosen for the analysis of the setups. In these analyses different broadening effects are characterized including pressure-broadening, optical power-broadening, and transit-time-broadening. Pressure-broadening is found to be the dominating broadening effect with a pressure-broadened linewidth of 567 $\pm$ 19 kHz of acetylene 2 and 476 $\pm$ 21 kHz of acetylene 3. Through the use of a large waist cavity configuration, interrogation beam width radii of

0.7 mm, 1.3 mm, and 3.0 mm are investigated. Given the amount of pressure-broadening, the configuration with a beam width radius of 0.7 mm is found to be the best choice with a transit-time-broadening of 99 kHz. Based on the measured linewidths and saturation powers, the optical power in the cavity yielding the optimum error-signal slope, was found.

A PI^{2}D servo-controller is used for applying feedback on both an AOM and a peizo-electric element in the laser. The feedback-loop shows a combined system bandwidth of 360 kHz of acetylene 2 and 370 kHz of acetylene 3. The frequency stability between acetylene 2 and acetylene 3 is measured, and an overlapping Allan deviation is calculated (figure 3.20). This Allan deviation shows a frequency stability of 12 Hz/$\tau^{-1/2}$ reaching the flicker noise floor of 25 Hz at $\tau = 0.2$ s. The frequency stability is believed to be limited by modulation instability primarily caused by etalon effects in the setup. Optical power fluctuations, caused by polarization variations created in the system's optical fibers, are also believed to influence the stability.

As isotope-pure, carbon-13 acetylene has become a scarce commodity, the possibilities of using carbon-12 acetylene is investigated. In the case of $^{12}C_2H_2$ the P(11)$\nu_1 + \nu_3$ line at 1531.59 nm is the line best suited for frequency stabilization based on linestrength and broadening effects. When comparing the two linestrengths, the error-signal slope of the $^{12}C_2H_2$ P(11)$\nu_1 + \nu_3$ line should be a factor of 2 greater than the $^{13}C_2H_2$ P(16)$\nu_1 + \nu_3$ line.

6.2 Micro-Resonator Kerr Frequency Combs

AlGaAs is a promising material with some appealing properties for Kerr comb generation. There are still challenges in achieving stable Kerr combs in the AlGaAs resonators. The solutions to these challenges is believed to be found in the chip fabrication processes. As this is outside the scope of this work, the focus here have been on the resonator design specifically targeting dispersion and single-mode operation.

A micro-resonator design including tapered waveguides gives a high degree of adaptability of dispersion engineering. At the same time it allows for much more flexibility in the dispersion design while ensuring a single-mode resonator. Using a tapered waveguide resonator design, a high degree of anomalous dispersion has been presented in single-mode resonators. Based on the single chip analyzed in this work, it is difficult to draw final conclusion. We can, however, state three observations: (1) there is a clear tendency of the measured dispersion being significantly larger than the design dispersion, (2) there is no evidence that the tapers have any effect on the resonator Q-value, and (3) single-mode resonators can be obtained without restricting the resonator dispersion. In the near future the tapered resonator design will be applied to other material platforms, namely SiC and a-Si:D.

High accuracy dispersion measurement of micro-resonators typically uses

a highly expensive or complex frequency comb as a reference. Here, we have presented a simple and low-cost setup for dispersion measurement of high FSR resonators, based on a low FSR reference cavity. The measurements done using this setup show close to the same spectral resolution and noise level as measurements done using commercial fiber-based frequency combs.

A number of frequency comb stabilization schemes are described. These will be applied and characterized once a stable comb is obtained. The combination of the micro-resonator combs and the acetylene frequency reference gives the possibility of a highly stable and compact frequency comb. This will allow for microwave generation with record high stability and possibly provide fiber-based telecommunication with a record high energy efficiency, among other outcomes.

6.3 Strontium Atomic Clock

In the strontium experiment the NICE-OHMS technique is used in a cyclic manner on an ensemble of Sr-atoms with a temperature of approximately 5 mK. This have been shown to produce a signal suitable for use as an error-signal for laser frequency stabilization. Here we have presented a proof-of-principle experiment where a laser was locked to the $^1S_0 \leftrightarrow {}^3P_1$ transition in ^{88}Sr using the NICE-OHMS technique. A low cycle time of down to 10 ms was achieved, moving atomic spectroscopic for clocks to a new regime. The error-signal produced has a signal-to-noise ratio of 115.

The stability reported here is not impressive. We have, however, shown the possibility and the strength of the method. Later work have concluded a projected shot-noise limited linewidth of a laser stabilized in this way to be ≈ 40 mHz [25]. Furthermore, two separate projects are currently underway to produce a continuous beam of cold strontium atoms allowing for continuous interrogation. These projects also aim at continuous superradiance on the narrow strontium transition.

Acetylene Technical Drawings

A

A.1 Enclosure

The technical drawing of the airtight aluminium box in which the free-space optics for the acetylene stabilized laser is placed.

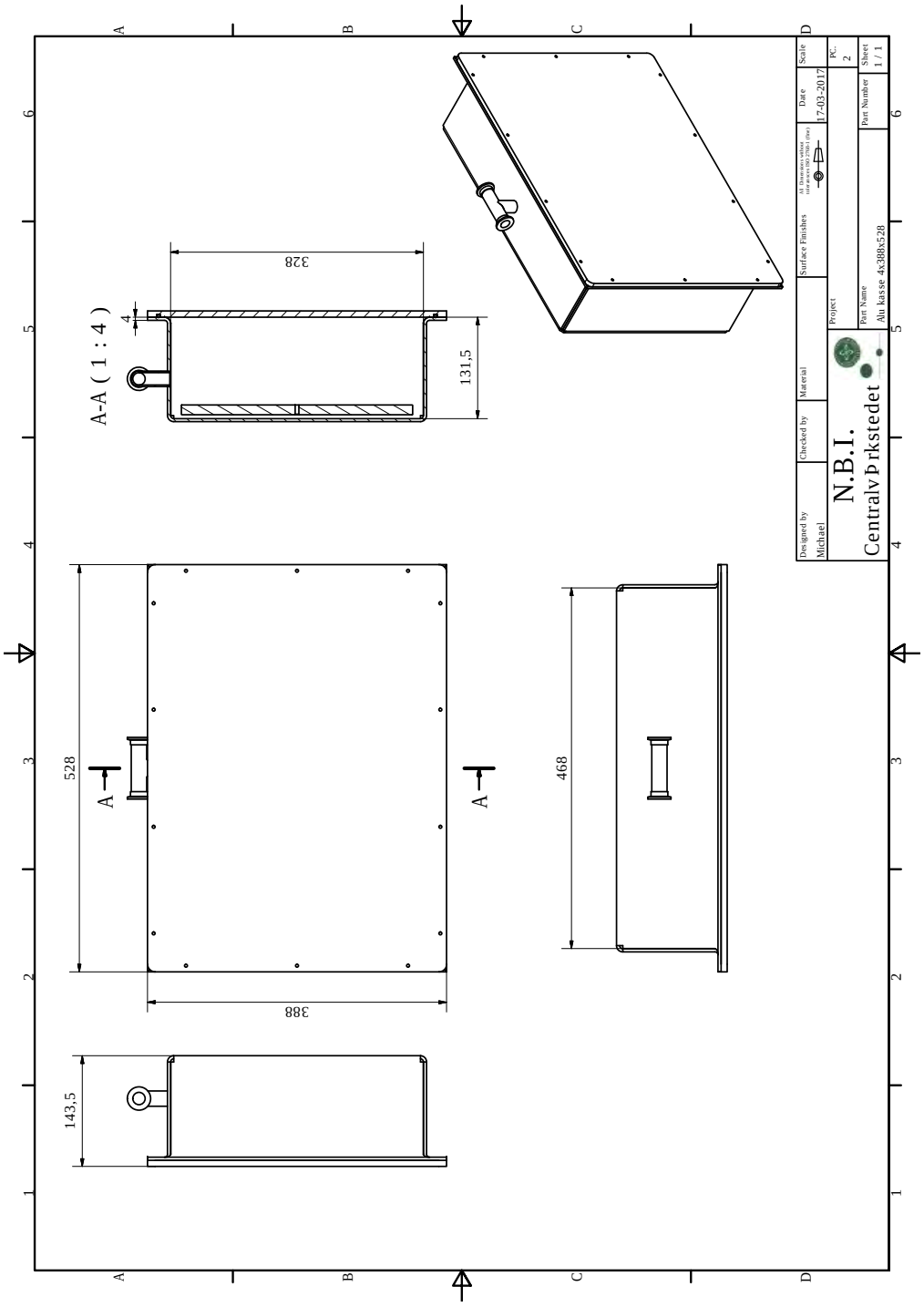
A-A (1 : 4)
328
4
131,5
528
388
143,5
468
A
A
N.B.I.
Centralværkstedet
Designed by
Michael
Checked by
Material
Surface Finishes
Project
Part Name
Alu kasse 4x388x528
Part Number
Date
17-03-2017
Scale
PC.
2
Sheet
1 / 1

A.2 Glass Cell

The technical drawing of the acetylene glass cell.

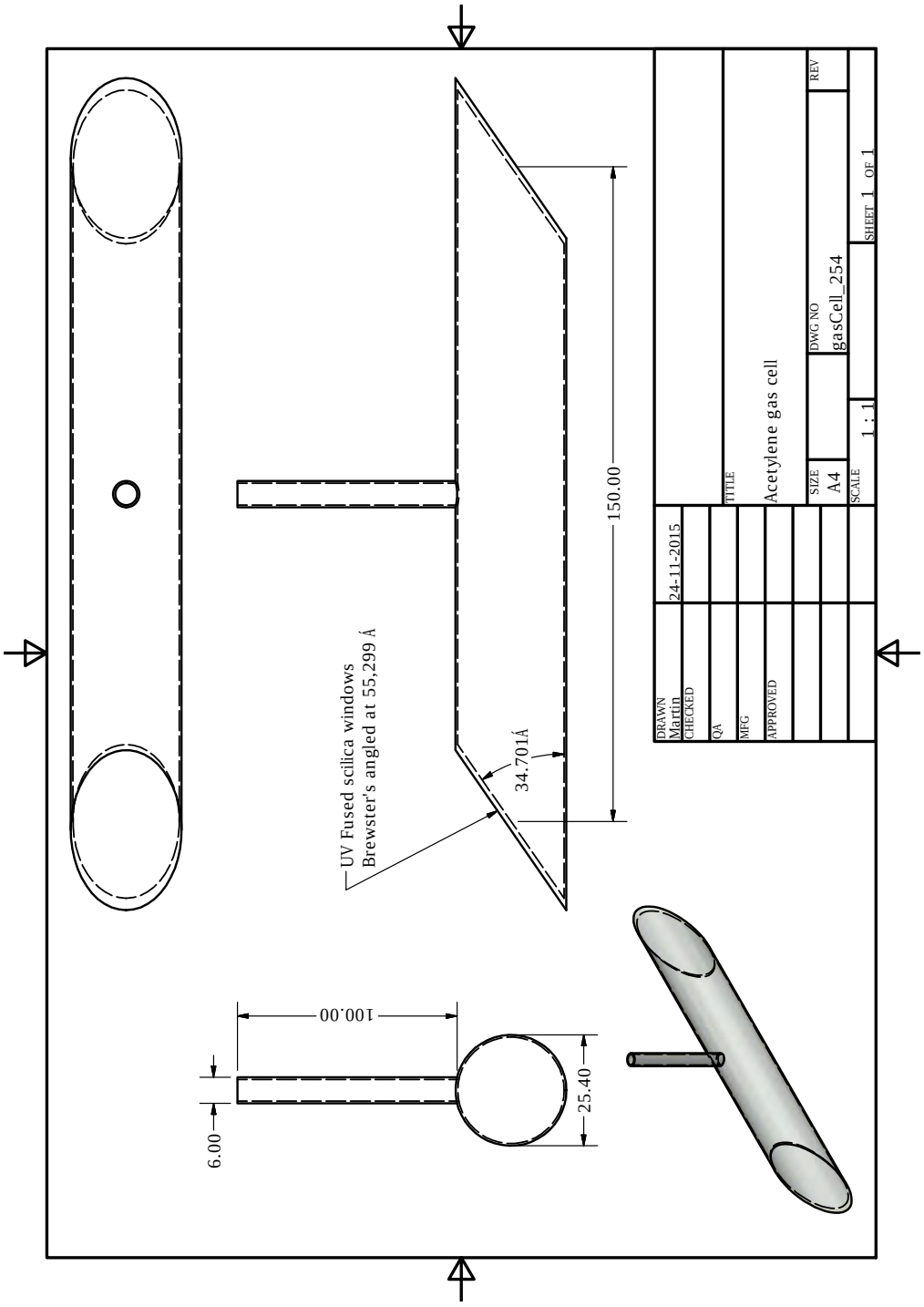
UV Fused scilica windows
Brewster's angled at 55,299 Á
34.701Á
150.00
100.00
25.40
6.00
DRAWN Martin
CHECKED
QA
MFG
APPROVED
24-11-2015
TITLE
Acetylene gas cell
SIZE A4
DWG NO gasCell_254
REV
SCALE 1 : 1
SHEET 1 OF 1

B

Micro Ring Resonators

B.1 Dispersion Measurements

Dispersion measurements of chip CG49.

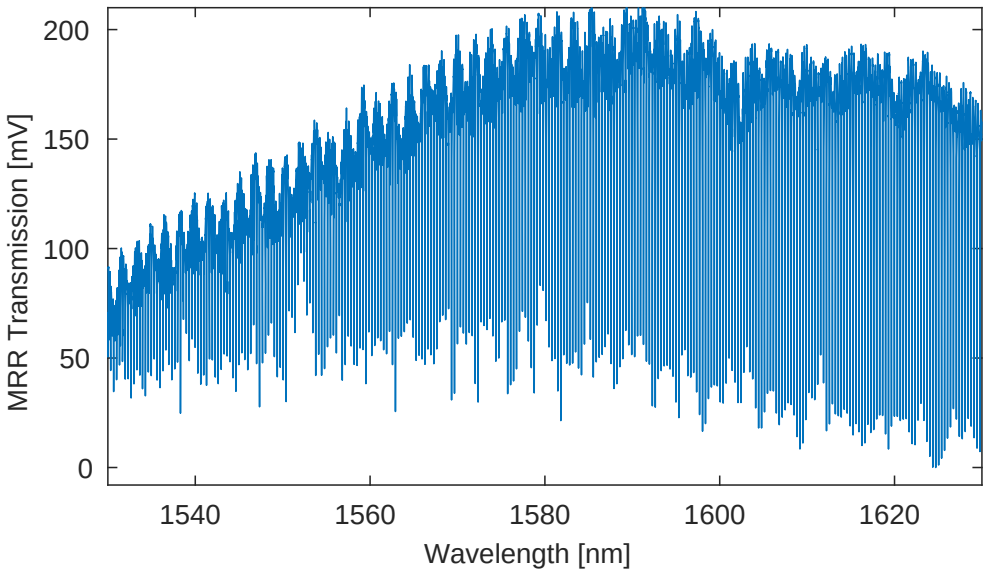

Figure B.1: Transmission spectrum of MRR number 75.

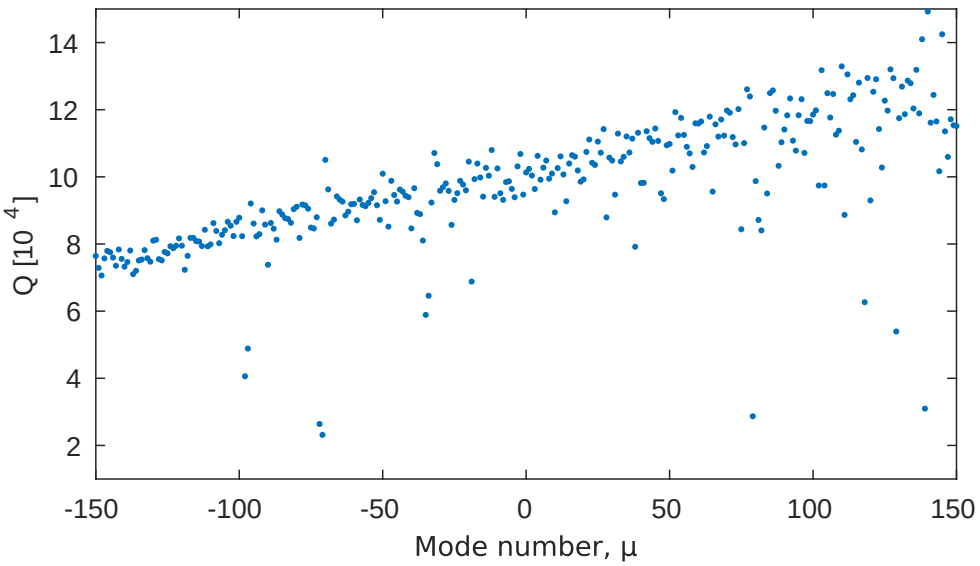

Figure B.2: Q-values of the modes in MRR number 75.

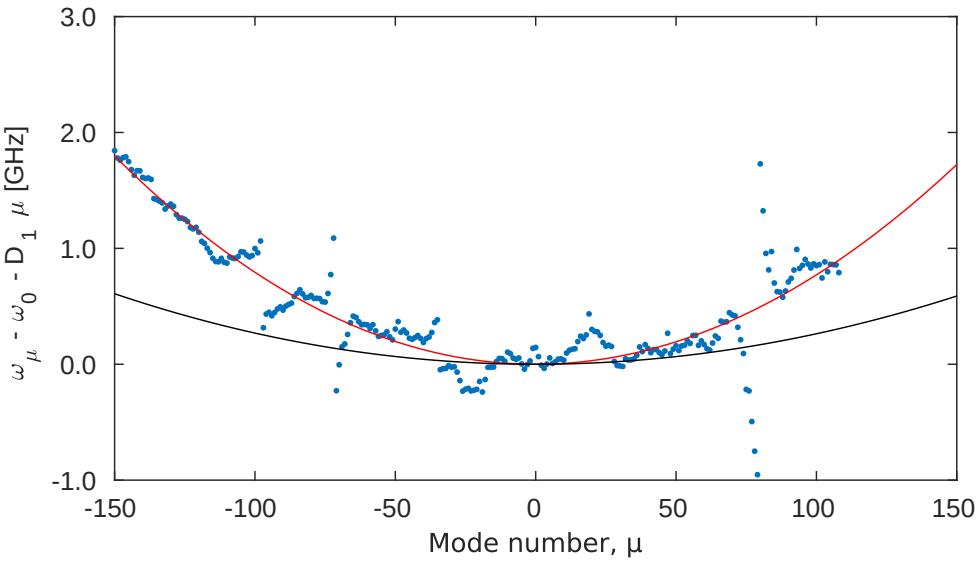

Figure B.3: Mode structure of MRR number 75.

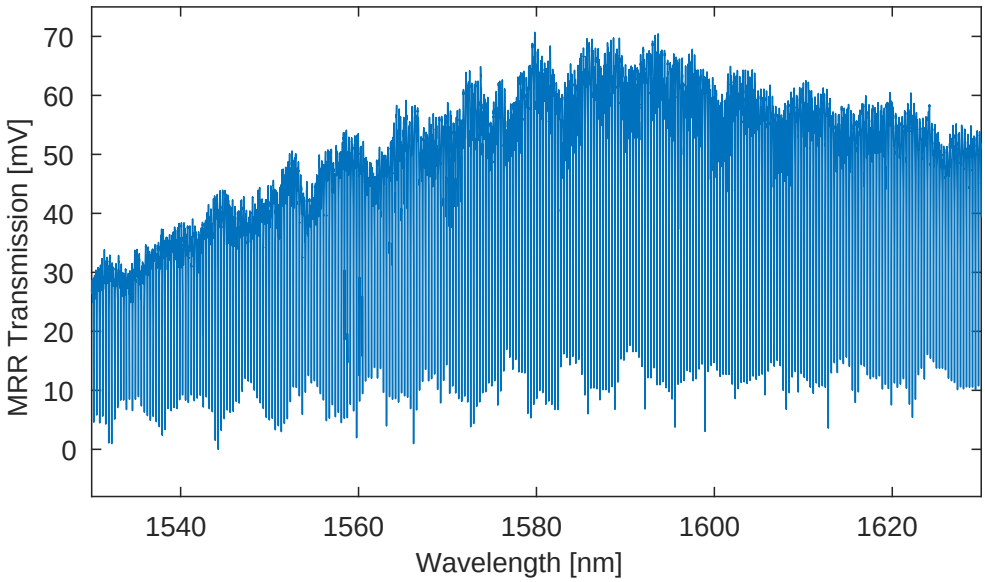

Figure B.4: Transmission spectrum of MRR number 79.

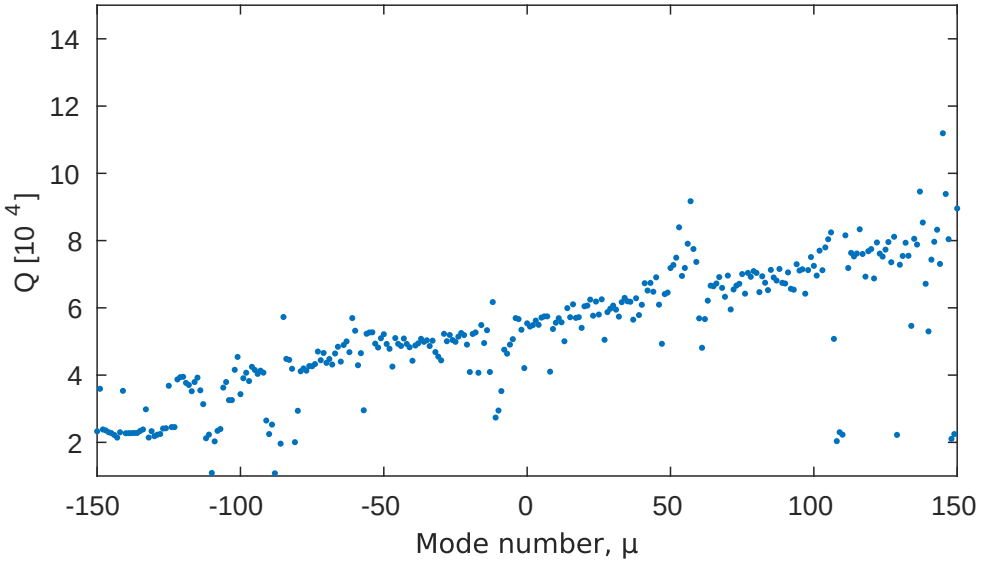

Figure B.5: Q-values of the modes in MRR number 79.

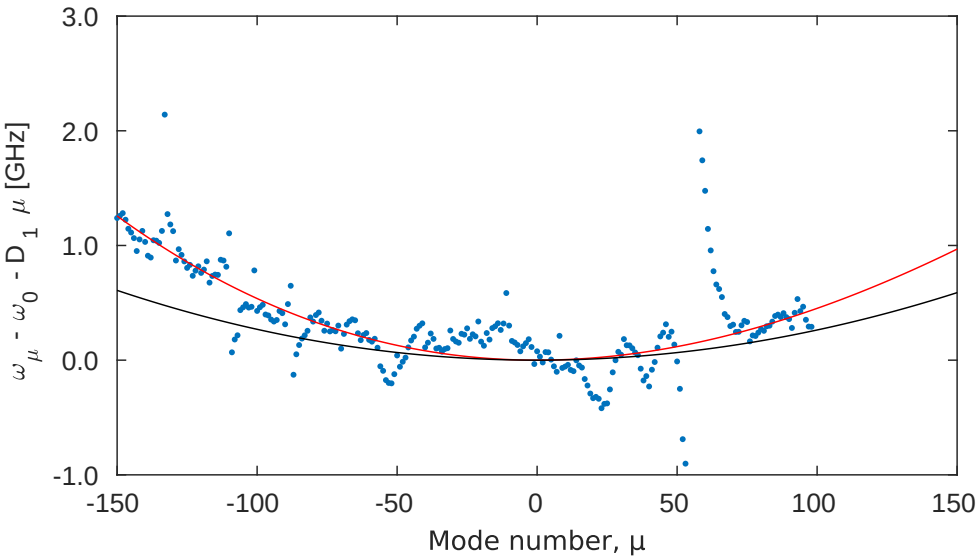

Figure B.6: Mode structure of MRR number 79.

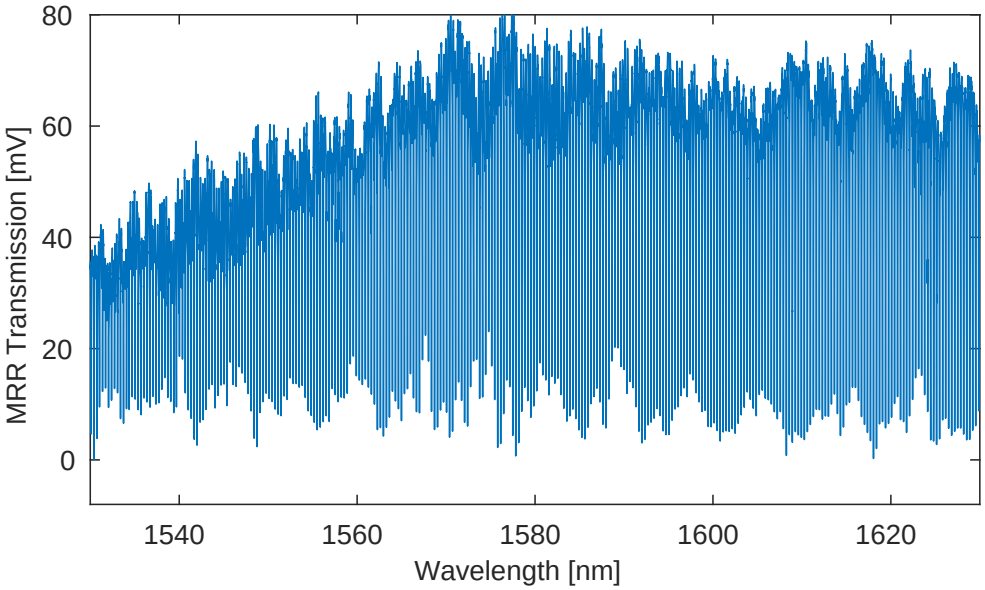

Figure B.7: Transmission spectrum of MRR number 80.

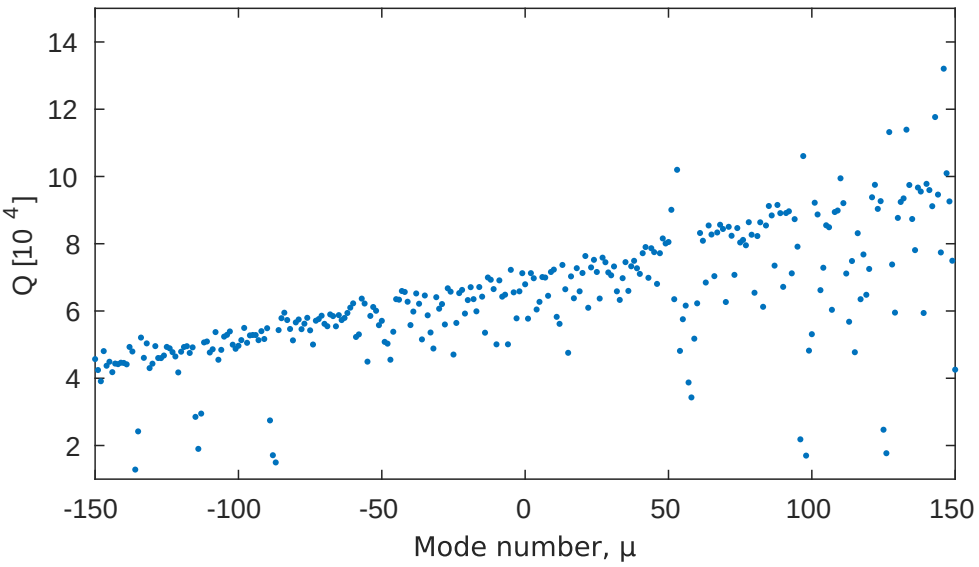

Figure B.8: Q-values of the modes in MRR number 80.

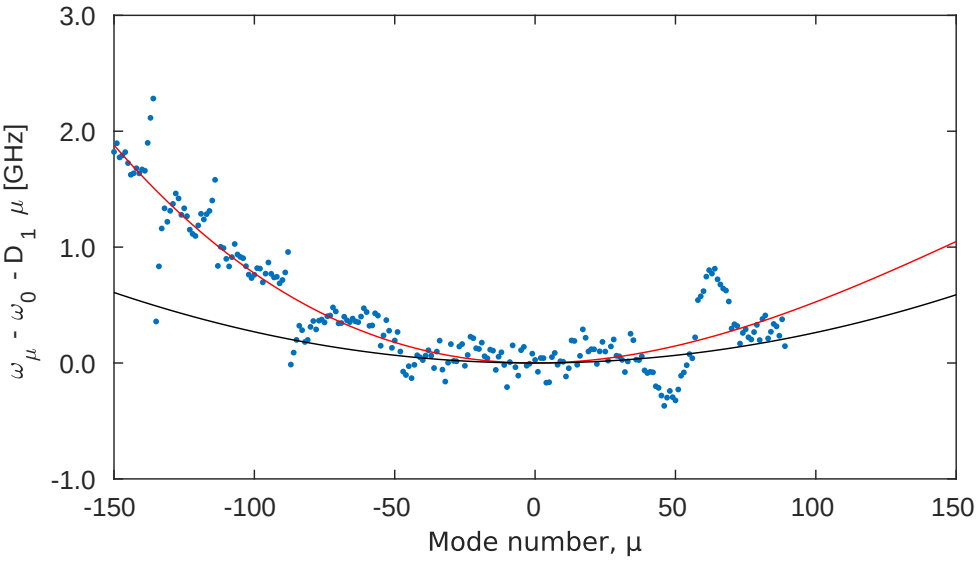

Figure B.9: Mode structure of MRR number 80.

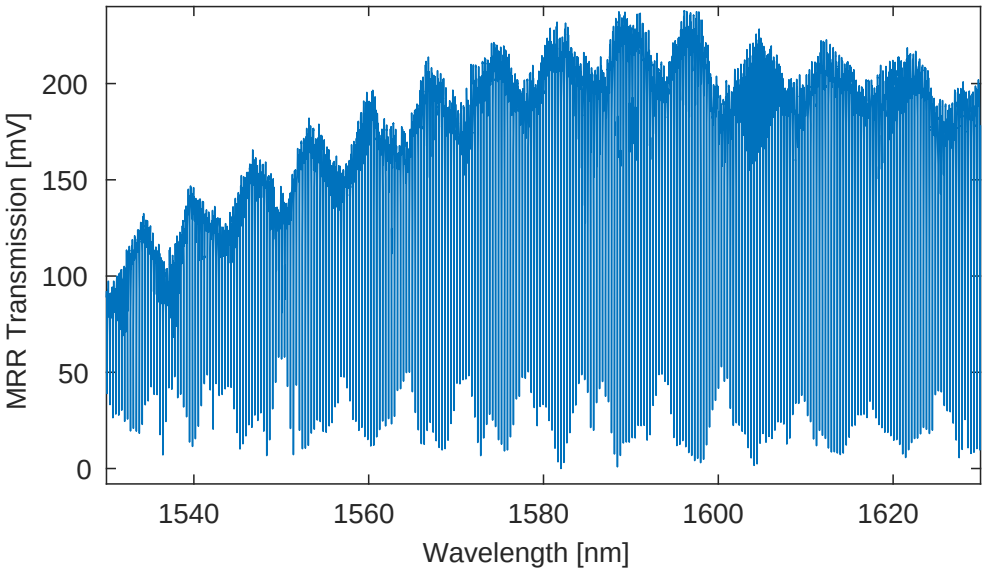

Figure B.10: Transmission spectrum of MRR number 85.

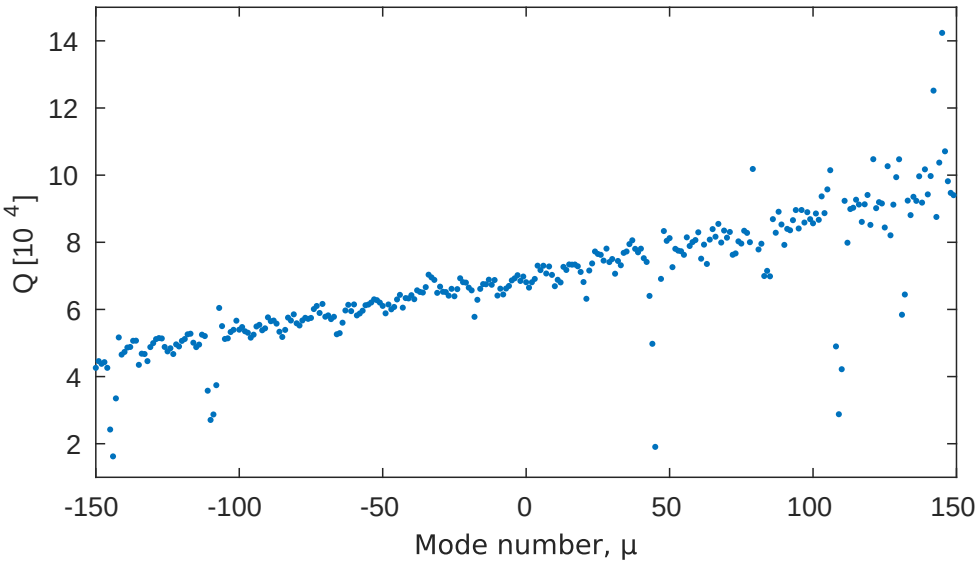

Figure B.11: Q-values of the modes in MRR number 85.

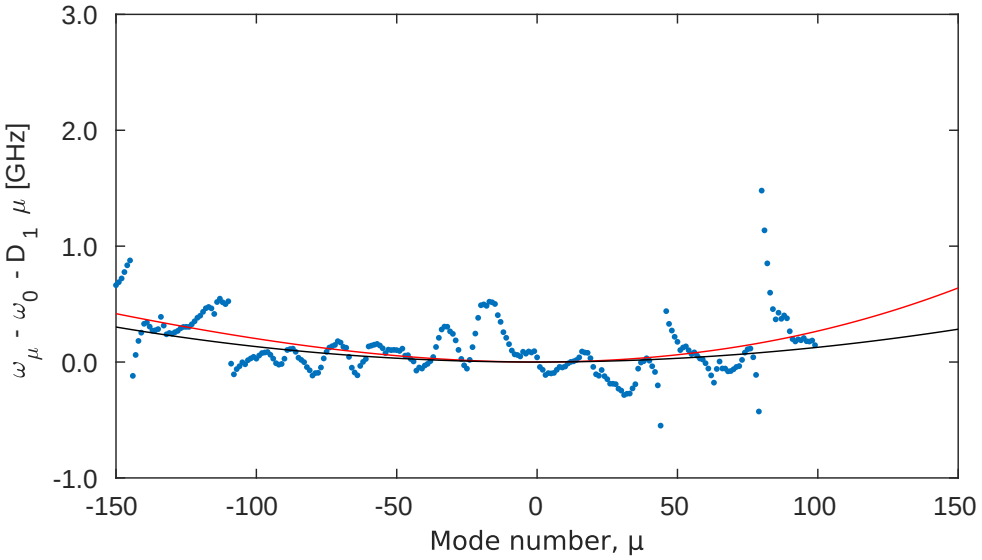

Figure B.12: Mode structure of MRR number 85.

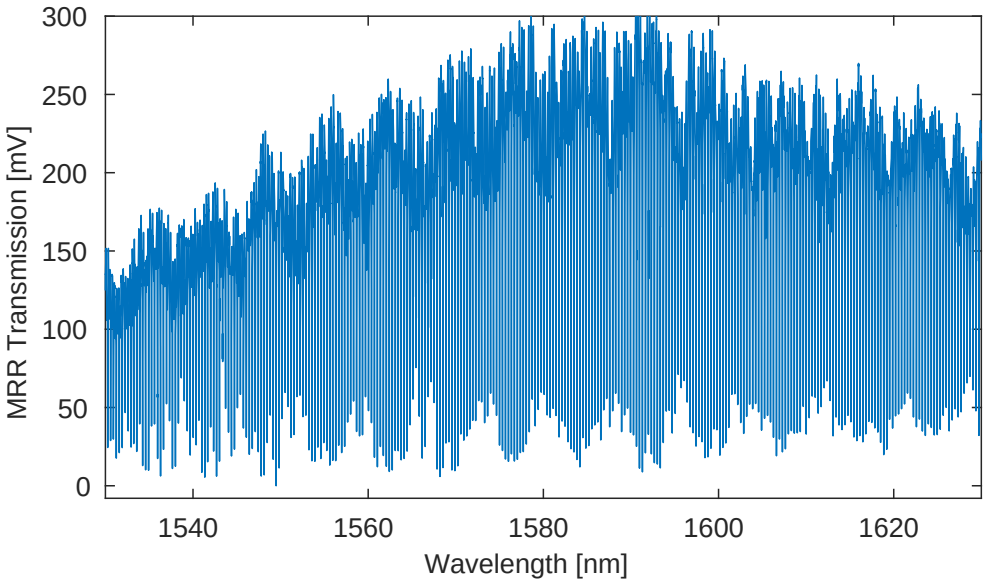

Figure B.13: Transmission spectrum of MRR number 90.

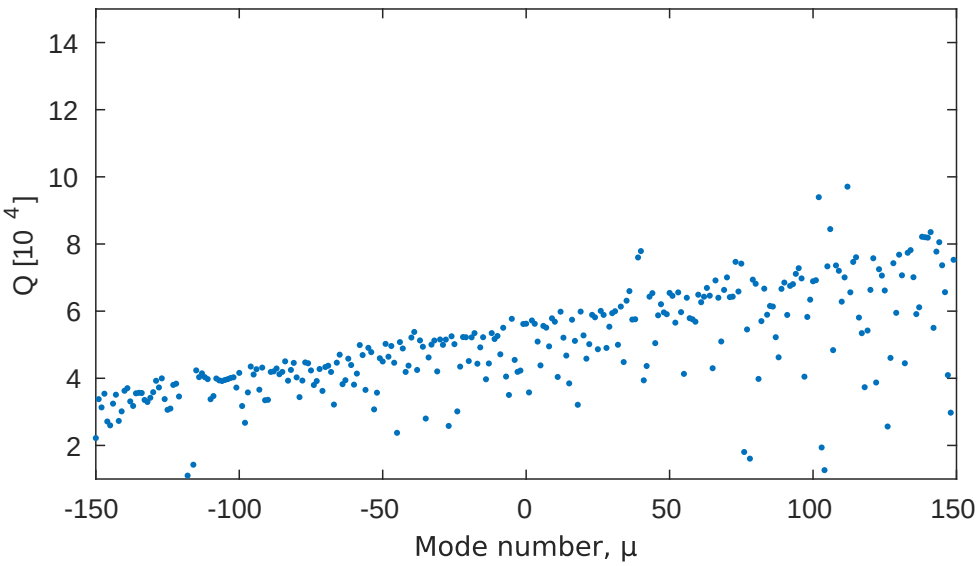

Figure B.14: Q-values of the modes in MRR number 90.

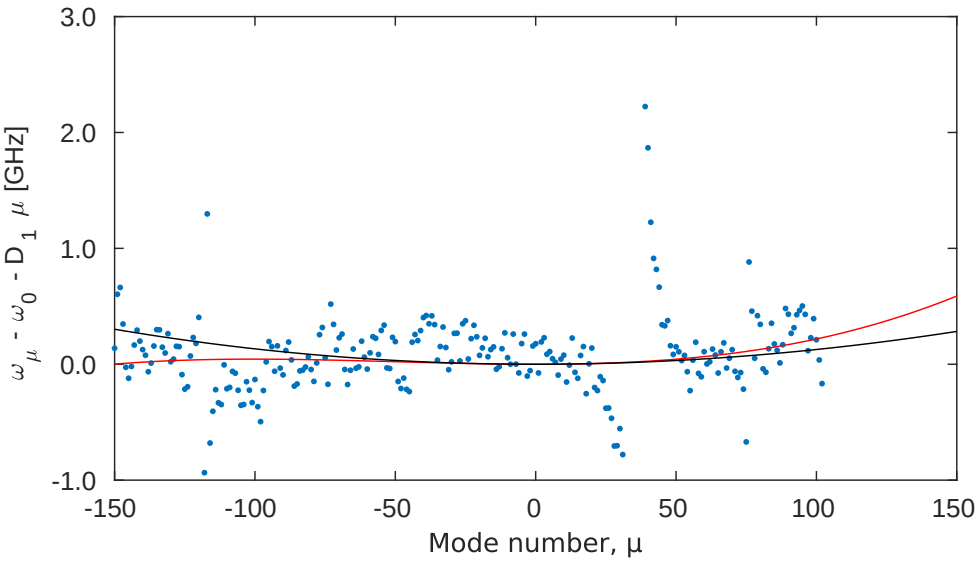

Figure B.15: Mode structure of MRR number 90.

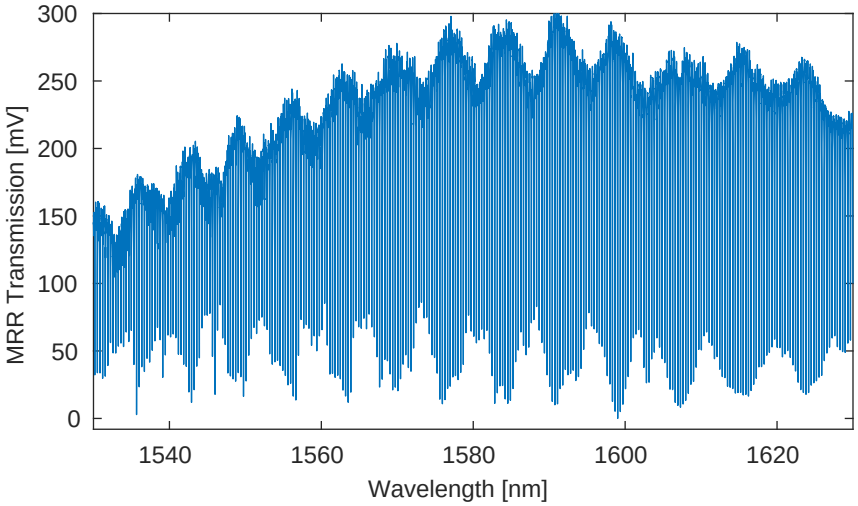

Figure B.16: Transmission spectrum of MRR number 95.

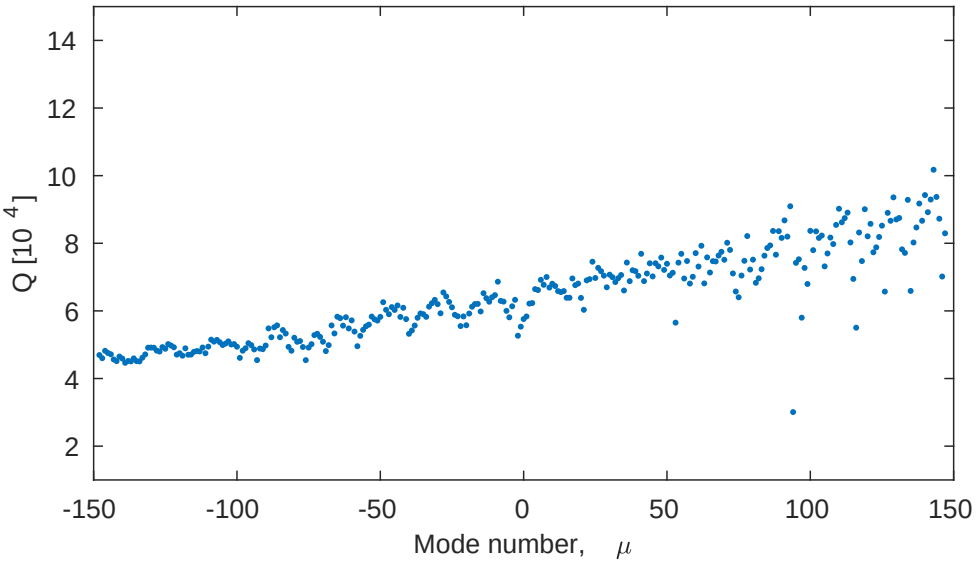

Figure B.17: Q-values of the modes in MRR number 95.

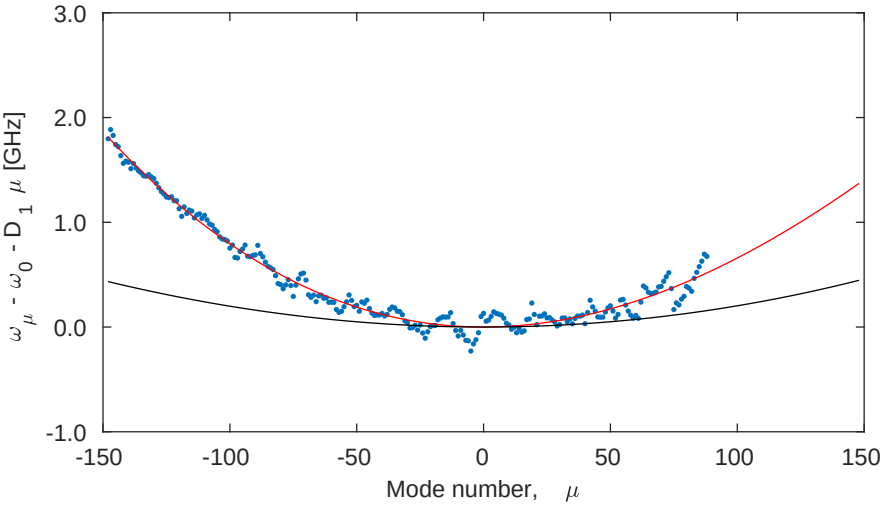

Figure B.18: Mode structure of MRR number 95.

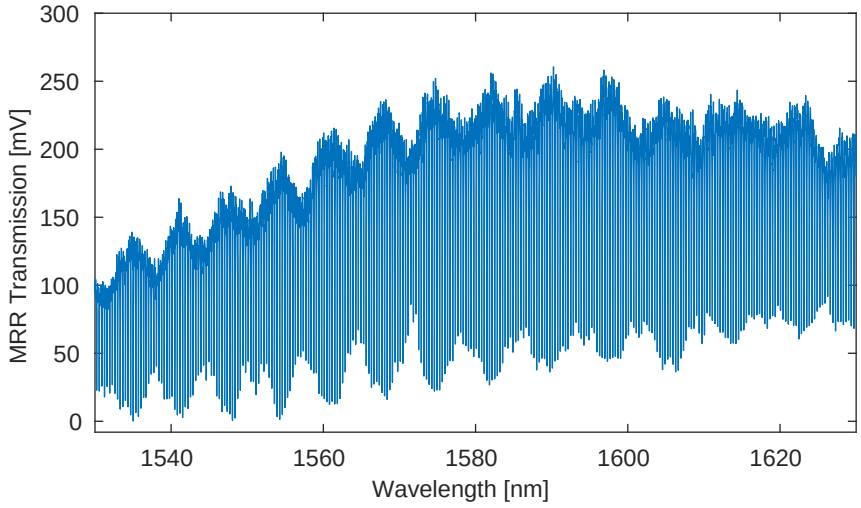

Figure B.19: Transmission spectrum of MRR number 98.

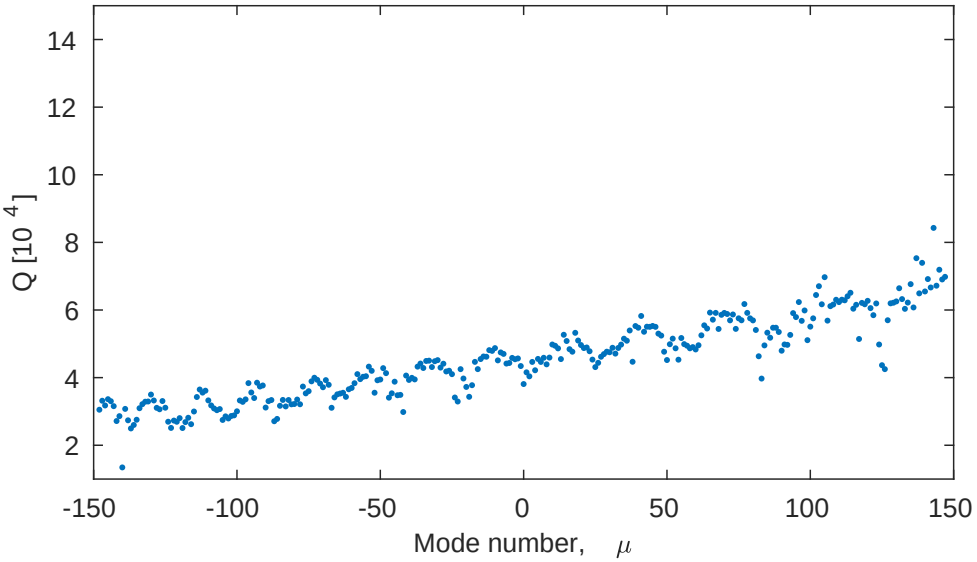

Figure B.20: Q-values of the modes in MRR number 98.

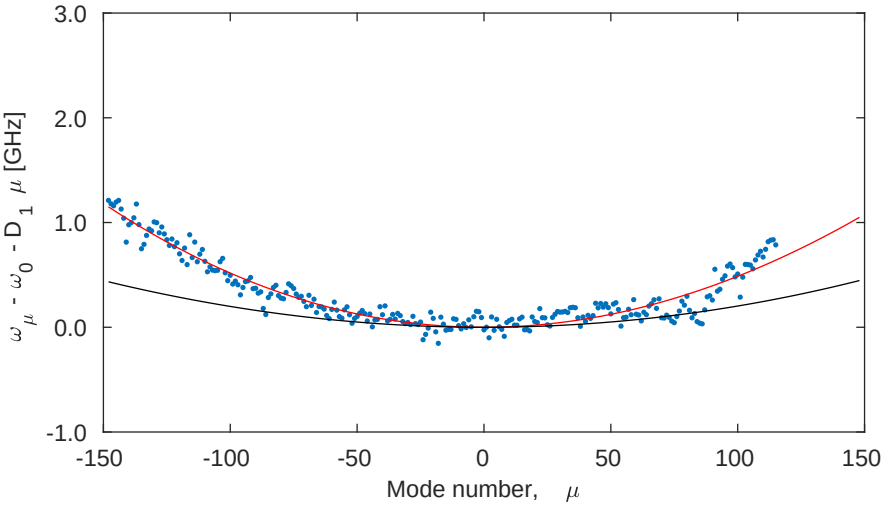

Figure B.21: Mode structure of MRR number 98.

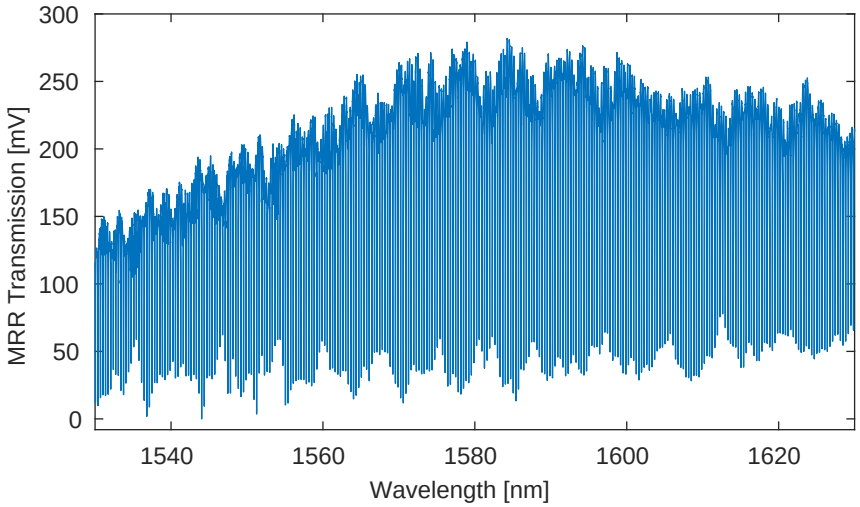

Figure B.22: Transmission spectrum of MRR number 99.

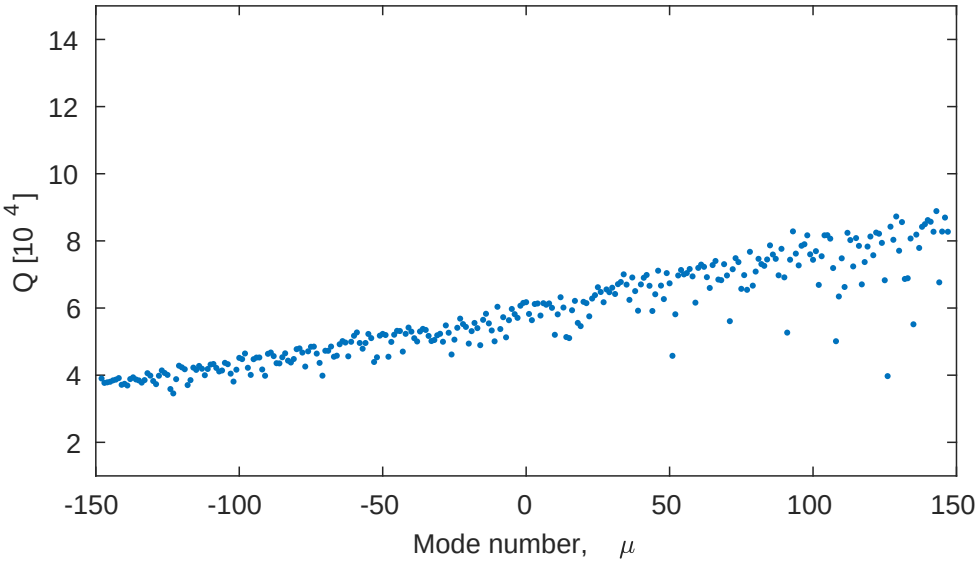

Figure B.23: Q-values of the modes in MRR number 99.

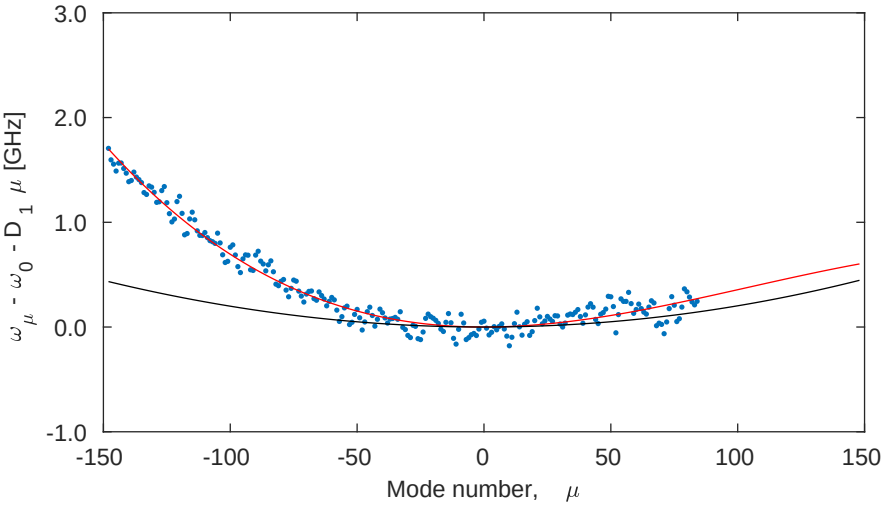

Figure B.24: Mode structure of MRR number 99.

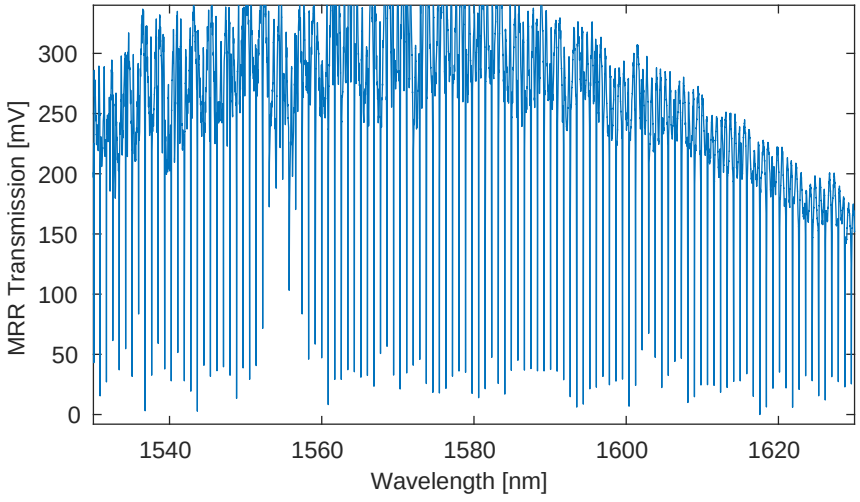

Figure B.25: Transmission spectrum of MRR number 115.

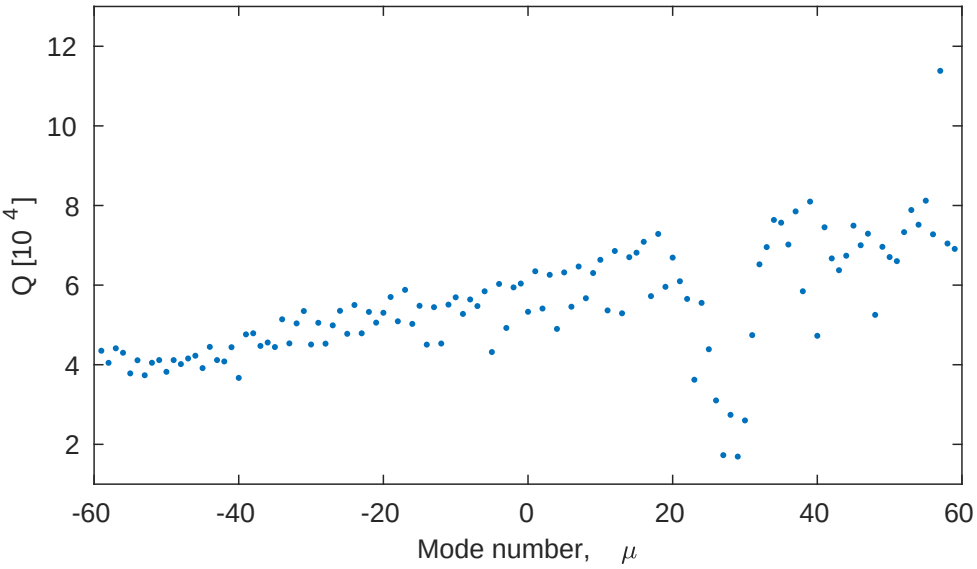

Figure B.26: Q-values of the modes in MRR number 115.

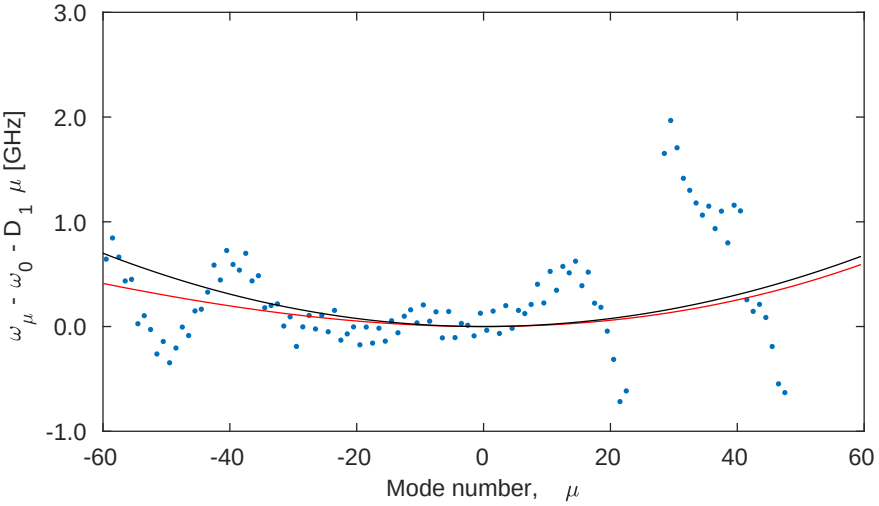

Figure B.27: Mode structure of MRR number 115.

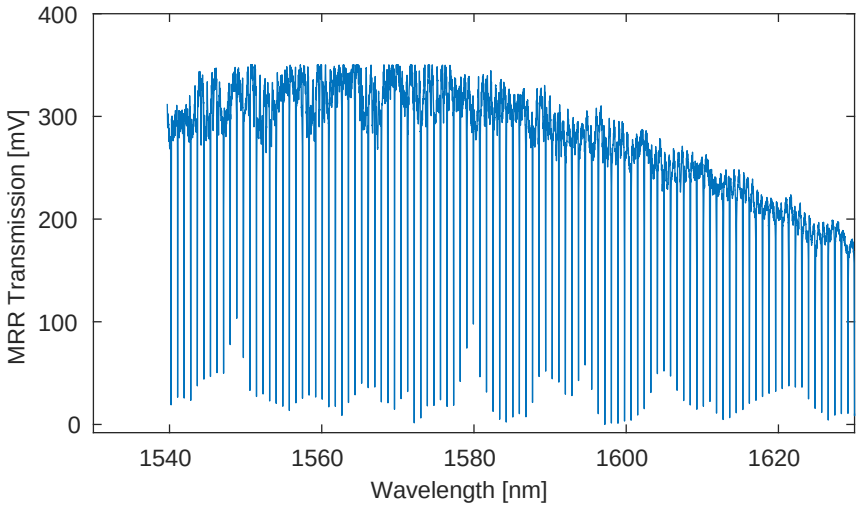

Figure B.28: Transmission spectrum of MRR number 124.

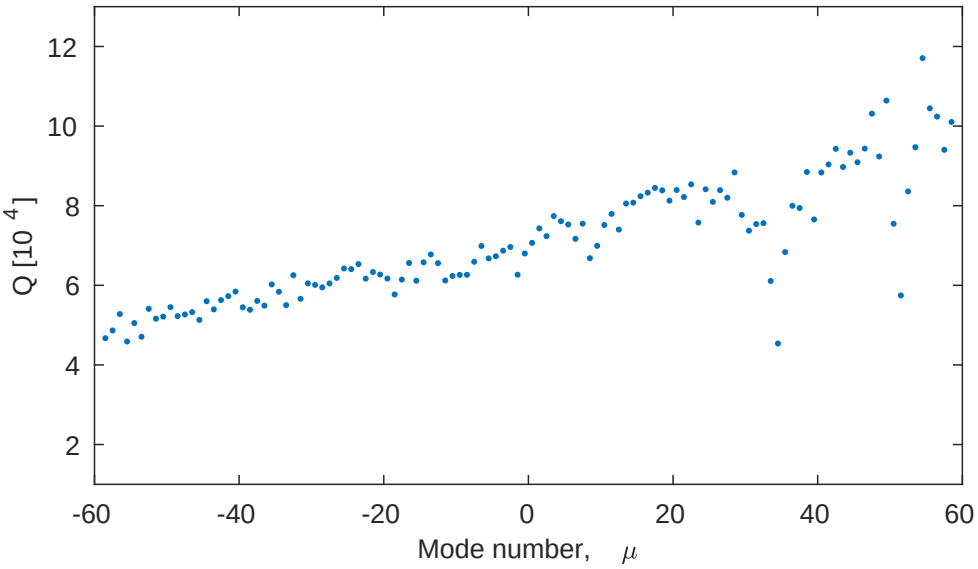

Figure B.29: Q-values of the modes in MRR number 124.

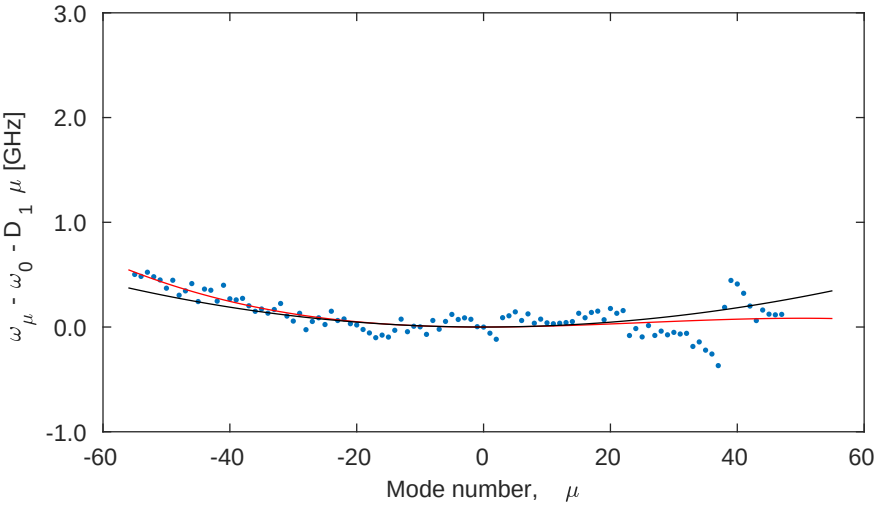

Figure B.30: Mode structure of MRR number 124.

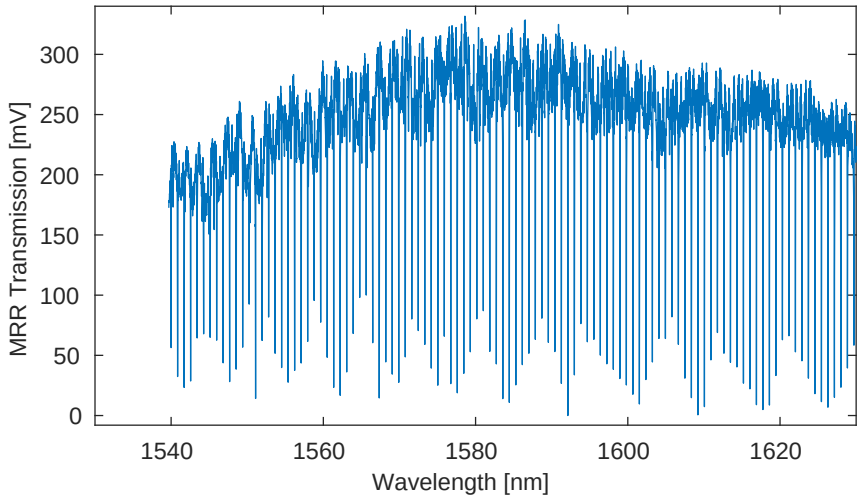

Figure B.31: Transmission spectrum of MRR number 142.

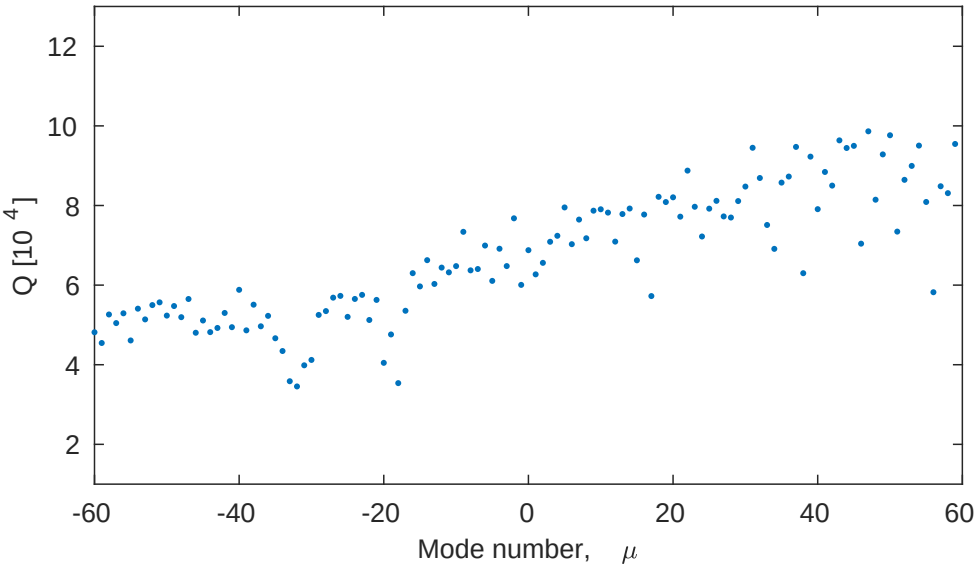

Figure B.32: Q-values of the modes in MRR number 142.

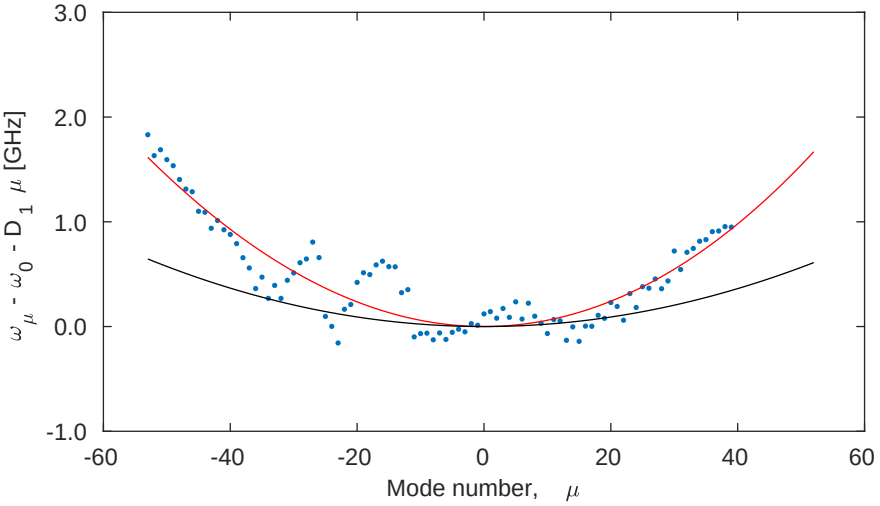

Figure B.33: Mode structure of MRR number 142.

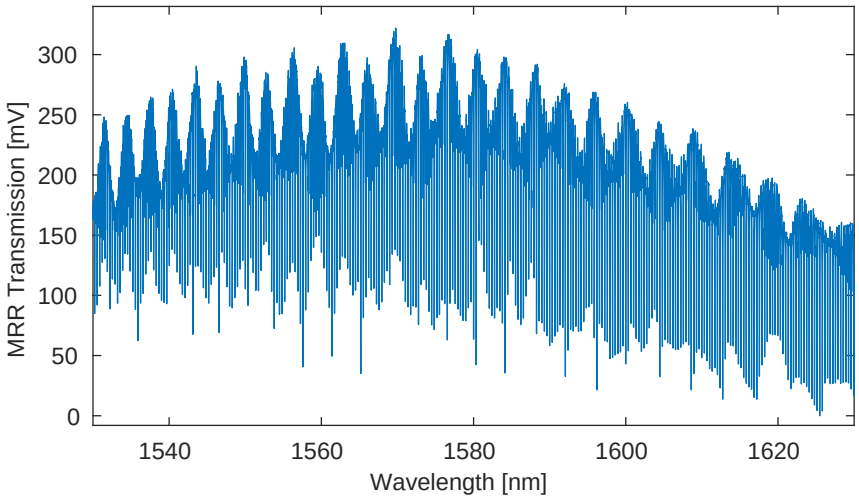

Figure B.34: Transmission spectrum of MRR number 173.

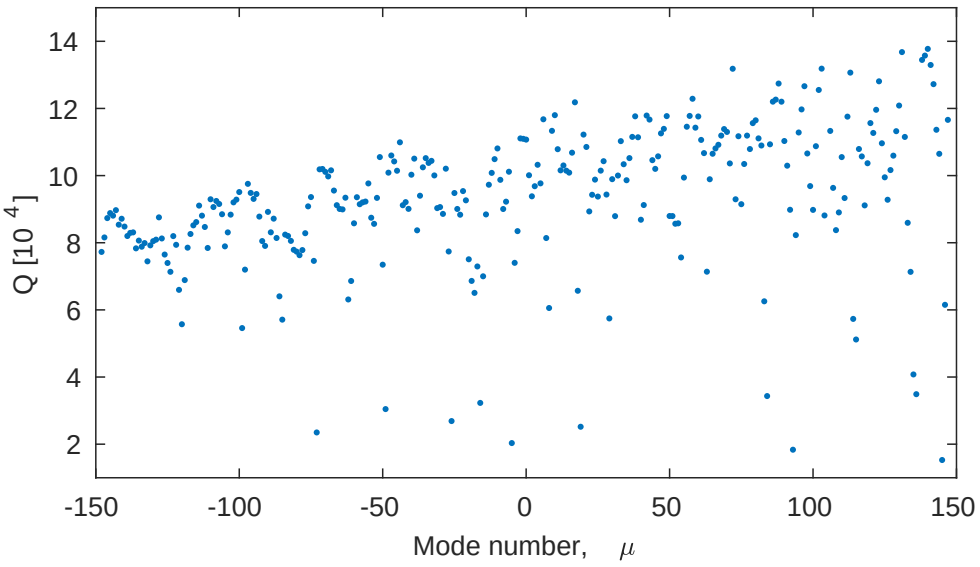

Figure B.35: Q-values of the modes in MRR number 173.

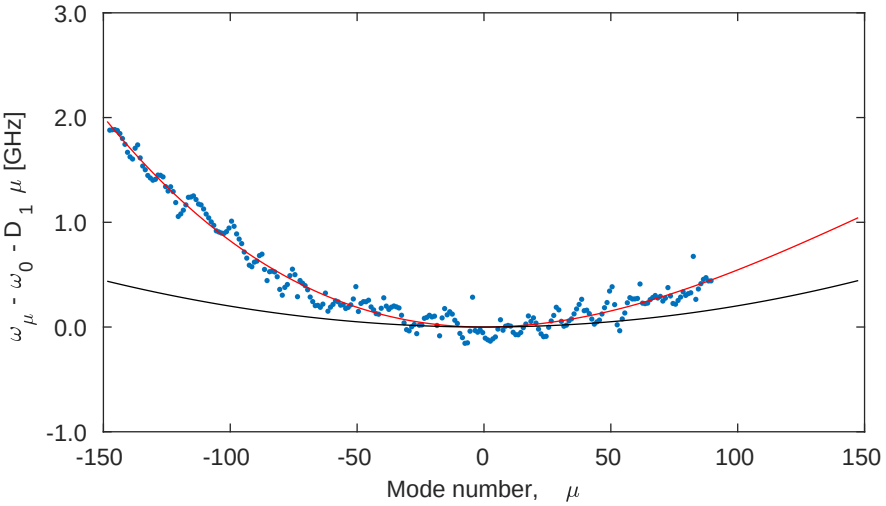

Figure B.36: Mode structure of MRR number 173.

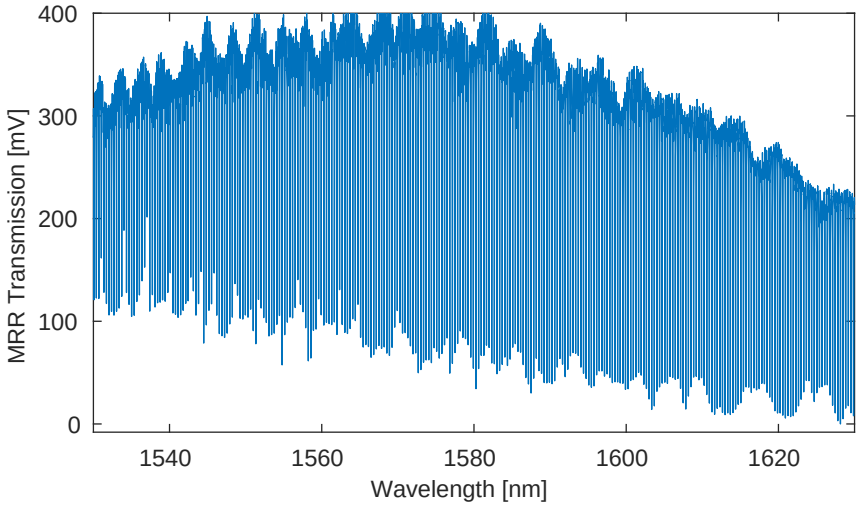

Figure B.37: Transmission spectrum of MRR number 174.

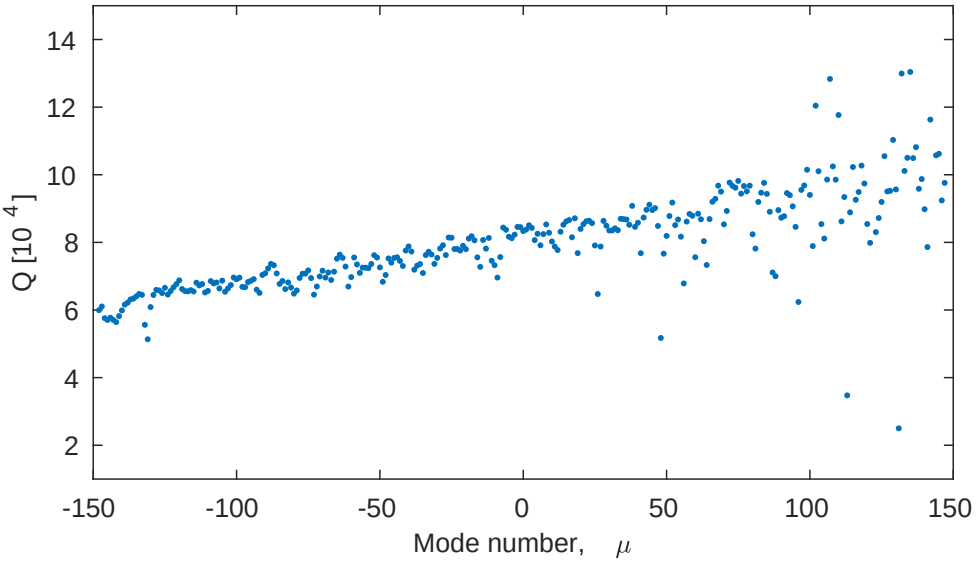

Figure B.38: Q-values of the modes in MRR number 174.

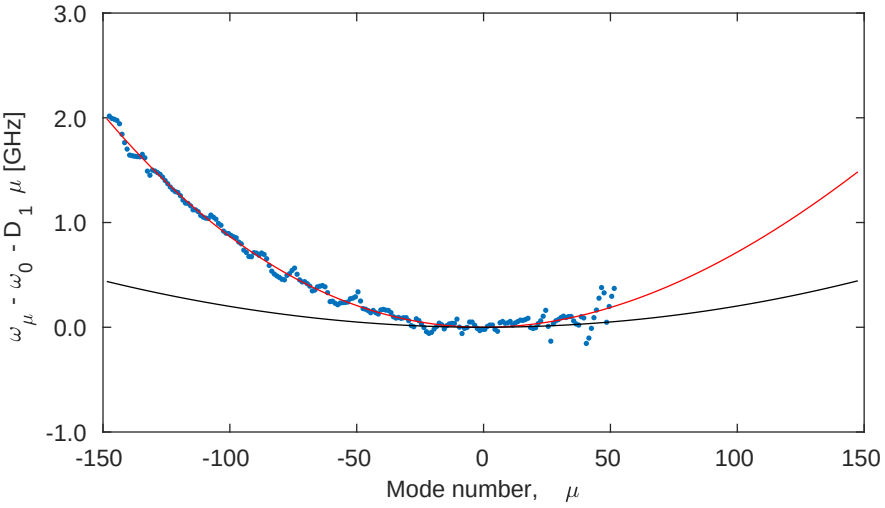

Figure B.39: Mode structure of MRR number 174.

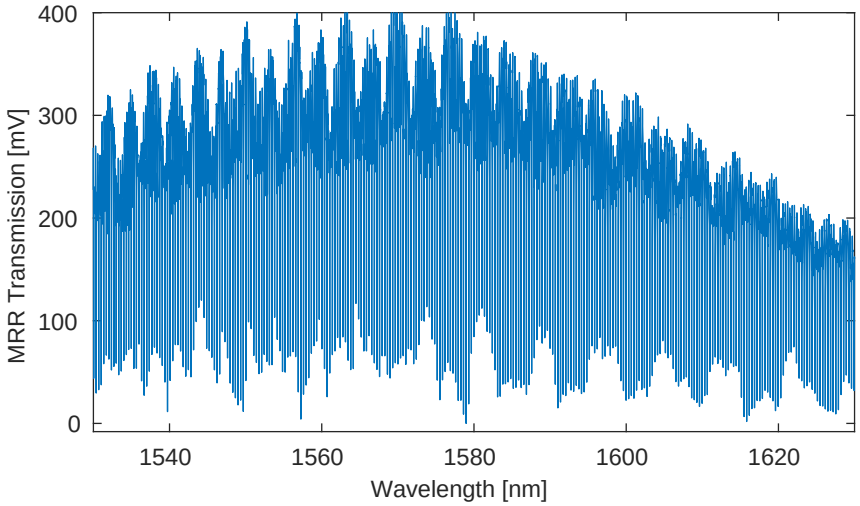

Figure B.40: Transmission spectrum of MRR number 176.

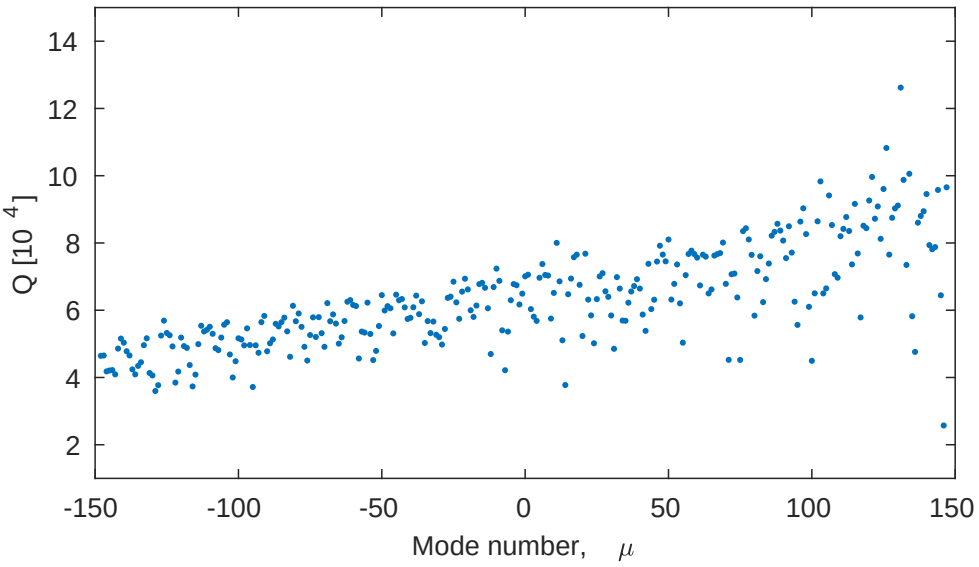

Figure B.41: Q-values of the modes in MRR number 176.

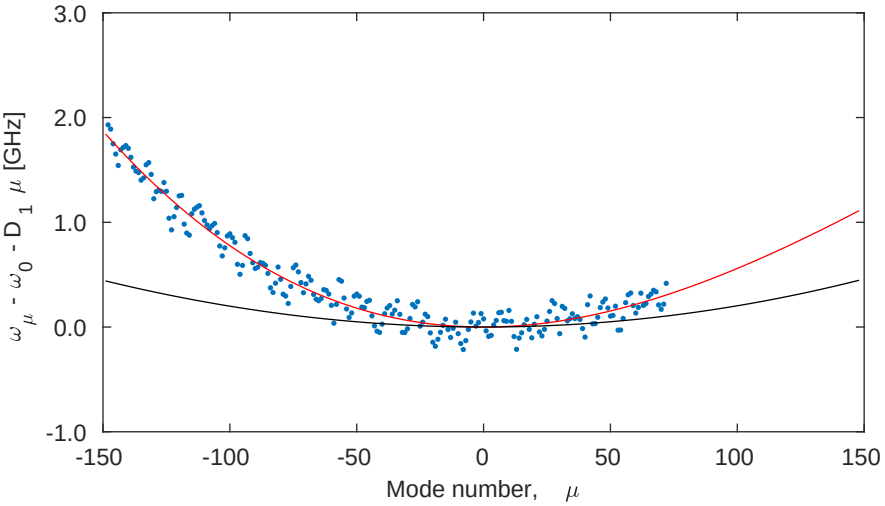

Figure B.42: Mode structure of MRR number 176.

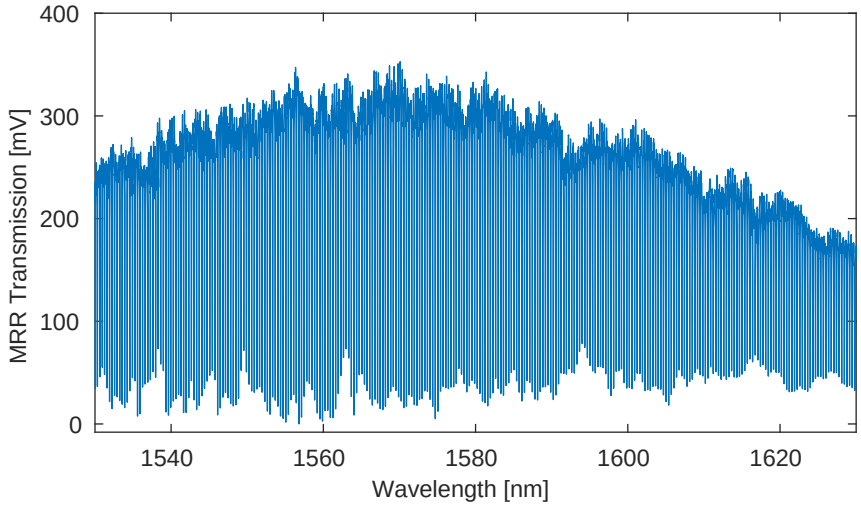

Figure B.43: Transmission spectrum of MRR number 177.

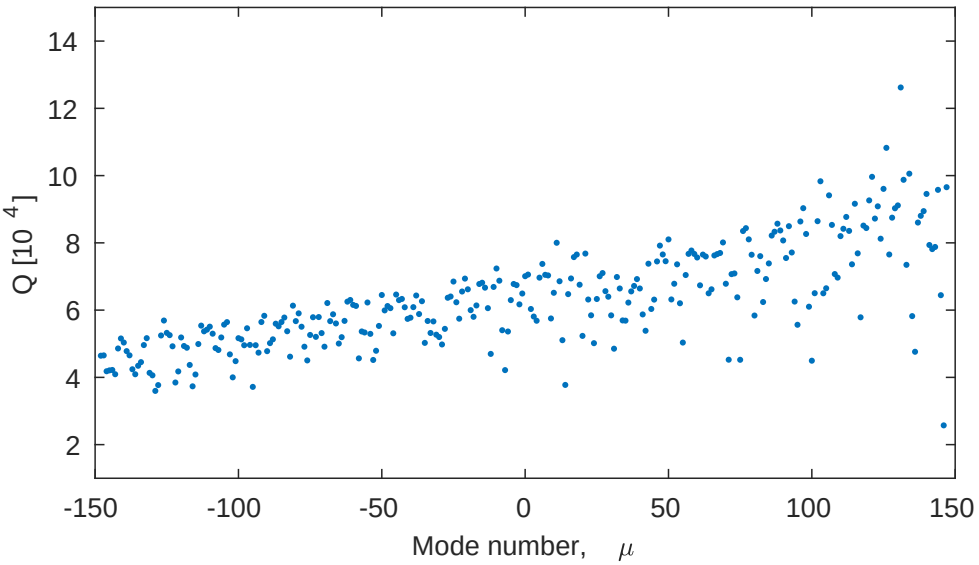

Figure B.44: Q-values of the modes in MRR number 177.

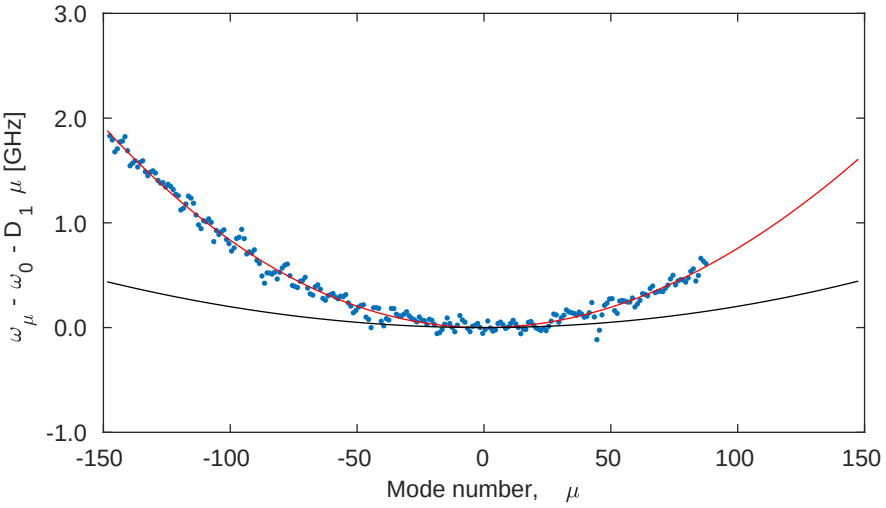

Figure B.45: Mode structure of MRR number 177.

Bibliography

[1] A. Einstein, "Über einen die erzeugung und verwandlung des lichtes betreffenden heuristischen gesichtspunkt," *Annalen der physik*, vol. 322, no. 6, pp. 132–148, 1905.

[2] N. Bohr, "I. on the constitution of atoms and molecules," *The London, Edinburgh, and Dublin Philosophical Magazine and Journal of Science*, vol. 26, no. 151, pp. 1–25, 1913.

[3] I. Ushijima, M. Takamoto, M. Das, T. Ohkubo, and H. Katori, "Cryogenic optical lattice clocks," *Nature Photonics*, vol. 9, no. 3, p. 185, 2015.

[4] C. Grebing, A. Al-Masoudi, S. Dörscher, S. Häfner, V. Gerginov, S. Weyers, B. Lipphardt, F. Riehle, U. Sterr, and C. Lisdat, "Realization of a timescale with an accurate optical lattice clock," *Optica*, vol. 3, no. 6, pp. 563–569, 2016.

[5] M. Schioppo, R. C. Brown, W. F. McGrew, N. Hinkley, R. J. Fasano, K. Beloy, T. Yoon, G. Milani, D. Nicolodi, J. Sherman, *et al.*, "Ultrastable optical clock with two cold-atom ensembles," *Nature Photonics*, vol. 11, no. 1, p. 48, 2017.

[6] W. F. McGrew, X. Zhang, R. J. Fasano, S. A. Schäffer, K. Beloy, D. Nicolodi, R. C. Brown, N. Hinkley, G. Milani, M. Schioppo, *et al.*, "Atomic clock performance enabling geodesy below the centimetre level," *Nature*, p. 1, 2018.

[7] S. L. Campbell, R. Hutson, G. Marti, A. Goban, N. D. Oppong, R. McNally, L. Sonderhouse, J. Robinson, W. Zhang, B. Bloom, *et al.*, "A Fermi-degenerate three-dimensional optical lattice clock," *Science*, vol. 358, no. 6359, pp. 90–94, 2017.

[8] T. Nicholson, S. Campbell, R. Hutson, G. Marti, B. Bloom, R. McNally, W. Zhang, M. Barrett, M. Safronova, G. Strouse, *et al.*, "Systematic evaluation of an atomic clock at 2×10^{-18} total uncertainty," *Nature communications*, vol. 6, p. 6896, 2015.

[9] C.-w. Chou, D. Hume, J. Koelemeij, D. J. Wineland, and T. Rosenband, "Frequency comparison of two high-accuracy Al+ optical clocks," *Physical review letters*, vol. 104, no. 7, p. 070802, 2010.

[10] A. D. Ludlow, M. M. Boyd, J. Ye, E. Peik, and P. O. Schmidt, "Optical atomic clocks," *Reviews of Modern Physics*, vol. 87, no. 2, p. 637, 2015.

[11] C. Lisdat, G. Grosche, N. Quintin, C. Shi, S. Raupach, C. Grebing, D. Nicolodi, F. Stefani, A. Al-Masoudi, S. Dörscher, *et al.*, "A clock

network for geodesy and fundamental science," *Nature communications*, vol. 7, p. 12443, 2016.

[12] S. M. Brewer, J.-S. Chen, A. M. Hankin, E. R. Clements, C. W. Chou, D. J. Wineland, D. B. Hume, and D. R. Leibrandt, "$^{27}al^{+}$ quantum-logic clock with a systematic uncertainty below 10^{-18}," *Phys. Rev. Lett.*, vol. 123, p. 033201, Jul 2019.

[13] L. Essen and J. Parry, "An atomic standard of frequency and time interval: a caesium resonator," *Nature*, vol. 176, no. 4476, p. 280, 1955.

[14] B. I. des Poids and Mesures, *International System of Units (SI)*. Sèvres, France: Le Bureau, 2006.

[15] R. Felder, "Practical realization of the definition of the metre, including recommended radiations of other optical frequency standards (2003)," *Metrologia*, vol. 42, no. 4, p. 323, 2005.

[16] BIPM, "Mise en pratique for the definition of the metre," 2018.

[17] F. Riehle, *Frequency standards: basics and applications*. 2004.

[18] J. Ye, S. Blatt, M. M. Boyd, S. M. Foreman, E. R. Hudson, T. Ido, B. Lev, A. D. Ludlow, B. C. Sawyer, B. Stuhl, *et al.*, "Precision measurement based on ultracold atoms and cold molecules," *International Journal of Modern Physics D*, vol. 16, no. 12b, pp. 2481–2494, 2007.

[19] T. Kessler, C. Hagemann, C. Grebing, T. Legero, U. Sterr, F. Riehle, M. Martin, L. Chen, and J. Ye, "A sub-40-mHz-linewidth laser based on a silicon single-crystal optical cavity," *Nature Photonics*, vol. 6, no. 10, p. 687, 2012.

[20] Y. Jiang, A. Ludlow, N. D. Lemke, R. W. Fox, J. A. Sherman, L.-S. Ma, and C. W. Oates, "Making optical atomic clocks more stable with 10-16-level laser stabilization," *Nature Photonics*, vol. 5, no. 3, p. 158, 2011.

[21] D. G. Matei, T. Legero, S. Häfner, C. Grebing, R. Weyrich, W. Zhang, L. Sonderhouse, J. M. Robinson, J. Ye, F. Riehle, and U. Sterr, "1.5 μm lasers with sub-10 mHz linewidth," *Phys. Rev. Lett.*, vol. 118, p. 263202, Jun 2017.

[22] G. D. Cole, W. Zhang, M. J. Martin, J. Ye, and M. Aspelmeyer, "Tenfold reduction of brownian noise in high-reflectivity optical coatings," *Nature Photonics*, vol. 7, no. 8, p. 644, 2013.

[23] P. G. Westergaard, B. T. R. Christensen, D. Tieri, R. Matin, J. Cooper, M. Holland, J. Ye, and J. W. Thomsen, "Observation of motion-dependent nonlinear dispersion with narrow-linewidth atoms in an optical cavity," *Physical review letters*, vol. 114, no. 9, p. 093002, 2015.

[24] B. T. R. Christensen, M. R. Henriksen, S. A. Schäffer, P. G. Westergaard, D. Tieri, J. Ye, M. J. Holland, and J. W. Thomsen, "Nonlinear spectroscopy of Sr atoms in an optical cavity for laser stabilization," *Physical Review A*, vol. 92, no. 5, p. 053820, 2015.

[25] S. A. Schäffer, B. T. R. Christensen, M. R. Henriksen, and J. W. Thomsen, "Dynamics of bad-cavity-enhanced interaction with cold sr atoms for laser stabilization," *Physical Review A*, vol. 96, no. 1, p. 013847, 2017.

[26] B. T. R. Christensen, *Laser Stabilization with Laser Cooled Strontium.* PhD thesis, 2016.

[27] J. L. Hall, "Nobel lecture: Defining and measuring optical frequencies," *Reviews of Modern Physics*, vol. 78, no. 4, p. 1279, 2006.

[28] F. Adler, M. J. Thorpe, K. C. Cossel, and J. Ye, "Cavity-enhanced direct frequency comb spectroscopy: technology and applications," *Annual Review of Analytical Chemistry*, vol. 3, pp. 175–205, 2010.

[29] M. J. Thorpe and J. Ye, "Cavity-enhanced direct frequency comb spectroscopy," *Applied Physics B*, vol. 91, no. 3-4, pp. 397–414, 2008.

[30] N. Hoghooghi, R. J. Wright, A. S. Makowiecki, W. C. Swann, E. M. Waxman, I. Coddington, and G. B. Rieker, "Broadband coherent cavity-enhanced dual-comb spectroscopy," *Optica*, vol. 6, no. 1, pp. 28–33, 2019.

[31] M.-G. Suh, Q.-F. Yang, K. Y. Yang, X. Yi, and K. J. Vahala, "Microresonator soliton dual-comb spectroscopy," *Science*, p. aah6516, 2016.

[32] J. Mandon, G. Guelachvili, and N. Picqué, "Fourier transform spectroscopy with a laser frequency comb," *Nature Photonics*, vol. 3, no. 2, p. 99, 2009.

[33] A. Foltynowicz, T. Ban, P. Masłowski, F. Adler, and J. Ye, "Quantum-noise-limited optical frequency comb spectroscopy," *Physical review letters*, vol. 107, no. 23, p. 233002, 2011.

[34] C. Gohle, B. Stein, A. Schliesser, T. Udem, and T. W. Hänsch, "Frequency comb Vernier spectroscopy for broadband, high-resolution, high-sensitivity absorption and dispersion spectra," *Physical review letters*, vol. 99, no. 26, p. 263902, 2007.

[35] A. Khodabakhsh, L. Rutkowski, J. Morville, and A. Foltynowicz, "Mid-infrared continuous-filtering Vernier spectroscopy using a doubly resonant optical parametric oscillator," *Applied Physics B*, vol. 123, no. 7, p. 210, 2017.

[36] S. Coburn, C. B. Alden, R. Wright, K. Cossel, E. Baumann, G.-W. Truong, F. Giorgetta, C. Sweeney, N. R. Newbury, K. Prasad, *et al.*, "Regional trace-gas source attribution using a field-deployed dual frequency comb spectrometer," *Optica*, vol. 5, no. 4, pp. 320–327, 2018.

[37] G. B. Rieker, F. R. Giorgetta, W. C. Swann, J. Kofler, A. M. Zolot, L. C. Sinclair, E. Baumann, C. Cromer, G. Petron, C. Sweeney, *et al.*, "Frequency-comb-based remote sensing of greenhouse gases over kilometer air paths," *Optica*, vol. 1, no. 5, pp. 290–298, 2014.

[38] M. J. Thorpe, D. Balslev-Clausen, M. S. Kirchner, and J. Ye, "Cavity-enhanced optical frequency comb spectroscopy: application to human breath analysis," *Optics Express*, vol. 16, no. 4, pp. 2387–2397, 2008.

[39] H. Hu, F. Da Ros, M. Pu, F. Ye, K. Ingerslev, E. P. da Silva, M. Nooruzzaman, Y. Amma, Y. Sasaki, T. Mizuno, *et al.*, "Single-source chip-based frequency comb enabling extreme parallel data transmission," *Nature Photonics*, vol. 12, no. 8, p. 469, 2018.

[40] S. A. Diddams, D. J. Jones, J. Ye, S. T. Cundiff, J. L. Hall, J. K. Ranka, R. S. Windeler, R. Holzwarth, T. Udem, and T. Hänsch, "Direct link between microwave and optical frequencies with a 300 THz femtosecond laser comb," *Physical Review Letters*, vol. 84, no. 22, p. 5102, 2000.

[41] T. Udem, R. Holzwarth, and T. W. Hänsch, "Optical frequency metrology," *Nature*, vol. 416, no. 6877, p. 233, 2002.

[42] N. R. Newbury, "Searching for applications with a fine-tooth comb," *Nature photonics*, vol. 5, no. 4, p. 186, 2011.

[43] C.-H. Li, A. J. Benedick, P. Fendel, A. G. Glenday, F. X. Kärtner, D. F. Phillips, D. Sasselov, A. Szentgyorgyi, and R. L. Walsworth, "A laser frequency comb that enables radial velocity measurements with a precision of 1 cm s-1," *Nature*, vol. 452, no. 7187, p. 610, 2008.

[44] T. Steinmetz, T. Wilken, C. Araujo-Hauck, R. Holzwarth, T. W. Hänsch, L. Pasquini, A. Manescau, S. D'odorico, M. T. Murphy, T. Kentischer, *et al.*, "Laser frequency combs for astronomical observations," *Science*, vol. 321, no. 5894, pp. 1335–1337, 2008.

[45] P. Trocha, M. Karpov, D. Ganin, M. H. Pfeiffer, A. Kordts, S. Wolf, J. Krockenberger, P. Marin-Palomo, C. Weimann, and S. e. a. Randel, "Ultrafast optical ranging using microresonator soliton frequency combs," *Science*, vol. 359, no. 6378, pp. 887–891, 2018.

[46] V. Ataie, P. P. Kuo, A. Wiberg, Z. Tong, C. Huynh, N. Alic, and S. Radic, "Ultrafast absolute ranging by coherent parametric comb," in *Optical Fiber Communication Conference*, pp. OTh3D–2, 2013.

[47] J. Reichert, M. Niering, R. Holzwarth, M. Weitz, T. Udem, and T. Hänsch, "Phase coherent vacuum-ultraviolet to radio frequency comparison with a mode-locked laser," *Physical Review Letters*, vol. 84, no. 15, p. 3232, 2000.

[48] X. Xie, R. Bouchand, D. Nicolodi, M. Giunta, W. Hänsel, M. Lezius, A. Joshi, S. Datta, C. Alexandre, M. Lours, *et al.*, "Photonic microwave signals with zeptosecond-level absolute timing noise," *Nature Photonics*, vol. 11, no. 1, p. 44, 2017.

[49] D. T. Spencer, T. Drake, T. C. Briles, J. Stone, L. C. Sinclair, C. Fredrick, Q. Li, D. Westly, B. R. Ilic, A. Bluestone, *et al.*, "An optical-frequency synthesizer using integrated photonics," *Nature*, vol. 557, no. 7703, p. 81, 2018.

[50] R. Drever, J. L. Hall, F. Kowalski, J. Hough, G. Ford, A. Munley, and H. Ward, "Laser phase and frequency stabilization using an optical resonator," *Applied Physics B*, vol. 31, no. 2, pp. 97–105, 1983.

[51] R. V. Pound, "Electronic frequency stabilization of microwave oscillators," *Review of Scientific Instruments*, vol. 17, no. 11, pp. 490–505, 1946.

[52] E. D. Black, "An introduction to Pound–Drever–Hall laser frequency stabilization," *American journal of physics*, vol. 69, no. 1, pp. 79–87, 2001.

[53] J. Ye, L.-S. Ma, and J. L. Hall, "Ultrasensitive detections in atomic and molecular physics: demonstration in molecular overtone spectroscopy," *JOSA B*, vol. 15, no. 1, pp. 6–15, 1998.

[54] L.-S. Ma, J. Ye, P. Dubé, and J. L. Hall, "Ultrasensitive frequency-modulation spectroscopy enhanced by a high-finesse optical cavity: theory and application to overtone transitions of C_2H_2 and c_2hd," *JOSA B*, vol. 16, no. 12, pp. 2255–2268, 1999.

[55] W. Demtröder, *Laser Spectroscopy, Vol. 2: Experimental Techniques*, vol. 2. Springer, 2008.

[56] M. R. Henriksen, "Cavity enhanced spectroscopy on ultra cold atoms," Master's thesis, 2014.

[57] E. A. Whittaker, M. Gehrtz, and G. C. Bjorklund, "Residual amplitude modulation in laser electro-optic phase modulation," *JOSA B*, vol. 2, no. 8, pp. 1320–1326, 1985.

[58] L. Li, F. Liu, C. Wang, and L. Chen, "Measurement and control of residual amplitude modulation in optical phase modulation," *Review of Scientific Instruments*, vol. 83, no. 4, p. 043111, 2012.

[59] W. Zhang, M. Martin, C. Benko, J. Hall, J. Ye, C. Hagemann, T. Legero, U. Sterr, F. Riehle, G. Cole, *et al.*, "Reduction of residual amplitude modulation to 1×10^{-6} for frequency modulation and laser stabilization," *Optics letters*, vol. 39, no. 7, pp. 1980–1983, 2014.

[60] J. L. Hall, W. Zhang, and J. Ye, "Accurate removal of RAM from FM laser beams," in *Frequency Control Symposium & the European Frequency and Time Forum (FCS), 2015 Joint Conference of the IEEE International*, pp. 713–716, 2015.

[61] S. A. Schäffer, S. S. Adsersen, B. T. Christensen, and J. W. Thomsen, "Large waist cavity for ultra-narrow transition spectroscopy," in *Frequency Control Symposium & the European Frequency and Time Forum (FCS), 2015 Joint Conference of the IEEE International*, pp. 625–629, IEEE, 2015.

[62] W. J. Riley, *Handbook of frequency stability analysis*. 2008.

[63] J. Hald, L. Nielsen, J. C. Petersen, P. Varming, and J. E. Pedersen, "Fiber laser optical frequency standard at 1.54 μm," *Opt. Express*, vol. 19, pp. 2052–2063, Jan 2011.

[64] M. Triches, M. Michieletto, J. Hald, J. K. Lyngsø, J. Lægsgaard, and O. Bang, "Optical frequency standard using acetylene-filled hollow-core photonic crystal fibers," *Optics express*, vol. 23, no. 9, pp. 11227–11241, 2015.

[65] S. Saraf, P. Berceau, A. Stochino, R. Byer, and J. Lipa, "Molecular frequency reference at 1.56 μm using a $^{12}C^{16}O$ overtone transition with the noise-immune cavity-enhanced optical heterodyne molecular spectroscopy method," *Optics letters*, vol. 41, no. 10, pp. 2189–2192, 2016.

[66] T. Ikegami, S. Sudo, and Y. Sakai, *Frequency stabilization of semiconductor laser diodes*. Boston: Artech House, 1995.

[67] I. E. Gordon, L. S. Rothman, C. Hill, R. V. Kochanov, Y. Tan, P. F. Bernath, M. Birk, V. Boudon, A. Campargue, K. Chance, *et al.*, "The HITRAN2016 molecular spectroscopic database," *Journal of Quantitative Spectroscopy and Radiative Transfer*, vol. 203, pp. 3–69, 2017.

[68] M. Kusaba and J. Henningsen, "The $\nu_1+\nu_3$ and the $\nu_1+\nu_2+\nu_4^1+\nu_5^1$ combination bands of $^{13}C_2H_2$. linestrengths, broadening parameters, and pressure shifts," *Journal of molecular Spectroscopy*, vol. 209, no. 2, pp. 216–227, 2001.

[69] K. Nakagawa, M. De Labachelerie, Y. Awaji, and M. Kourogi, "Accurate optical frequency atlas of the 1.5-μm bands of acetylene," *JOSA B*, vol. 13, no. 12, pp. 2708–2714, 1996.

[70] P. Ehlers, A. C. Johansson, I. Silander, A. Foltynowicz, and O. Axner, "Use of etalon-immune distances to reduce the influence of background signals in frequency-modulation spectroscopy and noise-immune cavity-enhanced optical heterodyne molecular spectroscopy," *JOSA B*, vol. 31, no. 12, pp. 2938–2945, 2014.

[71] G. Zhao, T. Hausmaninger, F. M. Schmidt, W. Ma, and O. Axner, "High-resolution trace gas detection by sub-Doppler noise-immune cavity-enhanced optical heterodyne molecular spectrometry: application to detection of acetylene in human breath," *Optics Express*, vol. 27, no. 13, pp. 17940–17953, 2019.

[72] R. J. Jones, W.-Y. Cheng, K. Holman, L. Chen, J. L. Hall, and J. Ye, "Absolute-frequency measurement of the iodine-based length standard at 514.67 nm," *Applied Physics B*, vol. 74, no. 6, pp. 597–601, 2002.

[73] L. Chen, *High-precision spectroscopy of molecular iodine: From optical frequency standards to global descriptions of hyperfine interactions and associated electronic structure*. PhD thesis, 2005.

[74] S. S. Adsersen, "An iodine based thermal optical frequency reference using nice-ohms detection," Master's thesis, 2016.

[75] A. A. Jørgensen, M. R. Henriksen, S. A. Schäffer, and J. W. Thomsen, "Folded-beam waist-expanding cavity for iodine based frequency reference," in *676 W.E. Haereus Seminar (Bonn, Germany)*, 2018.

[76] T. J. Kippenberg, R. Holzwarth, and S. A. Diddams, "Microresonator-based optical frequency combs," *science*, vol. 332, no. 6029, pp. 555–559, 2011.

[77] J. Ye and S. T. Cundiff, *Femtosecond optical frequency comb: principle, operation and applications*. 2005.

[78] D. J. Jones, S. A. Diddams, J. K. Ranka, A. Stentz, R. S. Windeler, J. L. Hall, and S. T. Cundiff, "Carrier-envelope phase control of femtosecond mode-locked lasers and direct optical frequency synthesis," *Science*, vol. 288, no. 5466, pp. 635–639, 2000.

[79] U. Keller, "Recent developments in compact ultrafast lasers," *Nature*, vol. 424, no. 6950, p. 831, 2003.

[80] M. Kourogi, K. Nakagawa, and M. Ohtsu, "Wide-span optical frequency comb generator for accurate optical frequency difference measurement," *IEEE Journal of Quantum Electronics*, vol. 29, no. 10, pp. 2693–2701, 1993.

[81] L. Razzari, D. Duchesne, M. Ferrera, R. Morandotti, S. Chu, B. Little, and D. Moss, "CMOS-compatible integrated optical hyper-parametric oscillator," *Nature Photonics*, vol. 4, no. 1, p. 41, 2010.

[82] J. S. Levy, A. Gondarenko, M. A. Foster, A. C. Turner-Foster, A. L. Gaeta, and M. Lipson, "CMOS-compatible multiple-wavelength oscillator for on-chip optical interconnects," *Nature photonics*, vol. 4, no. 1, p. 37, 2010.

[83] A. A. Savchenkov, A. B. Matsko, V. S. Ilchenko, I. Solomatine, D. Seidel, and L. Maleki, "Tunable optical frequency comb with a crystalline whispering gallery mode resonator," *Physical review letters*, vol. 101, no. 9, p. 093902, 2008.

[84] B. Hausmann, I. Bulu, V. Venkataraman, P. Deotare, and M. Lončar, "Diamond nonlinear photonics," *Nature Photonics*, vol. 8, no. 5, p. 369, 2014.

[85] P. Del'Haye, T. Herr, E. Gavartin, M. Gorodetsky, R. Holzwarth, and T. J. Kippenberg, "Octave spanning tunable frequency comb from a microresonator," *Physical Review Letters*, vol. 107, no. 6, p. 063901, 2011.

[86] S.-W. Huang, H. Liu, J. Yang, M. Yu, D.-L. Kwong, and C. Wong, "Smooth and flat phase-locked Kerr frequency comb generation by higher order mode suppression," *Scientific reports*, vol. 6, p. 26255, 2016.

[87] T. Herr, K. Hartinger, J. Riemensberger, C. Wang, E. Gavartin, R. Holzwarth, M. Gorodetsky, and T. Kippenberg, "Universal formation dynamics and noise of Kerr-frequency combs in microresonators," *Nature Photonics*, vol. 6, no. 7, p. 480, 2012.

[88] M. Pu, L. Ottaviano, E. Semenova, and K. Yvind, "Efficient frequency comb generation in AlGaAs-on-insulator," *Optica*, vol. 3, no. 8, pp. 823–826, 2016.

[89] I. H. Agha, Y. Okawachi, and A. L. Gaeta, "Theoretical and experimental investigation of broadband cascaded four-wave mixing in high-Q microspheres," *Optics Express*, vol. 17, no. 18, pp. 16209–16215, 2009.

[90] A. B. Matsko, A. A. Savchenkov, D. Strekalov, V. S. Ilchenko, and L. Maleki, "Optical hyperparametric oscillations in a whispering-gallery-mode resonator: Threshold and phase diffusion," *Physical Review A*, vol. 71, no. 3, p. 033804, 2005.

[91] J. Li, H. Lee, T. Chen, and K. J. Vahala, "Low-pump-power, low-phase-noise, and microwave to millimeter-wave repetition rate operation in microcombs," *Physical review letters*, vol. 109, no. 23, p. 233901, 2012.

[92] T. Kippenberg, S. Spillane, and K. Vahala, "Kerr-nonlinearity optical parametric oscillation in an ultrahigh-Q toroid microcavity," *Physical review letters*, vol. 93, no. 8, p. 083904, 2004.

[93] D. J. Moss, R. Morandotti, A. L. Gaeta, and M. Lipson, "New CMOS-compatible platforms based on silicon nitride and Hydex for nonlinear optics," *Nature photonics*, vol. 7, no. 8, p. 597, 2013.

[94] X. Ji, F. A. Barbosa, S. P. Roberts, A. Dutt, J. Cardenas, Y. Okawachi, A. Bryant, A. L. Gaeta, and M. Lipson, "Ultra-low-loss on-chip resonators with sub-milliwatt parametric oscillation threshold," *Optica*, vol. 4, no. 6, pp. 619–624, 2017.

[95] H. Jung, C. Xiong, K. Y. Fong, X. Zhang, and H. X. Tang, "Optical frequency comb generation from aluminum nitride microring resonator," *Optics letters*, vol. 38, no. 15, pp. 2810–2813, 2013.

[96] P. Girouard, L. H. Frandsen, M. Galili, and L. K. Oxenløwe, "A deuterium-passivated amorphous silicon platform for stable integrated nonlinear optics," in *CLEO: Science and Innovations*, pp. SW4I–2, 2018.

[97] Y. Zheng, M. Pu, A. Yi, B. Chang, T. You, K. Huang, A. N. Kamel, M. R. Henriksen, A. A. Jørgensen, X. Ou, *et al.*, "High-quality factor, high-confinement microring resonators in 4H-silicon carbide-on-insulator," *Optics express*, vol. 27, no. 9, pp. 13053–13060, 2019.

[98] L. Ottaviano, M. Pu, E. Semenova, and K. Yvind, "Low-loss high-confinement waveguides and microring resonators in AlGaAs-on-insulator," *Optics letters*, vol. 41, no. 17, pp. 3996–3999, 2016.

[99] E. Hemsley, D. Bonneau, J. Pelc, R. Beausoleil, J. L. O'Brien, and M. G. Thompson, "Photon pair generation in hydrogenated amorphous silicon microring resonators," *Scientific reports*, vol. 6, p. 38908, 2016.

[100] S. K. Selvaraja, E. Sleeckx, M. Schaekers, W. Bogaerts, D. Van Thourhout, P. Dumon, and R. Baets, "Low-loss amorphous silicon-on-insulator technology for photonic integrated circuitry," *Optics Communications*, vol. 282, no. 9, pp. 1767–1770, 2009.

[101] J. S. Pelc, K. Rivoire, S. Vo, C. Santori, D. A. Fattal, and R. G. Beausoleil, "Picosecond all-optical switching in hydrogenated amorphous silicon microring resonators," *Optics express*, vol. 22, no. 4, pp. 3797–3810, 2014.

[102] K. Li, M. R. Kossey, and A. C. Foster, "Ultra-low power wavelength conversion in a hydrogenated amorphous silicon microring resonator," in *CLEO: Science and Innovations*, pp. SM1D–7, 2018.

[103] L. Di Cioccio, Y. Le Tiec, F. Letertre, C. Jaussaud, and M. Bruel, "Silicon carbide on insulator formation using the Smart Cut process," *Electronics Letters*, vol. 32, no. 12, pp. 1144–1145, 1996.

[104] Y. Fu, T. Ye, W. Tang, and T. Chu, "Efficient adiabatic silicon-on-insulator waveguide taper," *Photonics Research*, vol. 2, no. 3, pp. A41–A44, 2014.

[105] Q. Li, A. A. Eftekhar, Z. Xia, and A. Adibi, "Unified approach to mode splitting and scattering loss in high-Q whispering-gallery-mode microresonators," *Physical Review A*, vol. 88, no. 3, p. 033816, 2013.

[106] X. Yi, Q.-F. Yang, K. Y. Yang, M.-G. Suh, and K. Vahala, "Soliton frequency comb at microwave rates in a high-q silica microresonator," *Optica*, vol. 2, no. 12, pp. 1078–1085, 2015.

[107] T. Herr, V. Brasch, J. Jost, I. Mirgorodskiy, G. Lihachev, M. Gorodetsky, and T. Kippenberg, "Mode spectrum and temporal soliton formation in optical microresonators," *Physical review letters*, vol. 113, no. 12, p. 123901, 2014.

[108] S. Coen, H. G. Randle, T. Sylvestre, and M. Erkintalo, "Modeling of octave-spanning Kerr frequency combs using a generalized mean-field Lugiato–Lefever model," *Optics letters*, vol. 38, no. 1, pp. 37–39, 2013.

[109] A. K. Vinod, "New route towards internally phase stabilized kerr combs," Master's thesis, 2017.

[110] P. Del'Haye, O. Arcizet, A. Schliesser, R. Holzwarth, and T. J. Kippenberg, "Full stabilization of a microresonator-based optical frequency comb," *Physical Review Letters*, vol. 101, no. 5, p. 053903, 2008.

[111] S. B. Papp, K. Beha, P. Del'Haye, F. Quinlan, H. Lee, K. J. Vahala, and S. A. Diddams, "Microresonator frequency comb optical clock," *Optica*, vol. 1, no. 1, pp. 10–14, 2014.

[112] P. Del'Haye, A. Coillet, T. Fortier, K. Beha, D. C. Cole, K. Y. Yang, H. Lee, K. J. Vahala, S. B. Papp, and S. A. Diddams, "Phase-coherent microwave-to-optical link with a self-referenced microcomb," *Nature Photonics*, vol. 10, no. 8, p. 516, 2016.

[113] S.-W. Huang, J. Yang, M. Yu, B. H. McGuyer, D.-L. Kwong, T. Zelevinsky, and C. W. Wong, "A broadband chip-scale optical frequency synthesizer at 2.7× 10- 16 relative uncertainty," *Science advances*, vol. 2, no. 4, p. e1501489, 2016.

[114] M. R. Henriksen, A. N. Kamel, M. Pu, K. Yvind, and J. W. Thomsen, "Towards actively stabilized micro ring resonator based frequency combs," in *2017 Conference on Lasers and Electro-Optics (CLEO)*, pp. 1–2, IEEE, 2017.

[115] T. Herr, V. Brasch, J. D. Jost, C. Y. Wang, N. M. Kondratiev, M. L. Gorodetsky, and T. J. Kippenberg, "Temporal solitons in optical microresonators," *Nature Photonics*, vol. 8, no. 2, p. 145, 2014.

[116] B. Bloom, T. Nicholson, J. Williams, S. Campbell, M. Bishof, X. Zhang, W. Zhang, S. Bromley, and J. Ye, "An optical lattice clock with accuracy and stability at the 10^{-18} level," *Nature*, vol. 506, no. 7486, p. 71, 2014.

[117] K. Debnath, Y. Zhang, and K. Mølmer, "Lasing in the superradiant crossover regime," *arXiv preprint arXiv:1809.01602*, 2018.

[118] S. A. Schäffer, "Studies of collective effects in atomic strontium," Master's thesis, 2015.

[119] M. Tang, "Modeling lasing in a thermal strontium ensemble," Master's thesis, 2018.

[120] A. Kramida, Yu. Ralchenko, J. Reader, and and NIST ASD Team. NIST Atomic Spectra Database (ver. 5.5.6), [Online]. Available: `https://physics.nist.gov/asd` [2018, October 19]. National Institute of Standards and Technology, Gaithersburg, MD., 2018.